Dynamics of the Plasma-Surface Interface in Capacitively Coupled Radio-Frequency Oxygen Plasmas: Coupling Numerical Simulations with Optical Diagnostics

Arthur Greb

A thesis submitted for the degree of:

PhD

University of York

Department of Physics

September 2013

for Maria

my little angel

Abstract

Plasma processing on industrial scale is becoming increasingly complex, demanding new strategies for process control and monitoring. Of particular interest is the energy transport in the interface region between the non-equilibrium low-pressure plasma and the surface. The individual plasma components have varying properties and exhibit different dynamics, which enable numerous chemical and physical modifications of surfaces simultaneously. Measurements of the *in-situ* surface condition and important chemically active radical species are extremely challenging. The most promising approach to overcome these challenges to achieve advanced process control is the active coupling of numerical simulations and experiments. In this regard, numerical simulations are a well-established technique to study fundamental plasma parameters and plasma dynamics for a variety of discharge sources.

The utilised numerical simulation is an experimentally benchmarked 1D fluid model, with semi-kinetic treatment of electrons and an improved energy dependent ion mobility treatment. This model is applied for a geometrically symmetric and asymmetric capacitively coupled oxygen RF discharge. Within the investigated pressure range of 10 Pa$-$100 Pa the simulations predict that changing surface conditions have a significant effect on dynamics of the plasma-surface interface. In particular, the surface loss probability and lifetime of metastable singlet delta oxygen as well as the secondary electron emission coefficient are identified to substantially influence the electronegativity and the plasma sheath dynamics on a nanosecond timescale. Phase resolved optical emission spectroscopy measurements, utilising different surface materials, confirm these predictions by comparing measured and simulated excitation features for three different optical emission lines.

Through the synergistic coupling of numerical simulations and experiments, the surface work functions as well as other key surface parameters are assessed. Furthermore, the use of an advanced actinometry technique, demonstrated by coupling simple electron kinetic simulations and optical measurements, enables measurements of the spatial distribution of radical atomic oxygen densities and local electron energies over the total discharge volume.

Contents

Abstract iii

List of Figures vii

List of Tables xii

Acknowledgements xiii

Declaration xiv

1. Introduction 1
1.1. Motivation . . . 1
1.2. Outline . . . 3

2. Theoretical Background 5
2.1. Low Temperature Plasmas . . . 5
2.2. Capacitively Coupled Radio-Frequency Plasmas . . . 11
2.3. Plasma Sheath . . . 16
2.4. Population Dynamics of Excited States . . . 19
2.4.1. Corona Model . . . 19
2.4.2. Collisional Radiative Model . . . 21
2.5. Advanced Actinometry . . . 23

3. Plasma Modelling 29
3.1. Modelling Methods . . . 29
3.2. Geometrical Considerations . . . 31
3.3. Governing Equations . . . 32
3.4. Boundary Conditions . . . 35
3.4.1. Self-Consistent Bias Voltage Calculation . . . 37
3.4.2. Secondary Electron Emission . . . 38
3.5. Kinetic Simulation of Electrons . . . 40
3.5.1. Boltzmann Equation and Two-Term Approximation . . . 41
3.5.2. Electron Energy Mobility . . . 42
3.6. Heavy Particle Transport Coefficients . . . 44
3.6.1. Ion Mobility and Diffusion . . . 44
3.6.2. Neutral Particle Diffusion . . . 47
3.6.3. Gas Mixtures . . . 48
3.7. Plasma Chemical Reactions . . . 49
3.8. Solution of the Model . . . 50
3.8.1. Time-Dependent Solver . . . 51

3.8.2. Stationary Solver for Slow Species 53

4. Parameter Studies in a Symmetric Helium-Oxygen Model 55
4.1. Reaction Scheme 55
4.2. Influence of Variable Oxygen Admixture 58
4.3. Parameter Variations with 0.5% Oxygen Admixture 65
4.3.1. Power 65
4.3.2. Pressure 67
4.3.3. Discharge Gap Size 69
4.4. Analysis of Reaction Rates 70

5. Influence of Ion Mobility Treatment on Plasma Dynamics 72
5.1. Reaction Scheme 72
5.2. Symmetric Discharge Geometry 74
5.3. Asymmetric Discharge Geometry 80
5.4. Comparison with Previous Work 84

6. Role of Singlet Delta Oxygen in Oxygen Discharges 90
6.1. Reaction Scheme 90
6.2. Singlet Delta Oxygen Surface Loss Probability 92
6.3. Effective Lifetime of Singlet Delta Oxygen 94
6.4. Impact on Discharge Properties and Dynamics 96

7. Plasma-Surface Interaction 101
7.1. Investigation of Important Surface Parameters 101
7.2. Frequency Analysis of Excitation Rate 106
7.3. Impact of Changing Surface Condition on Plasma Dynamics 110

8. Experiment and Diagnostics 112
8.1. Discharge Chamber and Peripheral Equipment 112
8.2. Electrical Setup 114
8.3. Optical Diagnostics 115
8.3.1. Calibration of Spectral Sensitivity 120
8.3.2. Correction for ICCD Camera Limitations 121
8.3.3. Angle of Incidence Considerations 122

9. Characteristics of Investigated Wafer Materials 126
9.1. Work Function Analysis 126
9.2. Power-Voltage Characteristics 127
9.3. Surface Modifications due to Plasma Treatment 130

10. Determination of Surface Parameters from Excitation Dynamics 133
10.1. Excitation Dynamics under Power and Pressure Variation 133
10.2. Comparison with Simulations to Determine Surface Parameters 138
10.2.1. Surface Parameters from PROES Measurements 138
10.2.2. Surface Parameters from Excitation Frequency Spectrum 140

11. Oxygen Dissociation Degree using Advanced Actinometry **145**
11.1. Local Atomic Oxygen Densities 145
11.2. Radial Atomic Oxygen Distribution 150

12. Conclusions **155**

A. Relevant Energy Levels of Oxygen and Argon **161**

B. Additional Excitation Profiles **163**

C. Optical Narrow Bandpass Filter Transmittance Data **168**

D. List of Publications and Conference Contributions **170**

List of Abbreviations **173**

Bibliography **174**

List of Figures

2.1. General characteristics of a DC discharge. 9
2.2. Illustration of the concept of plasma frequency and quasineutrality 10
2.3. Typical capacitively coupled radio-frequency plasma setup. 11
2.4. Spatial variation of time resolved normalised net charged particle number density and total potential across a symmetric and asymmetric discharge for four different times during the RF cycle. 14
2.5. Typical shape of EEDF for different dominant heating mechanisms. 15
2.6. Classical plasma sheath definition. 16
2.7. Schematic of an equivalent electron step to determine the sheath position. . 18
2.8. Illustration of population dynamics in corona model. 19
2.9. Cross sections and resulting rate coefficients for direct and dissociative electron-impact excitation of the $Ar(2p_1)$, $O(3p^5P)$, and $O(3p^3P)$ states. . . . 25
2.10. Excitation ratios for various values of the dissociation degree over a range of 0 eV−50 eV. 27

3.1. One-dimensional model domain in (a) symmetric and (b) asymmetric configuration of the CCP. 32
3.2. Secondary electron emission coefficients for atomic helium and molecular oxygen ions in dependence of the surface work function. 39
3.3. Ratios of approximated and exact values of the electron energy mobility and diffusion coefficient. 43
3.4. Ion mobility scaling for O_2 and He as background gases in high field region in comparison to experimental data. 45
3.5. Schematic illustration of the distribution of mesh elements in a linear modelling domain. 51
3.6. Flow diagram for time-dependent plasma fluid model solver. 52
3.7. Illustration of a combined time-dependent and stationary solution process, monitoring the convergence of slow and fast species. 54

4.1. Global average particle densities as function of the O_2 admixture. 59
4.2. Mean electron energy and weighted mean electron energy as a function of the O_2 admixture. 60

4.3. Time averaged spatial profiles of electrons, O_2^+ and O^- for two different oxygen admixtures. 61
4.4. Electronegativity as function of the O_2 admixture. 62
4.5. Time and space averaged direct electron-impact ionisation of molecular oxygen. 63
4.6. Time and space resolved direct electron-impact ionisation of molecular oxygen. 64
4.7. Simulated power-voltage and voltage-current characteristic for 0.5% O_2 admixture. 66
4.8. Mean electron energy, weighted mean electron energy, and electronegativity as function of applied power. 67
4.9. Pressure dependence of current density, voltage and voltage-current phase relationship at the centre of the discharge for 0.5% O_2 admixture. 68
4.10. Discharge gap size dependence of dominant charged species densities and weighted mean electron energy for 0.5% O_2 admixture. 69
4.11. Time and space averaged reaction rates for all reactions as stated in table 4.1 on semi-logarithmic scale for 0.5% O_2 admixture. 70

5.1. Voltage-current density characteristic for modified and non-modified models and resulting power density. ($p = 40$ Pa, $V_{rf} = 300$ V) 75
5.2. Time and space resolved ionisation of O_2 molecules through direct electron impact obtained from non-modified and modified symmetrical model. 76
5.3. Weighted time and space averaged ion energies. 77
5.4. Time averaged density profiles of O_2^+, electrons and O^- in the discharge volume for a symmetric discharge geometry using the non-modified and modified models. 78
5.5. Emitted secondary electron number density and total electron number densities in both models at the powered electrode over one rf period. . . . 79
5.6. Time and space resolved ionisation of O_2 molecules through direct electron impact obtained from non-modified model and modified asymmetric model. 81
5.7. Time averaged density profiles of O_2^+, electrons and O^- along the discharge gap for an asymmetric geometry using the non-modified and modified model. 81
5.8. Weighted time and space averaged ion energies with direct comparison of the effect of geometrical asymmetry as well as modification to the model. . 82
5.9. Comparison of experimentally and numerically obtained average electron and negative atomic oxygen ion densities. 84

5.10. Density distributions of electrons, O_2^+ and O^- within discharge domain obtained from RCT model and fluid model simulations. 86
5.11. Density distributions of electrons and O^- within discharge domain obtained from fluid model simulations and experiments. 87
5.12. Density distributions of electrons, O_2^+ and O^- within discharge domain obtained from fluid model simulations and PIC-MCC simulations. 88
5.13. Phase resolved excitation profiles measured and simulated for the corresponding emission at 844.6 nm. 89

6.1. Effective SDO loss rate in plasma volume and at the surface. 94
6.2. Effective loss rate of SDO in plasma region based on volume destruction processes through electrons and negative ions. 95
6.3. Dependence of global SDO content and electronegativity on SDO surface loss probability. 97
6.4. Time averaged spatial distribution of electrons, O_2^+ and O^- for SDO surface loss probability of 6×10^{-4} and 0.6×10^{-4}. 98
6.5. Phase and space resolved electron-impact ionisation of O_2 for SDO surface loss probability of 6×10^{-5} and 2×10^{-3}. 99

7.1. Illustration of relevant surface reaction mechanisms: surface neutralisation and secondary electron emission. 102
7.2. Time and space averaged particle densities of electrons, negative atomic oxygen ions, and positive molecular oxygen ions in dependence of SDO surface loss probability and secondary electron emission coefficient. 102
7.3. Weighted electron energy in dependence of SDO surface loss probability and secondary electron emission coefficient. 103
7.4. Phase and space resolved dissociative excitation of O_2 leading to emission into the 844.6 nm optical emission line for $s_{SDO} = 1 \times 10^{-5}$, $\gamma(O_2^+) = 0.01$ and $s_{SDO} = 2 \times 10^{-3}$, $\gamma(O_2^+) = 0.05$. 104
7.5. Correlation of global electronegativity and the ratio of sheath collapse excitation versus sheath expansion excitation as a function of the SDO surface loss probability. 105
7.6. Excitation function and amplitudes of corresponding frequency components for dissociative electron-impact excitation of oxygen leading to optical emission at $\lambda = 844.6$ nm. 107
7.7. Normalised frequency components of the excitation function in dependence of variable SDO surface loss probability and secondary electron emission coefficient. 109

7.8. Illustration of actual surface condition impact on plasma parameters and plasma dynamics. 110

8.1. Illustration of experimental setup and discharge chamber geometry. 113
8.2. Configuration of image intensifier of the ICCD camera and wavelength dependent photo cathode sensitivity. 117
8.3. Schematic diagram to illustrate PROES measurements. 118
8.4. Illustration of spectral sensitivity calibration of ICCD camera. 121
8.5. Normalised LED emission at 750.0 nm for 25 consecutive time frames (2 ns time step each frame) and the corresponding sinusoidal fit. 122
8.6. Illustration of optical setup for angle of incidence calibration and typical emission profiles for the three optical filter positions. 123
8.7. Measured and fitted transmittance ratios as function of the angle of incidence for the 750.4 nm, 777.4 nm, and 844.6 nm optical bandpass filters. . . 125

9.1. Surface work functions of various wafer materials. 127
9.2. Power-voltage characteristics obtained with a stainless steel wafer in comparison to 1D simulations. 128
9.3. Illustration of hysteresis effect in power-voltage characteristic for a SiO_2 wafer. 130
9.4. Visual comparison of wafer materials before and after exposed to an oxygen plasma for several hours. 131

10.1. Comparison of excitation into the $Ar(2p_1)$ state leading to emission of $\lambda = 750.4$ nm for aluminium, silicon, and gold wafers. 134
10.2. Comparison of excitation into the $O(3p^3P)$ state leading to emission of $\lambda = 844.6$ nm for constant pressure and varying voltage. 136
10.3. Comparison of excitation into the $O(3p^3P)$ state leading to emission of $\lambda = 844.6$ nm for constant voltage and varying pressure. 137
10.4. Phase and space resolved excitation ($\lambda = 844.6$ nm) obtained experimentally for silicon and Teflon wafers, and corresponding simulations matching the experimental observation. 139
10.5. Normalised excitation functions resulting from the observed optical emission line $\lambda = 844.6$ nm for silicon, Teflon, and the matching simulations. . . 141
10.6. Simulated and experimentally obtained frequency components of the excitation rate for the wafer materials silicon, Teflon, and stainless steel. . . . 142

11.1. Maximum excitation ratios under variation of driving voltage and pressure for a silicon wafer. 146
11.2. Dissociation degree as a function of pressure for different wafer materials. 148

11.3. Atomic oxygen density as a function of pressure for different wafer materials. 149
11.4. Dissociation degree and atomic oxygen density as a function of voltage for different wafer materials. 150
11.5. Normalised emission across the wafer surface from the 844.6 nm optical emission line at $t = 15$ ns and corresponding radial emission profile at 5 mm above the electrode. 151
11.6. Radial distribution of electron energy under driving voltage variation and constant pressure of 80 Pa. 152
11.7. Radial distribution of dissociation degrees and corresponding atomic oxygen densities under driving voltage variation and constant pressure of 80 Pa. 153
11.8. Radial distribution of dissociation degrees and corresponding atomic oxygen densities under driving voltage variation and constant pressure of 40 Pa. 154

A.1. Energy levels of Ar I. 161
A.2. Energy levels of O I. 162

B.1. Phase resolved excitation into the Ar($2p_1$), O($3p^5P$), and O($3p^3P$) states using a silicon (Si) wafer under voltage variation. 164
B.2. Phase resolved excitation into the Ar($2p_1$), O($3p^5P$), and O($3p^3P$) states using a silicon (Si) wafer under pressure variation. 165
B.3. Phase resolved excitation into the Ar($2p_1$), O($3p^5P$), and O($3p^3P$) states using a silicon dioxide (SiO_2) wafer under voltage variation. 166
B.4. Phase resolved excitation into the Ar($2p_1$), O($3p^5P$), and O($3p^3P$) states using a silicon dioxide (SiO_2) wafer under pressure variation. 167

C.1. Transmittance data for (750.46 ± 0.50) nm optical bandpass filter. 168
C.2. Transmittance data for (777.45 ± 1.75) nm optical bandpass filter. 169
C.3. Transmittance data for (844.79 ± 0.95) nm optical bandpass filter. 169

List of Tables

3.1. Zero field ($E = 0$) mobility μ_0 and diffusion coefficient D_0 for selected species in helium and oxygen as background gases. 47
3.2. Diffusion coefficients $D_{i,j}$ for main neutral species in helium and oxygen as background gases for a given set of Lennard-Jones parameters σ and ϵ/k_B. 48
3.3. Some reaction processes important for plasma modelling. 50

4.1. Elementary reactions and corresponding rate coefficients in a He/O_2 discharge 56

5.1. Elementary reactions and corresponding rate coefficients in a O_2 discharge 73
5.2. Zero field ($E = 0$) mobilities μ_0 and diffusion coefficients D_0 in a O_2 discharge. 74

6.1. Elementary reactions and corresponding rate coefficients in a O_2 discharge including $O_2(^1\Delta)$ 91

8.1. Emission wavelength, radiative lifetime, and quenching coefficients of $Ar(2p_1)$, $O(3p^5P)$, and $O(3p^3P)$ atoms at room temperature. 120
8.2. Spectral sensitivity calibration factors for the ICCD camera in two different optical system setups. 121

10.1. Overview of estimated surface work functions and resulting secondary electron emission coefficient (using equation 3.21) 135
10.2. Overview of determined SDO surface loss probabilities. 143

Acknowledgements

First and foremost, I would like to thank my supervisors Timo Gans and Deborah O'Connell for giving me the opportunity to pursue application oriented plasma physics research and making the transition from the Queen's University Belfast to the University of York seemingly effortless. Thanks to their supervision, I was able to work independently, but could rely on their critical assessment of my results whenever a second opinion was needed. Without the invaluable discussions we had, this thesis would only be half as exciting.

I would like to express my deepest gratitude to Kari Niemi and Jochen Waskoening who were majorly responsible for making my start at the Queen's University Belfast an enjoyable endeavour. It has been a great pleasure to work with Kari over the whole course of the PhD and I very much appreciate his friendship.

My most humble and sincere thanks to Bill Graham for his support and good cheer. Special thanks goes to Charles Mahony for his friendship and company during my time in Belfast, but mainly for his endless good humour. I would also like to acknowledge all fellow PhD students both at the Queen's University Belfast as well as the University of York, and in particular: Andrew Gibson, for his calm and pleasant nature and his invaluable help with the experimental part of my research; Andrew West and Andrew Allen for the great company during my time in York.

I thank Intel Ireland (Ltd.) for financial support and in particular Niall MacGearailt and Gerard J. Ennis for motivating me and making me believe that my research might make a difference.

The entire team of support staff at the Physics Department of the University of York, with very special thanks to Rachel Stephenson and Laurie Whiteley, who were a great help in all administrative matters; Richard Armitage and Neil Johnson, who made sure the experiments could be run smoothly and with as little delay as possible; John Bramley from IT for his expertise with Linux; Lydia Aarons, who reminded me of all formal university report submission deadlines; and Anne Stroughair for her support and guidance in all financial matters.

I also thank my parents for their unconditional support and my lovely grandmother, who couldn't believe I was writing a "book".

Last, but not least I would like to thank my extraordinary wife, Anna, for her love and patience with the writing process, and especially for her moral support during the hard times we had to go through. Without her, I would have never come thus far.

Declaration

Statement of originality

It is essential to state that the work presented here is original and that no part of this thesis has been submitted for a degree elsewhere. However, the contents of several chapters have appeared, or are to appear, in journals. Also the content of several chapters was presented at conferences. An overview can be found in appendix D: List of Publications and Conference Contributions.

Role of the author

The presented numerical model was developed by the author, based on approaches used in the literature. Furthermore, the experiments were set up and experimental data was taken by the author with the assistance of A. R. Gibson from Queen's University Belfast. The data was subsequently processed and interpreted by the author only. The author developed the advanced actinometry method to compare experimentally obtained ratios of the 750.4 nm Ar I, 777.4 nm O I, and 844.6 nm O I optical emission lines with simple kinetic simulations.

This thesis was written by the author only.

1. Introduction

1.1. Motivation

Plasmas have undoubtedly become an important part of modern day life with particular regard to their applicability in the lighting, semiconductor or material processing industry. Generally, plasmas can be classified as forth state of matter beside solids, liquids and gases. By definition, a plasma is a quasineutral fully or partially ionised gas in which all charged particles, i.e. electrons, positive and negative ions, exhibit collective behaviour. Apart from technical applications they are interesting for fundamental research due to their variability and flexibility. A common categorisation of plasmas is done in thermal and non-thermal plasmas.

In thermal or high temperature plasmas all components are usually in thermal equilibrium with a significant fraction of the gas being ionised. Electrons, ions and neutrals can be described by the same temperature ranging from several thousand Kelvin to millions of Kelvin. This makes them important as energy converters in fusion experiments or as deliverers of heat to surfaces in welding applications.

In contrast, in low temperature plasmas the components are not in thermal equilibrium and only a very small fraction of the gas is ionised. Electrons, as the much lighter particles, exhibit much higher temperatures than the heavy particles which stay roughly at room temperature. Despite this, chemically active species are efficiently produced by the much hotter electrons, e.g. by dissociation of an inert molecular gas. Generally, non-thermal plasmas are operated at low gas pressures where the lower collisionality helps to prevent thermodynamical equilibrium.

These unique properties make non-thermal plasmas play a key role in technological applications. Some of the most prominent application examples are treatment of thermally sensitive materials, use as light sources (lighting, display industry), for surface

modifications (surface hardening, wettability), in various fields of medicine (influence on cell growth, sterilisation) or in etching and deposition processes (microelectronics, coatings).

The development of non-equilibrium low pressure plasma sources, especially for technological applications, has been of rapidly growing interest over the past years. In this context, non-equilibrium low pressure capacitively coupled plasmas (CCP) are well established for technological applications, in particular for etching and deposition processes in the semiconductor industry. Capacitively coupled discharges can be operated at pressures ranging from about 0.1 Pa to atmospheric pressures and at powers ranging from a few W to several kW. Typically, the driving frequency is $f = 13.56$ MHz and the plasma density is $n_p \approx (10^{15} - 10^{18})$ m^{-3} in the bulk.

Despite the enormous relevance of such non-thermal plasmas for industrial applications the fundamental processes are usually not fully understood. The delicate environment of these low pressure plasmas and the increasing complexity in plasma processing for nano-structures demand new strategies for process control and plasma monitoring. The energy transport mechanisms and radical species formation in the plasma-surface interface region are of particular importance. Without detailed comprehension of power dissipation mechanisms under industrially relevant conditions, plasma processes can only be optimised empirically, but not predictively on a scientific basis. The non-intrusive measurement of *in-situ* surface conditions and radial species densities, which strongly affect the plasma-surface interaction processes, is therefore of key importance but extremely challenging. Particularly, the surface loss probability of metastable particles and the secondary electron emission through impacting ions as well as atomic oxygen in these complex environments are expected to strongly influence the plasma.

Despite the actual plasma complexity, numerical simulations are capable of accurately describing the intrinsic plasma processes and thereby improving the fundamental understanding of low temperature and low pressure radio-frequency driven plasmas. In particular, fluid simulations are commonly used due their capability to easily solve complex plasma chemical reactions. Therefore, new concepts for process control and plasma monitoring have been developed based on the combination of numerical simulations and advanced ultra-fast optical plasma diagnostics.

Using this technique for new process control strategies will significantly benefit critical nano-structure etching processes and radical-sensitive material treatments.

1.2. Outline

The thesis is organised as follows:

Chapter 2 contains a brief description of properties associated with low-temperature plasmas, with special regard to capacitively coupled radio-frequency plasmas. Plasma sheath formation as well as population dynamics of excited states are presented.

Chapter 3 gives a general overview of available numerical modelling methods, including a detailed description of the applied modelling method in this thesis.

In **Chapter 4**, the impact of residual oxygen in a helium-oxygen plasma is analysed by means of an systematic parametric study. Reaction rates are discussed and set into relation allowing to draw conclusions on the importance of oxygen in such plasmas.

Chapter 5 discusses the relevance of a correct ion mobility treatment in fluid simulations of plasma discharges. Therefore, symmetric and asymmetric discharge geometries are considered and the results are compared to research of independent work groups.

In **Chapter 6**, the role of metastable singlet delta oxygen in oxygen discharges is explored on the basis of the surface loss probability and the effective lifetime. As result, the impact on discharge properties and dynamics is investigated.

In **Chapter 7**, important plasma-surface interaction processes are identified and a systematic study of their influence, particularly on electron-impact excitation is examined. Conclusively, the mutual dependence of actual surface condition and plasma properties is discussed.

Chapter 8 introduces the experimental measurements, including the used discharge chamber, electrical and other peripheral equipment as well as the applied optical diagnostics. Furthermore, the experimental method to measure nanosecond resolved excitation dynamics, from which various plasma parameters can be deduced, is presented.

In **Chapter 9**, the utilised wafer materials with distinct surface conditions and properties are characterised.

Chapter 10 presents the conducted phase resolved excitation dynamics measurements

and discusses the determination of relevant surface parameters by comparing experiments to simulations.

Chapter 11 discusses the measured local and spatially resolved atomic oxygen densities as well as electron energies.

In **Chapter 12**, the main conclusions are summarised and a brief outlook for future research is presented.

2. Theoretical Background

In this chapter, a general overview of low temperature plasmas is given. Basic characteristics of plasma discharges and the sustainment criterion are discussed for direct current discharges. For alternating current discharges, the plasma frequency is derived and the concept of quasineutrality is explained. A typical setup for a capacitively coupled radio-frequency plasma is presented and the spatio-temporal behaviour of the plasma is discussed based on the electrode configuration, development of a bias voltage, heating mechanisms and the sheath motion. Population dynamics of excited states is introduced by means of a simple corona model and an extended collisional-radiative model. Finally, the use of an advanced actinometry approach is motivated.

2.1. Low Temperature Plasmas

Low temperature plasmas, or non-thermal plasmas, are defined to be weakly ionised (ionisation degree $< 10^{-4}$) and not to be in thermal equilibrium. Thus, they are generally referred to as non-equilibrium plasmas. In a regime where the plasma is in thermal equilibrium all plasma species (*neutrals, ions, electrons*) will have the same temperature $T = T_n = T_i = T_e$. For example, this condition is fulfilled in fusion plasmas. However, due to the high mass difference between electrons and ions many collisions are necessary to achieve a thermal equilibrium. In that case the energy content of the plasma can be described by a Maxwellian distribution function which represents a velocity distribution $f(v)$ of maximum entropy:

$$f(v) = n \left(\frac{m}{2\pi k_B T} \right)^{\frac{3}{2}} \exp\left(-\frac{mv^2}{2k_B T} \right) \tag{2.1}$$

Here, n represents the number density, m the mass, v the velocity and T the temperature of the involved particles, $k_B = 1.3807 \times 10^{-23}$ JK^{-1} is the Boltzmann constant. From this

velocity distribution the mean kinetic particle energy $\langle \epsilon \rangle$ follows as:

$$\langle \epsilon \rangle = \frac{\int \frac{1}{2} m v^2 f(v) d^3 v}{\int f(v) d^3 v} = \frac{3}{2} k_B T \tag{2.2}$$

Equation 2.2 motivates the use of a temperature concept to describe the particles' energy within a plasma. In spite of that, several different temperatures can be associated with a plasma so that ions and electrons can have individual Maxwellian distributions with different temperatures T_i and T_e. This originates from the fact that the collision rate of ions and electrons among themselves is much higher than the direct collision rate between ions and electrons. Accordingly, both species can be associated with their own partial thermal equilibrium temperature while usually no interchange of temperatures takes place between different species [1].

Temperatures within the plasma mainly depend on the electrical power coupled into the plasma. Due to their much higher mobility electrons are heated more effectively by electrical excitation, whereas ions efficiently interchange energy with neutral particles through collisions. Generally, in non-thermal plasmas it can be assumed that electrons as well as ions do not reach thermal equilibrium and exhibit a non-Maxwellian distribution. In this respect, electrons typically possess a much higher temperature than ions and neutral particles ($T_e \geq 11\,000\,K \gg T_i, T_n$) which temperatures lie in the range of the room temperature ($T_i \approx T_n \approx 300$ K).

Discharges where a relatively small number of collisions occurs and a thermal equilibrium is effectively suppressed can be realised easily at low pressures (0.1 Pa$-$1000 Pa). This creates a broad spectrum of possible applications especially for industrial purposes. For example, those discharges can be used as miniature factories where feed gases are used to produce "cold" chemically active species to then modify thermally sensitive surfaces at room temperature.

The fundamental production processes of non-thermal plasmas can be divided into two groups regarding the electrical power coupling. Firstly, direct current (DC) discharges and secondly, alternating current (AC) discharges.

DC discharges have an apparent advantage - their macroscopic time independence. Thereby, DC discharges are theoretically easier to describe than AC discharges. However, the necessity for continuous current, that provides the power to sustain the dis-

charge presents an additional complication to the operation.

Generally, a cylinder symmetrical enclosed configuration with the anode on one side and the cathode on the other side is considered. The gap between the electrodes is filled with gas. This type of configuration has been well studied [2].

In case of an applied voltage difference at the electrodes, free charge carriers are accelerated in the electric field and may ionise gas particles on impact. As possible sources for the initial charge carriers serve usually cosmic radiation or photo-ionisation. The ionisation can be amplified under the presence of a sufficient voltage by an electron avalanche that increases the charge flux Γ in direction of the electric field. Nevertheless, the flux will still remain dependent on the initial number of available free charge carriers, i.e. the source term S_{ext}:

$$d\Gamma = \alpha_{Td}\Gamma dx + S_{ext}dx \tag{2.3}$$

The amplification factor α_{Td} equates to the number of ionisation processes per unit length and electron, and is also referred to as "1st Townsend coefficient".

The discharge ignition depends on the quantity of initial free charge carriers, on the strength of the electric field as well as on the gas pressure. The latter is proportional to the particle number density and to the mean free path of the electrons respectively. Since these kind of discharges are strictly bound to an external electron source they are also called dependent or Townsend discharges.

In contrast to Townsend discharges the electron production in independent discharges is not solely caused by an external source. These glow discharges are sustained mainly by secondary electron emission from the surfaces. The production process is strongly driven by the applied electric field. If it is sufficient high, secondary electrons will be emitted through electron-impact at the anode as well as through ion impact at the cathode. However, secondary electrons produced at the anode cannot contribute to sustain the plasma because they are immediately accelerated back to the anode and lost. In contrast, secondary electrons emitted at the cathode as a result of ion impact are beam like accelerated into the plasma due to the electric field and ionise gas particles. The yield of secondary electrons, produced by positive ions at the cathode, is described by the so-called γ_{Td}-coefficient or "2nd Townsend coefficient".

An important condition for sustaining the glow discharge is that the charge carrier loss must balance their gain. Thereby, the ignition criteria for glow discharges with an electrode gap d can be derived as:

$$\alpha_{Td} d = \ln\left(1 + \frac{1}{\gamma_{Td}}\right) \tag{2.4}$$

Discharges where the charge carrier multiplication is dominated by electron avalanches in the plasma bulk are also known as "α-mode discharges" corresponding the amplification factor α_{Td}. In spite of that, discharges where the charge carrier multiplication is mainly driven by ion impact at the cathode are called "γ-mode discharges". It is obvious that in the γ-mode the electron production is determined by the electrode material. Whilst the discharge is normally in α-mode at low power, an increase of power yields a higher ion impact at the cathode and thereby an increased production of secondary electrons so that the discharge transits into the γ-mode.

Considering that α_{Td} depends on the ionisation energy of the background gas as well as on the applied voltage and pressure, equation 2.4 can be transformed to:

$$V = \frac{B_P pd}{\ln(A_P pd) + \ln[\ln(1 + \gamma_{Td}^{-1})]} \tag{2.5}$$

Where V is the ignition voltage, B_P corresponds to a gas specific factor which includes the ionisation energy and the electron-impact ionisation cross section, p is the pressure and A_P is an empirically obtained proportionality factor.

By means of equation 2.5 the so-called "Paschen curve" can be illustrated (figure 2.1(a)). For high values of pd the voltage for which ignition is possible increases linearly with $B_P pd$. However, for lower values of pd the curve exhibits a minimum ignition voltage under which the ignition of the plasma is not possible any more. From a power efficiency perspective, this minimum ignition voltage and the corresponding pd value can be regarded as optimal plasma operation parameters. Furthermore, a lower threshold exists for the pd value, which depends on the γ_{Td}-factor and the electrode material respectively. This threshold follows from the divergence of the denominator in equation 2.5.

The properties of Townsend and glow discharges can be described in a general voltage-

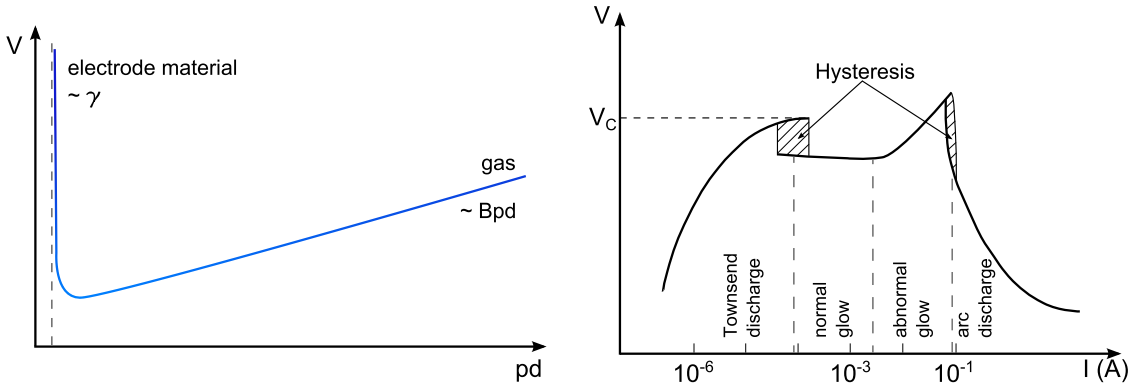

(a) "Paschen curve". (b) Voltage-current characteristic.

Figure 2.1.: General characteristics of a DC discharge.

current characteristic if one assumes the current I as main controlling variable. The current values shown in figure 2.1(b) are representative for a typical DC discharge in a glass cylinder of several cm diameter at a few 100 Pa pressure. However, it has to be noted that the current values are also influenced by several other parameters such as the used gas or the surface area of the electrodes. Therefore, these values need to be understood as rough reference points.

At currents below $I \approx (10^{-4} - 10^{-5})$ A the discharge is dependent on an external source of initial electrons. As the current increases the glow steadily builds up until the transition into the normal glow is reached at a voltage V_C. This transition is characterised by its rapid voltage drop due to the expansion of the plasma and is usually accompanied by a hysteresis effect.

The following flat normal glow discharge region generally exhibits a slightly negative slope dV/dI. Here, the voltage remains roughly constant while the current increases which is a consequence of an expanding plasma. If the currents exceeds a certain value (here: $I \approx 5 \times 10^{-2}$ A) the voltage also starts to increase again (abnormal glow). A further increase of the current leads to an sudden voltage drop at $I \approx 10^{-1}$ A, again characterised by hysteresis. This regime is known as arc discharge because a direct breakdown of secondary electrons between anode and cathode develops. The voltage continues to decrease asymptotically with increasing current.

Apart from the use of a direct current to operate low temperature plasmas, an AC voltage can also be applied at the electrodes to excite the gas. However, electrons and

ions respond to the electric field differently due to their distinct inertia.

If electrons and ions are displaced in a plasma against each other by a distance Δ, an internal electric field builds up which counteracts the particles' motion to re-establish quasineutrality (see figure 2.2). The essential criterion for quasineutrality is that the considered plasma dimension must be bigger than the Debye length $\lambda_D = \sqrt{\epsilon_0 k_B T/(e^2 n_e)}$ [3]. Due to their lower inertia electrons oscillate around the equilibrium position with a characteristic frequency, the so-called plasma frequency ω_p. This oscillation takes place on a small enough timescale so that the heavier ions cannot respond to the alternating electric field and therefore are assumed to remain static.

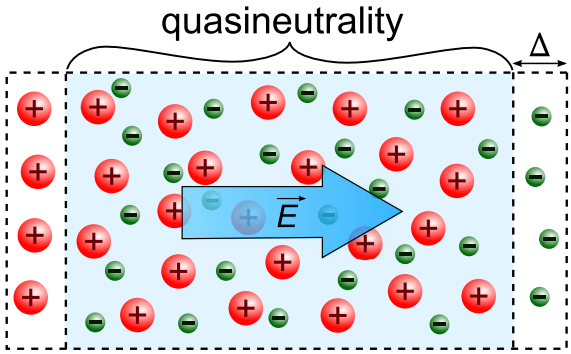

Figure 2.2.: Illustration of the concept of plasma frequency and quasineutrality

A mathematical expression for the plasma frequency ω_p can be obtained under the following assumptions: (1) no external magnetic field; (2) no thermal motion ($k_B T = 0$); (3) the plasma is infinite and (4) the electron and ion motion is confined to one dimension [4].

$$\omega_{p_{e,i}} = \sqrt{\frac{e^2 n_{e,i}}{\varepsilon_0 m_{e,i}}} \tag{2.6}$$

Here, e is the elementary charge, $n_{e,i}$ are the number densities of electrons and ions, respectively, $m_{e,i}$ are their masses and ε_0 is the permittivity of vacuum.

Three possible scenarios can be distinguished, if an external electric field with frequency ω is applied. Firstly, the external driving frequency lies below the ion and electron plasma frequency ($\omega < \omega_{p_i} < \omega_{p_e}$). In this case, both particle species can easily follow the change of the electric field and the discharge shows a similar behaviour as a

DC discharge. Secondly, the driving frequency exceeds both the ion and electron plasma frequency ($\omega_{p_i} < \omega_{p_e} < \omega$). A plasma cannot be ignited under this conditions because neither ions nor electrons can follow or be accelerated by the external field. Finally, if an external driving frequency is chosen which lies between the plasma frequencies of electrons and ions ($\omega_{p_i} < \omega < \omega_{p_e}$), electrons will respond to the changing electric field while ions won't. Because of the AC excitation charge carriers will remain "trapped" within the plasma and not easily get lost at the electrodes so that much higher particle number densities are achievable than in DC discharges. Typical excitation frequencies lie in the range of several kHz to MHz (radio-frequency), with $f = 13.56$ MHz as the most prominent example, and for this reason these plasmas are mainly known as RF plasmas or RF discharges.

2.2. Capacitively Coupled Radio-Frequency Plasmas

A typical setup for capacitively coupled plasmas (CCP) consists of two plane parallel electrodes embedded in a vacuum chamber and is illustrated in figure 2.3.

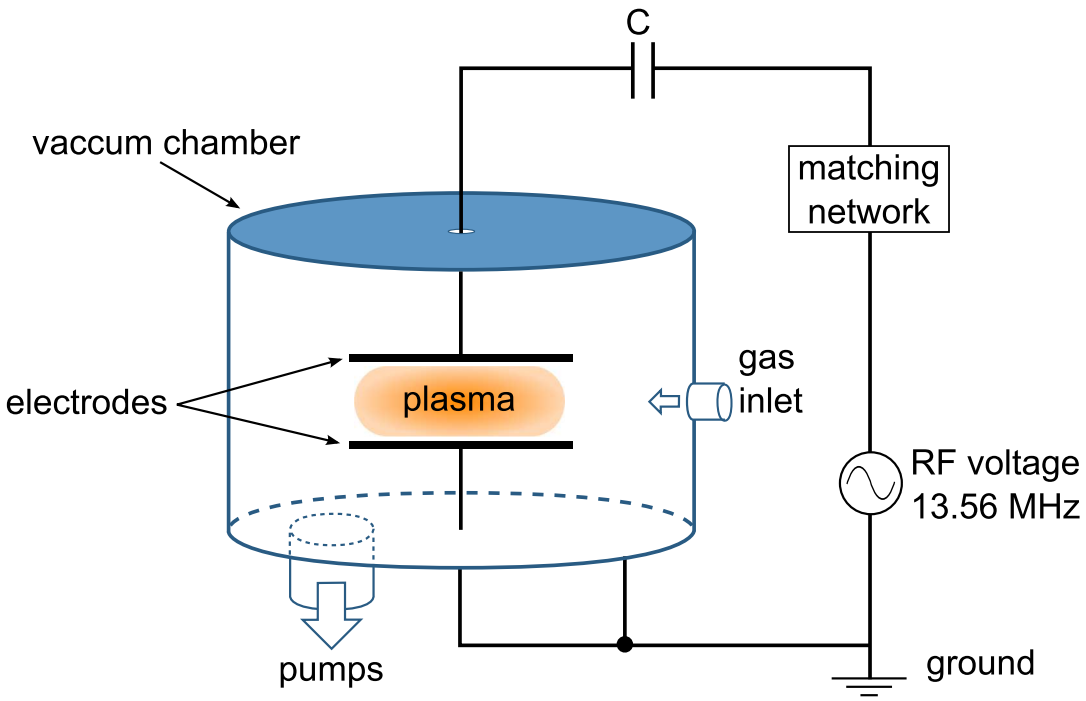

Figure 2.3.: Typical capacitively coupled radio-frequency plasma setup.

The vacuum chamber and one of the electrodes are electrically grounded while the other electrode is powered by a sinusoidal RF voltage via an impedance matching network. This matching network guaranties an efficient power coupling into the discharge by matching the impedance of the discharge setup to the output impedance of the RF voltage generator. Furthermore, a blocking capacitor C is typically located between powered electrode and matching network or more often integrated into the matching network.

Due to this blocking capacitor, there is no net charge transport across the discharge time averaged over one RF cycle (T_{rf}). This means that the positive particle (ions) fluxes balance the negative particle (electrons) fluxes. However, as result of the higher electron mobility compared to the ion mobility a positive net charge region emerges in the discharge in front of the electrodes - the so-called sheath region. In the sheath region positive charge carriers are accelerated towards and impact the electrodes so that effectively positive charge is lost from the discharge within one RF cycle. To compensate the loss of positive charge, electrons leave the discharge during the period of sheath collapse.

In practice, the discharge dynamics are not ideally symmetric. Generally, the symmetry is determined by the electrode surface areas. Since the vacuum chamber walls are typically grounded as indicated in figure 2.3, the total grounded electrode surface area exceeds the powered electrode surface area. This can create a highly asymmetric discharge with a larger voltage drop between plasma and driven electrode than between plasma and grounded electrode. As consequence, a so-called "DC bias voltage" develops at the driven electrode with respect to ground. The DC bias voltage is predominantly negative and results in an enhanced ion impact of the driven electrode. This is a welcome effect which is widely exploited in technological applications, in particular for plasma etching applications in the semiconductor industry. The DC bias voltage is determined by the voltage drops between plasma and electrode and can be related to the surface areas in the following way:

$$\frac{V_1}{V_2} = \left(\frac{S_2}{S_1}\right)^q \tag{2.7}$$

$$\Rightarrow \quad V_{dc} = -(V_1 - V_2) = -V_1\left[1 - \left(\frac{S_1}{S_2}\right)^q\right] \tag{2.8}$$

Here the indices 1 and 2 denote the powered and grounded electrodes, respectively, V_1 and V_2 are the corresponding potential drops, S_1 and S_2 the surface areas and $q \leq 2.5$ is an empirically found scaling factor depending on additional experimental parameters.

The distinct ion and electron dynamics are illustrated in figure 2.4 for a symmetric and asymmetric discharge. There, the spatial variation of the normalised net charged particle number density ($\sum n_i - n_e$) within one period of the discharge as well as the total potential ϕ variation across the discharge gap is shown for a capacitively coupled radio-frequency oxygen plasma operated at 100 Pa pressure and 300 V driving voltage. The quasineutral region corresponds to a zero net charge (blue colour) and the positively region is indicated on a false colour scale with a maximum positive charge of 1 in the sheath regions (red colour).

Figures 2.4(a) and 2.4(c) show that the plasma bulk exhibits approximately a net zero charge, i.e. quasineutrality. This also manifests in a spatially almost constant plasma potential > 0 in the plasma bulk (figures 2.4(b), 2.4(d)). However, the sheath region at each electrode undergoes a period of expansion and collapse forcing the bulk region to follow its dynamics. During the sheath expansion a high electric field develops that accelerates the ions within the sheath and inhibits electrons from entering it. During sheath collapse the electric field decreases significantly allowing electrons to propagate into the sheath region and to reach the electrodes so that in total the positive particle flux is balanced. It has to be noted that the sheath region is significantly bigger in the asymmetric discharge due to the developing DC bias voltage, which typically lies between $0.5 - 1$ times the applied voltage amplitude V_{rf} (see figure 2.4(d)).

Apart from the geometric configuration, heating mechanisms are an important factor for sustaining CCP discharges. Generally, they depend on several experimental parameters such as pressure, frequency and the applied driving voltage. The dominant energy coupling mechanism is the energy coupled to electrons by the oscillating electric field.

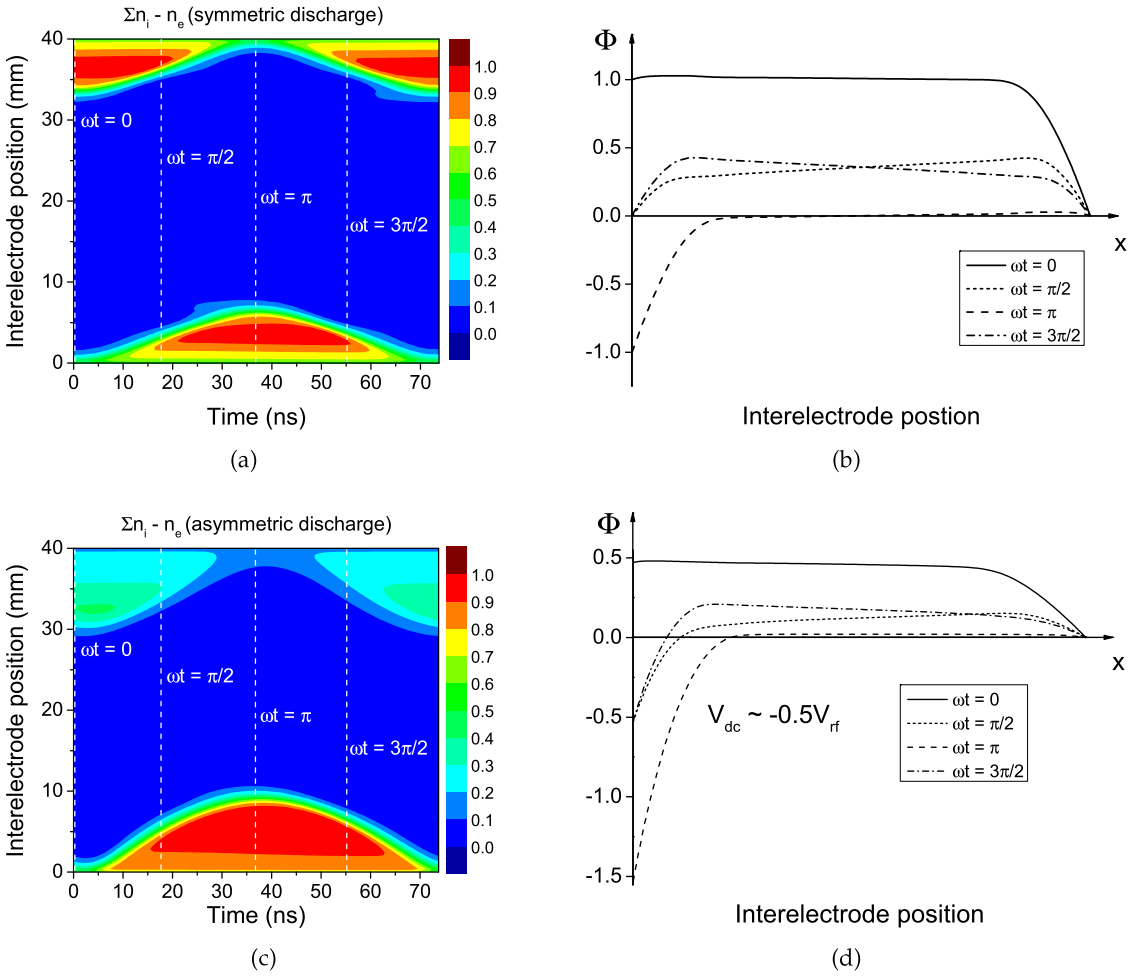

Figure 2.4.: Spatial variation of (a) time resolved normalised net charged particle number density ($\sum n_i - n_e$) and (b) total potential ϕ across a symmetric discharge for four different times during the RF cycle. (c) and (d) correspond to an asymmetric discharge.

As already mentioned above electrons can follow the electric field instantaneously which leads to their oscillatory motion within the RF cycle with the applied driving frequency, because the necessary condition $\omega_{p_e} > \omega$ is fulfilled. The oscillatory motion is usually in phase with the electric field. Net energy is gained whenever this phase-coherent motion of electrons is destroyed. This can occur in two ways - by electron collisions with other particles, also referred to as collisional or ohmic heating, and by other collisionless mechanisms, namely, stochastic heating.

Both heating mechanisms occur in a typical CCP discharge, however the dominance of one mechanism over the other depends on the specific experimental conditions. For

example, ohmic heating is the dominant energy transfer mechanism for elevated pressures ($>$ 10 Pa) whereas a decrease of operating pressure results in a transition to the collisionless mode [5]. Despite the pressure, several other discharge properties can help distinguish between ohmic and collisionless heating modes. The most prominent distinguishing feature is the shape of the electron energy distribution function (EEDF), which is illustrated in figure 2.5. The EEDF is usually obtained in the experiment only on time average as an approximation from the second derivative of Langmuir probe current measurements because its time resolved dynamics are generally very difficult to measure. In case of collisional heating the EEDF is Druyvesteyn-like with overall high electron mean energies. When the heating is predominantly collisionless the EEDF exhibits generally a bi-Maxwellian shape.

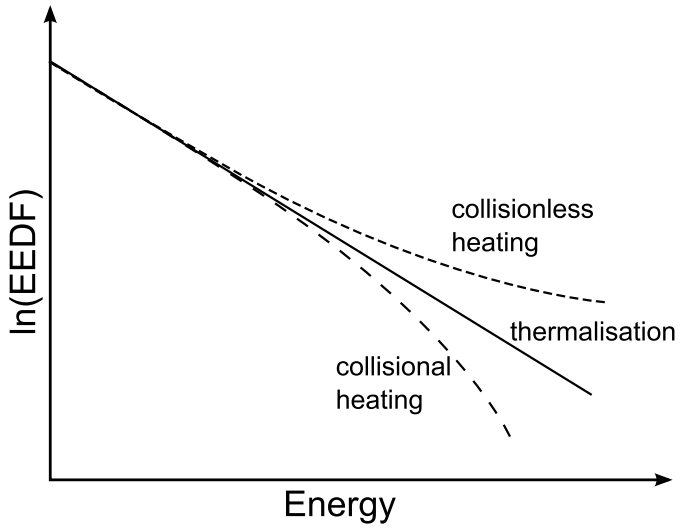

Figure 2.5.: Typical shape of EEDF for different dominant heating mechanisms.

However, the details of the exact mechanisms involved in collisionless heating are still not fully understood and an ongoing research topic. There are numerous models to describe collisionless heating. One of the most prominent approaches is the hard-wall model introduced by Lieberman *et al.* [6, 7] which assumes that electrons are reflected at the oscillating sheath edges that serve as hard walls. Thereby, electrons can only gain energy if they are in stochastic phase with the oscillation of the sheath edges.

Recent studies suggest that such hard-wall models of the sheath are inadequate in explaining collisionless heating and alternative theories may be necessary [8–10].

2.3. Plasma Sheath

Classically, the plasma sheath is defined as the region between bulk plasma and electrode surface where the quasineutrality breaks down, because the positive ion density exceeds the electron density, as illustrated in figure 2.6. The sheath region is a result of the difference in thermal motion of electrons and ions. Electrons, having a smaller mass and higher temperature than ions, thus a significantly higher thermal velocity, are not confined by the quasineutral plasma bulk and can therefore be rapidly lost to the electrode surfaces. To satisfy the condition of a zero-net flux at the surfaces, a positive space charge region develops, which repels electrons and accelerates ions towards the surfaces, respectively.

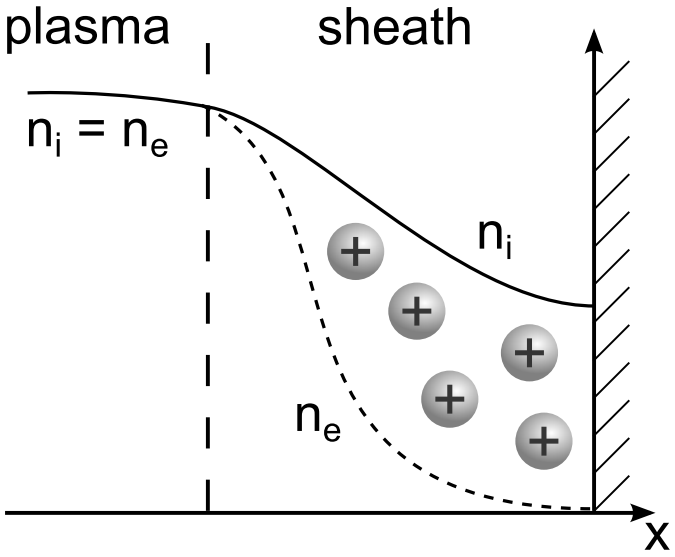

Figure 2.6.: Classical plasma sheath definition.

Theoretically, the plasma sheath can be described by the Child-Langmuir law, which is based on ion and electron current calculations in simple DC gas discharges using various electrode shapes [11, 12].

Two cases can be distinguished from one another. Firstly, a collisionless plasma sheath where no ionisation and no collisions take place, and secondly, a collision dominated plasma sheath.

As consequence of the collisionless plasma sheath assumption, the ion energy and flux are conserved and the electron density can be described in first approximation by

the Boltzmann relation. This leads to a minimal velocity with which the ions enter the sheath, the so-called Bohm velocity $v_B = \sqrt{k_B T_e / m_i}$. Using the Bohm velocity and corresponding Bohm flux $j_B = e n_i v_B$ an expression for the sheath width s can be derived:

$$s = \frac{\sqrt{2}}{3} \lambda_D \left(\frac{2eV_s}{k_B T_e} \right)^{3/4} \propto \frac{V_s^{3/4}}{T_e^{1/4} n_e^{1/2}} \tag{2.9}$$

Here, V_s is the voltage drop over the sheath and λ_D is the Debye length at the sheath edge. From this follows, that the sheath width can be estimated for a given plasma discharge and scales with voltage, electron temperature and electron density. With increasing voltage the sheath width increases, whereas it decreases with increasing electron temperature or electron density.

For technological applications, however, the detailed quantitative relationship is important and usually depends on the assumption whether ion collisions in the sheath can be neglected or not. For pure α-mode discharges the collisionless assumption holds, however, if the discharge is dominated by secondary electron release at the surfaces (γ-mode discharge), ion energy conservation is not fulfilled. Thus, the ion dynamics is strongly modified.

Similar calculations, under the assumption that the ion mean free path can be regarded constant in low pressure discharges, yield a modified expression for the sheath width dependency:

$$s \propto \frac{V_s^{3/5}}{(p\, T_e)^{1/5} n_e^{2/5}} \tag{2.10}$$

This expression is very similar to equation 2.9, however showing slightly different weighting and an additional dependence on the background gas pressure. Assuming a constant electron temperature of 4 eV, a constant electron density of 0.5×10^{15} m^{-3}, typical operation pressures of 10 Pa$-$100 Pa, and voltage drops across the sheath of 100 V$-$500 V, the collision dominated sheath width will generally be smaller than the collisionless sheath width. Only for pressures below 20 Pa and voltages below 300 V, the collision dominated sheath can be bigger than the collisionless sheath.

Analytical and numerical models, describing the sheath motion in RF discharges and its effect on electron heating and ion energy distributions for both the collisionless and

collision dominated cases can be found in the literature [6, 13–16].

Generally, the actual time dependent sheath position is a matter of definition. In this work, the sheath position is defined on the basis of spatial particle density profiles using the concept of an equivalent sharp electron step [17]. This concept is illustrated in figure 2.7. Here, the sheath position $s(t)$ results from the balance of the electron excess left of $s(t)$ and the lack of electrons on the right hand side of $s(t)$.

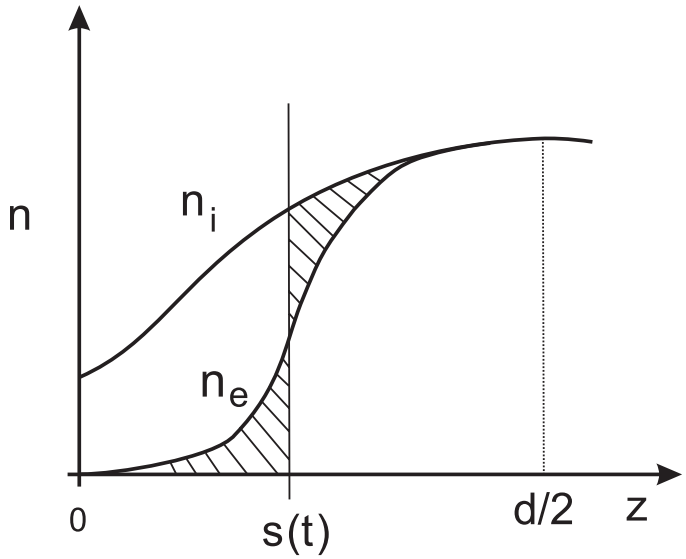

Figure 2.7.: Schematic of an equivalent electron step to determine the sheath position.

Quantitatively, the sheath position $s(t)$ can then be defined as the solution of:

$$\int_0^{s(t)} n_e(z,t)dz = \int_{s(t)}^{d/2} \left(\sum_i \mathrm{sgn}(q) n_i(z,t) - n_e(z,t) \right) dz \tag{2.11}$$

Here $d/2$ represents the distance from the electrodes to the symmetry axis, i.e. the centre of the plasma bulk, n_e is the total electron density, and $\sum_i n_i$ is the sum over the total densities of all ion species including negative ions by taking into account their charge sign via $\mathrm{sgn}(q)$. Consequently, the determined sheath widths will be smaller compared to the classical approach (see figure 2.6), in which the sheath position is given when the condition of quasineutrality breaks down.

2.4. Population Dynamics of Excited States

The simplest models to describe population dynamics of excited states are the so-called equilibrium models in which it is assumed that individual or all components of a plasma can be described by distribution functions due to their interactions. The most prominent distribution functions are the Boltzmann and Maxwell distribution functions. They characterise the population of excited, bound or ionised states, velocities etc.. However, they mostly presume high electron densities and have thereby only a limited applicability for low temperature plasmas.

The transition to low electron densities in the range of $\leq 1 \times 10^{19}$ m^{-3} for low temperature and low pressure plasmas can be described by the so-called corona model. There, it is assumed that during the lifetime of an excited state no additional collisions leading to excitation or de-excitation take place. Additional excitation and de-excitation mechanisms that are not covered by the corona model will be discussed in the extended collisional radiative model. The population dynamics of excited states can then be characterised appropriately, as demonstrated in [18].

2.4.1. Corona Model

The corona model accounts in its simplest form merely the electron-impact excitation out of the ground state and the de-excitation by spontaneous emission into lower states, as illustrated in figure 2.8. These processes affect the population density n_i of an excited state i and can be described by the following rate equation [19–21]:

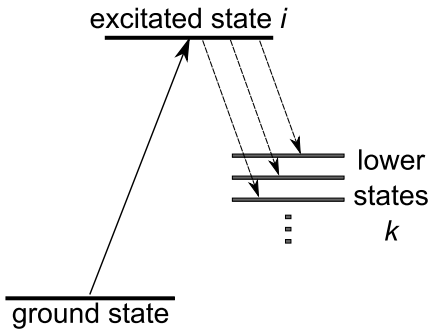

Figure 2.8.: Illustration of population dynamics in corona model.

$$\frac{dn_i(t)}{dt} = n_0 E_i^e(t) - \sum_k A_{ik} n_i(t) \qquad (2.12)$$

Here, n_0 represents the ground state density, E_i^e the electron-impact excitation rate out of the ground state into the state i and $\sum_k A_{ik} n_i$ the sum over all transition rates due to spontaneous emission out of state i into lower states k with A_{ik} as the corresponding

Einstein coefficient.

The hereby occurring electron-impact excitation rate E_i^e of the excited state i can be expressed by the electron number density n_e, the integral over the normalised electron energy distribution function $f(\epsilon)$ and the energy dependent electron-impact excitation cross section $\sigma_i(\epsilon)$:

$$E_i^e = n_e \int_0^\infty \sigma_i(\epsilon) \sqrt{\frac{2\epsilon}{m_e}} f(\epsilon) d\epsilon = k_e n_e \,, \tag{2.13}$$

where k_e is the electron energy dependent excitation rate coefficient.

Now, two special cases can be examined to simplify equation 2.12 which lead to a constant excitation and a pulsed excitation, respectively.

In the case of a constant excitation the population density reaches an equilibrium between excitation and de-excitation processes. For this stationary condition the following applies:

$$\begin{aligned} \frac{dn_i(t)}{dt} &= 0 \\ \Rightarrow n_i &= n_0 \frac{E_i^e}{\sum_k A_{ik}} \end{aligned} \tag{2.14}$$

In case of a pulsed excitation a prerequisite that the excitation process stops after a distinct time t_0 applies, i.e. $E_i^e(t > t_0) = 0$. If this condition is fulfilled, the population density n_i can be simplified for times $t > t_0$:

$$\begin{aligned} \frac{dn_i(t)}{dt} &= -\sum_k A_{ik} n_i \\ \Rightarrow n_i &\propto \exp\left(-\sum_k A_{ik} t\right) \end{aligned} \tag{2.15}$$

The resulting exponential decay of the population density of an excited state i thus is determined by the inverse of the sum over all transition rates for spontaneous emission out of state i. From this relationship the lifetime τ_i of such an excited state can be derived:

$$\tau_i = \left(\sum_k A_{ik} \right)^{-1} \tag{2.16}$$

Due to additional excitation and de-excitation processes that might influence the population density except the already discussed electron-impact excitation and spontaneous de-excitation it is evident that the applicability of the corona model is relatively limited. These additional processes will be discussed in the following section.

2.4.2. Collisional Radiative Model

Possible excitation processes within the plasma volume that are not covered by the corona model are heavy particle impact excitation processes, cascade processes out of energetically higher states, electron-impact excitation out of metastable states, or re-absorption of the emitted radiation. The most important de-excitation process is the radiation free impact de-excitation, also referred to as "quenching". For this reason the corona model needs to be extended to a collisional radiative model to describe the observed plasma appropriately.

Excitation processes triggered by heavy particle impact can be expressed by a generalised excitation rate E_i:

$$E_i = E_i^e + E_i^H \tag{2.17}$$

Here, E_i^e is the already known electron-impact excitation rate introduced in equation 2.13 and E_i^H is the additional rate term from heavy particle impact excitation.

The excitation of the observed state i by a first order cascade process out of state c which population density is n_c can be described through introduction of an additional excitation rate A_{ci} to rate equation 2.12. A_{ci} is equatable to a transition rate out of cascade state c into the observed state i. Cascade processes of higher order are neglected in this approximation.

Metastable states are depleted relatively slow and can thereby be populated very effectively so that they subsequently contribute to the excitation of state i. To account for these excitation processes out of metastable states m with a population density n_m the excitation function $E_{i,m}$ is introduced. The resulting modified rate equation for the

population density of the observed state i is:

$$\begin{aligned}\frac{dn_i}{dt} &= \underbrace{\left(E^e_{i,0} + E^H_{i,0}\right)}_{E_{i,0}} n_0 + \underbrace{\left(E^e_{i,m} + E^H_{i,m}\right)}_{E_{i,m}} n_m \\ &+ A_{ci} n_c - \underbrace{\left(\sum_k A_{ik} g_{ik} + \sum_q k_q n_q\right)}_{A_i} n_i \end{aligned} \tag{2.18}$$

Here, $E_{i,0}$ and $E_{i,m}$ are the generalised excitation functions for the excitation out of the ground state and out of the metastable state, respectively, including additional heavy particle impact excitation processes; A_i is the effective de-excitation rate which takes into account spontaneous emission, radiation reabsorption and collisional de-excitation processes.

Radiation reabsorption is represented by so-called escape factors g_{ik}. These g_{ik} are a measure for the probability that an emitted photon leaves the plasma volume during the transition from state i into state k without being absorbed by other particles within state k. Thus, this reabsorption can reduce the effective loss rate and as a result increase the effective lifetime of an excited state. Consequently, two extreme cases can be distinguished. If either no emitted photons ($g_{ik} = 1$) or all emitted photons ($g_{ik} = 0$) are reabsorbed, the plasma will be called "optically thin" or "optically thick", respectively.

Equation 2.18 also includes quenching in form of an additional de-excitation rate. This rate results from the sum of the products between quenching coefficients k_q and the involved collision partner number densities n_q. The k_q's can be understood as effective collisional de-excitation coefficients which include all de-excitation and excitation processes of the observed state through inelastic collisions with the collision partner q. The denotation as de-excitation coefficients originate from the generally dominant nature of de-excitation processes over excitation processes. De-excitation based on collisional processes are characterised by energy transfer from excited particles to the internal energy of collisional partner q as well as to the translational motion of both collisional partners. A more detailed description of these processes can be found in references [22–25].

The quenching coefficient depends predominantly on the square root of the tempera-

ture of the particles involved due to the weak temperature dependence of the collisional de-excitation cross section σ_q [26, 27] if one assumes a mean thermal velocity distribution $\langle v \rangle$ [28]:

$$k_q(T) = \sigma_q \langle v \rangle = \sigma_q \sqrt{\frac{8 k_B T_q}{\pi m_{red}}} \tag{2.19}$$

m_{red} is the reduced mass of both collisional partners. Equation 2.19 shows that it is not sufficient to know the number densities of the involved particles, but also their temperature.

The collisional radiative model shows that generally the extension of the corona model to describe additional excitation and de-excitation processes is possible, yet requires the knowledge of atomic and molecular data as well as numerous plasma parameters. A more detailed overview of the discussed models can also be found in the literature [19–21, 29, 30].

2.5. Advanced Actinometry

In a wide range of industrial plasma processes, where oxygen is used, atomic oxygen radicals can play a substantial role in determining the outcome of these processes. However, measuring this chemically active species non-intrusively is challenging. A qualitative method was first introduced by Harshbarger *et al.* in 1977 [31] by observing atomic oxygen emission intensities in order to monitor a silicon etch process.

Later, the classical actinometry approach was introduced by Coburn and Chen [32] to quantify reactive species densities by deliberately adding a suitable noble tracer gas and observing the ratio of both the tracer gas emission and the reactive species emission induced by direct electron-impact excitation. This concept is based on the assumption of similar energy levels of both involved excited states and thereby by similar excitation efficiencies of these levels. The time averaged emission intensity $\langle I \rangle_{rf}$ from one state is given by:

$$\langle I \rangle_{rf} = h\nu \, a_{ik} \langle k_e n_e \rangle_{rf} \, n_0 \tag{2.20}$$

Here, $h\nu$ is the photon energy, k_e the excitation rate coefficient (see equation 2.13), n_0 the ground state density and a_{ik} the optical branching ratio. The a_{ik} depend on the Einstein coefficient for spontaneous emission A_{ik} and the optical decay rate of the excited state A_i, which also includes the effective collisional quenching rate $\sum_q k_q n_q$ (see equation 2.18):

$$a_{ik} = \frac{A_{ik}}{A_i} \tag{2.21}$$

More recently, in case of atomic oxygen, the classical approach was extended to also include dissociative excitation of the reactive species due to its dominance, especially in the case of low dissociation degrees of the background gas [33]. Generally, absolute values for atomic oxygen densities are obtained through observing the upper O($3p^3P$) ($\lambda = 844.6$ nm) atomic oxygen state and the upper Ar($2p_1$) ($\lambda = 750.4$ nm) tracer state. The reactive species density can then be expressed by:

$$n_O = \frac{I_O}{I_{Ar}} \frac{h\nu_{Ar}}{h\nu_O} \frac{k^*_{Ar,d}}{k^*_{O,d}} \frac{a_{ik,Ar}}{a_{ik,O}} n_{Ar} - \frac{k^*_{O,de}}{k^*_{O,d}} n_{O_2} \tag{2.22}$$

$$\text{where :} \quad k^* = \frac{\langle k_e n_e \rangle_{rf}}{\langle n_e \rangle_{rf}} \tag{2.23}$$

The first term of equation 2.22 corresponds formally to the classical actinometry approach and the second term is the correction for dissociative excitation. The effective excitation rate coefficient k^* for direct electron-impact excitation is indexed with d, while the dissociative electron-impact excitation is indexed with de.

Usually, the k^* can adequately describe the time and space integrated optical emission intensity, which supports the use of actinometry. Furthermore, several research groups have shown the validity of the actinometry approach for various plasma sources [33–36]. However, the major drawback is the uncertainty in the knowledge of effective excitation rate coefficients because they are strongly dependent on the electron energy, so that they are often treated as constant and based on crude assumptions of the electron energy distribution.

To overcome this, the electron energy distribution needs to be explicitly calculated including the respective (complex) plasma chemistry to obtain correct effective excitation

rate coefficients. This has already been successfully demonstrated in high pressure micro plasma jets [37] as well as low pressure CCP plasma discharges [38], but generally requires high computational power to achieve.

In this work, a much simpler approach that does not require an explicit fluid dynamic treatment is proposed. Therefore, the effective excitation rate coefficients are determined using the two-term approximation Boltzmann equation solver BOLSIG+ to calculate the appropriate EEDF, as will be described in section 3.5. Furthermore, the usual actinometry approach is extended to also include the atomic oxygen emission from the excited state $O(3p^5P)$ ($\lambda = 777.4$ nm) and modified to account for the pressure independent excitation ratios instead of the emission intensity ratios. This opens the possibility to directly obtain not only the atomic oxygen density but also the electron energy simultaneously, and spatially resolved instead of spatially integrated.

The used cross sections and resulting rate coefficients for direct and dissociative electron-impact excitation of the $Ar(2p_1)$, $O(3p^5P)$, and $O(3p^3P)$ atoms are shown in figure 2.9. The rate coefficient is only dependent on the gas composition, gas temperature, and the cross section data.

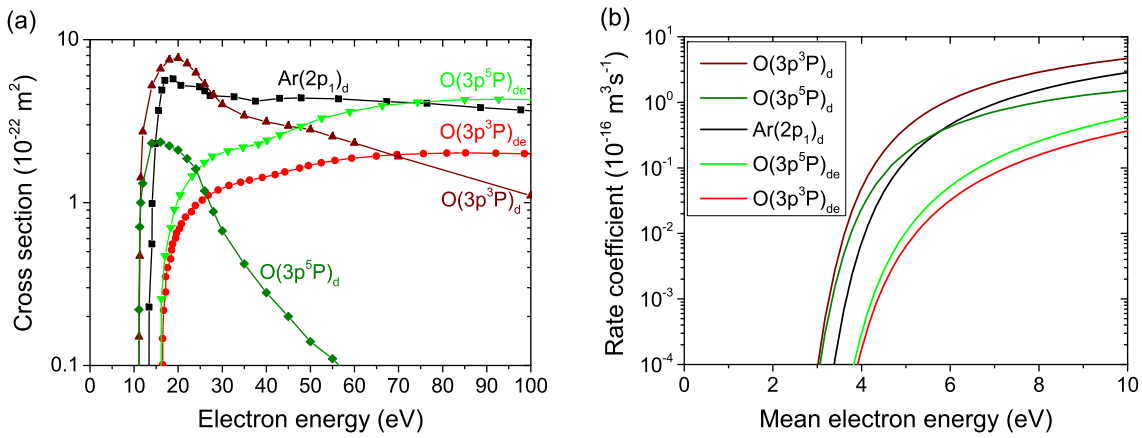

Figure 2.9.: (a) Cross sections and (b) resulting rate coefficients for direct and dissociative electron-impact excitation of the $Ar(2p_1)$, $O(3p^5P)$, and $O(3p^3P)$ states.

Cross section data for direct electron-impact excitation into the $Ar(2p_1)$ state is taken from reference [39], for the direct and dissociative electron-impact excitation into the $O(3p^5P)$ and $O(3p^3P)$ states from references [40, 41].

Similar for all direct electron-impact excitation channels is the relatively low threshold

energy with a rapid increase in cross section, followed by a monotonic decline with increasing electron energy. The dissociative channels show higher threshold energies but increase monotonically with increasing electron energy, even exceeding the direct channel cross sections for high electron energies.

Comparing the two oxygen states, the O($3p^5P$) state has a slightly lower threshold energy (10.73 eV) than the O($3p^3P$) state (10.98 eV). Same applies for the dissociative channels which have threshold energies of 16.1 eV and 16.3 eV, respectively. The threshold energy for the argon Ar($2p_1$) state lies between the direct and dissociative channel energies (13.48 eV). An overview of the relevant energy levels of argon and oxygen can be found in appendix A.

As result, the corresponding rate coefficients behave similarly, as shown in figure 2.9(b). For mean electron energies in the range of 0 eV$-$10 eV, especially in the lower energy range, the direct channel rate coefficients of excited states O($3p^3P$) and O($3p^5P$) are dominant over the rate coefficients of the dissociative channels. This generally justifies the use of classical actinometry if a considerable density of atomic oxygen can build up. However, atomic oxygen usually constitutes a minority species in pure oxygen discharges so that the dissociative channel can be expected to be dominant over the direct channel even for relatively high dissociation degrees. This is particularly true for the O($3p^5P$) state, for which the discrepancy between direct and dissociative channel is comparably smaller than for the O($3p^3P$) state.

Here, an effective excitation rate $E^* = \sum_n f_n E^e_{i,n}$ is introduced, which results from the sum over all products of the electron-impact excitation rates $E^e_{i,n}$ and the density fraction f_n of the corresponding collision partner. To account for the two excitation channels in case of oxygen, the dissociation degree r_O is considered for the direct channel and is defined as the ratio of the atomic oxygen density and the molecular oxygen density. The effective excitation ratios as function of the dissociation degree and electron energy can then be derived:

$$\frac{E^*_{750}}{E^*_{844}} = \frac{f_{Ar}\, k_{750,d}(\epsilon)}{r_O\, k_{844,d}(\epsilon) + k_{844,de}(\epsilon)} \tag{2.24}$$

$$\frac{E^*_{777}}{E^*_{844}} = \frac{r_O\, k_{777,d}(\epsilon) + k_{777,de}(\epsilon)}{r_O\, k_{844,d}(\epsilon) + k_{844,de}(\epsilon)} \tag{2.25}$$

Here, f_{Ar} is the argon fraction. These ratios are generally time and space dependent, which complicates the analysis. To overcome this, only the maximum excitation for each considered state is taken into account, since additional excitation processes, such as cascade processes, excitation through secondary electrons, or excitation via heavy particles have the lowest contribution in that case, as shown by T. Gans [18], so that the error is minimal. The main advantages of this approach are its independence of pressure effects, simple gas composition adjustability, and very low demand for computational power. Furthermore, the observation of two excitation ratios instead of one allows to obtain the atomic oxygen density as well as the mean electron energy simultaneously.

For oxygen as main gas with 2% argon admixture, figure 2.10 shows the obtained excitation ratios for values of the dissociation degree between $0.1\% - 5.0\%$ over a range of 0 eV$-$50 eV.

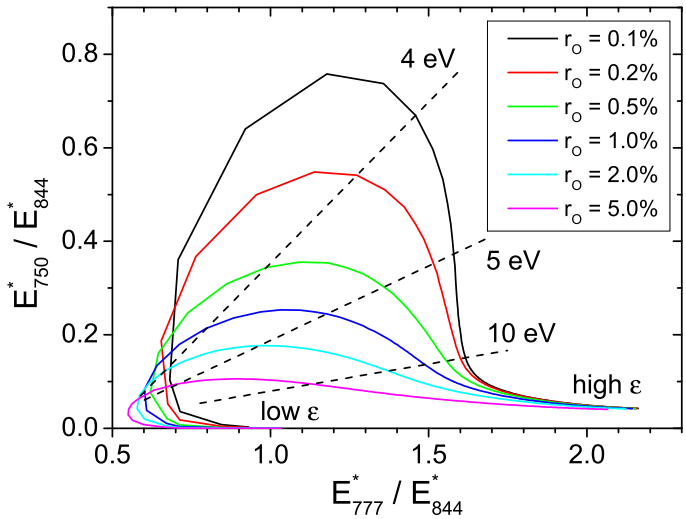

Figure 2.10.: Excitation ratios for various values of the dissociation degree over a range of 0 eV$-$50 eV. Gas composition: 98% O_2, 2% Ar; $T_g = 300$ K.

The abscissa is the excitation ratio of the oxygen states O($3p^5P$) and O($3p^3P$), and the ordinate is the excitation ratio of the argon state Ar($2p_1$) and the oxygen state O($3p^3P$). For any two given excitation ratios, specific values for the mean electron energy ϵ and dissociation degree of oxygen r_O can be assigned easily.

The mean electron energy in figure 2.10 increases from left to right, exhibiting a spread at relatively low electron energies that depends on the dissociation degree and converges at high energies. The three dashed lines indicate a dissociation degree change for equal

energy values.

Generally, under equal energetic conditions, an increase in dissociation degree entails a decrease of both excitation ratios. This can be understood by means of the dominant behaviour of the direct channel of oxygen state O($3p^3P$) at low energies, which becomes more pronounced with increasing dissociation degree (compare figure 2.9(b)).

Under relevant discharge conditions ($\epsilon \approx 3$ eV-5 eV, assuming constant dissociation degree) if the energy is increased, the E^*_{777}/E^*_{844} ratio will also increase because the rate coefficient for dissociative excitation of the O($3p^5P$) state gets progressively bigger than the rate coefficient of the dissociative channel of the O($3p^3P$) state.

For low energies, the E^*_{750}/E^*_{844} ratio first increases until reaching a maximum at a certain threshold energy and subsequently decreases with increasing electron energies. However, this threshold energy also changes with the dissociation degree because the balance of rate coefficients changes.

3. Plasma Modelling

In this chapter plasma modelling methods are introduced. The chosen modelling method is then discussed in detail beginning with relevant geometrical considerations. Governing equations and boundary conditions are presented with special regard to validity and limits. The Boltzmann equation together with the applied two-term approximation is discussed as part of the kinetic simulation of electrons. Associated with the latter, a proper treatment of the electron energy mobility is compared to a commonly used approximation. Furthermore, heavy particle transport coefficients are considered for charged and neutral particles, with special emphasis on their mobility and diffusion in pure gases and gas mixtures. Apart from that, a general overview of important plasma chemical reactions for plasma modelling is given. Finally, the multi-iterative solution method of the model is discussed, introducing the concept of a stationary solver for slow species in addition to the commonly used time-dependent solver.

3.1. Modelling Methods

The modelling of radio-frequency driven plasmas is generally very complex because it is almost impossible to account for all properties of a plasma in one single model. Numerical modelling, even when based on rather simplified assumptions, is still a valuable common tool to improve the fundamental understanding of low temperature and low pressure radio-frequency driven plasmas, despite their actual complexity.

Two different numerical simulation concepts exist: (a) Models based on experimental input data, allowing additional analysis and interpretation of not directly measurable quantities, so offering a potential advanced diagnostic tool. These models are generally computational efficient, but limited to specific plasma sources [42–44]. (b) Self-consistent models being able to cover different plasma sources under a variety of operational parameters [37, 45, 46]. These models can be subdivided into numerical and analytical

models, while the latter is generally more restrictive, since being based on more simplified assumptions. Numerical models can usually cover a much wider range of physical and chemical processes. Thus, making them the most widely-used simulation method of radio-frequency driven plasmas.

Several methods to apply numerical modelling exist, mainly differing in the methodology used for the management of charged particle transport.

One well established approach are so-called kinetic models, also referred to as Particle-in-Cell models (PIC) [47, 48]. These models evaluate the trajectories and distribution of charged particles and neutrals in the phase space by taking advantage of their collective behaviour. Since only the motion equation coupled to Maxwell's equations is solved, no assumptions about the EEDF are needed. To decrease the needed computational power and time it is useful to reduce the number of particles solved for. This is usually done by introducing a "few" super-particles ($\approx 10^6$ regular particles). However, these super-particles experience a lack of sufficient statistical representation of energetic particles and the solver time steps need to be low to account for all collisions. This generally leads to limitations in geometry (usually 1D only) and limited chemical reaction schemes unless the solution timescale is not of importance.

Another approach are fluid models where the plasma is described with the help of parameters such as the density, particle flux and mean energy [49–51]. Each species is treated as independent fluid and the moments of the Boltzmann equation as well as the Maxwell's equations are solved separately. However, certain restrictions to the validity of this approach apply. For example, assuming a Maxwellian distribution for the EEDF is often wrong for low temperature plasmas. Although, fluid models are generally regarded as less accurate than PIC models they emerge as clear favourites regarding the computational speed as well as the easy implementation of complex chemistries and system dimensions.

A third approach are the so-called hybrid models, which combine the advantages of fluid models with the accuracy of PIC-models [52].

The modelling approach used in this work is a self-consistent fluid model with semi-kinetic treatment of electrons. This method allows to couple an *a priori* kinetic simulation with a fluid model via the mean electron energy. Through the kinetic simulation the

EEDF is calculated up-front using the two-term approximation of the Boltzmann equation as a function of the reduced electric field [53]. The corresponding electron transport coefficients as well as electron-impact reaction rates are obtained and coupled into the fluid model, in which the densities of the accounted species as well as the electric field are simulated with the fluid approach. This method is widely used because it combines the advantages of fluid and kinetic approach.

However, particularly in the low pressure regime the description of sheath and ion dynamics in fluid models can be limited due to increased importance of kinetic properties [54, 55]. This can have a significant impact on the treatment of secondary electrons in the model because the applied fluid modelling approach is limited to one electron group. Thus, the spatial distribution of ionisation and excitation through secondary electrons is usually confined to the sheath region in the model, although secondary electrons are generally expected to penetrate the plasma bulk in real discharges. Also, energy transport mechanisms in the interface region between plasma and surface are important, in particular for industrial applications. Therefore, it is the aim to achieve an improved combination of treatment of plasma chemical reactions and charged particle dynamics in this interface region.

3.2. Geometrical Considerations

For the fundamental understanding of the charged particle dynamics, the numerical simulations are conducted in a symmetric as well as in an asymmetric one-dimensional domain across the discharge gap of the CCP. Both model domains are illustrated in figure 3.1.

To simulate the asymmetric discharge one has to account for the different surface areas of the powered and the grounded electrode, respectively. Therefore, the actual electrode geometry (complex, but cylindrical symmetric) is approximated by spherical shell segments according to Lieberman *et al.* [2]. This approximation offers the huge computational advantage of reducing the calculation to the axial dimension (spherical r-coordinate) only, under the assumption that the plasma is radially homogeneous (spherical θ and ϕ coordinates) for the region near the central axis of the actual discharge,

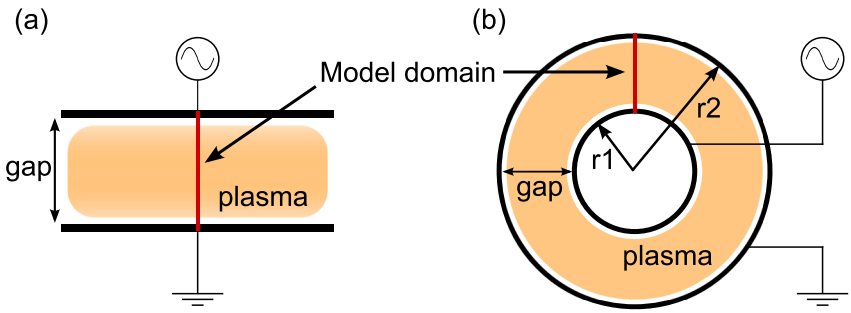

Figure 3.1.: One-dimensional model domain in (a) symmetric and (b) asymmetric configuration of the CCP.

which is given.

Here, the powered electrode's distance from the centre of the sphere, which determines its surface area, is r_1. The grounded electrode is located at r_2, thus exhibiting an overall greater surface area than the powered electrode. The asymmetry is given by the ratio of both electrode surface areas (S_1, S_2) and was chosen to be $S_2/S_1 = (r_2/r_1)^2 = 36$. This ratio is a realistic value with regard to ionisation and excitation features as observed by K. Dittmann [56] and comprises a reasonable approximation for the standard inductively coupled GEC RF reference cell considering the actual chamber geometry [57]. It has to be noted that for different geometries the asymmetry factor, determined by the surface ratio, might need to be readjusted.

3.3. Governing Equations

The basic set of equations of the fluid model is obtained from the first three moments of the Boltzmann equation. For the absence of a magnetic field the mass conservation (3.1), momentum conservation (3.2) and energy conservation (3.3) equations are explicitly given below [2]:

$$\frac{\partial n}{\partial t} + \vec{\nabla}\vec{\Gamma} = S_{ext}, \quad \text{with } \vec{\Gamma} = n\vec{u} \tag{3.1}$$

$$m\frac{\partial}{\partial t}\vec{\Gamma} = -m\vec{\Gamma}\vec{\nabla}\vec{u} + qn\vec{E} - \vec{\nabla}p - m\nu_m\vec{\Gamma} \tag{3.2}$$

$$\frac{\partial}{\partial t}(n\epsilon) = -\underbrace{\vec{\nabla}(\epsilon\vec{\Gamma})}_{\text{convection}} - \underbrace{p\vec{\nabla}\vec{u}}_{\text{compression}} - \underbrace{\vec{\nabla}\vec{q}}_{\text{conduction}} - \underbrace{q\vec{\Gamma}\vec{E}}_{\text{ohmic heating}} - \underbrace{L}_{\text{losses}} \tag{3.3}$$

Here, n, m, q, $\vec{u}$, ϵ and $\vec{\Gamma}$ are number density, mass, charge, mean velocity, mean energy and flux of the corresponding species. S_{ext} is the source term in the continuity equation and represents any gains and losses due to collisional interactions that create or destroy particles (e.g. ionisation, recombination). p, $\vec{E}$, ν_m and $\vec{q}$ are pressure, electric field, momentum transfer frequency and heat flux within the plasma environment. Finally, L in equation 3.3 represents the energy losses due to elastic and inelastic collisions in the plasma.

To simplify equation 3.2, the drift-diffusion approximation (DD) is used. This is especially valid at pressures above 10 Pa and typical excitation frequencies of 13.56 MHz, because the momentum transfer frequency is much higher than the angular frequency due to the high number of collisions [52]. Therefore, the temporal dependency of the mean velocity of the particles is very small and can be neglected. Additionally, the momentum transfer frequency is much higher than the ionisation and attachment frequencies, too. Furthermore, the distance particles can travel between collisions will be small, if the drift velocity is smaller than the thermal velocity. This is the case when the mean free path is at least a magnitude smaller than the system dimension so that the spatial derivative of the mean velocity does not change much and can therefore be neglected as well. Nevertheless, for typical system dimensions and at lower pressures than 10 Pa or higher frequencies the full flux equation 3.2 should be used to incorporate the particular species' inertia [52].

In equation 3.3 the following substitutions are made: $p = nk_BT = \frac{2}{3}n\epsilon$, $\vec{q} = \frac{5}{3}nD\vec{\nabla}\epsilon$, and $\vec{\Gamma}_\epsilon = \frac{5}{3}\vec{\Gamma}\epsilon - \vec{q}$.

As described in the introduction of chapter 2, ions are generally assumed to remain at room temperature, thereby the same energy as the background gas. This assumption

is especially fulfilled in the plasma bulk region, thus the ion energy equation does not need to be solved. However, in the sheath regions of the plasma this assumption often fails. The resulting error is usually small so that it is not accounted for in the present model. Nevertheless, to include a proper treatment of each species their actual velocity distribution would have to be assumed. Obviously, the simulation results would strongly depend on the velocity distribution functions that are chosen [52]. To overcome this problem and to account for the effect of higher ion temperatures in the sheath region due to high electric fields the generalised Einstein relation was implemented in the present simulations and shall be described later.

Equations (3.4)-(3.11) correspond to the resulting set of governing equations solved in the applied fluid simulation of a low temperature plasma. The continuity equation is evaluated for each considered species j in the drift-diffusion approximation. The electron energy equation (3.6) accounts for ohmic heating as well as for elastic and inelastic losses. However, collisionless heating is not included in equation (3.6) due to the dominance of collisional heating at elevated pressures ($>$ 10 Pa) [5]. The set of equations is closed by the Poisson equation for the electric potential (3.11).

Electrons:

$$\frac{\partial n_e}{\partial t} + \vec{\nabla}\vec{\Gamma}_e = \sum_j n_e n_j k_{je} \tag{3.4}$$

$$\vec{\Gamma}_e = -n_e \mu_e \vec{E} - D_e \vec{\nabla} n_e \tag{3.5}$$

$$\frac{\partial (n_e \epsilon)}{\partial t} + \vec{\nabla}\vec{\Gamma}_\epsilon = -e\vec{\Gamma}_e \vec{E} - \sum_j n_e n_j k_{L,je} - \sum_n 3\frac{m_e}{M_n} k_B \nu_m n_e (T_e - T_g) \tag{3.6}$$

$$\text{where:} \quad \vec{\Gamma}_\epsilon = \frac{5}{3}\vec{\Gamma}_e \epsilon - \frac{5}{3} n_e D_e \vec{\nabla}\epsilon$$

Ions:

$$\frac{\partial n_i}{\partial t} + \vec{\nabla}\vec{\Gamma}_i = \sum_j n_i n_j k_{ji} \tag{3.7}$$

$$\vec{\Gamma}_i = \mathrm{sgn}(q_i) n_i \mu_i \vec{E} - D_i \vec{\nabla} n_i \tag{3.8}$$

Neutrals:

$$\frac{\partial n_n}{\partial t} + \vec{\nabla}\vec{\Gamma}_n = \sum_j n_n n_j k_{jn} \tag{3.9}$$

$$\vec{\Gamma}_n = -D_n \vec{\nabla} n_n \tag{3.10}$$

Potential:

$$\Delta\phi = -\frac{1}{\varepsilon_0}\sum_j q_j n_j \tag{3.11}$$

Here e is the elementary charge, whereas q_j is the electric charge of species j; n_e, n_i and n_n are the electron, ion and neutral particle densities; $\vec{\Gamma}_e$, $\vec{\Gamma}_i$ and $\vec{\Gamma}_n$ the electron, ion and neutral fluxes; ϵ the mean electron energy; k_{ji} and $k_{L,ji}$ are the source terms for electrons, ions and neutrals resulting from collisional and radiative processes between species j and i (e.g. ionisation, recombination, etc.); μ and D the mobility and diffusion coefficient of the corresponding species; m_e and M_n the electron mass and the mass of collision partner n; ν_m is the momentum transfer frequency; T_e and T_g the electron and background gas temperatures in units of K; ϕ the electric potential and $\vec{E}(= -\vec{\nabla}\phi)$ is the electric field.

The self-consistent model is completed by the boundary conditions for each considered species, by the potential and mean electron energy.

3.4. Boundary Conditions

The boundary conditions for the above described transport equations are an important part of the solution of the model. A variety can be found in the literature [58–61]. Usually, a general approach is preferred where expressions for the particle fluxes, directed toward the surface, are used. For charged particles the drift term in equations (3.5, 3.8) is assumed to be dominant so that the contribution from the diffusion term is neglected. Thus, only local particles located directly at the surface are accounted for but the random motion flux of all particles within a certain mean free path from the surface is ignored, which can easily be justified in the presence of high electric fields.

This classical approach is adapted here for low pressure radio frequency discharges

and will be described in the following.

The boundary condition for charged and neutral heavy particles is:

$$\vec{\Gamma}_i \cdot \vec{n} = \frac{1}{4} v_{th} n_i + a \cdot \mathrm{sgn}(q) n_i \mu \vec{E} \cdot \vec{n} \tag{3.12}$$

Here $\vec{n}$ is the normal vector pointing toward the surface, q is the particle charge and v_{th} is the thermal velocity:

$$v_{th} = \sqrt{\frac{8 k_B T}{\pi m}} \tag{3.13}$$

For neutral and metastable particles, T is set to the gas temperature, whereas for ions it is set to an effective temperature, which will be discussed later. In equation 3.12, a is a Heaviside step function which is one if the electric field shows into direction of the surface and zero otherwise:

$$a = \begin{cases} 1\,, & \text{for } \mathrm{sgn}(q)\vec{E} \cdot \vec{n} > 0 \\ 0\,, & \text{otherwise} \end{cases} \tag{3.14}$$

Equivalent considerations in case of electrons result in a similar expression including the secondary-electron emission term:

$$\vec{\Gamma}_e \cdot \vec{n} = \frac{1}{4} v_{th,e} n_e - \vec{\Gamma}_\gamma \cdot \vec{n} \tag{3.15}$$

$$\text{where :} \qquad \vec{\Gamma}_\gamma \cdot \vec{n} = \sum_i \gamma_i (\vec{\Gamma}_i \cdot \vec{n}) \tag{3.16}$$

Here, the subscript e refers to electrons, the summation in the last term covers the boundary flux of all ion species that penetrate the wall and the secondary emission coefficient γ_i is the average number of emitted electrons per incident ion.

For the secondary electron flux $\vec{\Gamma}_\gamma$ (equation 3.16) the incident fluxes of charged and excited species are considered. This expression could be generalised to include secondary electron emission induced by incident bulk electrons or photons. However, this is believed to play an insignificant role in the investigated plasma discharges.

The actual secondary electron density at the wall can be approximated by comparing

the wall flux (3.16) with the corresponding drift-diffusion term (3.5).

$$n_\gamma \approx \frac{\vec{\Gamma}_\gamma \cdot \vec{n}}{\mu_e \vec{E} \cdot \vec{n}} \tag{3.17}$$

In the expression for the emitted secondary electron density (3.17) the diffusion term is neglected, since the emission is only important where a strong electric field is present. For small electric fields this expression fails, but in that case n_γ is negligible ($n_\gamma \ll n_e$), as will be shown later.

The boundary condition for electron energy transport to the surface is then obtained similarly to the one for electron transport (3.15):

$$\vec{\Gamma}_\epsilon \cdot \vec{n} = \frac{5}{3}\left(\frac{1}{4} v_{th,e} n_e \epsilon - \epsilon_\gamma \vec{\Gamma}_\gamma \cdot \vec{n}\right) \tag{3.18}$$

Here, ϵ_γ is the fixed initial energy of secondary electrons released from the electrode surfaces. Following the approach by Yuan *et al.* [62] this energy was set to 0.5 eV in all simulations.

3.4.1. Self-Consistent Bias Voltage Calculation

To close the self-consistent fluid model the boundary condition for the Poisson equation 3.11 needs to be incorporated. This is realised by applying Dirichlet boundary conditions at the electrodes, i.e. the value of the potential is explicitly specified externally on the boundary of the domain:

$$\phi_1 = V_{rf} cos(2\pi f t) + V_{dc} \tag{3.19}$$

$$\phi_2 = 0 \tag{3.20}$$

Here, ϕ_1 is the potential value at the electrode powered by a sinusoidal voltage signal with amplitude V_{rf} and driving frequency f; V_{dc} is the DC self-bias voltage; ϕ_2 is the potential value at the grounded electrode.

The bias voltage V_{dc} is based on the balance of positive and negative particle fluxes

onto the surfaces. In an experiment, it is caused by a blocking capacitor in a matching network, which is responsible to prevent a net DC current flow per RF cycle.

In perfectly symmetric discharges, the bias voltage is zero. In geometrically asymmetric discharges, this bias voltage is calculated self-consistently following the approach by Yonemura *et al.* [63]. There, the total boundary fluxes of electrons and positive ions are calculated separately and their ratio then determines whether the bias voltage needs to be increased or decreased. This procedure is repeated until convergence is reached, i.e. the ratio of boundary fluxes equals 1.

In this work, only geometrical aspects are considered since the discharge is driven by a single frequency sinusoidal voltage. Generally, electrical asymmetry can also develop in geometrically symmetric discharges by applying multiple sinusoidal frequencies [64] or tailored non-sinusoidal waveforms [65].

3.4.2. Secondary Electron Emission

The secondary emission coefficient γ_i is estimated using a commonly accepted empirical expression [66] based on the ionisation energy of the incident particle and the work function of the electrode surface:

$$\gamma_i \approx 0.016\,(\epsilon_{i,iz} - 2\epsilon_\Phi)\,, \quad \text{if} \quad \epsilon_{i,iz} > 2\epsilon_\Phi \tag{3.21}$$

Here, $\epsilon_{i,iz}$ is the ionisation potential of incident ion i and ϵ_Φ is the work function for the surface which is in the range of 4 eV$-$6 eV for most metals [67]. This expression should be understood as effective secondary electron emission coefficient which provides only a rough estimate because the actual value also depends sensitively on surface condition, morphology, impurities, and contamination [2]. Furthermore, it includes the contribution of kinetic ejection of electrons or their thermal emission from the surface in form of the empirically found scaling factor. The actual value is believed to be smaller according to measurements by M. Konuma [68].

For very high incident ion energies ($>$ 1 keV) the secondary electron emission coefficient induced by oxygen ions scales almost linearly with the ion energy [69]. However, since these ion energies are not common in processing plasmas [2], the dependence of the secondary electron emission coefficient on incident ion energies is not explicitly

taken into account. This is justified in the light of a reported general constancy of the secondary electron yield over two orders of magnitude of ion kinetic energies [70].

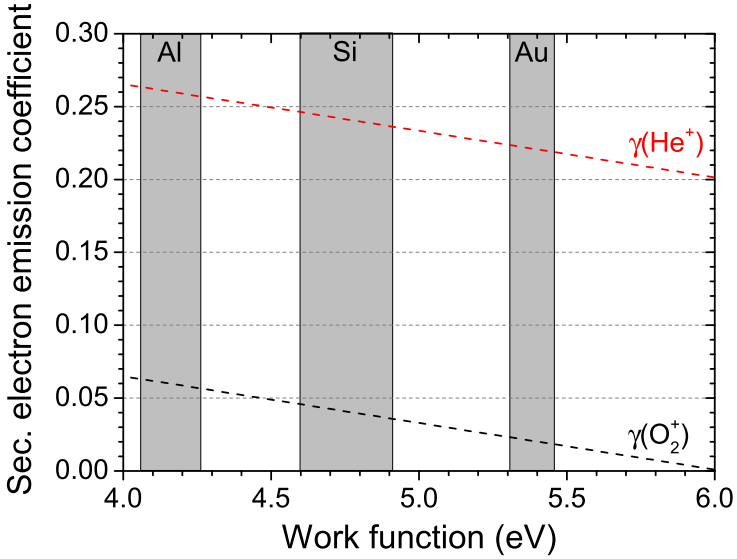

Figure 3.2.: Secondary electron emission coefficients for atomic helium and molecular oxygen ions in dependence of the surface work function. Work functions for aluminium (Al), silicon (Si), and gold (Au) are displayed as gray columns.

Figure 3.2 exemplarily shows the γ-coefficients for atomic helium and molecular oxygen ions using equation 3.21 in the dependence of the surface work function in the range of 4 eV$-$6 eV. Typical work function ranges for three materials, namely aluminium (Al), silicon (Si), and gold (Au) are also displayed in figure 3.2 [67].

The ionisation threshold of molecular oxygen (12.06 eV) is lower than the ionisation threshold of atomic helium (24.58 eV). Subsequently, the secondary electron emission probability for incident helium ions is much higher, lying between $0.20 - 0.27$, than for molecular oxygen ions, which is in the range of $0 - 0.07$. In particular, for a silicon surface, the γ-coefficient of incident molecular oxygen ions theoretically lies in the range of $0.03 - 0.05$.

For most of the simulations, the work function was assumed to be approximately 4.5 eV, resulting in a γ-coefficient of 0.25 for helium ions and 0.05 for oxygen ions, respectively.

3.5. Kinetic Simulation of Electrons

For the kinetic simulation of electrons the non-commercial software BOLSIG+ is used [53]. This software solves the electron Boltzmann equation and provides the EEDF for a series of reduced electric field values (E/N) as well as transport coefficients and rate coefficients as functions of the mean electron energy that are needed for fluid modelling (see section 3.3). The mean electron energy is coupled to the reduced electric field by the corresponding EEDFs and solved self-consistently in the fluid model, as described above.

Nevertheless, certain physical assumptions are necessary to facilitate the solution of the Boltzmann equation. For instance, BOLSIG+ only provides steady-state solutions in a spatially uniform electric field. The main numerical technique used is the classical two-term approximation of the Boltzmann equation, which will be described in the following section.

Additional effects accounted for in BOLSIG+ are collision processes that do not conserve the total number of electrons, also referred to as growth models. As default, exponential temporal growth without space dependence is applied since in general growth effects have only minor influence on the shape of the EEDF for a given mean electron energy.

Collision data in form of a database [71] that is mainly based on the compilation of electron cross sections from Phelps *et al.* [72] serves as input for BOLSIG+. These collision cross sections are given as a function of the corresponding electron energies for each considered reaction. The collision processes covered are elastic collisions, excitation and de-excitation, ionisation and attachment processes. Electron-electron collision may also be included as their influence usually becomes significant for ionisation degrees $> 10^{-5}$. However, the ionisation degree is assumed to stay well below this threshold since the electron density is believed not to exceed 10^{17} m^{-3}.

Except the "internal" physical parameter used for the calculation, i.e. reduced electric field, the gas temperature and the fractional concentration of the different species needs to be defined before the actual calculation can take place.

The resulting EEDF, the collision coefficients, the mobility and diffusion coefficient of electrons as functions of mean energy are obtained and then implemented in the form

of look-up tables into the fluid model to account for the individual spatial and temporal dependence of each quantity.

3.5.1. Boltzmann Equation and Two-Term Approximation

The general form of the Boltzmann equation describes the distribution function $f(\vec{x}, \vec{v}, t)$ of particle positions and velocities in the six-dimensional phase space $(\vec{x}, \vec{v})$. In case of electrons in an ionised gas it can be written as:

$$\frac{\partial f}{\partial t} + \vec{v} \cdot \vec{\nabla}_x f - \frac{e}{m_e} \vec{E} \cdot \vec{\nabla}_v f = \left[\frac{\partial f}{\partial t}\right]_c . \tag{3.22}$$

Here, f denotes the electron distribution function, $\vec{v}$ the velocity coordinates, e, m_e, and $\vec{E}$ are the elementary charge, electron mass and electric field, respectively. $\vec{\nabla}_v$ is the velocity-gradient operator and the term $[\partial f / \partial t]_c$ accounts for the rate of change in f due to collisions.

In low temperature plasmas the electron distribution is usually anisotropic due to existing electric fields that accelerate electrons, especially in the sheath regions (see section 2.3). Therefore, equation 3.22 needs to be solved numerically. This can be achieved by applying several simplifications, such as assuming the electric field and all collision probabilities to be spatially uniform on the scale of the electron mean free path. Consequently, the electron distribution is then symmetric in velocity space around the electric field direction and limited to one dimension in position space, along the field direction. The symmetry in velocity space can be described using spherical coordinates, hence, transforming equation 3.22 into:

$$\frac{\partial f}{\partial t} + v \cos\theta \frac{\partial f}{\partial x} - \frac{e}{m_e} E \left(\cos\theta \frac{\partial f}{\partial v} + \frac{sin^2\,\theta}{v} \frac{\partial f}{\partial \cos\theta} \right) = \left[\frac{\partial f}{\partial t}\right]_c . \tag{3.23}$$

Here, θ is the angle between the velocity v and the electric field and x is the position along the field direction. To further simply this equation, only steady-state cases are considered where the electric field and the electron distribution are stationary.

To solve equation 3.23, the classical two-term approximation is commonly used, which simplifies the θ-dependence by expanding f in terms of Legendre polynomials of $cos\,\theta$:

$$f(x, v, t, cos\,\theta) = f_0(z, v, t) + f_1(x, v, t)cos\,\theta\,, \tag{3.24}$$

where f_0 is the isotropic part of f and f_1 is the anisotropic perturbation caused by the electric field. Substituting equation 3.24 into equation 3.23, multiplying by the corresponding Legendre polynomials (1 and $cos\,\theta$), and integrating over $cos\,\theta$ gives equations for f_0 and f_1. A detailed description of the numerical technique used to solve the obtained equations for f_0 and f_1 is given by Hagelaar *et al.* [53].

However, the two-term approximation is known to be inaccurate for high values of the reduced electric field (in the order of several thousands Td) since most collisions are inelastic and the electron distribution function becomes strongly anisotropic [73]. The actual accuracy limit depends on gas mixture and associated EEDF shape. For high accuracy in the high field region six or more term have shown to be sufficient [74]. Nevertheless, extensive tests of the solver software BOLSIG+ showed that the errors of the calculated coefficients are acceptable for fluid modelling in the usual range of discharge conditions [53].

3.5.2. Electron Energy Mobility

Apart from the electron mobility (μ_e) and diffusion coefficient (D_e), BOLSIG+ also solves for the electron energy transport coefficients (μ_ϵ and D_ϵ). In most fluid simulations, the electron energy transport coefficients are approximated by $\mu_\epsilon \approx 5/3\mu_e$ and $D_\epsilon \approx 5/3D_e$, respectively.

Here, the consequences for the simulations will be discussed in terms of comparing the approximated values with the calculated exact values over a range of electron energies, as shown in figure 3.3.

Generally, the approximated values are significantly overestimating the actual electron energy transport coefficients for low and moderate energies. The approximated mobility values exceed the calculated values by at least 10% over a range of 100 eV. In the low energy range below 10 eV the approximated mobility is even higher by 20%−30%. In case of the diffusion coefficient, the discrepancy is more pronounced, exceeding the exact value by more than 30% for low energies, then quickly approaching the exact value for higher energies. At around 100 eV, the approximated diffusion coefficient even

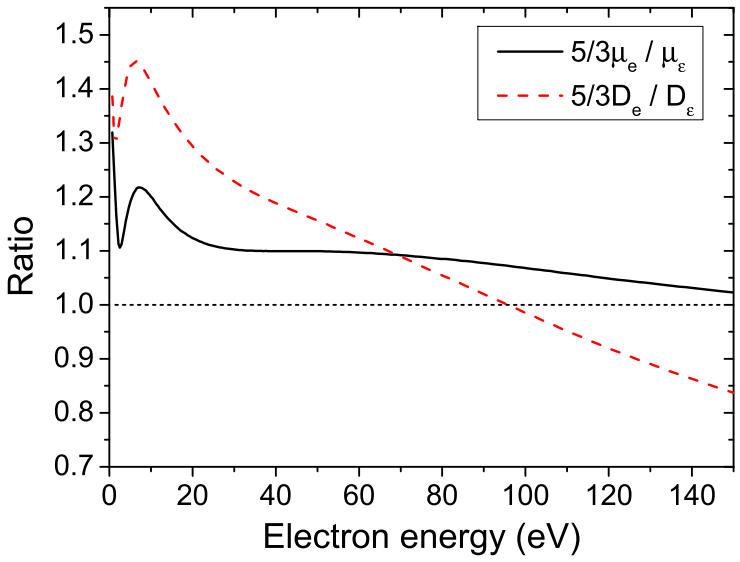

Figure 3.3.: Ratios of approximated and exact values of the electron energy mobility and diffusion coefficient.

underestimates the actual energy diffusion, dropping to about 85% of the calculated electron energy diffusion coefficient at 150 eV .

In low temperature plasmas, mean electron energies stay well below 10 eV, so that the approximated transport coefficients might exhibit a significant effect on plasma dynamics since they are higher than the exact calculated energy transport coefficients.

Indeed, the simulations show that the global mean electron energy decreases as a consequence of using the lower exact energy transport coefficients. However, the actual decrease in energy is less than 2%, leading to an increase of charged particle densities of less than 10%. This rather insignificant change has to be weighted against the computational disadvantage coming with the use of the exact values, namely, increasing the simulation time per iteration by about 75%. Therefore, the approximated values are used for simulations related to studying the fundamental plasma dynamics (chapters 4−7), and the exact values are used when comparing simulation results with experiments, where a higher accuracy is desirable (chapter 10).

3.6. Heavy Particle Transport Coefficients

The heavy particle transport coefficients cannot be obtained in the same manner as the electron transport coefficients, but have to be extrapolated from experimental data available. The applied theories and the methodology of obtaining mobilities and diffusion coefficients for ions and neutrals in pure gases is discussed in the following. Furthermore, the necessary adjustments for transport coefficients in gas mixtures is presented.

3.6.1. Ion Mobility and Diffusion

Ion mobility is directly related to the electric field under which influence ions move through a gas and collide with neutral background atoms or molecules. This allows them to gain energy from the field between collisions apart from their thermal energy. Under the condition that the field energy is lower than the thermal energy, i.e. small reduced electric field values, the ion movement can be described by a slow uniform drift velocity $\vec{v}_d = \mu\vec{E}$ [75].

Several theories describing the ion mobility exist, such as the simple mean free path theory and the rigorous theory by Langevin [76, 77], and the Chapman-Enskog theory [78, 79]. However, these theories fail for high E/N when the energy gained from the electric field is dominant compared with the thermal energy.

In 1953, G.H. Wannier [80] published a theory based on the Boltzmann transport equation, that is applicable for high fields and low fields likewise. It includes three types of interaction processes of which only two are important for the high field region in the investigated plasma discharges. Firstly, rigid sphere repulsion that is also included in the low field theories mentioned above. And Secondly, symmetry forces, that arise due to quantum mechanical effects when electrons are bouncing back and forth between the collision partners. The third interaction process, polarisation attraction, can be neglected because at high E/N the cross section for this process is small. The mobility then scales with $\mu \propto (E/N)^{-1/2}$ and is especially valid where a constant mean free path can be assumed.

For the low field region Wannier's theory predicts a different scaling law, however, in that case experimental data [81, 82] is used and then extrapolated for the high field

region where no experimental data is available.

The standard modelling approach is to assume mobilities to remain constant at their zero electric field mobility value. In contrast to that, here, a more realistic treatment is applied following Wannier's theory on mobility scaling in the high field region. Experiments by Lindinger *et al.* [83] suggest that ion mobilities follow the high field scaling law for reduced electric field values above $E/N > 50$ Td.

Figure 3.4 exemplarily shows the mobility of positive molecular oxygen ions (O_2^+), negative atomic oxygen ions (O^-), positive atomic helium ions (He^+), and positive molecular helium ions (He_2^+) in background gases oxygen (O_2) and helium (He), respectively, as a function of the reduced electric field.

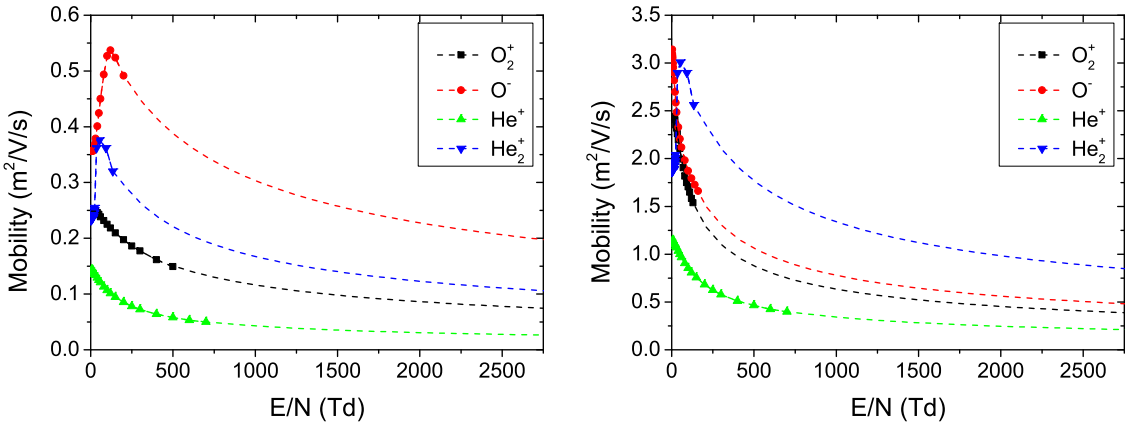

(a) Background gas O_2 (b) Background gas He

Figure 3.4.: Ion mobility scaling for (a) O_2 and (b) He as background gases in high field region (dashed lines) in comparison to experimental data [81–84] (symbols). (values based on $p = 100$ Pa and $T = 300$ K)

The experimental data indicates that the mobility decreases with increasing reduced electric field. This trend is then fitted according to the high field scaling described above. Comparing the fitted mobilities for high fields with the common assumption of a constant zero field mobility indicates that with increasing fields the discrepancy between experimental/fitted data and zero field mobility becomes higher. Especially in the interface region between plasma and surface this plays a significant role and should not be neglected. Considering that the maximum reduced electric field reached within the presented simulations is about 600 Td for a He discharge with 0.5% O_2 admixture and about 5000 Td for a pure oxygen discharge this becomes even more important.

For the ion diffusion, the generalised Einstein relation ($D_i = k_B T_i \mu_i / e$) is used to calculate the effective ion diffusion coefficients. However, knowledge of the actual ion temperature is necessary to obtain a correct diffusion coefficient. As described earlier, the ion temperature in the plasma bulk can be assumed to be the same as the background gas, because the field energy is low compared with the thermal energy. While, in the sheath region, ions gain considerable amounts of energy due to the high electric fields. To account for the effect of higher ion temperatures T_i induced by high electric fields in the sheath region the following approximation [80–82] is used:

$$T_i = T_g + \frac{1}{k_B} \frac{m_i + m_g}{5m_i + 3m_g} m_g (\mu_i |\vec{E}|)^2, \tag{3.25}$$

where m_i and m_g are the ion and background gas masses.

The transport coefficients used for ion species are presented in table 3.1. Here, the mobility μ_0 and diffusion coefficient D_0 are given for zero field ($E = 0$), a constant gas temperature of $T_g = 300$ K and constant background gas pressure of $p = 100$ Pa. These zero field mobilities are then scaled according to the rigid sphere model ($\mu \propto (E/N)^{-1/2}$) introduced above to account for high electric fields in the sheath region.

Table 3.1.: Zero field ($E = 0$) mobility μ_0 and diffusion coefficient D_0 for selected species in helium and oxygen as background gases.

Background gas	Species	μ_0 $[m^2/Vs]$	D_0 $[10^{-3}m^2/s]$	Reference/Comment
O_2	e	$f(\epsilon)$	$f(\epsilon)$	[53]
	O_2^+	$0.25^{a)}$	$6.5^{b)}$	[81]
	O^-	$0.36^{a)}$	$9.3^{b)}$	[81]
	He^+	$0.14^{a)}$	$3.6^{b)}$	$c)$
	He_2^+	$0.23^{a)}$	$5.9^{b)}$	$c)$
He	e	$f(\epsilon)$	$f(\epsilon)$	[53]
	O_2^+	$2.43^{a)}$	$62.8^{b)}$	[81, 83]
	O^-	$3.14^{a)}$	$62.8^{b)}$	[81]
	He^+	$1.15^{a)}$	$29.7^{b)}$	[81]
	He_2^+	$1.86^{a)}$	$48.1^{b)}$	[81, 82, 84, 85]

a) Zero electric field mobility and diffusion values based on gas temperature $T_g = 300$ K and pressure p = 100 Pa. Scaled with $\propto (E/N)^{-1/2}$ for high electric fields as shown in figure 3.4.
b) Generalised Einstein relation: $D_i = \mu_i k_B T_i / q$. The effect of higher ion temperatures T_i induced by high electric fields in the sheath regions is taken into account following equation 3.25.
c) No experimental data available. Approximated by multiplying the corresponding ion mobility in helium with the mass ratio of 0.125 between oxygen and helium.

3.6.2. Neutral Particle Diffusion

The interaction of neutral particles can be described by a simple mathematical approximation, the Lennard-Jones potential [86]. In order to calculate the diffusion coefficient, the Lennard-Jones parameters σ (collision diameter) and ϵ/k_B (potential well depth) for each considered neutral species are required. For two given interacting particles with masses m_i and m_j the diffusion coefficient for a background gas density n_g and temperature T is given by [87]:

$$D_{ij} = \frac{3}{16} \frac{\sqrt{2\pi k_B T / m_{ij}}}{n_g \pi \sigma_{ij}^2 \Omega(T^*)} \propto \frac{T^{1.66}}{p}, \tag{3.26}$$

where $m_{ij} = m_i m_j / (m_i + m_j)$ is the reduced mass, $\sigma_{ij} = (\sigma_i + \sigma_j)/2$ the effective collision diameter, $T^* = T/\sqrt{\epsilon_i \epsilon_j}$ the reduced temperature and $\Omega(T^*)$ the collision integral. The latter is usually approximated using an expression described in [87, 88].

From this follows that the diffusion coefficient shows a distinctive proportionality re-

lationship for any given pressure and temperature, which can be used to easily change the pressure and temperature in the model without the need of recalculating the corresponding diffusion coefficients.

It is noted that the applicability of equation 3.26 is limited to ionised gases with low ionisation degree, which is the case for the investigated plasma discharge.

In table 3.2, the resulting neutral particle diffusion coefficients, as used in the numerical simulations, are listed.

Table 3.2.: Diffusion coefficients $D_{i,j}$ for main neutral species in helium and oxygen as background gases for a given set of Lennard-Jones parameters σ and ϵ/k_B.

Species i	σ [10^{-10} m]	ϵ/k_B [K]	D_{i,O_2} [m^2/s]$^{a)}$	$D_{i,He}$ [m^2/s]$^{a)}$
O_2	3.46$^{b)}$	107.40$^{b)}$	0.0211	0.0756
He	2.58$^{b)}$	10.20$^{b)}$	0.0756	0.1667
He_2	2.67$^{c)}$	16.25$^{c)}$	0.0524	0.1342

a) Diffusion coefficient values are based on pressure p = 100 Pa and gas temperature T_g = 300 K.
b) Reference [89].
c) Reference [90].

3.6.3. Gas Mixtures

The transport coefficients presented in sections 3.6.1 and 3.6.2 are only applicable for pure background gases without any admixtures. To account for the transport coefficients in gas mixtures the Blanc formula has to be implemented [75]. For neutral particles the diffusion coefficient $D_{i,M}$ of a species i in a gas mixture M is given by:

$$\frac{1}{D_{i,M}(p,T)} = \sum_j \frac{f_j}{D_{i,j}(p,T)} \tag{3.27}$$

Here, f_j is the total fraction of species j and $D_{i,j}(p,T)$ is the diffusion coefficient from equation 3.26 of the species i in a pure gas of species j at pressure p and Temperature T.

For ions, Blanc's formula can only be used in case of very small electric field values. However, in the sheath region, where high fields are present, ions gain significant amounts of energy from the field so that their effective temperature T_i (equation 3.25) is different from the background gas temperature T_g and the assumption breaks down.

The full expression is complicated but can be simplified with help of Taylor expansions to [91, 92]:

$$\frac{1}{\mu} = \sum_j \frac{f_j}{\mu_j} + \frac{1}{2}\sum_j \frac{f_j}{\mu_j}(1-\Delta_j)\frac{\partial \ln(\mu_j)}{\partial \ln(E/N)}\left[1+\frac{\partial \ln(\mu_j)}{\partial \ln(E/N)}\right]^{-1} \quad (3.28)$$

$$\text{with:} \quad \Delta_j = (m+M_j)\mu_j^2\left(\sum_i \frac{f_i}{\mu_i}\right)\sum_i \frac{f_i}{\mu_i(m+M_j)}$$

Here, μ is the ion mobility in the gas mixture and μ_j is the ion mobility in the pure background gas j. This equation takes the field derivative of μ_j into account and is corrected by the term Δ_j.

3.7. Plasma Chemical Reactions

Reactions that occur in plasmas depend on the electric energy coupled into the discharge, mainly through heating of the electrons. Due to the electronic structure of the involved atoms and molecules a variety of reactions is possible. A comprehensive overview can be found in [93]. The most common interaction takes place between pairs of particles, either through elastic, inelastic or superelastic collisions.

In elastic collisions only momentum is transferred between the colliding particles and the total kinetic energy is conserved. Thereby, the particles only change direction which results in increasing diffusion times across the plasma.

Inelastic collisions in which the initial kinetic energy is transferred to the internal energy of one of the particles can lead to excitation, ionisation, attachment or dissociation processes. These collisions are mainly electron driven and exhibit dynamics on timescales of ns$-\mu$s. Heavy particle interaction can also be inelastic, but in this case the involved timescales are much longer in the range of μs$-$ms. The different timescales become even more important if a particle is excited into long living metastable states that usually have radiative lifetimes of ms$-$s. For plasma modelling this means that multi-iterative solution schemes have to be applied that are able to solve the plasma chemistry on the respective timescales.

In superelastic collisions the momentum between the colliding particles is redistributed and kinetic energy is gained from internal energy of one or both involved particles.

Usually, in low pressure plasmas most of the collisions involve only two particles and are therefore referred to as two-body collisions. With increasing pressure, three-body collisions become probable creating a more diverse plasma chemistry because the additional interaction with the third particle allows otherwise unphysical reactions between the initial two collision partners to occur.

Some of the important reactions in molecular plasmas are listed in table 3.3.

Table 3.3.: Some reaction processes important for plasma modelling.

Type	Name	Formula
Direct electron-impact	Momentum transfer	$e + M \rightarrow e + M$
	Excitation	$e + M \rightarrow e + M^*$
	Ionisation	$e + M \rightarrow 2e + M^+$
	Attachment	$e + M \rightarrow M^-$
	Dissociation	$e + M_2 \rightarrow e + 2M$
	Dissociative ionisation	$e + M_2 \rightarrow 2e + M + M^+$
	Dissociative attachment	$e + M_2 \rightarrow M + M^-$
	Rotation-vibrational excitation	$e + M_2 \rightarrow e + M_2$ (v, j $\geq$ 1)
Heavy particle interaction	Momentum transfer	$M + N \rightarrow M + N$
		$M^+ + N \rightarrow M^+ + N$
	Neutralisation	$M^+ + N^- \rightarrow M + N$
	Charge transfer	$M^+ + N \rightarrow M + N^+$
		$M^- + N \rightarrow M + N^-$
		$M^- + N^- \rightarrow e + MN$
	Dissociation	$M + N_2 \rightarrow M + 2N$
		$M^+ + N_2 \rightarrow M^+ + 2N$
	Recombination	$2M + N \rightarrow M_2 + N$
	Energy transfer	$M^* + N \rightarrow M + N^*$
	Relaxation	$M^* + N \rightarrow M + N$
	Penning ionisation	$M^* + N \rightarrow e + M + N^+$

3.8. Solution of the Model

The self-consistent model is solved using the time dependent solver in COMSOL Multiphysics [94] for the solution of partial differential equations (PDE). Each individual species is treated with its own set of partial differential equations as described in sections 3.3 and 3.4. When solving the model, COMSOL Multiphysics uses the finite element method (FEM) and runs it together with error control based on a variety of

numerical solvers. This concept of a discretisation of the original PDE problem by approximating it to a problem with a finite number of elements has proven to be effective [95, 96].

After the model parameters and look-up tables have been loaded into the model, the initial point for the FEM is the discretisation of the domain into mesh elements which are linear intervals in a one-dimensional problem and mainly triangular and tetrahedral in two- and three-dimensional domains. To account for the fact that plasmas generally exhibit large gradients in the sheath regions whereas showing a smooth behaviour in the bulk region, a non-linear mesh is applied. The mesh elements increase gradually in a symmetric distribution from the edges to the centre of the domain, i.e. it is finer in the sheath regions and coarser in the plasma bulk region (see figure 3.5).

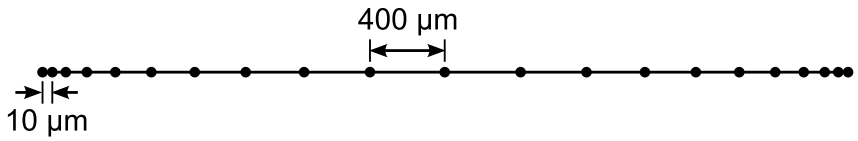

Figure 3.5.: Schematic illustration of the distribution of mesh elements in a linear modelling domain. The actual domain contains 200 linear mesh elements.

For the initialisation of the model initial values for all dependent variables need to be provided. Generally, the assumption of a spatially uniform electron energy of $1 - 5$ eV as well as spatially uniform densities (each positively charged species $\approx 10^{14}$ m^{-3}, negatively charged species $\approx \sum_{pos} n_{pos}$ to account for quasineutrality) has been proven not to cause any numerical instabilities.

The post-processing of the results is conducted with the help of the commercial software MATLAB [97]. For example, time and space averaged values of the densities are calculated, spatial profiles are obtained or phase and space resolved ionisation or excitation can be extracted for various parameters.

3.8.1. Time-Dependent Solver

After the model is initialised with the species densities, electron energy and potential the initial solver time step is started.

Figure 3.6 illustrates the solution process for the time-dependent solver in form of a flow diagram.

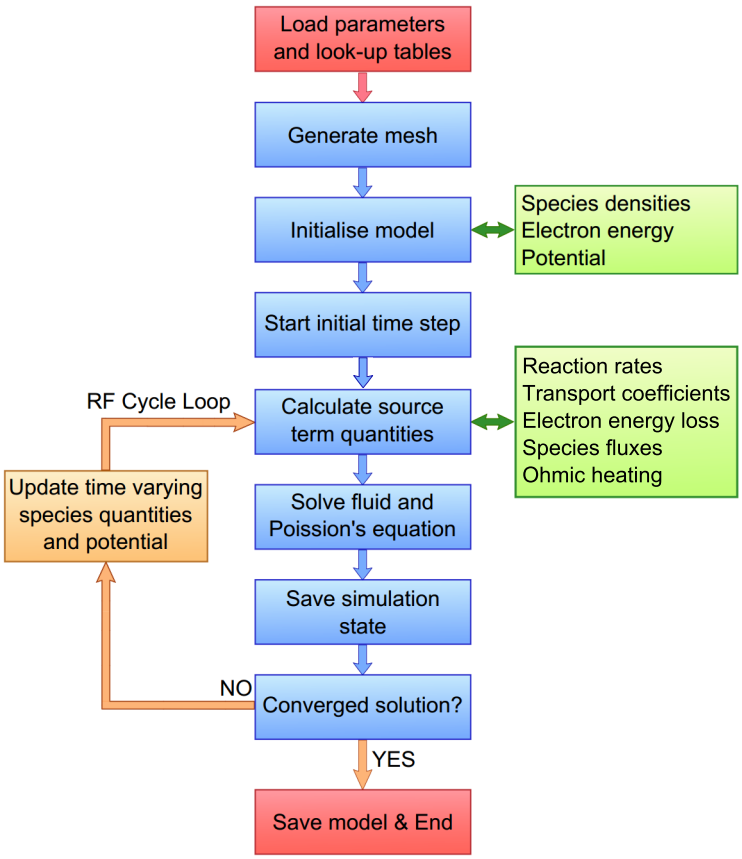

Figure 3.6.: Flow diagram for time-dependent plasma fluid model solver.

As first computational process, source term quantities such as reaction rates, transport coefficients, electron energy loss, species fluxes, and power dissipation via ohmic heating are determined. Subsequently, the fluid equations and Poisson's equation can be solved after which the simulation state is temporarily stored. Then an external check of convergence is conducted to decide whether to stop or continue the simulation by calling the RF cycle loop. In the RF cycle loop, the time varying species quantities and potential are updated so that every subsequent solution of the model is run with the parameter set from the previous solution. Usually, several thousands of RF cycles, i.e. iterations of the solution process are needed to reach a converged periodic steady state solution.

As described earlier, the intrinsic processes take place on different timescales. On the

one hand, electrons react almost instantaneously to changes in the driving electric field. On the other hand, ions only "see" time averaged fields because of their relatively low mobility, and chemically inert neutral metastable species react on even longer timescales. Therefore, it is particularly desirable to accelerate the convergence for the "slow" species in the discharge.

3.8.2. Stationary Solver for Slow Species

To create an effective acceleration for the slow species in the model, relevant production and destruction reactions have to be identified. These can either be rather stationary heavy particle interactions or time modulated electron impact reactions, the latter usually being dominant. Subsequently, effective time averaged production rates are calculated and implemented in the corresponding continuity equation (3.9) in a separate stationary solution process. This stationary solution process is directly executed once after a certain number of the completed time-dependent processes. A big advantage is that the stationary process is very fast because no time-dependent quantities have to be calculated, therefore it takes only a fraction of the time, needed for the time-dependent process, to complete.

Figure 3.7 illustrates such a combined time-dependent and stationary solution process by monitoring the corresponding convergence of slow and fast species, respectively, where a total number of 4000 iterations is shown with three acceleration steps once every 1000 iterations. Here, a convergence of 1 represents the final solution state and is equivalent to a certain density of the considered species. 1000 iterations are equivalent to 1000 RF cycles and correspond to approximately 73.75 μs, which is a relatively small timescale for chemical reactions.

From the convergence of the slow species it is evident that it does not change significantly with progressing RF cycle number. Theoretically, slow species can be solved using the time-dependent solver only, however, because their actual rate of change is very small it would probably take several 100,000 iterations to reach the final solution.

When the acceleration step is executed, the slow species almost instantaneously reach a converged state. The reason why they do not reach it completely is because the fast species are not converged at this stage, yet. Consequently, the fast species convergence

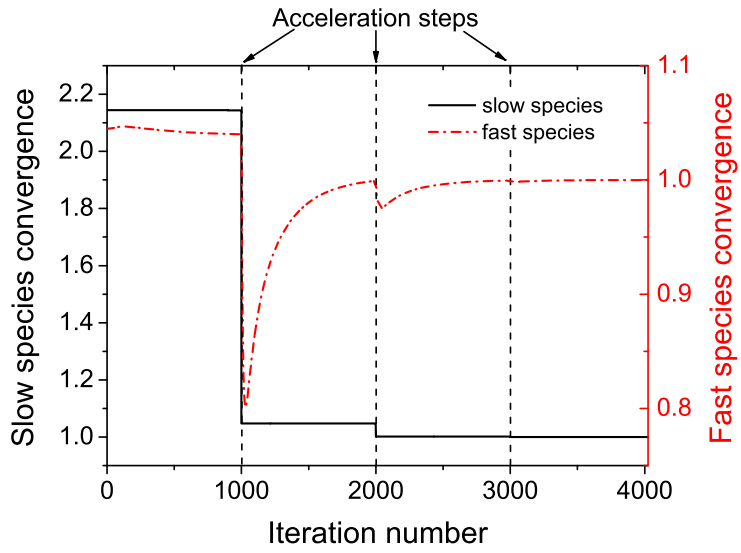

Figure 3.7.: Illustration of a combined time-dependent and stationary solution process, monitoring the convergence of slow (neutrals) and fast (electrons) species.

is also changed significantly but they can very quickly recover from the changes in the numerical simulation. When the second acceleration step is executed the overall changes are not as drastic as after the first step, because the convergence is already near the final solution state. Again, the fast species recovers swiftly and reaches convergence even before 3000 completed iterations so that the last acceleration step does not improve the overall convergence anymore.

The application of acceleration steps is a valuable tool for chemically complex plasma discharges because it is capable of significantly decreasing the computational solution time for these species without interfering much with other species.

4. Parameter Studies in a Symmetric Helium-Oxygen Model

In this chapter a systematic parameter study for a geometrically symmetric helium-oxygen model will be presented. Of particular interest is the knowledge of the influence of residual oxygen on discharge dynamics. To study the influence of oxygen as minority species a variety of oxygen admixtures to a helium feed gas is simulated. Firstly, the applied reaction scheme is discussed. Secondly, the influence of a variable oxygen admixture will be discussed. Special attention is paid to the spatial profiles of the dominant charged species, the resulting electronegativity and ionisation dynamics by means of direct electron-impact ionisation of molecular oxygen. Finally, the findings for numerous parameter variations including power, pressure and discharge gap size will be presented for a helium-oxygen discharge with 0.5% *of total oxygen admixture.*

4.1. Reaction Scheme

A total of 9 species are accounted for in the model. These species are electrons (e), the background gases helium (He) and molecular oxygen (O_2), positive molecular oxygen ions (O_2^+), negative atomic oxygen ions (O^-), helium metastable atoms (He^*), positive helium ions (He^+), positive molecular helium ions (He_2^+) and helium excimers (He_2^*).

The set of plasma reactions used in this chapter is based on a well-established reaction scheme for helium and oxygen species, as used for atmospheric pressure plasmas [61, 98]. However, for a much lower pressure, as applied here, it is expected that certain species and reactions that are dominant at atmospheric pressure will play a minor role (e.g. three body collisions, higher ionised species).

The oxygen related reaction scheme is therefore modified with special regard to dominant charged oxygen species in low pressure discharges, which were observed experi-

mentally [99, 100].

On the one hand, atomic oxygen negative ion densities have been measured by a photo detachment technique and were found to be the most dominant species under the given conditions with O_2^- and O_3^- constituting less than 20% of the total negative charge density. On the other hand, positive ions, determined by mass spectroscopy, show a dominance of O_2^+ ions over O^+ ions, the latter are typically in the range of 10% of the total positive ion density. These findings are confirmed by independent numerical simulations conducted by Gordiets *et al.* [101].

The 25 reactions taken into account are listed in table 4.1. The gas temperature is assumed to be $T_g = 300$ K.

Table 4.1.: Elementary reactions and corresponding rate coefficients in a He/O_2 discharge

No.	Reaction	Rate coefficient[a),b)]	Reference
R1	$e + He \rightarrow e + He$	$f(\epsilon)$	[53]
R2	$e + He \rightarrow e + He^*$	$f(\epsilon)$	[53]
R3	$e + He \rightarrow 2e + He^+$	$f(\epsilon)$	[53]
R4	$e + He^* \rightarrow 2e + He^+$	$f(\epsilon)$	[102]
R5	$e + He^+ \rightarrow He^*$	$6.76 \times 10^{-19}\, T_e^{-0.5}$	[103]
R6	$e + He^* \rightarrow e + He$	$3.17 \times 10^{-11}\, (7736 + T_e)^{-1}$	[104]
R7	$e + He_2^* \rightarrow e + 2He$	3.8×10^{-15}	[103]
R8a	$He^* + He^* \rightarrow e + He^+ + He$	0.45×10^{-15}	[105]
R8b	$He^* + He^* \rightarrow e + He_2^+$	1.05×10^{-15}	[105]
R9a	$He^* + He_2^* \rightarrow e + He^+ + 2He$	2.25×10^{-17}	[105]
R9b	$He^* + He_2^* \rightarrow e + He_2^+ + He$	1.275×10^{-16}	[105]
R10a	$He_2^* + He_2^* \rightarrow e + He^+ + 3He$	2.25×10^{-17}	[105]
R10b	$He_2^* + He_2^* \rightarrow e + He_2^+ + 2He$	1.275×10^{-16}	[105]
R11	$e + He + He_2^+ \rightarrow 2He + He^*$	$1.0 \times 10^{-38}\, (T_e/T_g)^{-2}\, m^6 s^{-1}$	[103]
R12	$2e + He^+ \rightarrow e + He^*$	$6 \times 10^{-32}\, (T_e/T_g)^{-4}\, m^6 s^{-1}$	[103]
R13	$2e + He_2^+ \rightarrow e + He_2^*\ (+ h\nu)$	$3 \times 10^{-32}\, (T_e/T_g)^{-4}\, m^6 s^{-1}$	[103]

Table 4.1 - continued.

No.	Reaction	Rate coefficient[a),b)]	Reference
R14	$2He + He^* \rightarrow He_2^* + He$	$1.5 \times 10^{-46}\, m^6 s^{-1}$	[105]
R15	$2He + He^+ \rightarrow He + He_2^+$	$6.64 \times 10^{-44}\, T_r^2\, m^6 s^{-1}$	[103]
R16	$e + O_2 \rightarrow e + O_2$	$f(\epsilon)$	[53]
R17	$e + O_2 \rightarrow 2e + O_2^+$	$f(\epsilon)$	[53]
R18	$e + O_2^+ \rightarrow 2O$	$f(\epsilon)$	[106]
R19	$e + O_2 \rightarrow O + O^-$	$f(\epsilon)$	[107]
R20	$e + O^- \rightarrow 2e + O$	$f(\epsilon)$	[108]
R21	$O^- + O_2^+ \rightarrow O + O_2$	$2 \times 10^{-13}\, T_r^{-1}$	[101]
R22	$O^- + O_2 \rightarrow e + O_3$	$5 \times 10^{-21}\, T_r^{0.5}$	[101]
R23	$O^- + O_2(^1\Delta)^{c)} \rightarrow e + O_3$	$3 \times 10^{-16}\, T_r^{0.5}$	[109]
R24a	$He^+ + O_2 \rightarrow O_2^+ + He$	$3.21 \times 10^{-17}\, T_r^{0.5}$	[109]
R24b	$He^+ + O_2 \rightarrow O^+ + O + He$	$1.04 \times 10^{-15}\, T_r^{0.5}$	[109]
R25a	$He^* + O_2 \rightarrow e + O_2^+ + He$	2.54×10^{-16}	[110]
R25b	$He^* + O_2 + He \rightarrow e + O_2^+ + 2He$	$1.63 \times 10^{-43}\, m^6 s^{-1}$	[110]

a) Units: Rate coefficients in m^3/s unless otherwise stated; gas temperature T_g and electron temperature T_e ($= \frac{2}{3}\frac{e}{k_B}\epsilon$) in K; $T_r = T_g/300$.

b) *f(ϵ)* indicates that the rate coefficients are obtained from the EEDF. Although not explicitly in the reaction scheme, electron-impact excitation of O_2 into vibrational, Rydberg states and into metastable states is accounted for in the calculation of the EEDF.

c) Estimated as $n_{O_2(^1\Delta)} \approx 1/6\, n_{O_2}$ [108].

The reactions cover a broad set of processes and can be divided into five groups based on the interaction process involved (for a brief overview of possible reaction processes see chapter 3.7). The first group includes elastic collisions of electrons with the background gases helium (R1) and oxygen (R16), which plays an important role for the electron energy conservation. The second group comprises direct electron-impact interaction with relevant helium (R2 - R7) and oxygen (R17 - R20) species, that include excitation, ionisation, attachment, dissociative, and combined processes. This second group is essential for driving the plasma discharge and its dynamics. The third group of reactions consists of two-body heavy particle interaction, R8 - R10 for helium and

R21 - R23 for oxygen. Two-body heavy particle collisions govern species conversion and can be effective electron production processes. Due to the small mobility of such heavy particles, the rate coefficient is usually assumed to be constant or has a slight temperature dependence. Consecutively, three-body reactions involving helium species (R11 - R15) comprise the forth group of reactions, but should not play a significant role for the plasma discharge under the given conditions. Finally, direct helium-oxygen interaction processes (R24, R25) are accounted for in direct and dissociative charge transfer and Penning-ionisation reactions. This last group has proven to be of significant importance for atmospheric pressure plasmas [111] and was therefore also included in the conducted simulations.

The electron, ion and neutral transport coefficients used are those presented in table 3.1.

4.2. Influence of Variable Oxygen Admixture

The admixture was varied from 0.5% up to 99% O_2 while a constant pressure ($p = 100$ Pa), discharge gap size ($d = 40$ mm) and input power density ($P/A = 1000$ W/m^2) are set. The simulation results are obtained from a periodic steady-state solution along the symmetry axis of the discharge as shown in figure 3.1(a).

Figure 4.1 shows the global average particle densities of electrons, positive molecular oxygen ions, negative atomic oxygen ions, helium metastables, and positive helium ions on a semi-logarithmic scale as a function of the O_2 admixture for a constant input power and pressure.

Even for the lowest oxygen admixture it is evident that oxygen ions are by far more dominant than helium ions, exceeding their density by at least two orders of magnitude. This is because oxygen has a significantly lower ionisation threshold than helium. Therefore, more oxygen molecules are ionised by direct electron-impact from lower energetic electrons than in case of helium. Furthermore, the high helium metastable density, which even exceeds the oxygen ion and electron densities for small oxygen admixtures, amplifies the dominance of oxygen ions over helium ions through Penning ionisation.

Although the power input is constant, the general trend is a monotonic decay of

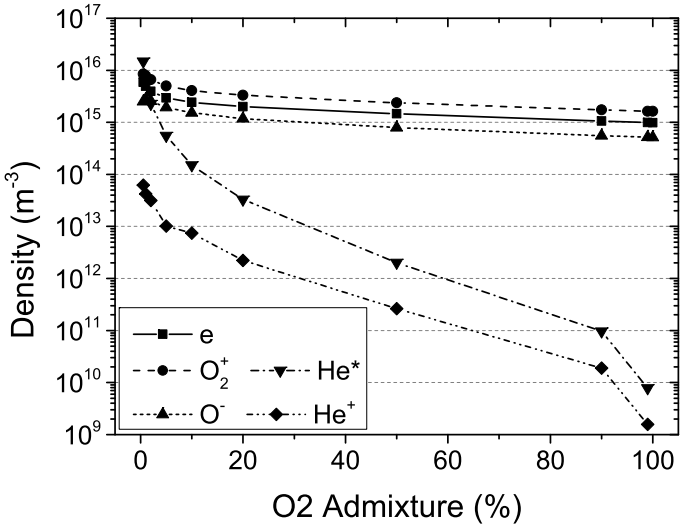

Figure 4.1.: Global average particle densities as function of the O_2 admixture. (p = 100 Pa, d = 40 mm, P/A = 1000 W/m^2)

global densities with increasing oxygen admixture. An increasing oxygen admixture is equivalent to an increasing partial pressure of oxygen, which leads to a more collisional discharge. Thereby, additional power loss channels are introduced, such as into vibrational and rotational states, and causes an effective decrease of power which subsequently leads to smaller global densities. The rapid decay of helium ion and metastable densities can be explained by means of its insignificant roles for the discharge and the increasing oxygen admixture.

Figure 4.2 illustrates the mean electron energy and the weighted mean electron energy in dependence of the O_2 fraction in the model. The weighted mean electron energy was obtained by weighting the mean electron energy with the electron density.

It can be observed that the not weighted mean electron energy exhibits a maximum for a O_2 fraction of $5\% - 10\%$ and decreases for higher oxygen admixtures. However, the weighted mean electron energy shows a monotonic decay with a higher gradient for small oxygen fractions. As already discussed, the discharge becomes more collisional with increasing oxygen admixture due to the increasing partial pressure. It is known that the electron energy decreases with increasing pressure because this leads to reduced losses at the walls and in turn results in a lower "production" of electron energy.

Another interesting observation is the influence of the oxygen admixture on the spatial

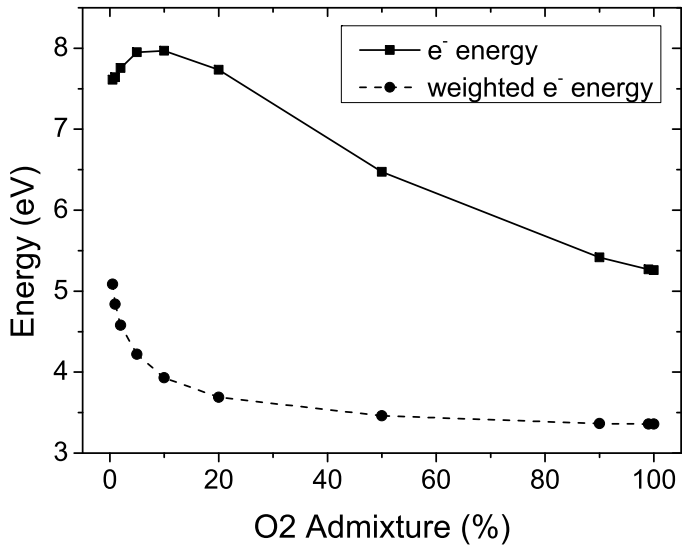

Figure 4.2.: Mean electron energy and weighted mean electron energy as a function of the O_2 admixture. ($p = 100$ Pa, $d = 40$ mm, $P/A = 1000$ W/m^2)

profiles of dominant charged species, i.e. electrons, O_2^+ and O^-. The density profiles of heavy particles are almost static because they can only follow the time-averaged fields due to their relatively small mobility. However, electrons are much more mobile and are able to follow the RF field movement. Therefore, figure 4.3 shows the resulting spatial density distribution of the heavy charged particles and the time-averaged electron density profile for two different oxygen admixtures (2% and 50%).

It can be observed that the negative atomic oxygen ion spatial profile exhibits a maximum within the centre of the bulk for a low oxygen admixture ($\leq$ 2%) (figure 4.3(a)) and even exceeds the local electron density in the centre of the discharge, whereas it shows a broader double peaked profile near the electrodes for higher O_2 admixtures (figure 4.3(b)).

Experimental results by Katsch *et al.* [112] suggest that the spatial profiles also depend on the pressure. They observed similarly a maximum of the negative oxygen ion profile in the bulk and a transition to a double peaked structure by increasing the pressure. This is in good agreement with the simulation since the oxygen admixture can also be understood as the partial pressure of oxygen in the discharge.

Furthermore, the O^- density decays faster than the electrons in the electrode region. This is a result of the average electric field that, in the sheath, is directed towards the elec-

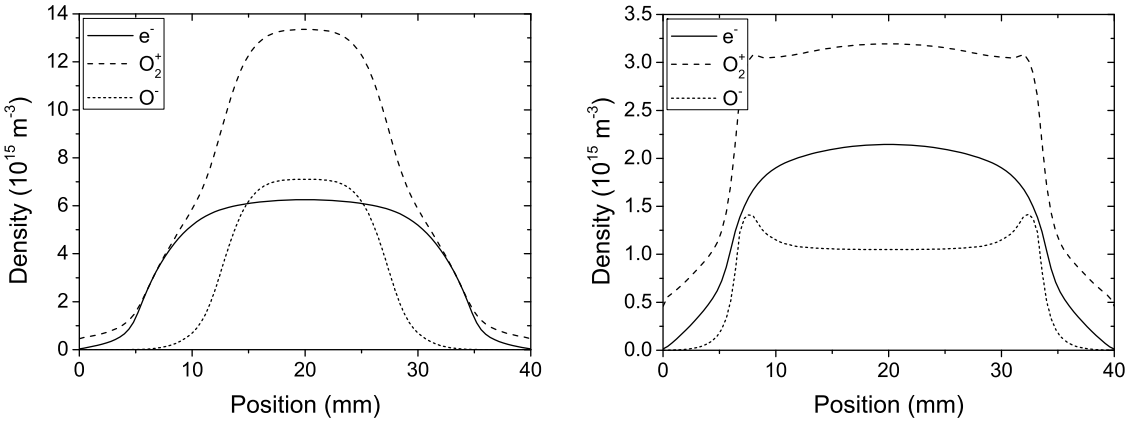

(a) 2% O_2 admixture (b) 50% O_2 admixture

Figure 4.3.: Time averaged spatial profiles of electrons, O_2^+ and O^- for two different oxygen admixtures. ($p = 100$ Pa, $d = 40$ mm, $P/A = 1000$ W/m^2)

trode, so that negative ions are repelled and positive ions are attracted to the electrode on time-average. Additionally, the negative ion density does not exceed the electron density. This is due to the dominant production and destruction mechanisms. Generally, the spatial variation of electrons entails a corresponding variation of the O^- density, since the latter is only generated by electron collisions in the model. However, in the bulk region the destruction of O^- exceeds the production due to collisions with $O_2(^1\Delta)$, which can be identified to be the main collision partner leading to destruction [112]. This leads to the observed double peaked structure in the O^- spatial profile.

Having analysed the spatial profiles, this gives the opportunity to gain information on the electronegativity by averaging the corresponding density profiles in space and time. In this work, the electronegativity (en) is defined as the time and space averaged density ratio of negative ions and electrons:

$$en = \frac{\langle n_{O^-} \rangle_{x,t}}{\langle n_e \rangle_{x,t}}. \tag{4.1}$$

Figure 4.4 shows the dependence of the electronegativity on the oxygen admixture for a constant power (1000 W/m^2) and pressure (100 Pa).

Starting from high admixtures of oxygen, the electronegativity increases over-linearly until it reaches a maximum value of 0.66 at 5% O_2 admixture. This means that the time and space averaged O^- density never exceeds the electron density. This is because with

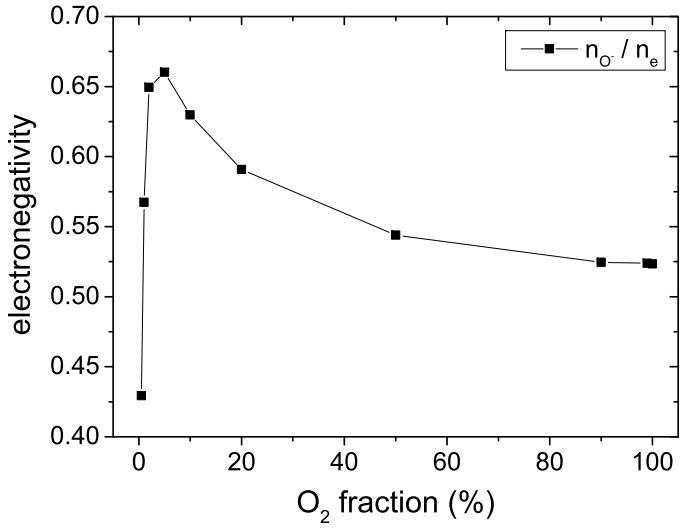

Figure 4.4.: Electronegativity as function of the O_2 admixture. ($p = 100$ Pa, $d = 40$ mm, $P/A = 1000$ W/m^2)

increasing oxygen content the volume destruction of negative ions becomes more dominant than the production induced by electrons. Thereby, the electron density changes at a smaller rate than the negative ion density. Experiments show typically slightly higher electronegativity but this may be explained due to the neglect of other possible negative ion species in the applied model or an overestimation of the destruction processes for negative atomic oxygen ions with $O_2(^1\Delta)$.

Furthermore, it can be observed that for very small admixtures of oxygen ($< 5\%$) the electronegativity drops rapidly to an even lower value. This is due to the rapid increase in the electron density with additional helium, whereas the negative atomic oxygen ion density does not increase at the same rate.

The influence of O_2 admixture on the ionisation dynamics, which serve as indicator for the electron dynamics, is exemplarily shown by means of the ionisation rate from direct electron-impact ionisation of oxygen molecules. Figure 4.5 illustrates the simulated time and space averaged ionisation in units of 10^{20} m^{-3}s^{-1}.

The time and space averaged ionisation also exhibits a maximum, although for a slightly higher oxygen admixture than in case of the electronegativity. To explain this, the ionisation features will be analysed phase and space resolved on a common scale for 0.5%, 10%, 50% and 99% O_2 in the gas mixture in the following (figure 4.6).

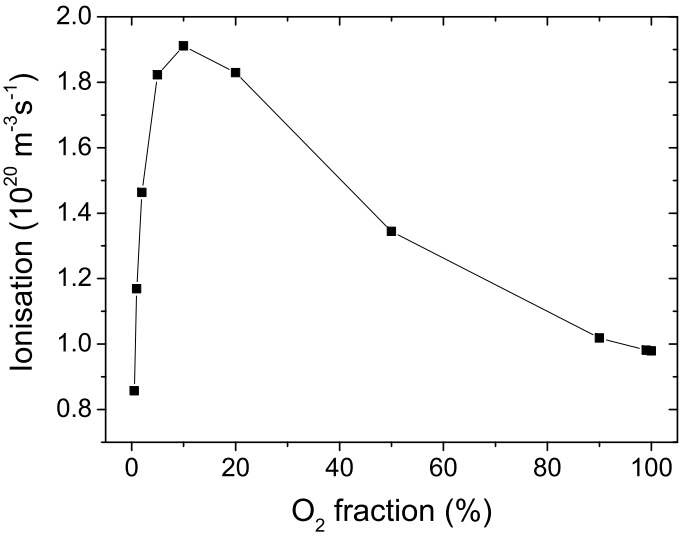

Figure 4.5.: Time and space averaged direct electron-impact ionisation of molecular oxygen. ($p = 100$ Pa, $d = 40$ mm, $P/A = 1000$ W/m^2)

Here, the x-axis spans over one full RF cycle (≈ 73.75 ns) and the y-axis covers the full discharge gap with the powered electrode at 0 mm and the grounded at 40 mm. For relatively low oxygen admixtures (figure 4.6(a)) only one broad but not particularly pronounced ionisation feature at each electrode that expands into the bulk is observable. This feature can be identified as ionisation induced by the sheath expansion and increases in intensity with increasing oxygen content. At the higher O_2 admixture of 10% (figure 4.6(b)) in addition to the much more pronounced sheath expansion ionisation, ionisation during the sheath collapse phase occurs. Since no ionisation induced by secondary electrons takes place this discharge mode is equivalent to an α-mode discharge.

For high oxygen admixtures ($\geq$ 50%) oxygen cannot be called the minority species anymore and clearly three ionisation features can be observed (figure 4.6(c)). These features agree very well with experimental results for a comparable set of parameters [113] and can be identified as sheath expansion, sheath collapse ionisation and ionisation due to secondary electrons. The latter becomes more dominant with additional oxygen admixture (figure 4.6(d)) and is equivalent to a transition to a γ-mode discharge. Please note, that in the transition to a collision dominated sheath, the sheath width decreases as predicted in section 2.3.

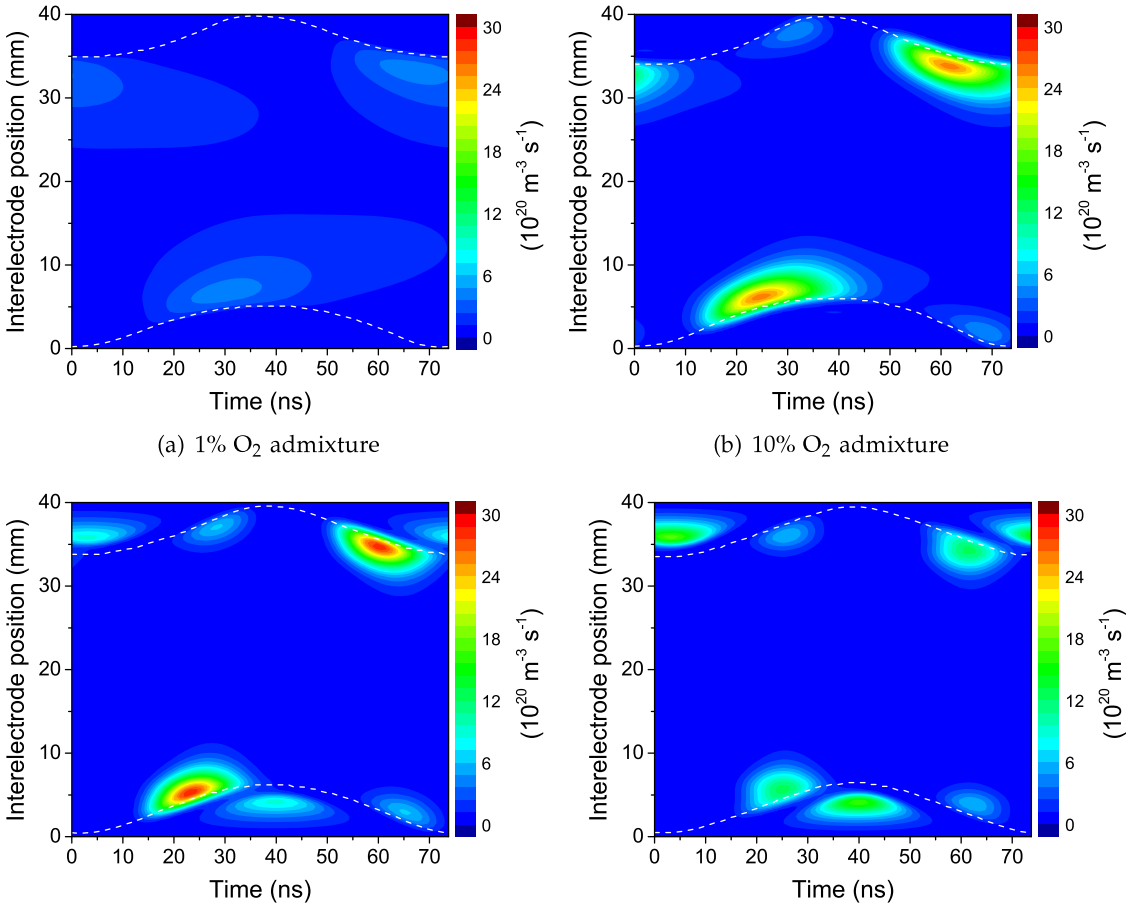

(a) 1% O_2 admixture

(b) 10% O_2 admixture

(c) 50% O_2 admixture

(d) 99% O_2 admixture

Figure 4.6.: Time and space resolved direct electron-impact ionisation of molecular oxygen. Dashed lines represent the sheath boundaries. ($p = 100$ Pa, $d = 40$ mm, $P/A = 1000$ W/m^2)

It needs to be emphasised that the ionisation features mainly depend on the oxygen content in the discharge since the oxygen ions are in each case the most dominant charged heavy species and exceed the incorporated helium ion species usually by several orders of magnitude independent of the oxygen admixture. Consequently, it is very important to account for this fact. However, it appears that helium acts as an inhibitor for the secondary electron-impact ionisation of molecular oxygen.

Apart from the influence of oxygen on discharge dynamics it is interesting to analyse the discharge behaviour at a constant oxygen admixture but various parameters such as power, pressure and discharge gap.

4.3. Parameter Variations with 0.5% Oxygen Admixture

Based on the assumption that residual oxygen will only constitute a small amount, the oxygen admixture was chosen to be 0.5% for all following conducted simulations.

First, the influence of the applied power on numerous plasma properties will be discussed followed by a voltage-current analysis under pressure variation. Finally, simulation results on the dominant charged species and mean electron energy will be presented under a variation of the discharge gap.

4.3.1. Power

For the power variation the pressure was chosen to be 100 Pa while the discharge gap was kept constant at 40 mm. To eliminate any misunderstandings, it has to be noted that all simulations were conducted setting a certain power density in units of W/m^2. Since the effective surface area is the same for all simulations, this power density will simply be referred to as power.

Generally, the voltage-current characteristic is an indication for the discharge regime as described in chapter 2. At low power the charge carrier production takes place mainly in the bulk due to electron avalanches giving this regime the name α-mode (compare equation 2.3). In the α-mode the voltage rises almost linearly with increasing power. At high power the charge carrier multiplication shifts towards the electrodes due to an increased ion impact of the electrode material leading to a transition into a discharge regime known as γ-mode. Usually, this leads to a decreasing gradient between voltage and power so that the power-voltage characteristic flattens out.

Figure 4.7 shows the simulated power-voltage and voltage-current characteristic in the range of $(1000 - 25000)\ W/m^2$. For higher power input, when the discharge is in pure γ-mode, it is anticipated that the voltage will drop while the current still increases, as shown in figure 2.1(b).

The point of maximum voltage for a given power is known as the α-γ-mode transition. Numerically, it is difficult to simulate this transition point just by applying a fixed voltage because there may be multiple solutions. To overcome this difficulty in the simulation, a constant current density can be applied as boundary condition instead of the

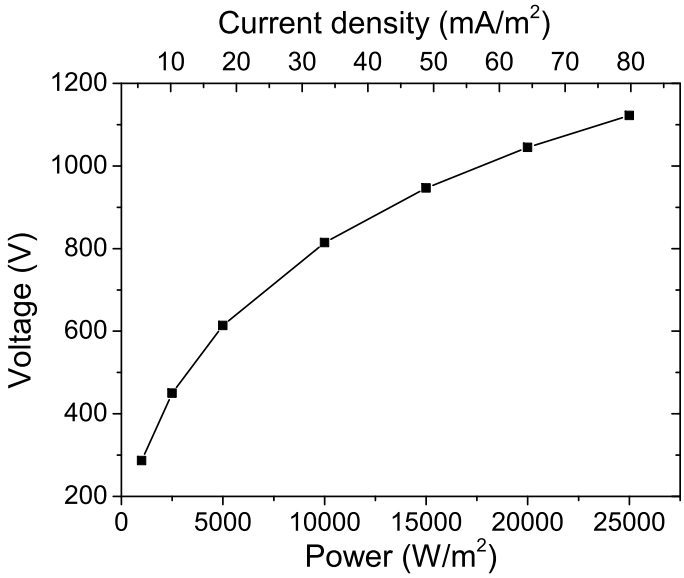

Figure 4.7.: Simulated power-voltage and voltage-current characteristic. ($p = 100$ Pa, $d = 40$ mm, 0.5% O_2 admixture)

voltage because each current density will correspond to a certain power and vice versa. The total current density $\vec{J}$ consists of the sum of the displacement current density and the conduction current:

$$\vec{J}(t) = \varepsilon_0 \frac{\partial \vec{E}}{\partial t} + \sum_i q_i \vec{\Gamma}_i \tag{4.2}$$

Here, the index i denotes all charged species including electrons.

It has to be pointed out that this current approach is only suitable for the simulations since setting a fixed current density is not possible under experimental conditions.

Apart from the increasing voltage the mean electron energy also rises monotonically with power, as shown in figure 4.8(a), while the weighted mean electron energy stays constant.

The growth of the mean electron energy is caused by a rapid rise of electron energy in the sheath region while the bulk energy is almost not affected by the increasing power. This shows the relevance of the weighted mean electron energy as the correct measure of the electron energy. Namely, it takes into account that there are only few very high energetic electrons (sheath), whereas the majority of electrons exhibit low energies (bulk).

The densities of the major species also show a similar trend as the voltage and mean

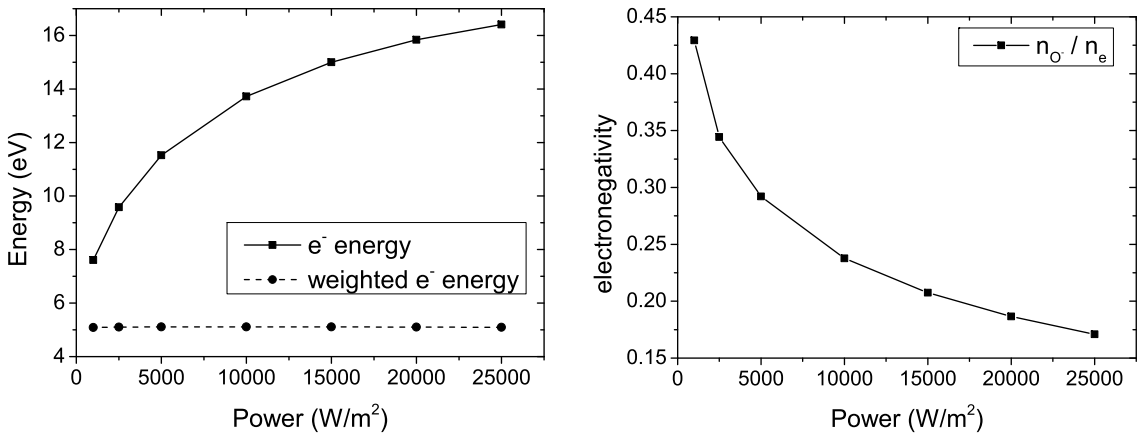

Figure 4.8.: (a) Mean electron energy and weighted mean electron energy, and (b) electronegativity as function of applied power. ($p = 100$ Pa, $d = 40$ mm, 0.5% O_2 admixture)

electron energy, i.e. they increase with power. However, the electron and O_2^+ ion densities have a much steeper slope than the density of O^- negative ions. This leads to a decreasing electronegativity as illustrated in figure 4.8(b) and agrees well with experimental results conducted in capacitively coupled plasmas in pure oxygen [55].

Direct electron-impact ionisation as well as spatial profiles are not shown here because they follow the same trends as already presented earlier (compare figures 4.3 and 4.6).

4.3.2. Pressure

For the pressure variation the power density was chosen to be 1000 W/m^2 and the discharge gap was kept 40 mm.

Initially, it is observed that with increasing pressure a lower voltage is needed to sustain the constant power set in the simulation since the neutral and charged particle densities increase with pressure. Furthermore, the total current density (equation 4.2) as wells as the voltage-current phase relationship change and are exemplarily examined in the centre of the discharge, as shown in figure 4.9. The current density and voltage are defined by means of their amplitude; the phase is given in degrees and the error bars indicate the uncertainty of the phase difference between current density and voltage.

Since the charged particle densities increase with pressure the plasma can be expected

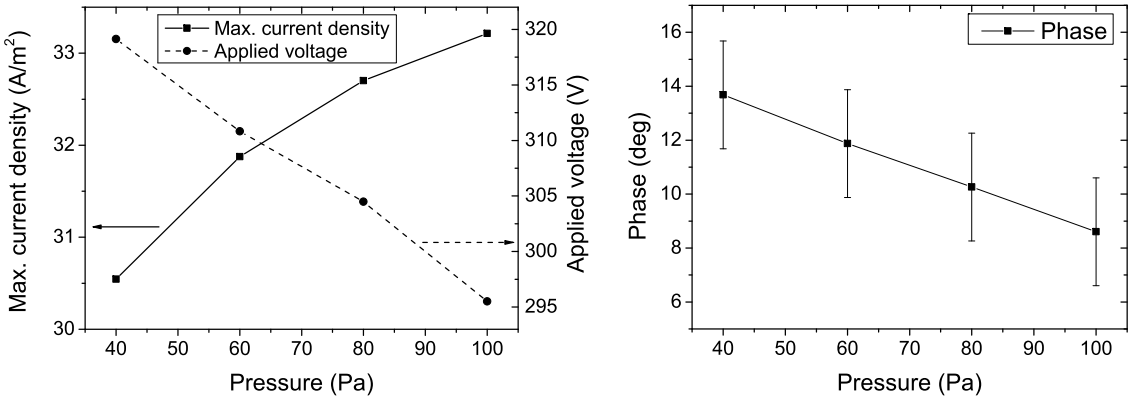

(a) (b)

Figure 4.9.: Pressure dependence of (a) current density (left y-axis) and voltage (right y-axis) and (b) voltage-current phase relationship at the centre of the discharge. ($P/A = 1000$ W/m^2, $d = 40$ mm, 0.5% O_2 admixture)

to become more conductive which is reflected in the increasing current density. This results in a change of the impedance and explains the phase change between current density and voltage with increasing pressure.

In turn, the power is the product of current, voltage and the cosine of their phase. Now, in case of a increasing current and a decreasing phase, which means that the cosine of the phase is increasing, the only possibility to uphold a constant power is a decreasing voltage.

These results need to be understood as a first indication on the pressure dependence of the voltage-current characteristic. For a more accurate description it would be appropriate to use Fourier analysis of both the current density and voltage. In particular, the current density tends to loose its sinusoidal character quickly, generally, by an increase of power since it is generated mainly by electron dynamics.

4.3.3. Discharge Gap Size

The variation of the discharge gap size will only be discussed briefly for the purpose of completeness. The simulations were conducted at constant pressure of 100 Pa, constant power density of 1000 W/m^2 and a 0.5% O_2 admixture.

The simulations yield that the dominant charged species densities increase with discharge gap size (see figure 4.10(a)). Again, O_2^+ shows to be the most dominant positively charged species exceeding the He^+ and He_2^+ densities by more than two orders of magnitude although the ratio of helium to oxygen gas is $\approx 200:1$. Thereby, O_2^+ compensates the negative species densities by its own. As in all previous simulations, the average electron density exceeds the O^- density. From the smallest to the biggest discharge gap, the electron density increases gradually by a factor of 1.8, while the negative ion density increases by a lower factor of 1.6. This results in a decrease of electronegativity by about 10%.

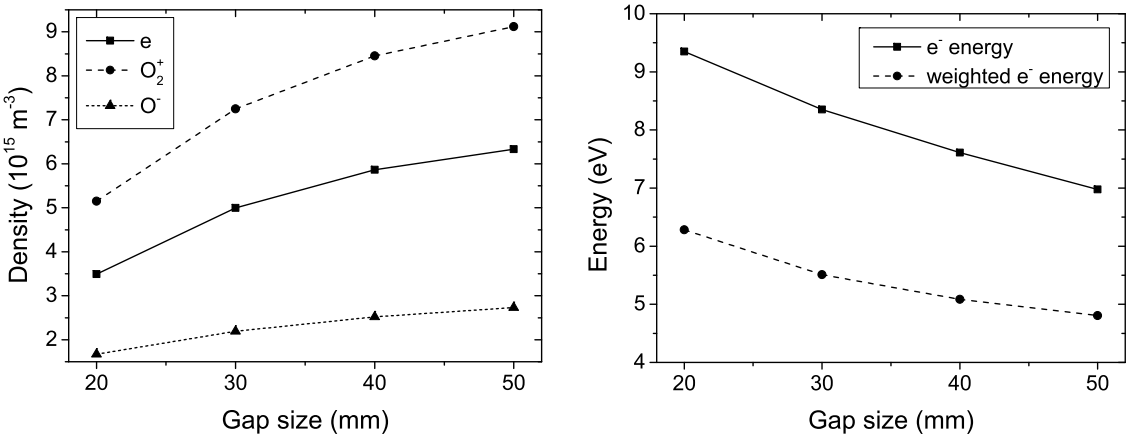

Figure 4.10.: Discharge gap size dependence of (a) dominant charged species densities and (b) weighted mean electron energy. ($P/A = 1000$ W/m^2, $d = 40$ mm, 0.5% O_2 admixture)

The mean electron energy as well as the weighted mean electron energy decrease with increasing discharge gap size (see figure 4.10(b)). This can be understood by taking into account that the discharge volume increases with increasing the gap size. As a result the volume to surface ratio increases and changes the particle balance, which leads to the observed energy decrease for bigger electrode gaps.

4.4. Analysis of Reaction Rates

A critical analysis of the reaction rates can help to further improve the numerical model. By means of this analysis it is possible to gain information on how different reactions contribute to the production and destruction of the incorporated species. This allows to understand whether some reactions or even species could be removed from the simulation without having significant effect on the final results but speeding up the total simulation process.

Figure 4.11 gives an overview of all reaction rates from a simulation with minimum amount of oxygen (0.5%) at constant power density ($P/A = 1000$ W/m^2), pressure ($p = 100$ Pa) and discharge gap size ($d = 40$ mm).

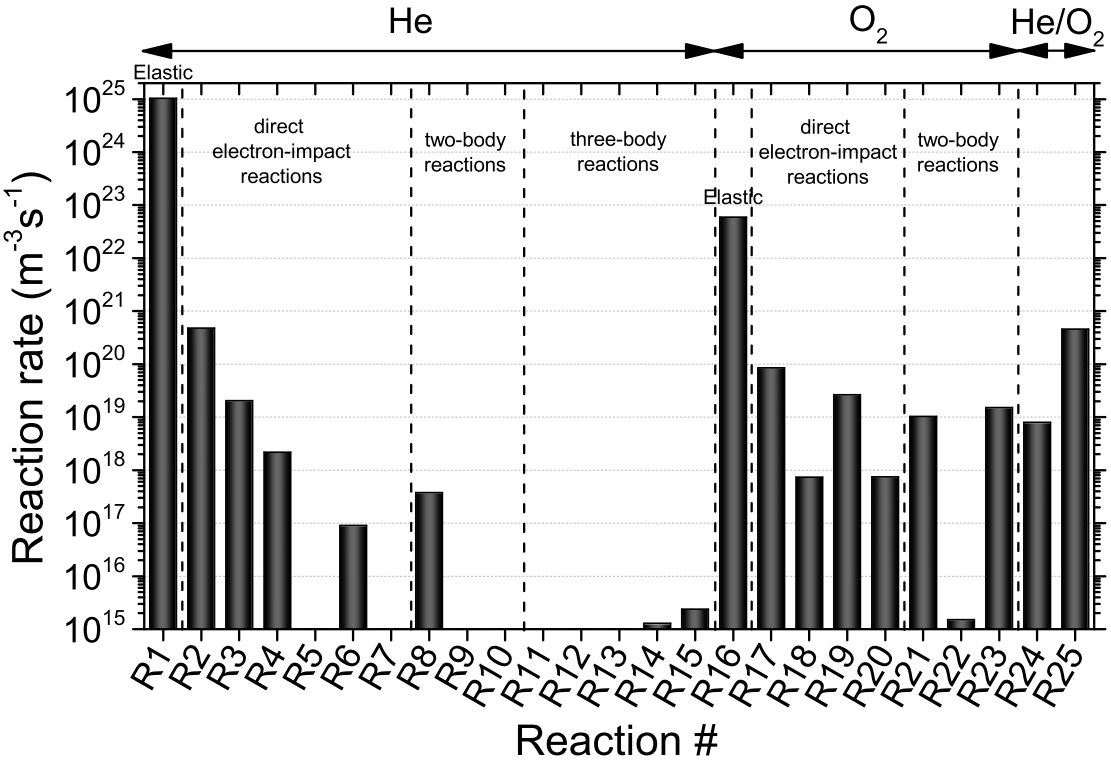

Figure 4.11.: Time and space averaged reaction rates for all reactions as states in table 4.1 on semi-logarithmic scale. ($P/A = 1000$ W/m^2, $d = 40$ mm, $p = 100$ Pa, 0.5% O_2 admixture)

The reaction numbers on the x-axis correspond to the reactions stated in table 4.1 and are sorted into corresponding groups. Since the different reactions have significantly varying reaction rates, a logarithmic scale was chosen visualising a range from (10^{15} –

10^{25}) $m^{-3}s^{-1}$. Reactions exhibiting an even lower rate are not visible.

Clearly, R1 and R16 which represent the elastic collisions of electrons with helium and oxygen, respectively, have the highest reaction rates. This means, elastic collisions comprise the dominant energy transfer mechanism in the plasma. The second most dominant processes are the excitation of helium (R2) and its immediate destruction through Penning-ionisation (R25), thus promoting the observed dominance of oxygen ions over helium ions for any admixture of oxygen.

Apart from that, direct electron-impact reactions generally have high reaction rates, which can easily be understood, since electron dynamics are the main driving force for any plasma discharge. However, electrons appear to be only effective at ion production reactions for He^+ (R3, R4), for O_2^+ (R17) and O^- (R19), whereas have poor ion destruction (R5, R18, R20) and de-excitation (R6, R7) effectiveness.

Two-body interaction between heavy particles seems to be more efficient at destroying ions and excited species (R8 & R25 > R6, R21 > R18, R23 > R20, R24 > R5).

For this reaction rate analysis, it can also be identified that metastable oxygen (R23) and positive ions (R21) are the dominant destruction partners for negative ions, together exceeding the reaction rate of negative ions with the background gas (R22) and electrons (R20) by several orders of magnitude.

Furthermore, all three-body reactions (R11 $-$ R15) in the model show a negligible reaction rate as well as all reactions involving helium molecular species (He_2^+, He_2^*) are of minor importance (R9 $-$ R11, R13).

By neglecting these reactions and the helium molecular species the computational time of the numerical simulation can be improved significantly. Thus, this analysis technique represents a valuable tool to modify the model, without having a major effect on the results.

5. Influence of Ion Mobility Treatment on Plasma Dynamics

As shown in the previous chapter, oxygen constitutes both the dominant positive and negative ions species in a He/O_2 gas mixture independent of the actual oxygen admixture. To speed up computational time and to provide best possible insight into the fundamental underlying plasma dynamics the numerical simulations are reduced to an oxygen only model.

In this chapter, 1D symmetric and asymmetric simulation results for a capacitively coupled electronegative oxygen plasma with a discharge gap of 40 mm are presented. A simplified reaction scheme including the dominant positive and negative ions, background gas, and electrons is considered. In the investigated parameter regime ($p = 10 - 100$ Pa, $V_{rf} = 200 - 500$ V amplitude, $f = 13.56$ MHz) qualitatively equivalent trends are observed. Therefore, only results obtained for a pressure of 40 Pa and a voltage amplitude of 300 V are discussed in the following.

An improved treatment, by accounting for the dependence of ion mobilities on E/N, is compared to the standard approach, based on using zero-field mobility values only. The charged particle dynamics as a result of direct electron-impact ionisation of oxygen, secondary electron release from the electrodes, the spatial distribution of all involved particles as well as impact of geometry and model modification on ion energies is analysed and compared to independent simulations and experiments.

5.1. Reaction Scheme

A total of 4 species are accounted for in these numerical simulations, namely electrons (e), the background gas molecular oxygen (O_2), positive molecular oxygen ions (O_2^+), and negative atomic oxygen ions (O^-). The negligence of other molecular and atomic oxygen ion species originates from experimental [99, 100] and modelling [101] results,

as already discussed in section 4.1.

The plasma reaction scheme is purposely chosen as simple as possible to provide the best possible insight into details of the fundamental consequences of the applied improvements in the model. With this limited set of species the chemical reactions can be reduced significantly to a minimum of 8 reactions, which are listed in table 5.1. The gas temperature is assumed to be $T_g = 300$ K.

Table 5.1.: Elementary reactions and corresponding rate coefficients in a O_2 discharge

No.	Reaction	Rate coefficient[a),b)]	Reference
R1	$e + O_2 \rightarrow e + O_2$	$f(\epsilon)$	[53]
R2	$e + O_2 \rightarrow 2e + O_2^+$	$f(\epsilon)$	[53]
R3	$e + O_2^+ \rightarrow 2O$	$f(\epsilon)$	[106]
R4	$e + O_2 \rightarrow O + O^-$	$f(\epsilon)$	[107]
R5	$e + O^- \rightarrow 2e + O$	$f(\epsilon)$	[108]
R6	$O^- + O_2^+ \rightarrow O + O_2$	$2 \times 10^{-13}\, T_r^{-1}$	[101]
R7	$O^- + O_2 \rightarrow e + O_3$	$5 \times 10^{-21}\, T_r^{0.5}$	[101]
R8	$O^- + O_2(^1\Delta)^{c)} \rightarrow e + O_3$	$3 \times 10^{-16}\, T_r^{0.5}$	[109, 114]

a) Units: Rate coefficients in m^3/s; gas temperature T_g in K; $T_r = T_g/300$.
b) *f(ϵ)* indicates that the rate coefficients are obtained from the EEDF via BOLSIG+ using cross section data. Additionally, electron-impact excitation of O_2 into vibrational, Rydberg states and into metastable states is accounted for in the calculation of the EEDF.
c) Estimated as $n_{O_2(^1\Delta)} \approx 1/6\ n_{O_2}$, see ref. [108].

Reactions R1 describes electron momentum transfer collisions with the background gas molecular oxygen. Dominant charged heavy particles volume production processes, such as ionisation (R2) and dissociative attachment (R4), as well as their destruction induced by collisions with electrons (R3, R5), are included. Furthermore, heavy particle interaction processes describing the destruction of positive and negative ions are incorporated with temperature dependent reaction rates (R6, R7 and R8).

The transport coefficients used are listed in table 5.2. Here, the values for mobility μ_0 and diffusion coefficient D_0 are given for zero electric field ($E = 0$), constant gas temperature of $T_g = 300$ K and constant oxygen background gas pressure of $p = 40$ Pa. In the regions of high electrical field above $E/N > 50$ Td, like the sheath regions [75], the mobilities are scaled according to the rigid sphere model ($\mu \propto (E/N)^{-1/2}$), as discussed in section 3.6.

Table 5.2.: Zero field ($E = 0$) mobilities μ_0 and diffusion coefficients D_0 in a O_2 discharge.

Species	μ_0 $[m^2/Vs]$	D_0 $[10^{-3}m^2/s]$	Ref.
e	$f(\epsilon)$	$f(\epsilon)$	[53]
O_2^+	$0.62^{a)}$	$16.0^{b)}$	[81]
O^-	$0.89^{a)}$	$23.0^{b)}$	[81]

a) In O_2 gas for $T_g = 300$ K and p = 40 Pa. Scaled with $\propto (E/N)^{-1/2}$ for $E/N \geq 50$ Td.
b) Generalised Einstein relation: $D_i = \mu_i k_B T_i / q$. The effect of higher ion temperatures T_i induced by high electric fields in the sheath region is taken into account following Wannier's formulation (equation 3.25).

5.2. Symmetric Discharge Geometry

As described in section 3.6.1, the particular difference of the modified fluid model to the non-modified model is the treatment of ion transport coefficients that now decrease with increasing reduced electrical field. To benchmark the implemented fluid model against the non-modified model as presented in [115] simulations were conducted under identical parameters as stated above.

A general observation is that all time and space averaged densities (i.e. electrons, O_2^+, O^-) in the modified model are higher by about 20% than in the non-modified model. However, the effective power is lower by 88 W/m^2. Since the input voltage waveform is the same for both models the power change can be explained by a change in the current and voltage-current phase relationship. Figure 5.1 shows the voltage-current characteristic for both models.

An examination of the current density reveals that although the effective power is lower in the modified model the actual current amplitude is considerably higher. The power drop can be explained by analysing the phase difference between voltage and current, which increases in relation to the voltage by only 1.0 ns. Even though this is a marginal change, it is the cause for the observed power drop.

Therefore, experimental measurements and results that only have power input as reference should be regarded critically. Instead, voltage input as reference should be preferred if direct comparisons between experiments and simulations are desired.

Nevertheless, because of a more accurate description of kinetic effects in the mod-

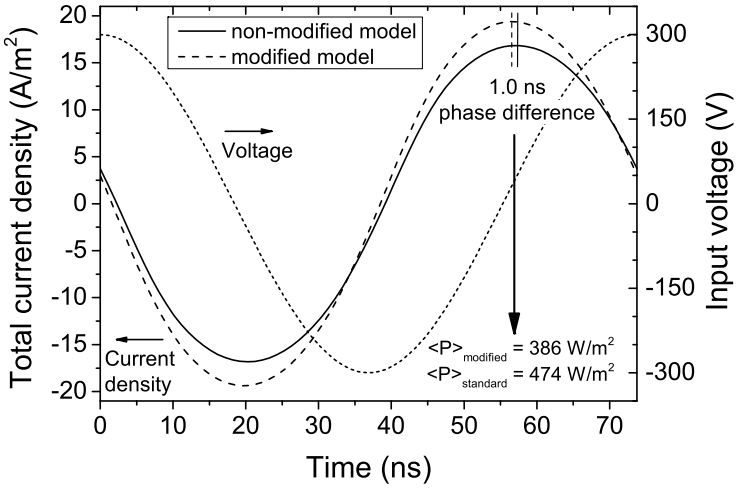

Figure 5.1.: Voltage-current density characteristic for modified and non-modified models and resulting power density. ($p = 40$ Pa, $V_{rf} = 300$ V)

ified model that become important in the investigated parameter regime, the results correspond better to experimental results [113, 116] as well as to kinetic PIC simulations [117], which also show higher averaged densities for all charged particles at comparable discharge conditions.

Furthermore, the comparison of the direct electron-impact ionisation pattern, as indicator for the electron dynamics, also shows a significant difference.

Figure 5.2 illustrates the predicted absolute direct electron-impact ionisation of O_2 in the non-modified against the modified model.

The calculated maximum sheath position in the modified model (≈ 8.9 mm) is smaller than in the non-modified model (≈ 10.2 mm), which also matches better the previously mentioned PIC-simulations by Matyash *et al.* [117] under similar conditions. The ionisation features such as from sheath expansion, secondary electrons and sheath collapse differ as well. In both model approaches the most dominant ionisation takes place in the sheath expansion phase. Further, the excitation through secondary electrons in the non-modified model is also pronounced. In contrast, the ionisation from secondary electrons as well as from the sheath collapse in the modified model are almost negligible against the sheath expansion.

This can be explained by means of analysing the surface losses in both models. This is of particular importance because the surface loss is the main destruction mechanism

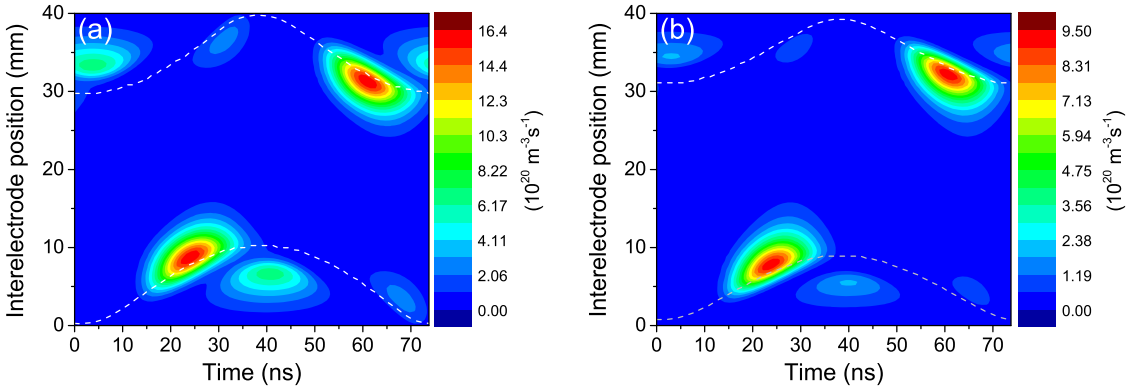

Figure 5.2.: Time and space resolved ionisation of O_2 molecules through direct electron impact obtained from (a) non-modified and (b) modified symmetrical model on a linear false colour scale. Dashed lines indicate the sheath position. ($p = 40$ Pa, $V_{rf} = 300$ V)

for positive molecular oxygen ions. Due to the different treatment of ion mobilities the surface loss in the non-modified model (9×10^{21} $m^{-3}s^{-1}$) is overestimated and more than twice as high as in the modified model (4×10^{21} $m^{-3}s^{-1}$). This might have significant implications for industrial applications, where an accurate description of sheath and surface dynamics is important.

Furthermore, the modified ion mobilities generally suggest a smaller boundary flux due to dominance of the drift term, in which the reduction of the ion mobility with increasing electric field is accounted for (see equation 3.12). As a consequence, the flux of emitted secondary electrons is decreased leading to the less pronounced ionisation in the modified model (figure 5.2(b)). It is also observed that the sheath collapse ionisation feature in the modified model occurs at an earlier phase than in the non-modified approach, and is less pronounced.

Comparing both models to experimental results via the applied voltage, the modified model again shows a greater accuracy in particular with regard to the dominant ionisation feature as well as the less pronounced ionisation from the sheath collapse phase and from secondary electrons.

The better accuracy of the modified model can be explained by means of the modified ion mobility treatment, where the transport coefficients decrease in accordance to the rigid sphere model, which leads to a more realistic description of ion dynamics especially in the sheath region.

A comparison of effective ion energies (O^- and O_2^+) for the symmetric model is presented in figure 5.3. These values result as average over time and space including a weighting with the corresponding species' spatial density profiles. By this, the impact of high density and low energy in the bulk is equally accounted for as the opposite trend in the sheath.

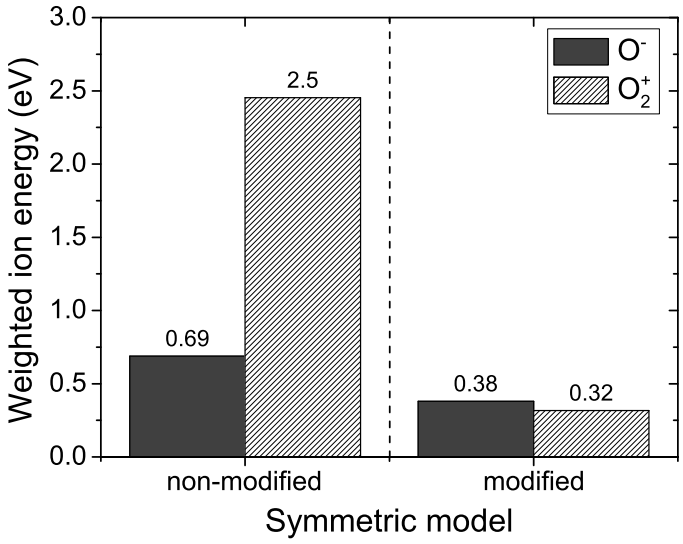

Figure 5.3.: Weighted time and space averaged ion energies.
($p = 40$ Pa, $V_{rf} = 300$ V)

The constant zero field transport coefficients, as used in the standard non-modified model, lead to an overestimation of ion energies especially for positive ions in presence of high electric fields. In the modified model, the effective energy of the negative atomic oxygen ions is lower by 45%, while the effective energy of positive molecular oxygen ions is significantly lower by a factor of 6.7. In case of O_2^+, this reduced ion energy, which is important for the sheath region, has an impact on the ion impact of the electrodes.

In spite of that, the weighted electron energy is not significantly affected by the modification of the ion mobilities and stays roughly constant at 3.86 eV $\pm$2%.

The electronegativity stays within a 1% margin. To explain this, one has to examine the spatial density distribution of all charged particles (O_2^+, O^-, e) along the discharge gap, as shown in figure 5.4. The profiles of the heavy particles remain almost static for all times, however, the density profile of electrons shows a temporal variation due to their higher mobility. To suppress the temporal variation in the electron profile, it has

been time averaged.

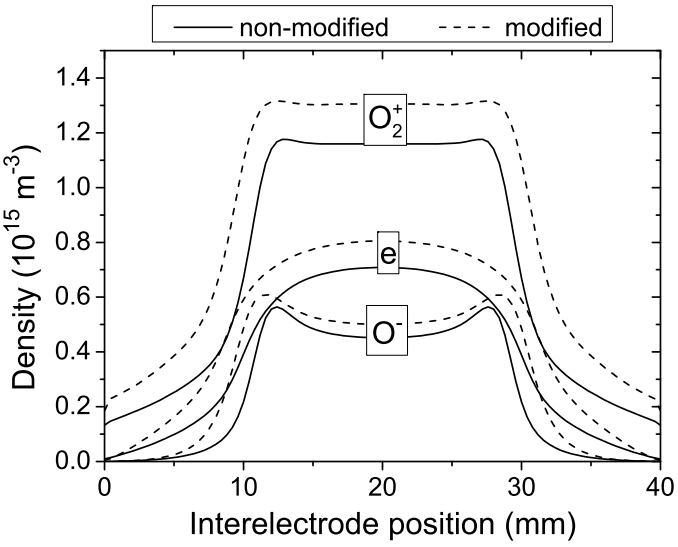

Figure 5.4.: Time averaged density profiles of O_2^+, electrons and O^- in the discharge volume for a symmetric discharge geometry using the non-modified (solid lines) and modified (dashed lines) models.
($p = 40$ Pa, $V_{rf} = 300$ V)

In both the modified and non-modified models the spatial particle distribution is similar. This is understandable since the incorporated modifications affect the boundary and sheath region of the plasma, not the bulk region. However, in the modified model all profiles exhibit higher maximum values and broader distribution, which indicates a bigger plasma bulk region. It can be observed that negative atomic oxygen ions exhibit a broad double peaked spatial profile, whereas positive molecular oxygen ions develop a plateau like distribution within the plasma bulk and compensate both the electrons and negative ions. These simulation results confirm experimentally observed spatial particle distributions [112, 118]. Furthermore, the O^- density decays with a steeper gradient in the sheath region than the electrons and stays below the electron density. This is due to the dominant production (R4) and destruction (R5, R8) mechanisms. Generally, the spatial distribution of electrons entails a similar distribution of the O^- density, since the latter is only generated by electron collisions in this simple reaction scheme. However, in the bulk region the destruction of O^- exceeds the production due to collisions with electrons and $O_2(^1\Delta)$. The latter can be identified as the main collision partner leading to destruction of O^-. This leads to the observed double peak structure in the O^- spatial

density profile.

Usually, in the non-modified model bulk and secondary electrons are not distinguished because both are treated as one fluid. In the modified model, however, the emitted secondary electrons is quantified at the boundary via equation 3.17. In figure 5.5, the temporal development of the total electron densities at the powered electrode in the modified and non-modified models over one RF period is illustrated. For the modified model, the total electron density is additionally divided into n_γ, which is of particular interest for applications where information on the contribution from secondary electrons is important.

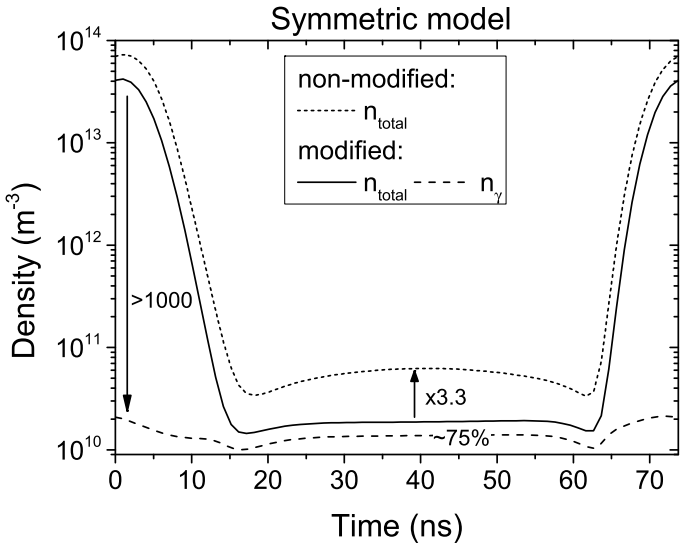

Figure 5.5.: Emitted secondary electron number density and total electron number densities in both models at the powered electrode over one rf period. ($p = 40$ Pa, $V_{rf} = 300$ V)

From figure 5.5 follows that the total electron density in the non-modified model is at all times larger than in the modified model by about a factor of 3.3. Furthermore, the emitted secondary electrons are the dominant electron group for approximately 2/3 of the RF period constituting roughly 75% of the total electrons at the powered electrode during the sheath expansion phase. They exceed the bulk electrons arriving at the electrode by a factor of 3 during this phase. The dominance of secondary electrons can be explained by means of the increased ion impact due to high electric fields, whereas bulk electrons are confined by the same in the bulk and can only reach the electrode through

their thermal motion. During the sheath collapse phase bulk electrons can in turn easily reach the electrodes and comprise the dominant electron group. The increase in secondary electron density during this period can be explained by means of the vanishing electric field, which leads to an incorrect calculation of the secondary electron density (see equation 3.17). But, as discussed before, in that case n_γ is negligible, comprising $< 0.1\%$ of the total electron density.

5.3. Asymmetric Discharge Geometry

Most discharges used for industrial applications involve an asymmetric electrode geometry, since the powered electrode is usually small compared to the grounded electrode, which includes the processing chamber walls. A numerical description of a strongly asymmetric system with a symmetric model is then insufficient. The choice of the right asymmetry in the model generally requires a possibility to benchmark the results with experimental observations. Additionally, the DC self-bias voltage in an asymmetric system needs to be accounted for, thus contributing to a more complicated (numerical) description.

The influence of the modified ion mobility treatment on ionisation dynamics is even more pronounced in the asymmetric model than in the symmetric model.

Figure 5.6 shows a direct comparison of the time and space resolved direct electron-impact ionisation pattern in the non-modified as well as the modified model for an identical set of parameters on a common linear false colour scale.

The simulations yield that the ionisation pattern in a non-modified treatment significantly differs from its modified counterpart. From the non-modified model follows that the most dominant ionisation takes place within the plasma sheath induced by secondary electrons, while ionisation in the sheath expansion and sheath collapse phases are less pronounced. Furthermore, both models predict a distinct ionisation through electrons that are accelerated from the grounded electrode towards the bulk.

The dominant ionisation in the modified version of the model is initiated through sheath expansion heating. Ionisation from secondary electrons is not over accounted for and only plays a minor role, as does the ionisation from the sheath collapse phase. The

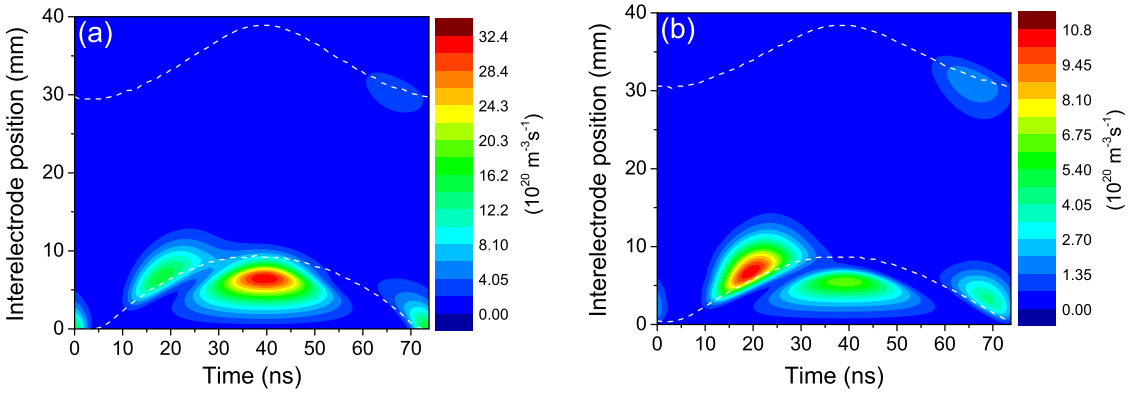

Figure 5.6.: Time and space resolved ionisation of O_2 molecules through direct electron impact obtained from (a) non-modified model and (b) modified asymmetric model on a linear false colour scale. Dashed lines indicate the sheath position. ($p = 40$ Pa, $V_{rf} = 300$ V)

latter exhibits a phase shift against the non-modified model.

Although, the ionisation patterns clearly differ due to the modifications in the model, the time averaged spatial density distributions do not change significantly, as already shown for the symmetric case. This is illustrated in figure 5.7.

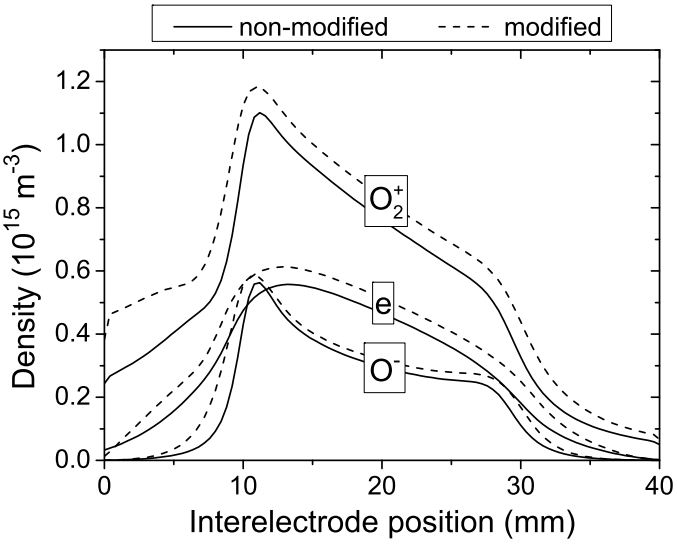

Figure 5.7.: Time averaged density profiles of O_2^+, electrons and O^- along the discharge gap for an asymmetric geometry using the non-modified (solid lines) and modified (dashed lines) model. ($p = 40$ Pa, $V_{rf} = 300$ V)

As expected, the spatial distribution for the charged heavy particles shows a shoulder like structure with the maximum near the powered electrode, which is caused by the

geometric asymmetry of the discharge, in contrast to the double peaked distribution obtained from symmetric simulations. These simulations confirm experimental results [99, 112, 119]. The time and space averaged electronegativity in this case can be determined as ≈ 0.66, which only differs by 1% from the symmetric simulations. Experiments show typically slightly higher electronegativity but this can be understood due to the *a priori* assumption for the $O_2(^1\Delta)$ fraction in the model. Since the metastable oxygen is the main destruction partner for O^-, the particular choice of the metastable oxygen content in the plasma will have a major effect on the negative ion dynamics and therefore affect the electronegativity in the periodic steady state.

Although the improved ion mobility treatment does not notably influence the spatial distribution of incorporated particles, the ion energies are affected significantly. The effect in the asymmetric case is even more pronounced than in the symmetric case. To allow a direct comparison of both geometrical regimes as well as of the modifications, figure 5.8 illustrates the weighted negative and positive ion energy for each simulated instance.

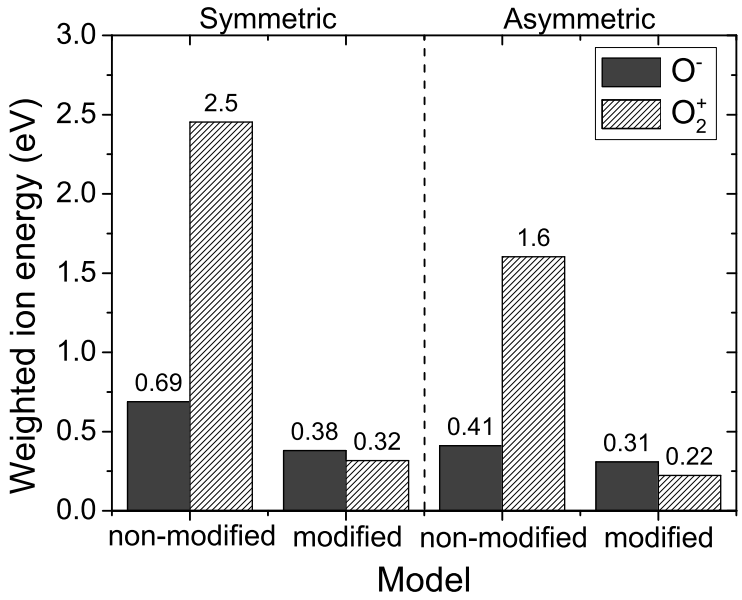

Figure 5.8.: Weighted time and space averaged ion energies with direct comparison of the effect of geometrical asymmetry as well as modification to the model. ($p = 40$ Pa, $V_{rf} = 300$ V)

The negative ion energy slightly decreases due to the changes in geometry and ion

mobility treatment but generally stays at a comparably low level (< 1 eV). This is due to the fact that negative ions are well confined within the plasma bulk (compare figure 5.7) and cannot penetrate the sheath region with its high electric fields. However, the weighted positive ion energy is strongly affected by the geometry and modifications in the model. In comparison to the non-modified symmetric counterpart the weighted energy of O_2^+ is already notably reduced. This can be explained by means of the geometry - since the asymmetric model is based on a spherical geometry (see figure 3.1(b)), the plasma volume in front of the powered electrode is considerably smaller than the volume near the grounded electrode. Thereby, the accounted volume decreases for the same step size Δr with r^2 from the powered to the grounded electrode.

Nevertheless, a modification of the asymmetric model leads to a significant drop of the positive ion energy so that it becomes lower than the negative ion energy. This observation certainly has an impact on the charged particle dynamics as already shown in figure 5.6, but might also have an influence on the surface interaction processes of positive ions, which is essential for industrial applications.

In general, the higher the pressure, the less important the modification is due to smaller reduced electric fields. Nonetheless, the modified model is able to decrease the lower limit of applicable pressure as opposed to the non-modified approach. It can therefore be a valuable tool in the intermediate pressure regime, where typical PIC simulations become slow and conventional fluid models fail.

5.4. Comparison with Previous Work

In this section, the presented modified model is critically compared to experimental and computational work from several independent groups with special regard to particle densities, particle distributions, and excitation dynamics for a range of parameters.

- Kuellig *et al.* [120]

Kuellig *et al.* measured the electron and negative atomic ion densities with 160 GHz microwave interferometry and laser photodetachment in oxygen capacitively coupled radio-frequency plasmas. Their plasma source comprises a purely asymmetric geometry, which is created by the big surface area of the chamber walls as opposed to the small surface area of the only physical electrode within the chamber. Using this approach, they obtained line integrated densities at about 20 mm above the powered electrode. Under the assumption that the densities are homogeneous over the overlapping length of microwave and laser beam the average densities can be estimated.

Figure 5.9 shows the fluid model results in comparison with experimental results for the global electron and negative atomic oxygen ion densities and resulting electronegativity.

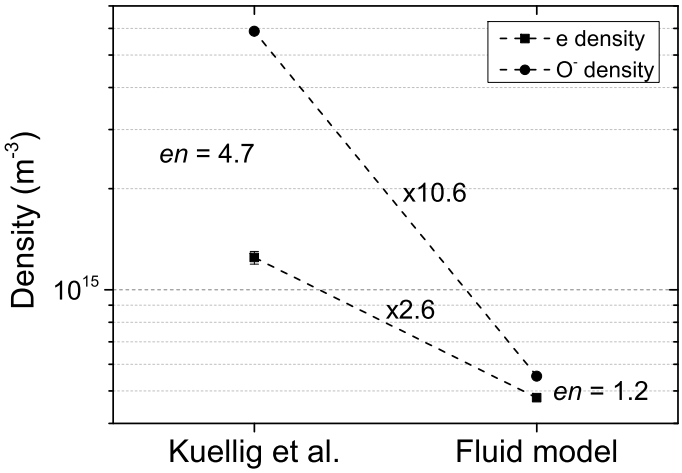

Figure 5.9.: Comparison of experimentally and numerically obtained average electron and negative atomic oxygen ion densities. *en* denotes the electronegativity. ($p = 40$ Pa, $P_{exp} = 30$ W, $V_{rf,sim} = 300$ V, $d_{sim} = 40$ mm, $f = 13.56$ MHz)

The experimentally obtained electron density is about 2.6 times higher and the negative ion density even 10.6 times higher than in the fluid model. This seems to be a big discrepancy between model and experiments, especially with regard to the negative ion density. However, this can be explained by analysing the underlying parameters that lead to this discrepancy. Firstly, the representation of the actual geometry is limited to a 1D domain in the simulation. Secondly, the power input in the experiment is measured in W, and thereby impedes a direct comparison to the fluid model voltage input, as discussed earlier in section 5.2. Therefore, a voltage amplitude increase in the model can easily increase the electron density to match the experiment. This would also lead to an increase in negative ion density, however not as pronounced as needed to match the experiment. To understand the negative ion density discrepancy, one has to analyse the main volume reaction and destruction reactions for those ions. It turns out that singlet delta oxygen ($O_2(^1\Delta)$), also referred to as SDO, is the main collision partner of negative atomic oxygen ions leading to their destruction (reaction R8 in table 5.1). The SDO density is set to 16.6% of the background gas density in the model, however, Kuellig *et al.* estimate a lower value of about 11% from their measurements. This lower SDO density can be responsible for the relatively higher negative ion density, because less negative ions will be destroyed in the volume.

- Shibata *et al.* [121]

Shibata *et al.* applied a relaxation continuum (RCT) model [50] for oxygen rf discharges between parallel plates. The fluid model was again set up using the same parameters for pressure, voltage, driving frequency and system dimension as in the RCT model. However, the reaction scheme in the used RCT model is more extensive because SDO was modelled as individual species, and not set to a certain density as in the fluid model. Although the underlying governing equations are based on the moments of the Boltzmann equation for both models, the main difference is that the RCT model *a priori* assumes constant time values for the relaxation kinetics of the momentum and energy charged particles instead of calculating them self-consistently from the reaction rates, as done in the fluid model.

Figure 5.10 shows a direct comparison of density distributions of electrons, and the main positive and negative oxygen ions along the symmetry axis of the discharge.

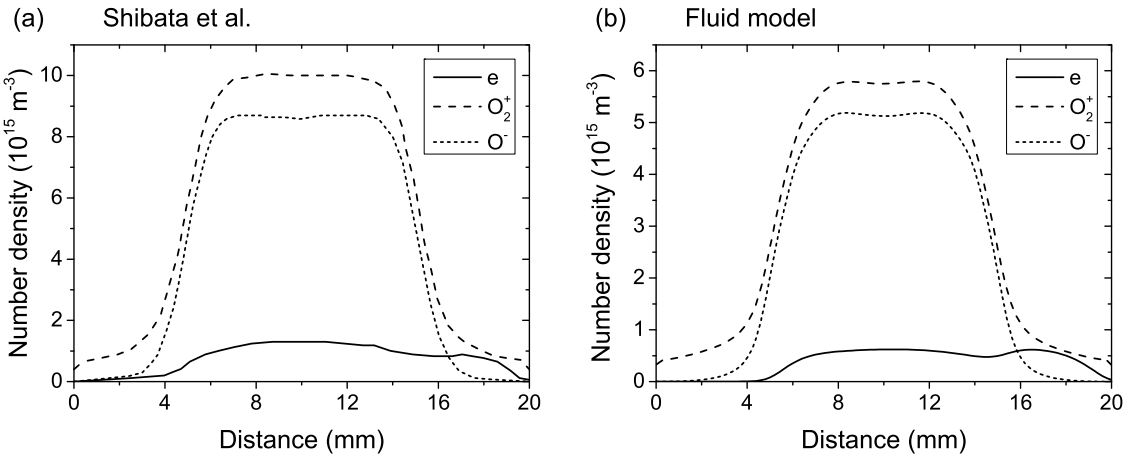

Figure 5.10.: Density distributions of electrons, O_2^+ and O^- within discharge domain obtained from (a) RCT model and (b) fluid model simulations. ($p = 133.3$ Pa, $V_{rf} = 200$ V, $d = 20$ mm, $f = 13.56$ MHz, $\omega t = \pi/2$)

Qualitatively both modelling results are very similar, showing a plateau like density profile for positive and negative ions in the plasma bulk, with a steep decay towards the electrodes. The electron density distribution shows in both cases a double peak structure, exhibiting a broad distribution in the bulk and an increased density at the right electrode. This is due to the sheath movement, for the particularly considered time ($\omega t = \pi/2$) the sheath is maximum at the left electrode (virtually no electron density) and minimum a the right electrode, allowing electrons to reach the surface.

The slight difference in absolute values can easily be explained by means of the differences in the modelling approaches, but partly also by means of the SDO density. The RCT produces a SDO density of about 7%, which is considerably lower than the set SDO density in the fluid model. This can explain why the negative ion density and thereby also the positive ion density (needed for preservation of quasineutrality) are slightly higher than in the fluid model.

- Katsch *et al.* [112]

Katsch *et al.* measured the axial distributions of negative oxygen ions in a capacitively coupled radio-frequency oxygen discharge by detecting the electrons released after photodetachment with a Langmuir probe. For the low power and pressure case, their obtained axial density profiles are compared to the fluid model and are show in figure 5.11.

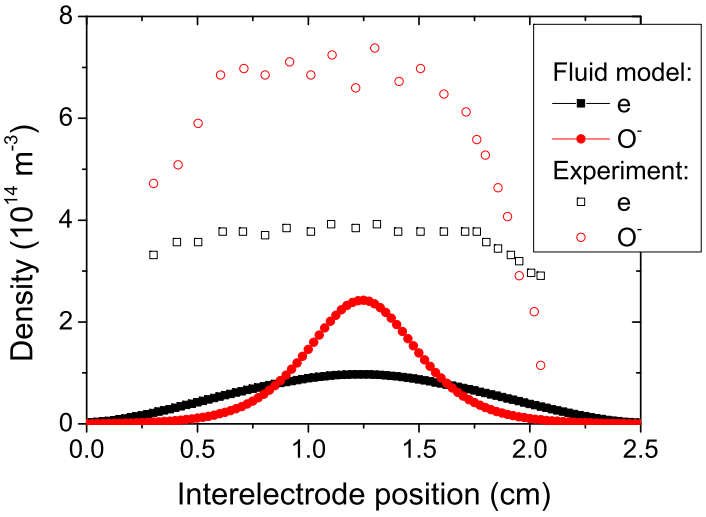

Figure 5.11.: Density distributions of electrons and O^- within discharge domain obtained from fluid model simulations (solid symbols) and experiments (open symbols). ($p = 13.8$ Pa, $V_{rf} = 150$ V, $d = 25$ mm, $f = 13.56$ MHz)

Experimentally, Katsch *et al.* find that the spatial distribution of both electrons and negative ions are rather flat, with the negative ions exceeding the electron density by a factor of about 2. Towards the sheath, the negative ions show a steep decay in density. Qualitatively similar results are obtained from the fluid simulation, in which the electron density is also flat and the negative ions density shows a twice as high density in the plasma bulk, though not as flat as in the experiment. The total discrepancy between measured and simulated densities is approximately a factor of only 3, which can be regarded as a good agreement considering that the pressure is relatively low and at the limits of the fluid simulation.

- Bronold *et al.* [108]

Bronold *et al.* conducted a particle-in-cell Monte Carlo collisions (PIC-MCC) simulation of a radio-frequency discharge in oxygen. The fluid model was set up using the same parameters for pressure, voltage, driving frequency and system dimension as in the PIC-MCC model, however, the reaction scheme differs slightly.

Main charged particle densities are compared spatially resolved and are illustrated in figure 5.12. It has to be noted that, as before, at such low pressures fluid models are at their (validity) limits, because kinetic effects become more dominant with decreasing

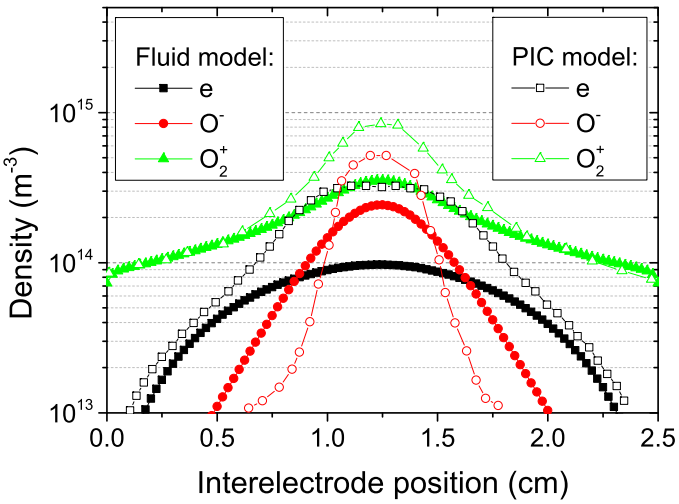

Figure 5.12.: Density distributions of electrons, O_2^+ and O^- within discharge domain obtained from fluid model simulations (solid symbols) and PIC-MCC simulations (open symbols). ($p = 13.8$ Pa, $V_{rf} = 150$ V, $d = 25$ mm, $f = 13.56$ MHz)

pressure. Nonetheless, the qualitative agreement between both simulation approaches is very good. In the sheath regions near the electrodes, where kinetic effects are dominant, there is even a very good quantitative agreement. This is a result of the improved ion mobility treatment in the fluid model, which describes the ion kinetics more accurately than in standard fluid modelling approaches.

- K. Dittmann [56]

In his PhD thesis, K. Dittmann, conducted experiments in asymmetric capacitively coupled radio-frequency oxygen discharges and measured amongst others phase resolved excitation dynamics of the atomic oxygen $\lambda = 844.6$ nm optical emission line, which will be compared to fluid simulations.

Figure 5.13 shows the normalised phase resolved excitation for the corresponding emission at 844.6 nm with its effective lifetime of $\tau_{\text{eff}} = 26.7$ ns, as obtained experimentally (a) and from simulations (b). Please note, the fluid model uses voltage input in contrast to the experimental power input, which complicates the direct comparison.

In the experimental measurement, two distinct features are observed, the sheath expansion excitation at the beginning of the RF cycle ($t \approx 0 - 20$ ns) and the sheath collapse excitation at the end of the cycle ($t \approx 50 - 60$ ns), which is less pronounced than the first

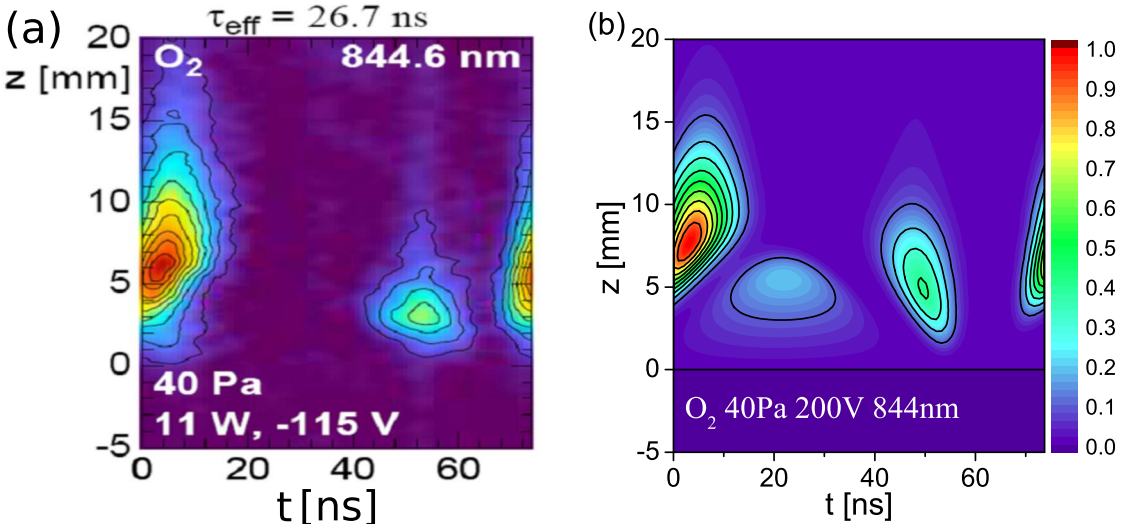

Figure 5.13.: Phase resolved excitation profiles (a) measured and (b) simulated for the corresponding emission at 844.6 nm. ($p = 40$ Pa, $P_{exp} = 11$ W, $V_{rf,sim} = 200$ V, $d_{exp} = 25$ mm, $d_{sim} = 40$ mm, $f = 13.56$ MHz)

feature. The simulation shows qualitative and quantitative agreement for both features. However, a third excitation feature in the simulation is observed that can be identified as excitation via secondary electrons released from the surface. This feature is a result of the explicitly set secondary electron emission coefficient and can be understood as a material constant. It seems, that the electrode material used in the experiment exhibits a much lower secondary electrons coefficient, so that this feature is not visible in the measurements. In turn, the simulation could be adjusted to fit the measurement better by using a smaller secondary electrons coefficient, to reduce the pronunciation of this third feature.

6. Role of Singlet Delta Oxygen in Oxygen Discharges

As shown in the last section of the previous chapter, metastable singlet delta oxygen (SDO) seems to play an important role in oxygen discharges by influencing the charged particle dynamics in the investigated parameter regime ($d = 40$ mm, $p = 10 - 100$ Pa, $V_{rf} = 200 - 500$ V amplitude, $f = 13.56$ MHz).

In this chapter the role of SDO is analysed in terms of treating it as individual species in the fluid model and investigating its impact on plasma dynamics. The simulations are conducted in a one-dimensional domain and account for a geometrical asymmetry, as described previously. The role of the SDO surface loss probability and effective SDO lifetime is discussed for the exemplar discharge parameters $p = 40$ Pa and $V_{rf} = 300$ V amplitude. To distinguish from a possible impact from secondary electron emission the secondary electron emission coefficient is explicitly set to a constant value of $\gamma = 0.05$. General observations of the resulting electronegativity and SDO content for a wide range of SDO surface loss probabilities are presented. Two different SDO surface loss probability values are chosen in order to examine and compare the corresponding spatial distributions of charged particles and the phase and space resolved ionisation.

6.1. Reaction Scheme

An extended oxygen reaction scheme is considered, including electrons, O_2^+ positive ions, O^- negative ions and $O_2(^1\Delta)$ metastable singlet delta oxygen as individual species. Depletion of the background gas density is neglected in this type of discharge [62, 122, 123].

Here, the explicit implementation of SDO as an individual fluid species is emphasised as an improvement over the usual modelling approach, which is to assume a constant

SDO content based on analytical approximations (e.g. 12% [124] or 16.6% [108]). These calculations are based on *a priori* assumptions for the surface-to-volume ratio and the SDO surface loss probability, although the real value for the latter is in most cases rather insufficiently known.

Under the investigated pressure range of 10 Pa−100 Pa, SDO is the main collision partner for negative atomic oxygen ions leading to their destruction [125]. This means that despite its metastable character, SDO can play an important role for the overall plasma dynamics, should the SDO density change significantly.

The used reaction scheme, listed in table 6.1, results from an analysis of several detailed reaction schemes [61, 101, 109], which supports the chosen extension for the incorporated SDO reactions in the investigated (low pressure) conditions.

Table 6.1.: Elementary reactions and corresponding rate coefficients in a O_2 discharge including $O_2(^1\Delta)$

No.	Reaction	Rate coefficient[a),b)]	Reference
R1	$e + O_2 \rightarrow e + O_2$	$f(\epsilon)$	[53]
R2	$e + O_2 \rightarrow 2e + O_2^+$	$f(\epsilon)$	[53]
R3	$e + O_2^+ \rightarrow 2O$	$f(\epsilon)$	[106]
R4	$e + O_2 \rightarrow O + O^-$	$f(\epsilon)$	[107]
R5	$e + O^- \rightarrow 2e + O$	$f(\epsilon)$	[108]
R6	$O^- + O_2^+ \rightarrow O + O_2$	$2 \times 10^{-13}\, T_r^{-1}$	[101]
R7	$O^- + O_2 \rightarrow e + O_3$	$5 \times 10^{-21}\, T_r^{0.5}$	[101]
R8	$O^- + O_2(^1\Delta) \rightarrow e + O_3$	$3 \times 10^{-16}\, T_r^{0.5}$	[109, 114]
R9	$e + O_2(^1\Delta) \rightarrow e + O_2(^1\Delta)$	$f(\epsilon)$	[109]
R10	$e + O_2 \rightarrow e + O_2(^1\Delta)$	$f(\epsilon)$	[109]
R11	$e + O_2(^1\Delta) \rightarrow 2e + O_2^+$	$f(\epsilon)$	[109]
R12	$e + O_2(^1\Delta) \rightarrow O + O^-$	$f(\epsilon)$	[109]
R13	$e + O_2(^1\Delta) \rightarrow e + O_2$	$f(\epsilon)$	[109]
R14	$e + O_2(^1\Delta) \rightarrow e + 2O^{(*)c)}$	$f(\epsilon)$	[109]

a) Units: Rate coefficients in m^3/s; gas temperature T_g in K; relative gas temperature $T_r = T_g/300$.
b) *f(ϵ)* indicates that the rate coefficients are obtained from the EEDF calculated with Boltzmann solver BOLSIG+ using cross section data. Additionally, electron-impact excitation of O_2 into rotational, vibrational and metastable states is accounted for in the EEDF calculation.
c) $O^{(*)}$ denotes O atoms in the ground state or in the excited O^1p and O^3p states, respectively.

Reactions R1 to R8 have already been introduced in chapter 5 and sufficiently describe

electron momentum transfer (R1), dominant charged heavy particles volume production processes (R2 and R4) as well as their destruction induced by collisions with electrons (R3, R5) and other heavy particles (R6, R7 and R8).

To account for the SDO formation self-consistently, reactions R9 to R14 are added: Electron momentum transfer (R9), the main volume production reaction (R10), and volume destruction induced by collisions with electrons (R11-R14). Collisions with negative ions are already included in R8. The reaction rate coefficient for R8 has recently been revised towards slightly smaller values by two independent groups. On the one hand, S. G. Belostotsky *et al.* report a value of 1.9×10^{-16} m^3/s [126], and on the other hand A. Midey *et al.* report a value of 1.1×10^{-16} m^3/s [127] with a positive, almost linear, temperature dependence [128]. Considering the accuracy of the rate constant measurements, all three reported values are in agreement within the combined uncertainties of the experiments. Although, the reaction rate coefficient for R8 might be up to a factor of 3 lower than the reaction rate used for the presented simulations, it is still justified to neglect atomic oxygen in the model as another negative ion destruction channel considering reported atomic oxygen number densities of at least one order of magnitude lower than for SDO in a very similar experimental set up [112].

The particle transport coefficients used are the same as in table 5.2.

6.2. Singlet Delta Oxygen Surface Loss Probability

The SDO surface loss probability, which significantly depends on the actual surface condition, describes a neutralisation mechanism for the collision of SDO with the surface through thermal motion and its conversion into ground state oxygen with a certain probability.

There are several approaches to detecting SDO using its specific chemical, spectroscopic and magnetic features, which are discussed in the literature [129, 130]. An accurate method for absolute SDO concentration measurements is to use VUV absorption at 128.4 nm [131] because the cross sections are well known. From the difference of absolute SDO densities before and after contact with a surface, the surface loss probability can roughly be estimated. Another more direct method is to measure the heterogeneous

relaxation of SDO as presented in [132]. It should be noted that the data for the SDO surface loss probability obtained by different researchers for the same base materials can differ by several orders of magnitude and is likely a result of the different states of the surface under investigation [133].

A real value for the SDO surface loss probability at the chamber walls is very difficult to assess either experimentally or theoretically. Generally, the loss probability for any species hitting the chamber walls depends not only on the considered species itself, but also on the surface material, the surface temperature, the surface roughness, and the actual surface condition, which can vary substantially. The literature values found for the SDO surface loss probability varies from 1×10^{-5} [101] to 1×10^{-2} [132, 134].

To calculate the effects of the surface loss on the local SDO densities in the simulations, diffusion theory is applied using the concept of a "linear extrapolation length" λ derived by P. J. Chantry [135]. This linear extrapolation length is related to the density and density gradient at the boundary b in the following way:

$$\left(\frac{dn}{dx}\right)_b = -\frac{1}{\lambda}n \tag{6.1}$$

For a very low surface loss probability ($s \ll 1$) the linear extrapolation length can be expressed in terms of the reflection coefficient r:

$$\lambda = \frac{2D}{v_{th}}\frac{1+r}{1-r} \quad , \tag{6.2}$$

where, v_{th} is the thermal velocity. Using equation 3.10 for the particle flux and the relationship $r = 1 - s$ the boundary flux follows as:

$$\vec{\Gamma} \cdot \vec{n} = s_{SDO} \cdot \frac{1}{4} v_{th} n \tag{6.3}$$

Here, s_{SDO} is the SDO specific surface loss probability. Expression 6.3 is equivalent to the expression from the standard kinetic theory considering only the thermal flux of SDO towards the chamber walls.

The SDO surface loss probability is then varied in the numerical simulations over the stated range allowing analysis of the fundamental influence on plasma dynamics and to overcome the uncertainty of its actual value.

6.3. Effective Lifetime of Singlet Delta Oxygen

The natural radiative lifetime of SDO is 64.4 minutes ($\approx$ 3900 s) and it is therefore often assumed that SDO, as a long living metastable species, has no effect on the fast plasma dynamics within the RF cycle [136]. This includes that changes in the surface loss probability are usually believed not to cause any noticeable shift in plasma dynamics. This might be true for recombination dominated discharges as treated in the literature by Lichtenberg *et al.* [44, 137] or Gudmundsson *et al.* [124, 138]. However, in the present case of a detachment dominated discharge, in which SDO is the main collision partner for negative ions, that assumption fails.

The natural SDO lifetime is compared to two processes determining the effective SDO lifetime, namely wall losses and volume destruction through electrons and negative ions. Figure 6.1 shows surface and volume averaged effective SDO loss rates as a function of the actual SDO surface loss probability on a double logarithmic plot.

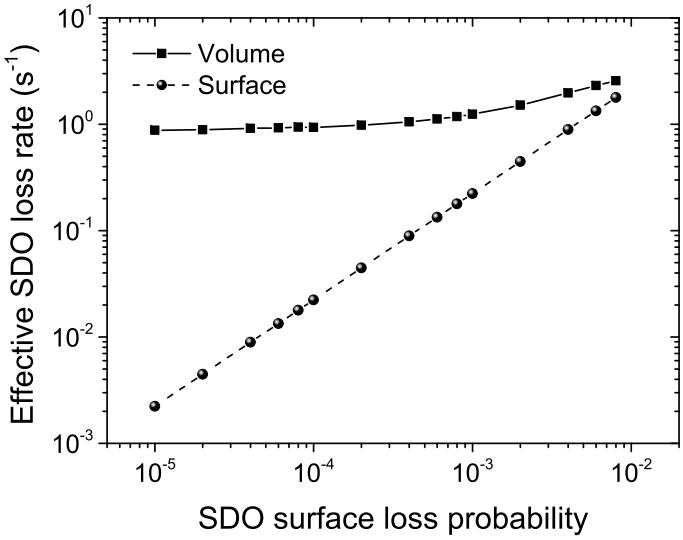

Figure 6.1.: Effective SDO loss rate in plasma volume and at the surface. ($p = 40$ Pa, $V_{rf} = 300$ V)

In the volume, the effective SDO loss rate stays in the region of 1 s^{-1}, monotonically increasing to about 2.5 s^{-1} for high SDO surface loss probabilities, which corresponds to an effective lifetime of 400 ms . This is more than three orders of magnitudes lower than the natural lifetime and is mainly governed by the electron and negative ion densities.

The trend of increasing effective loss rates is due to increasing negative ion densities that contribute to the volume loss of SDO.

At the surface, the effective loss rate exhibits a reciprocal dependence on the SDO surface loss probability. Following this scaling, if every SDO molecule hitting the surface was converted into its ground state ($s_{SDO} = 1$), the effective loss rate could be estimated as 222 s^{-1}, which would correspond to an effective lifetime of 4.5 ms. Nevertheless, even for the lowest applied SDO surface loss probability the effective lifetime at the surfaces is still considerably lower than the natural lifetime.

A third possible process limiting the effective SDO lifetime is the gas flow, which is not considered in the simulations. However, under the assumption of the actual geometry the simulations aim to describe and a gas flow of 50 sccm, the gas residence time can be estimated to be in the order of 0.5 s.

Despite the fact that the effective SDO lifetime changes significantly, the SDO distribution across the discharge gap only slightly drops near the electrodes due to surface loss processes, and can practically be regarded as homogeneous.

For a constant SDO surface loss probability of $s_{SDO} = 1 \times 10^{-4}$ the effective SDO volume loss rate is analysed and illustrated in figure 6.2.

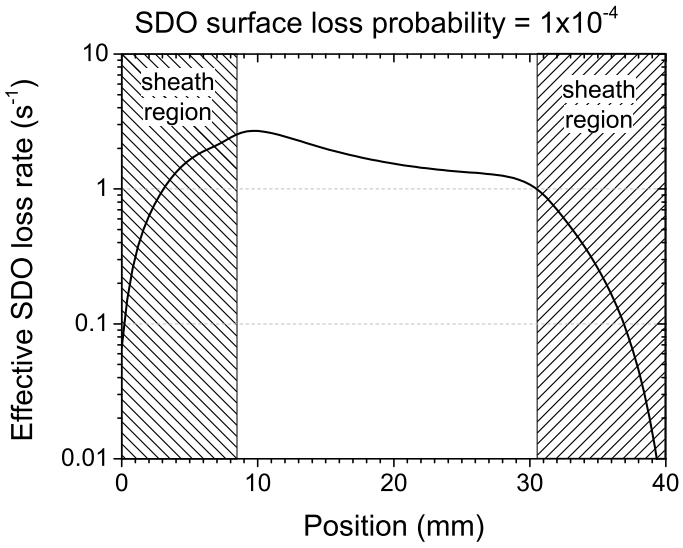

Figure 6.2.: Effective loss rate of SDO in plasma region based on volume destruction processes through electrons and negative ions. ($p = 40$ Pa, $V_{rf} = 300$ V)

The slightly asymmetric loss rate distribution is due to the geometric asymmetry of

the discharge and follows the combined electron and negative ions spatial distribution. In the plasma bulk, where volume processes are dominant, the loss rate lies above 1 s^{-1}. Towards the plasma sheath edges these volume processes become less dominant, so that the effective loss rate decreases in the sheath regions. Within the sheath regions, with decreasing distance from the electrodes, free diffusion, which subsequently leads to a wall loss, becomes the dominant SDO destruction process.

From this follows, that the SDO loss rate is relatively small so that the effective lifetime is still long enough (thousands of RF cycles) to allow a build-up of significant SDO metastable densities in O_2 discharges as observed experimentally [112] and theoretically [121]. Nonetheless, due to the significantly reduced effective SDO lifetime, SDO can actually respond to surface changes on a timescale below seconds that are likely to occur in plasma processing applications, and consequently, it is important to take this into account.

6.4. Impact on Discharge Properties and Dynamics

Apart from an impact on effective lifetimes, it is found that the SDO surface loss probability has a major impact on the charged particle dynamics, and consequently on the global electronegativity (see equation 4.1). In contrast to the rather homogeneous spatial SDO distribution, the global SDO content varies significantly as well, as shown in figure 6.3. Here, the SDO surface loss probability was varied from 1×10^{-5} to 8×10^{-3}.

The $O_2(^1\Delta)$ content shows a clear dependence on the SDO surface loss probability, dropping from about 15% to below 1%. This can be understood by analysing the continuity equation. For the steady state condition, the SDO density can be expressed taking into account the flux gradient as well as the main volume production and destruction processes, the latter can be combined in the effective lifetime τ_{eff} (compare equation 3.9):

$$n_{SDO} = (\underbrace{n_e\, n_{O_2}\, k_{p,e}}_{\approx \text{constant}} - \underbrace{\vec{\nabla} \cdot \vec{\Gamma}}_{>0})\tau_{\text{eff}}\,, \tag{6.4}$$

where $k_{p,e}$ is the reaction rate coefficient responsible for SDO production. The first term in the bracket on the right hand side stays roughly constant independent of the SDO surface loss probability under the investigated parameter regime. Thus, the SDO content

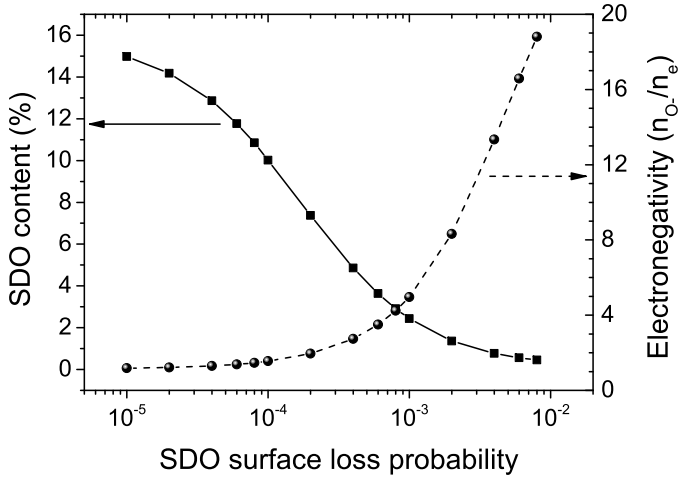

Figure 6.3.: Dependence of global SDO content and electronegativity on SDO surface loss probability. ($p = 40$ Pa, $V_{rf} = 300$ V)

follows the trend governed by the effective volume lifetime, as shown in figure 6.1. However, this trend is further strongly enhanced by the product of effective lifetime and flux gradient $\vec{\nabla} \cdot \vec{\Gamma}$, which is equivalent to the second derivative of the density gradient (see equation 3.10). In case of SDO, the flux gradient is always positive and increases over linearly with the surface loss probabilities. If the SDO distribution was perfectly homogeneous ($\vec{\nabla} \cdot \vec{\Gamma} = 0$), the SDO content would only drop to about 6.6% for maximum applied SDO surface loss probability in the model ($s_{SDO} = 8 \times 10^{-3}$). However, due to the additional contribution from the flux gradient it drops to an almost 15 times smaller value of 0.45%. This makes the flux gradient the dominant factor determining the SDO content in the discharge for increasing SDO surface loss probabilities ($s_{SDO} > 10^{-4}$).

The electronegativity shows an oppositional, so increasing trend, since $O_2(^1\Delta)$ dominates the volume destruction of O^-, whereas the electron density stays approximately constant.

Typically, the SDO content is assumed to be in the range of about 12%−17% for stainless steel electrodes on the basis of an SDO surface loss probability of $(4 - 7) \times 10^{-3}$ [132, 134]. In contrast, the simulation results presented here imply a SDO surface loss probability of below 6×10^{-5}, which will be verified in chapter 10.

To show the impact on the spatial distributions of charged particles, two SDO surface loss probability values are considered, namely $s_{SDO} = 0.6 \times 10^{-4}$ and $s_{SDO} = 6 \times 10^{-4}$.

For the considered pressure of 40 Pa, a SDO surface loss probability of 0.6×10^{-4} corresponds to a SDO content of 11.8%, whereas for the surface loss probability of 6×10^{-4} the SDO concentration is smaller by a factor of about 3-4, levelling off at 3.6%.

Figure 6.4 shows the almost static spatial ion density distributions and the time-averaged electron density profile for both SDO surface loss probability values, while keeping the secondary electron emission coefficient equal in both cases. The corresponding values for the global SDO content and the global electronegativity (denoted as *en*) are indicated, respectively.

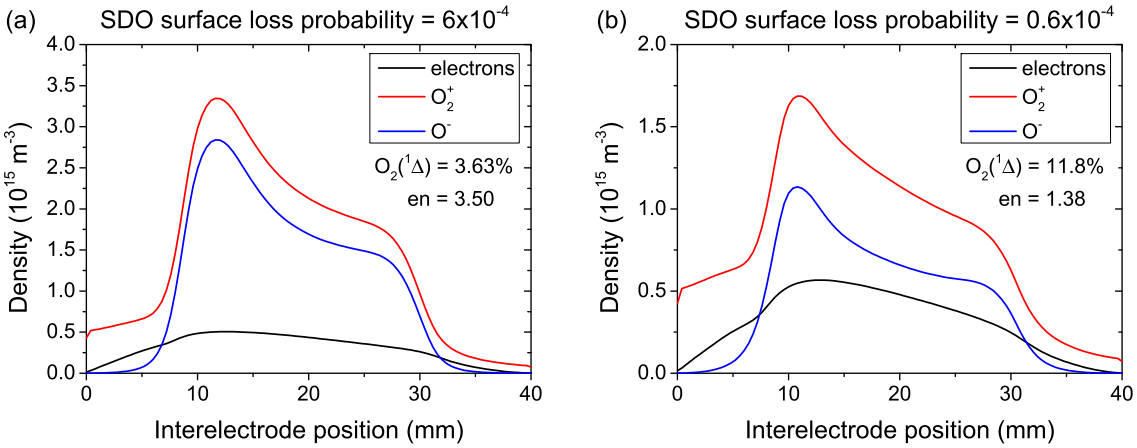

Figure 6.4.: Time averaged spatial distribution of electrons, O_2^+ and O^- for SDO surface loss probability of (a) 6×10^{-4} and (b) 0.6×10^{-4}, *en* denotes the global electronegativity. ($p = 40$ Pa, $V_{rf} = 300$ V)

In both cases, the ion density distributions exhibit a similar shoulder like structure with maxima near the powered electrode, as expected in an asymmetric discharge. The mean electron density distribution is found rather flat and almost independent of the SDO surface loss probability, whereas the negative ion density increases with increasing surface loss probability. The overall increased negative net charge density is accordingly balanced by an increased positive molecular oxygen ion density. Since the electron density remains almost unaffected, while the charged heavy particle densities increase, the electronegativity of the system increases correspondingly. The global electronegativity values found, $en = 3.50$ and $en = 1.38$, are in a reasonable agreement with independent measurements [112, 120] in view of the differences in discharge design and operational parameters.

Apart from the charged particle distributions the ionisation features are also affected by the SDO surface loss probability. Figure 6.5 shows the phase and space resolved direct electron-impact ionisation of O_2 (R2, table 6.1) for two different SDO surface loss probability values along the discharge gap. The abscissa covers one full RF cycle ($\approx$ 73.75 ns) and the ordinate the whole inter-electrode gap, with the powered electrode at the bottom and the grounded electrode at the top. The roman letters in figure 6.5 denote the expected three distinct ionisation features associated with: (I) sheath expansion, (II) sheath collapse and (III) ionisation induced by secondary electrons. The sheath edge positions, as obtained according to the equivalent sharp electron step criterion [17], are indicated by white dashed lines.

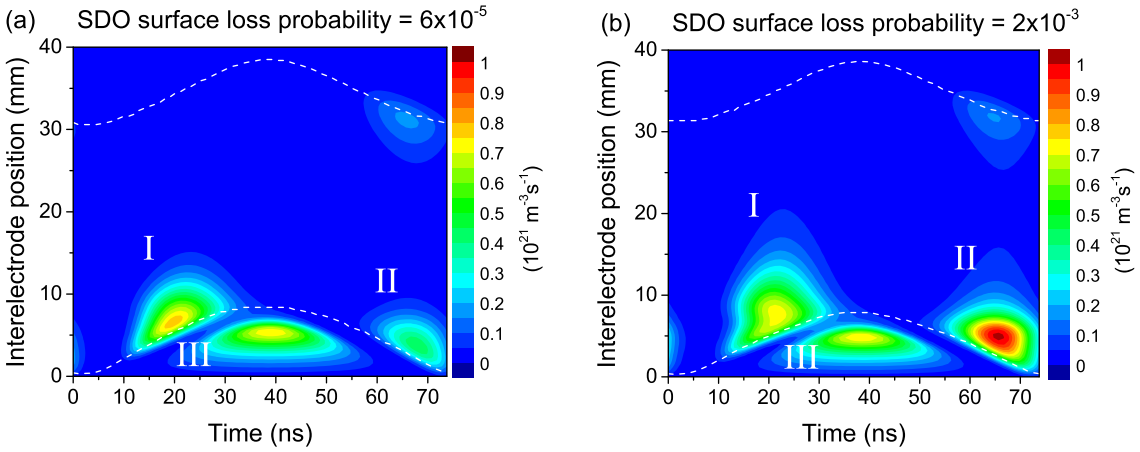

Figure 6.5.: Phase and space resolved electron-impact ionisation of O_2 ($10^{21}\ m^{-3}s^{-1}$) for SDO surface loss probability of (a) 6×10^{-5} and (b) 2×10^{-3} on a common false colour scale. Dashed lines indicate the sheath edge positions. ($p = 40$ Pa, $V_{rf} = 300$ V)

Since the gamma coefficient is kept constant for both figures 6.5(a) and 6.5(b), the contribution of secondary electrons (feature III) to the total ionisation stays practically the same, keeping in mind that the electron density in the sheath regions (at the same background gas density) is similar for both cases and not affected by negative ions, because those are effectively confined in the plasma bulk (compare with figure 6.4).

In particular, the weighting of the two ionisation features during the sheath expansion and sheath collapse phases, apart from their individual spatio-temporal position and shape, turns out to depend strongly on the SDO surface loss probability. For low SDO

surface loss probabilities the dominant ionisation takes place during the sheath expansion phase (feature I). With increasing SDO surface loss probability the magnitude of the sheath expansion feature (I) remains the same, while the sheath collapse feature (II) becomes more significant. This trend reflects the simulation results of an increased global electronegativity according to the explanation stated in [139, 140], which also confirms a correspondingly deeper extension of the ionisation features into the plasma bulk.

7. Plasma-Surface Interaction

Generally, physical and chemical plasma-surface interaction processes play a vital role for plasma processing in the form of etch and deposition processes. Thus, these processes are central in determining gas-phase species concentrations and the discharge equilibrium itself, since it is affected by plasma-surface interaction processes. This requires a good end-point detection system and knowledge of the actual surface condition.

In the previous chapter the role of SDO in oxygen discharges was discussed and it was shown that the SDO surface loss probability plays an important role for plasma dynamics and can therefore be used as sensitive indicator for the actual surface condition under the investigated regime.

In this chapter plasma-surface interaction is investigated by means of identifying other relevant surface reaction mechanisms, such as positive ion neutralisation and secondary electron emission, and determining their effects on plasma parameters and excitation dynamics. An extensive analysis of the excitation rate in the frequency domain is presented and the behaviour of different frequency components is discussed under changing surface condition. Furthermore, conclusions are drawn as to how the actual surface conditions can change discharge dynamics and vice versa. The numerical simulation results presented here have the following discharge parameters as basis: geometrical asymmetry, discharge gap size $d = 40$ mm, pressure $p = 40$ Pa, and $V_{rf} = 300$ V amplitude.

7.1. Investigation of Important Surface Parameters

The simulations predict that plasma dynamics are highly sensitive to the SDO surface loss probability. Apart from that, another important surface reaction mechanism responsible for changes in plasma dynamics and parameters can be identified as positive ion neutralisation, which subsequently leads to release of secondary electrons into the

plasma (illustrated in figure 7.1).

As discussed previously, the SDO surface loss probability describes the collision of SDO with the surface through thermal motion and its conversion into ground state oxygen with a certain probability (typically $s_{SDO} = 10^{-5} - 10^{-2}$). In addition, the surface condition determines the secondary electron release from the surface induced by impact of positive molecular oxygen ions. Typically, the values for the secondary electron emission coefficient depend on the ionisation threshold of the involved ion species. In case of positive molecular oxygen ions the coefficient can lie between $\gamma(O_2^+) = 0.0 - 0.2$.

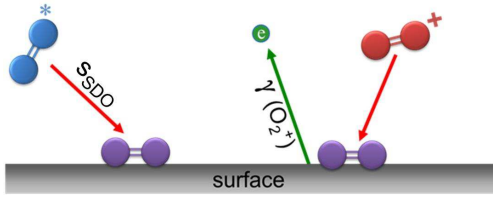

Figure 7.1.: Illustration of relevant surface reaction mechanisms: surface neutralisation (left); secondary electron emission (right).

The impact of the actual surface condition on particle densities is demonstrated in figure 7.2 and shows the global (time and space averaged) density of charged particles as function of the SDO surface loss probability and the secondary electron emission coefficient. Arrows indicate the direction of strongest dependence.

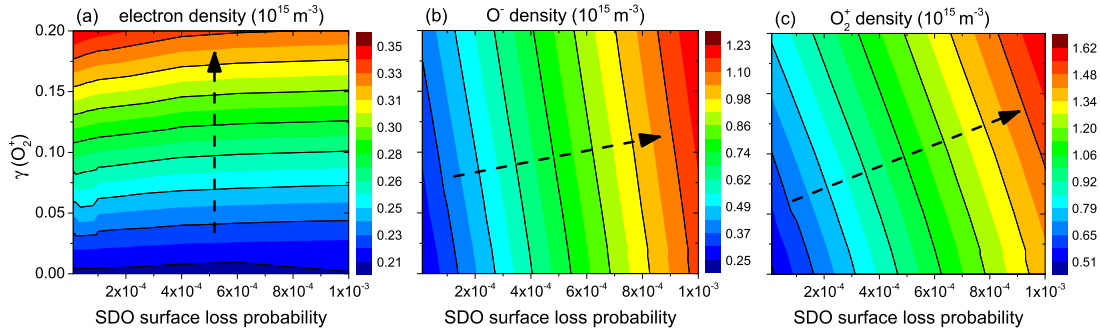

Figure 7.2.: Time and space averaged particle densities of (a) electrons, (b) negative atomic oxygen ions, and (c) positive molecular oxygen ions in dependence of SDO surface loss probability and secondary electron emission coefficient $\gamma(O_2^+)$. Arrows indicate the direction of strongest correlation. (p = 40 Pa, V_{rf} = 300 V)

The global particle densities seem to be decoupled by the two investigated surface interaction processes. On the one hand, the electron density mainly depends on $\gamma(O_2^+)$, especially at higher SDO surface loss probabilities (vertical arrow in figure 7.2(a)). This is

because the impact of SDO on electrons is rather indirect, through affecting the density of negative atomic ions in the sheath regions and subsequently the positive molecular ion density. The wall flux of positive ions together with the secondary electron emission coefficient determine the yield of secondary electrons.

On the other hand, the density of negative atomic ions, figure 7.2(b), increases significantly with increasing SDO surface loss probability by almost a factor of 5. This reflects the dominant role of SDO for the volume destruction of O^- as described in section 6.4. The O_2^+ density, shown in figure 7.2(c), exhibits a mixed correlation (indicated by tilted arrow), since the changes in negative ion density and electron density have both to be compensated for sustaining quasineutrality in the plasma bulk region. Therefore, the positive ion density increases by more than a factor of 5, comparing the density for the the lowest and highest investigated surface parameter values.

Equivalently, the weighted mean electron energy, illustrated in figure 7.3, also shows a dependence on both surface parameters, however, the actual change in energy is less than 10%.

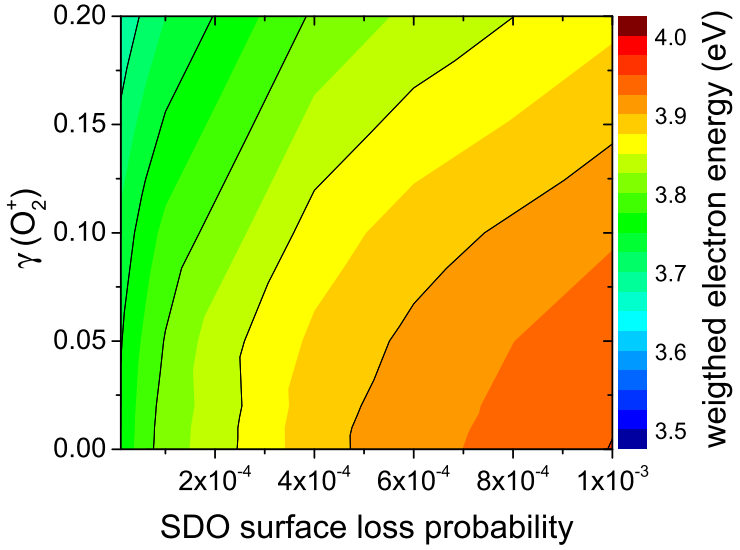

Figure 7.3.: Weighted electron energy in dependence of SDO surface loss probability and secondary electron emission coefficient. (p = 40 Pa, V_{rf} = 300 V)

For increasing secondary electron coefficient, the weighted mean electron energy slightly decreases. This has two reasons: with increasing $\gamma(O_2^+)$-coefficient, more secondary electrons are released which are immediately accelerated into the plasma bulk, where the

majority of electrons accumulates. On their way to the bulk, these electrons absorb most of the power in the sheath region, so that as a result there is a small number of very high energetic electrons and increasingly more low energetic electrons. This then leads to the observed effective decrease in weighted mean electron energy.

For increasing SDO surface loss probability, the weighted mean electron energy increases and can be explained by similar considerations as for the $\gamma(O_2^+)$-coefficient. However, here the increasing power is mainly absorbed by bulk electrons, which in turn increases the weighted mean electron energy.

Both effects have different balances so that the gradients of energy change are different for the particular change in surface parameter.

After having identified the effect of these two major plasma-surface interaction processes on the particle densities and mean electron energy, their contribution to the different excitation mechanisms, i.e. sheath expansion excitation (feature I), sheath collapse excitation (feature II), and excitation through secondary electrons (feature III) will be quantified.

Similar to the presented ionisation features, the excitation exhibits analogous behaviour, shown in figure 7.4 on a common false colour scale for one full RF cycle. White dashed lines represent the sheath edge positions.

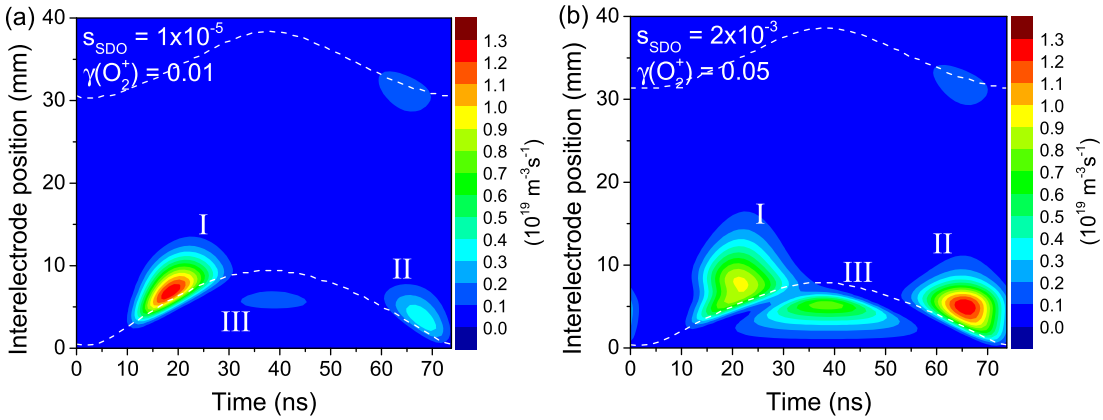

Figure 7.4.: Phase and space resolved dissociative excitation of O_2 leading to emission into the 844 nm optical emission line for (a) $s_{SDO} = 1 \times 10^{-5}$, $\gamma(O_2^+) = 0.01$ and (b) $s_{SDO} = 2 \times 10^{-3}$, $\gamma(O_2^+) = 0.05$ on a common false colour scale. (p = 40 Pa, V_{rf} = 300 V)

From figure 7.4(a) to figure 7.4(b) the SDO surface loss probability has been increased

by a factor of 200 and the $\gamma(O_2^+)$-coefficient by a factor of 5. Interestingly, both surface parameters seem to be decoupled from one another exhibiting impact on distinct excitation features. A similar decoupled behaviour was observed for the charged particle densities in figure 7.2. Here, the secondary electron emission coefficient only affects feature III, increasing its contribution to the total excitation. The other two features (I & II) are significantly affected by the SDO surface loss probability, where not only the shape, but also the pronunciation of these features changes.

On the one hand, the sheath expansion excitation loses its dominance, while becoming broader and reaching further into the bulk with increasing SDO surface loss probability. On the other hand, the excitation during the sheath collapse phase strongly increases and becomes the dominant feature. The responsible effects for this change in dominance are the increased electronegativity, which leads to a high present electric field in the bulk, and the increased positive ion density, which leads to a higher flux towards the surfaces that can only be compensated by an increased electron flux. Thus, the dominant excitation shifts to the sheath collapse phase.

Because of the shift in pronunciation, the ratio of sheath collapse excitation versus sheath expansion excitation also changes with the SDO surface loss probability and can be correlated with the electronegativity of the discharge as shown in figure 7.5 for a fixed $\gamma(O_2^+)$ value.

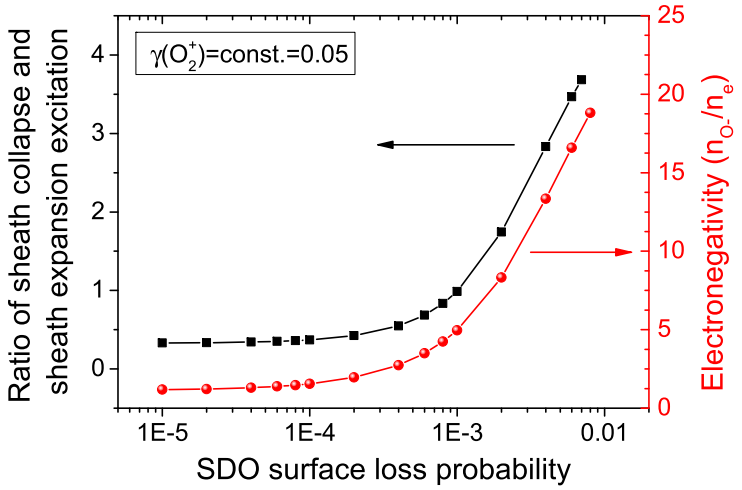

Figure 7.5.: Correlation of global electronegativity and the ratio of sheath collapse excitation versus sheath expansion excitation as a function of the SDO surface loss probability. ($\gamma(O_2^+)$ = 0.05, p = 40 Pa, V_{rf} = 300 V)

Both the electronegativity and the ratio of the excitation mechanisms exhibit similar dependencies. An electronegativity value of 5, corresponding to an SDO surface loss probability of 10^{-3}, appears to be the turning point in the dominance between the two excitation mechanisms. Recursively, the ratio of the excitation mechanisms allows not only the electronegativity to be determined but also the actual surface condition by assigning it a value for the SDO surface loss probability for a known $\gamma(O_2^+)$-coefficient.

Surface conditions, difficult to quantify experimentally, represent a big uncertainty in modern technological applications. The presented modelling approach opens the opportunity to gain a better understanding of various plasma parameters by comparing the numerical simulation with corresponding measurements. This enables fundamental plasma parameters to be linked to the actual surface condition. For example, the SDO concentration, the electronegativity and the charged particle densities can be obtained experimentally using well established optically active diagnostic methods. The experimental results can be correlated with results from numerical simulations, in order to obtain the corresponding SDO surface loss probability and secondary electron emission coefficient, both of which act as a sensitive indicators for the actual surface condition.

7.2. Frequency Analysis of Excitation Rate

In industrial plasma processing tools access for diagnostics is often restricted due to geometrical constraints or when process disturbance is undesirable. Thereby, intrusive probe diagnostics are almost always excluded as a diagnostic method. Instead, non-intrusive optical diagnostic techniques are often applied. However, to achieve a high degree of homogeneity and reproducibility the optical access is also usually limited to a minimum. This means that spatial resolution is often difficult to obtain. Nevertheless, time resolved and spatially integrated measurements are possible, e.g. through photomultiplier tubes.

Therefore, a theory is developed, which accounts for the experimental restrictions. It builds upon the previously obtained phase and space resolved simulations and extends the examination into the frequency domain via Fast Fourier Transformations (FFT) of the optical excitation signal.

Particularly, phase and space resolved dissociative electron-impact excitation of oxygen $E_{844}(t,x)$, leading to optical emission at $\lambda = 844.6$ nm, is examined because it is directly accessible from the numerical simulation via the product of corresponding energy dependent reaction rate coefficient $k_{844}(\epsilon)$ and electron density:

$$E_{844}(t,x) = k_{844}(\epsilon) n_e(t,x) \tag{7.1}$$

Here, ϵ denotes the mean electron energy. By averaging over space the periodic excitation function $E_{844}(t)$ can be obtained and further analysed in its frequency domain.

Figure 7.6 shows a typical excitation function $E_{844}(t)$ and its corresponding amplitudes for the first 11 frequency components for $s_{SDO} = 4 \times 10^{-4}$ and $\gamma(O_2^+) = 0.02$.

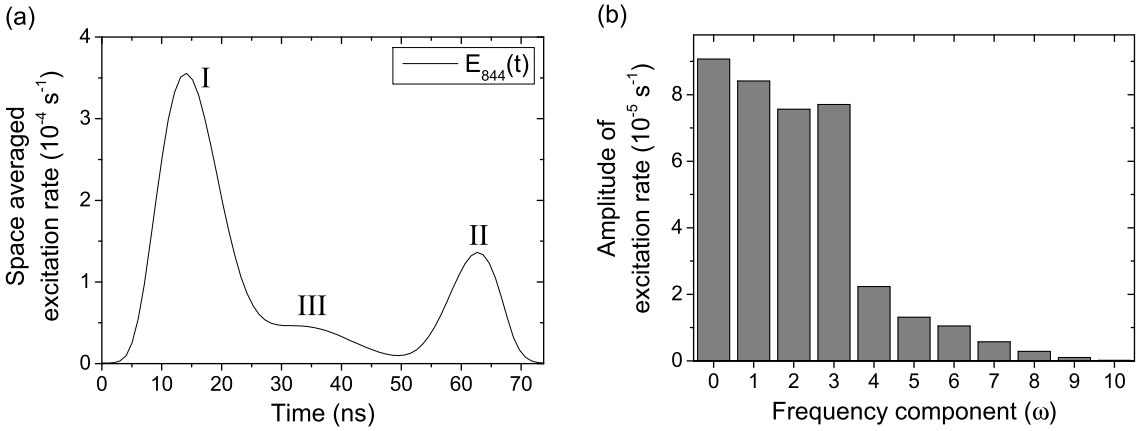

Figure 7.6.: (a) Excitation function $E_{844}(t)$ and (b) amplitudes of corresponding frequency components for dissociative electron-impact excitation of oxygen leading to optical emission at $\lambda = 844.6$ nm.
($s_{SDO} = 4 \times 10^{-4}$, $\gamma(O_2^+) = 0.02$, $p = 40$ Pa, $V_{rf} = 300$ V)

As can be seen from figure 7.6(a), the three excitation features described earlier can be distinguished from one another. In this particular example, the excitation in the sheath expansion phase (feature I) is dominant followed by the sheath collapse excitation (feature II) with about half the amplitude. Since the excitation function is spatially averaged the excitation signal from secondary electrons (feature III) superimposes the first feature. The position of maximum excitation of the first two features can shift dependent on the SDO surface loss probability, whereas the maximum of the third feature stays at about 37 ns, i.e. half a RF cycle. This is because the SDO surface loss probability affects

the sheath dynamics, whilst the excitation from secondary electrons is always highest when the ion impact of the surface is highest, which is when the sheath is extended to its maximum.

An analysis of the excitation function in the frequency domain (figure 7.6(b)) reveals that the amplitudes of the first four frequency components ($0 - 3\ \omega$) are the dominant components, with the following components rapidly decreasing. The $0\ \omega$-component is the so called DC component and equals the total time averaged excitation; its amplitude is usually the highest of all components. The following components represent the driving frequency ($1\ \omega \triangleq 13.56$ MHz), the second harmonic ($2\ \omega$), the third harmonic ($3\ \omega$) and so forth.

Figure 7.7 shows the FFT analysis of the dominant frequency components of the excitation under variation of the SDO surface loss probability and secondary electron emission coefficient $\gamma(O_2^+)$ for otherwise equal discharge conditions. Each frequency component is normalised to its maximum value.

The first component ($0\ \omega$) shows a monotonic increase with both the SDO surface loss probability and secondary electron emission coefficient, with the latter having a stronger effect on the total time averaged excitation signal. This is because the excitation through secondary electrons becomes the dominant process with increasing $\gamma(O_2^+)$-coefficient.

The driving frequency component ($1\ \omega$) seems to be almost unaffected by the SDO surface loss probability, but shows a strong dependence on the $\gamma(O_2^+)$-coefficient. However, this dependence is not monotonic, showing a minimum value band between $\gamma(O_2^+) \approx 0.02 - 0.05$.

For the second harmonic ($2\ \omega$), three distinctive gradients can be observed. In case of $\gamma(O_2^+)$ values above 0.1 the excitation signal shows a similar dependence as for the driving frequency component, being almost only dependent on the $\gamma(O_2^+)$-coefficient. Below 0.1 and above 0.05, the second harmonic excitation increases significantly with increasing SDO surface loss probability, the increase with the secondary electron emission coefficient is less pronounced than for higher values. Below 0.05, the excitation still significantly increases with increasing SDO surface loss probability, however, shows an opposing trend with increasing $\gamma(O_2^+)$-coefficient.

The third frequency component ($3\ \omega$) of the excitation signal also shows different

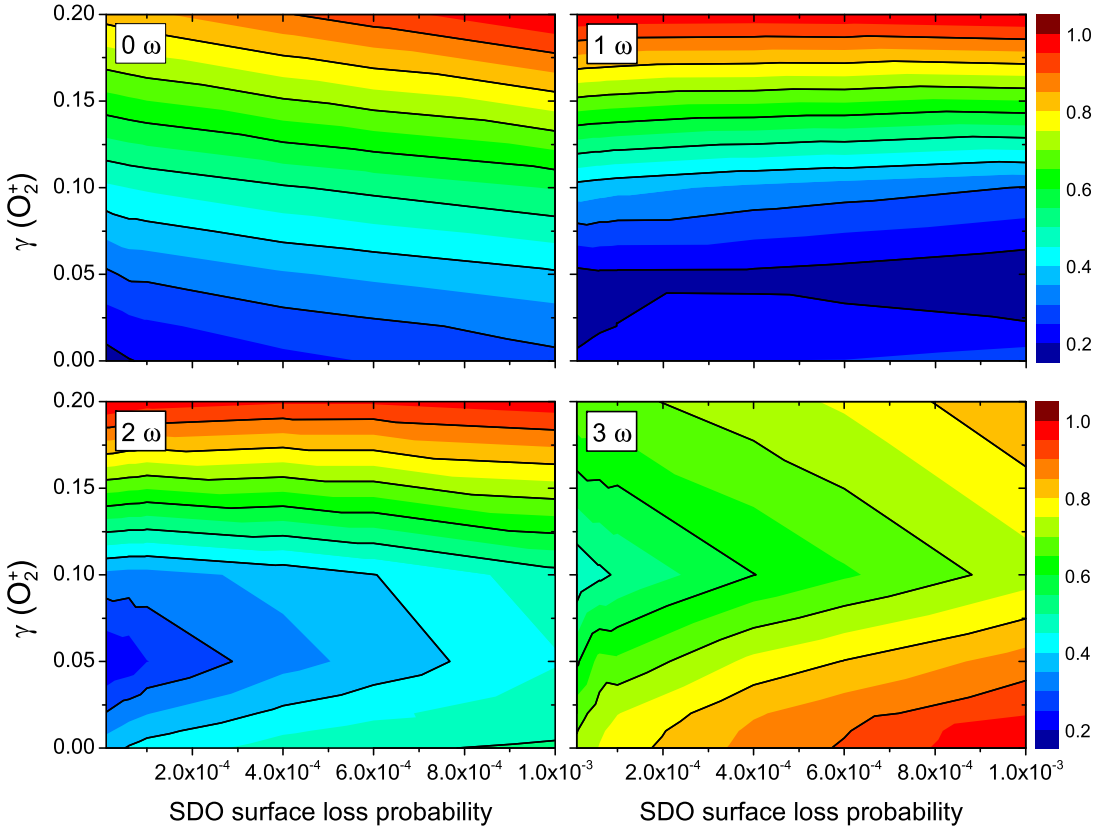

Figure 7.7.: Normalised frequency components of the excitation function in dependence of variable SDO surface loss probability and secondary electron emission coefficient. 0 ω comprises the DC component, 1 ω corresponds to the applied radio-frequency at 13.56 MHz, 2 ω is the second harmonic, and 3 ω is the third harmonic. ($p = 40$ Pa, $V_{rf} = 300$ V)

gradients. Here, a $\gamma(O_2^+)$-coefficient value of 0.1 seems to be the boundary value determining the dependence of the excitation. Below, it decreases with increasing secondary electron emission coefficient; above, it increases. The dependence on an increasing SDO surface loss probability is almost symmetric around $\gamma(O_2^+) = 0.1$ increasing monotonically.

The explanation for the behaviour of the frequency components shown above 0 ω are not trivial, but can usually be associated with different power coupling mechanisms and the electron dynamics [141]. Nevertheless, it is evident that they are highly sensitive to and even show different dependencies on changes of the surface parameters. This might be used to track similar changes experimentally and correlate them to the actual surface condition with the help of the numerical calculations.

7.3. Impact of Changing Surface Condition on Plasma Dynamics

The investigated surface parameters, namely surface loss probabilities of metastable singlet delta oxygen and secondary emission coefficient induced by positive ions, both have a major influence on the plasma dynamics, thus representing important indicators for the actual surface condition. However, the surface condition is often neglected or wrongly treated in simulations due to absence of consistent data. Therefore, modelling a set of different surface loss probabilities and secondary electron emission coefficients was used to gain further insight on their fundamental impact on plasma properties in quantitative terms.

Figure 7.8 illustrates how the actual surface condition affects particles within the discharge and how these particles in turn affect the plasma dynamics.

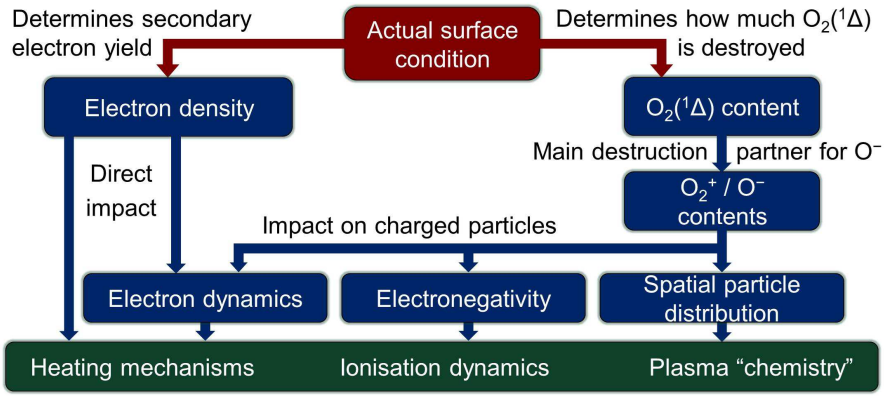

Figure 7.8.: Illustration of actual surface condition impact on plasma parameters and plasma dynamics.

Generally, a change in SDO surface loss probability determines how effectively SDO is destroyed (right hand branch in figure 7.8). Thereby, an increasing SDO surface loss probability evokes in the first place a reduction of the total SDO concentration in the system. A quasi-reciprocal dependence of the concentration on the surface loss probability has been observed. Furthermore, the numerical simulations yield that SDO is the main collision partner of O^- leading to its destruction. Thus, a decreasing total SDO concentration implies an increasing negative atomic oxygen ion density. The negative ions on their part will affect other charged particles. In order to compensate the in-

creased negative net charge in the plasma, the positive ion density will increase as well. On time average, only electrons are minorly affected by the changes of the SDO surface loss properties, thus leading to an increasing electronegativity in the system, because O^- becomes successively more dominant over electrons.

It was shown that the time and space averaged electron density is significantly affected by the secondary electron emission coefficient and thereby directly impacts the electron dynamics and plasma dynamics (left hand branch in figure 7.8).

Time and space resolved electron dynamics, however, are also affected by changing the SDO surface loss probability and the secondary electron emission coefficient. It was shown that, on the one hand, an increasing SDO loss at the surfaces leads to a successively more pronounced excitation during the sheath collapse phase. This can be explained by the increasing electronegativity, which promotes electrons to be accelerated to a higher extent during sheath collapse than with less electronegativity, thus enhancing excitation in this region. On the other hand, excitation dynamics from secondary electrons only change with varying secondary electron emission coefficients because this influences the production of secondary electrons and their possibility to excite molecular oxygen on their path towards the plasma bulk.

These findings have a significant impact for the understanding of processing plasmas in industrially relevant applications, such as plasma etching. Usually, it is assumed that processing plasmas modify the treated surfaces without being influenced by the modified surface itself. However, it was shown that changing surface conditions can exhibit a strong impact on the heating mechanisms, ionisation dynamics and influence the plasma "chemistry". In a dynamic plasma process an interaction between actual surface condition and plasma dynamics develops. This mutual feedback can now be exploited by assessing the actual surface condition via numerical simulations and the plasma dynamics via experimental measurements.

Coupling experimental observations to easily adjustable numerical simulations will then enable experimental setups to be modified more efficiently allowing the development of advanced real-time process control and monitoring tools.

8. Experiment and Diagnostics

In this chapter the experimental setup and applied diagnostic methods are presented. Firstly, the discharge chamber geometry and peripheral equipment such as the pumps and gas supply is discussed. Secondly, the electrical setup for power supply, voltage measurements and control of the optical equipment is described. Thirdly, optical diagnostic methods are introduced with emphasis on non-intrusive phase resolved optical emission spectroscopy. Finally, the fundamentals and limitations of operation of the considered optical system are discussed and necessary spectral sensitivity calibrations as well as corrections are investigated.

8.1. Discharge Chamber and Peripheral Equipment

The experimental setup is illustrated in figure 8.1 and will be described in the following.

The discharge chamber geometry is based on the geometry of the inductively coupled Gaseous Electronics Conference (GEC) reference cell [57]. However, a number of modifications have been applied to effectively operate the plasma in an asymmetric capacitively coupled regime. Usually, the power is applied to the top coil and a stainless steel disk lies on top of the grounded lower electrode, that serves as electrode extension to achieve high homogeneity of the plasma discharge. In the present work, however, the top coil is grounded and the lower electrode, without the extension, is powered. The lower electrode is then equivalent to the standard electrode used in a CCP GEC reference cell [142] with a diameter of 102 mm. The resulting discharge gap is 43 mm. Around the lower electrode a grounded guard ring is situated to guarantee a well defined and reproducible plasma confinement. The top coil is shielded by a quartz window, which is on floating potential. Nevertheless, due to the different effective surface areas the created plasma is highly asymmetric, given the geometry the asymmetry factor can be estimated to be $S_{gnd}/S_{pwd} \approx 36$. Combined with the facts, that the grounded chamber

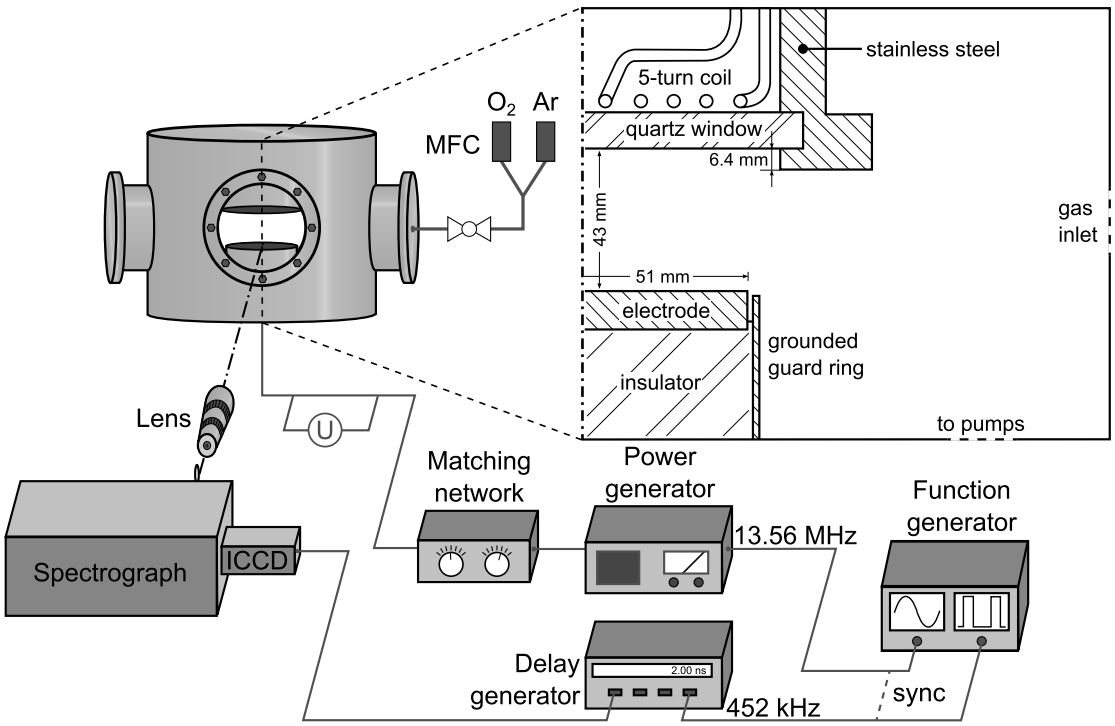

Figure 8.1.: Illustration of experimental setup and discharge chamber geometry.

walls are sufficiently far away from the central symmetry axis and that the main ionisation and excitation takes place immediately above the powered lower electrode, the idealised one-dimensional simulation constitutes a justified approximation of the real geometry, as discussed previously in section 3.2.

To guarantee a controlled and reproducible discharge environment, the pump system is located radially around the symmetry axis. A combination of a rotary-slide-vane pump (*Pfeiffer Vacuum DUO-20MC; max. 6.7 l/s, 1800 min*$^{-1}$) and a turbo molecular pump (*Pfeiffer Vaccum TPU-170; max. 170 l/s, 43000 min*$^{-1}$) is used to pump down the chamber to a pressure of up to 10^{-4} Pa. This is achieved in two steps. Firstly, only the rotary pump is activated to ensure that no lubricant solvent enters the chamber. This pump is capable of reaching a pressure of several Pa. Subsequently, an ultra-high-vacuum pneumatic linear valve (*Nor-Cal Products 11212-0400R*) is used to open a bypass for the turbo pump. The turbo pump is equipped with water cooling due to its high rotation frequency (> 25000 min^{-1}). In general, the cooling of the powered electrode is also of special importance because the plasma needs to be operating as stable as possible for the sensitive optical emission measurements. The cooling unit (*Applied Thermal Control*

K1-P10) used to cool the turbo pump as well as the electrodes is set to 20 ± 0.1 °C and has a cooling capacity of 1.75 kW at a flow rate of 10 l/min.

After reaching the final pressure, the turbo pump is decoupled from the chamber and the discharge can be operated in the pressure range of 40 Pa−100 Pa using corresponding gas flow.

The gas flow and mixture is controlled by an MKS controller unit (*Type 247 Four-Channel Readout*) that is connected to two mass flow controllers (MFC) with different maximum flow rates of 50 sccm and 10 sccm. Both MFC are calibrated for the use of nitrogen gas, for different gases corresponding gauge factors need to be accounted for (gauge factor $O_2 = 1.00$, gauge factor $Ar = 1.44$).

The utilised gas mixture consists of 98% oxygen (purity: 5.1) and 2% argon (purity: 4.8), achieved by applying 50 sccm oxygen and 1 sccm argon mass flow, respectively. The small argon admixture serves as reference gas for the optical measurements and is known not to change the discharge dynamics [37, 98].

In the low pressure range, when pumping down, a pressure gauge based on the principle of the inverted magnetron and Pirani measurement system is used (*Oerlikon Leybold Vacuum PENNINGVAC PTR90:* 5×10^{-7} *Pa* -1×10^{5} *Pa*) and in the plasma operation pressure range a capacitive pressure gauge (*MKS Baratron Type 627 pressure transducer:* 2.6 *Pa* -1.3×10^{5} *Pa*), which is independent of the gas species and directly connected to a variable valve (*MKS Type 600 series pressure controller*), is used to measure and control the pressure.

8.2. Electrical Setup

The electrical setup to operate the plasma and conduct the optical measurements consists of several elements, also illustrated in figure 8.1. A function generator (*TTi 100 MHz Arbitrary Wavefrom Generator TGA-12104*) is used to provide synchronised trigger signals for the power and delay generators, respectively, to ensure that the intensified charge-coupled device (ICCD) camera and plasma discharge voltage are always in sync. The function generator can supply an output voltage of ±10 V. For this work, an output voltage of ±5 V has been found to be ideal. The two output signals are sinusoidal at

13.56 MHz and rectangular (TTL) at 452 kHz.

The sinusoidal trigger signal is coupled into the fixed frequency power generator (*Coaxial Power Systems RFG 150-13*) that is capable of producing up to 150 W output power, however, a maximum of 100 W is not exceeded during the conducted experiments to ensure that the discharge is operated in a low power α-mode regime. The matching network (*Coaxial Power Systems MMN 150-13*) is used to match the impedance of the discharge to the output impedance of the power generator, so that a most efficient power coupling into the discharge is given. In this work, the reflected power has been found to stay below 1%.

The voltage measurements are performed with a capacitive voltage probe (*LeCroy PPE 20kV*) that measures the voltage directly applied to the lower electrode in a ratio of 1000:1.

The delay generator (*Standford Research Systems DG 645*) generates the trigger signal for the ICCD camera with a variable delay and a constant phase angle to the RF plasma voltage. The trigger frequency for the ICCD camera needs to be below 500 kHz by specification, therefore, a frequency of 452 kHz is chosen which is exactly 1/30 of the driving frequency. The actual output signal of the delay generator is a 5.5 ns wide TTL signal with 2 ns full width at half maximum (FWHM), with amplitude of 3 V. This ensures that the ICCD camera receives every trigger signal with the correct width.

For time-resolved monitoring of the signals, a digital storage oscilloscope (*LeCroy WaveSurfer 104 MXs-B 1 GHz*) is used that has a temporal resolution of 1 ns.

8.3. Optical Diagnostics

Optical diagnostic methods can roughly be divided into active and passive techniques. Microwave interferometry and laser based techniques that can essentially be differentiated in absorption spectroscopy and fluorescence spectroscopy are counted among the active diagnostic techniques. In these direct and reliable methods generally an external source is used to examine changes in the plasma to conclude on plasma parameters. However, active diagnostic methods are usually associated with complex and costly technological requirements and often the required optical access is not sufficient due to

the available system dimensions.

In contrast to active diagnostic methods, passive techniques offer an uncomplicated and flexible access to the plasma discharge. The most prominent passive diagnostic technique is the optical emission spectroscopy (OES) which exhibits several advantages over active techniques. The two most important advantages of OES at the examination of plasma parameters are its non-interfering nature and low requirements regarding the equipment because only the emitted photons from the plasma serve as information source. Additional benefits of OES are the high achievable spatial and temporal resolution. This allows an accurate analysis of excited states and the dynamics within the discharge cycle.

Principally, OES allows the diagnosis of major plasma parameters (e.g. particle number densities and their temperatures, electrical field strengths, etc.) that are closely connected to population densities of excited states and thereby also to measured emission intensities of the involved species. For instance, the electron density can be deduced from Stark broadening of emission lines, the electron temperature from ratios of different emission lines, the temperature of neutral particles from Doppler broadening of emission lines and the density of neutral particles can be obtained from actinometry.

Due to the passive nature of OES and thereby the indirect access to plasma parameters many atomic and molecular excitation and de-excitation processes need to be accounted for, as described in section 2.4.

Since the emission is caused by very fast dynamics processes, phase resolved optical emission spectroscopy (PROES) measurements of the excitation dynamics in the RF cycle of plasma discharges require fast optical diagnostics. Using this technique the dynamics of plasma excitation and ionisation by energetic electrons can be probed observing the emission intensity on a nanosecond timescale [143]. The used ICCD camera (*Andor iStar DH344T-18U-73*) allows optical gate times of up to 1.9 ns. For this reason, the camera is well suited for phase resolved measurements at driving frequencies of 13.56 MHz and beyond. In this work, optical gate times of 2 ns are used, which have been found suitable to perform phase resolved measurements of a full RF cycle with 73.75 ns width.

On the basis of figure 8.2(a), which illustrates the configuration of the image intensifier, the mode of operation of the ICCD camera will be discussed in detail.

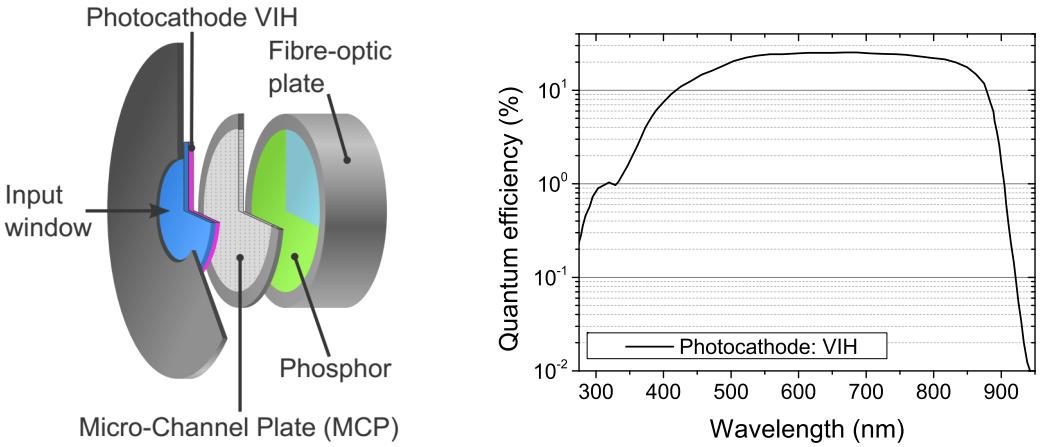

Figure 8.2.: (a) Configuration of image intensifier of the ICCD camera and (b) wavelength dependent photo cathode sensitivity (REF).

Photons that reach the camera and enter through the glass input window, generate electrons via photoionisation on the photocathode, which is tuned to cover the visible and near infrared region VIH ($280 - 910$ nm). In this context, the quantum efficiency of the photocathode, shown in figure 8.2(b), describes the probability of releasing an electron through the photoelectric effect, and thus allowing to detect an impacting photon. The examined plasma discharges are operated in an oxygen and argon gas mixture, with prominent emission lines in the range of $750 - 850$ nm, thereby, providing almost the maximum possible quantum efficiency ($> 20\%$).

A variable voltage between the photocathode and the so-called micro-channel plate (MCP) provides adjustable controllability of the electron gain. The MCP is made of honeycomb micro-structured glass with electrodes on both sides and contains a multitude of parallel channels ($\approx 10^6$) with 10 μm diameter. If it is off, electrons can pass through the MCP without noticable multiplication. Whereas, in case of a switched on MCP a positive potential is applied and electrons are accelerated from the photocathode to the MCP and multiply via electron-wall collisions. For maximum MCP potential the multiplication factor of electrons is 243. Secondary electrons generated in this way impact the phosphorescent layer. The emitted photons from the phosphorescent layer are then transported via the fibre-optic plate to be detected on the CCD chip.

The CCD chip consists of 1024 x 1024 pixels each of size 13 x 13 μm^2, thus the square shaped CCD chip has a total side length of 13.3 mm. This two-dimensional CCD sensor

is not only suitable for time and spatially resolved measurements, but also offers the possibility to obtain wavelength resolved one-dimensional images along the central discharge axis (43 mm) with the help of a motorised imaging spectrograph (*Andor Shamrock SR-500i-B1*). The spectrograph has a focal length of 0.5 m and a wavelength resolution of up to 0.06 nm using a grating of 1200 mm^{-1}. The entrance slit width is manually set to 50 μm, this is found to be a good compromise between intensity and resolution.

For two-dimensional observations custom optical narrow bandpass filters (*L.O.T. Oriel:* 750.46 ± 0.50 *nm;* 777.45 ± 1.75 *nm;* 844.79 ± 0.95 *nm*) are used to obtain wavelength selectivity.

The high spatial resolution is achieved using a commercially available camera lens system (*SIGMA* $18 - 200$ *mm* $F3.5 - 6.5II$ *DC OS*) which is mounted in front of the ICCD camera (see figure 8.1). The resulting spatial resolution is 41.2 ± 0.2 μm and 105.7 ± 0.2 μm for one- and two-dimensional measurements, respectively. The reason for a different resolution in the case of two-dimensional measurements is that the full electrode width of 102 mm instead of only the discharge gap is covered on the CCD chip.

Figure 8.3 illustrates the realisation of phase resolved emission spectroscopy measurements.

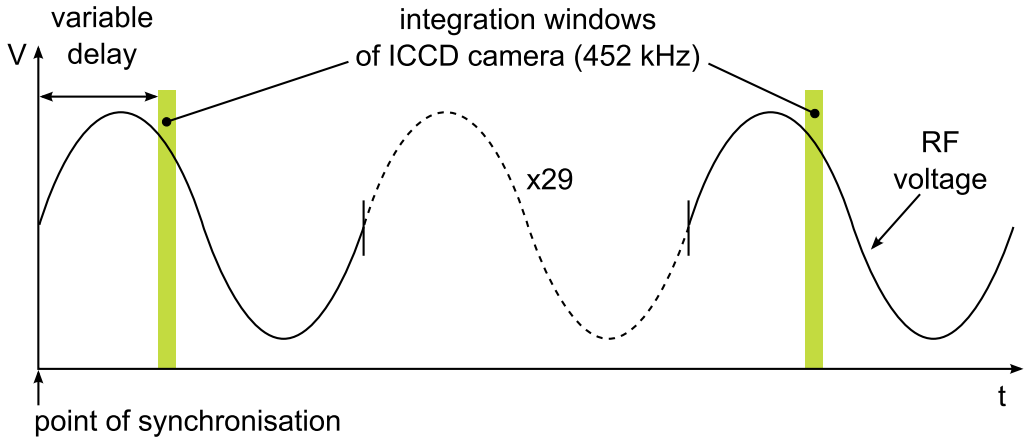

Figure 8.3.: Schematic diagram to illustrate PROES measurements.

A trigger pulse is induced by the delay generator with a variable delay time beginning from the point of synchronisation. Once every 30 RF cycles, the trigger signal activates the intensifier of the ICCD camera in the same phase position (green columns in fig-

ure 8.3). Thus, the detected emission is integrated with typical exposure times of several seconds within the integration window over thousands of RF cycles. At the end of the exposure period, all detected photons are exported from the CCD chip as image data. The phase resolution is achieved by increasing the variable delay stepwise within the RF cycle, with a step size of equivalently 2 ns to the optical gate time, while keeping the integration window constant. Hence, a progressive scan of the entire cycle is possible resulting in a total of 37 images per RF cycle.

From the PROES measurement of the emission intensity the excitation dynamics can be obtained by means of calculating the corresponding excitation rate. This is necessary to compare experimental results with numerical simulations. The emission intensity is determined by the excitation rate and the effective lifetime of the emitting state. Hence, the excitation rate can be calculated by deconvolution of the emission intensity, which is proportional to the excited state density n_i, with the effective lifetime [143, 144]:

$$E_i(t,x) = \frac{1}{n_0}\left(\frac{dn_i(t,x)}{dt} + \frac{1}{\tau_{\text{eff}}} n_i(t,x)\right) \tag{8.1}$$

$$\text{where :} \qquad \frac{1}{\tau_{\text{eff}}} = \frac{1}{\tau_{\text{nat}}} + \sum_q k_q n_q \tag{8.2}$$

Here, the effective lifetime τ_{eff} is derived from the natural radiative lifetime τ_{nat} and the quenching coefficient k_q of the excited state with quenching partner n_q.

The spatial profiles of neutral particles, determined through gas temperature profiles or depletion, are not taken into account for the quenching contribution in this simple relationship. Table 8.1 gives an overview of the natural radiative lifetimes and quenching coefficients used for the three considered excited states Ar($2p_1$), O($3p^5P$), and O($3p^3P$) at temperature $T_g = 300$ K.

The effective lifetime is then calculated using the ideal gas law to determine the number density of the corresponding quenching partner, which is either the background gas oxygen or argon.

Table 8.1.: Emission wavelength, radiative lifetime, and quenching coefficients of $Ar(2p_1)$, $O(3p^5P)$, and $O(3p^3P)$ atoms at room temperature.

Atomic state	Emission wave-length (nm)	radiative lifetime (ns)	Ref.	quenching coefficient (10^{-16} m^3s^{-1})		Ref.
				in O_2	in Ar	
$Ar(2p_1)$	750.4	22.5 ± 0.7	[145]	7.6 ± 0.8	0.16 ± 0.02	[146]
$O(3p^5P)$	777.4	27.1	[147]	10.8 ± 1.1	–	[148]
$O(3p^3P)$	844.6	34.7 ± 1.7	[149]	9.4 ± 0.9	0.14 ± 0.01	[149]

8.3.1. Calibration of Spectral Sensitivity

The spectral sensitivity of the optical system needs to be calibrated because each of the optical components (lens, spectrograph, bandpass filters) has an influence on the final detection efficiency of the ICCD camera. Therefore, it is calibrated with the help of a broadband USB spectrometer (*Ocean Optics HR4C4860 VIS*). An optical fibre (*Ocean Optics QR600-2-SR; 600 µm diameter*) is used as a light guide and is attached at one end to the spectrometer and at the other mounted to a side window of the discharge chamber. This spectrometer comprises a linear CCD chip with a total of 3648 pixels, thus providing a spectral resolution of 0.05 nm over a range of $680 - 870$ nm. However, the efficiency of it varies strongly with wavelength. Therefore, the absolute spectral response of the spectrometer was calibrated using a well defined tungsten halogen light source (*Ocean Optics LS-1-CAL-220; 350-1050 nm*) which provides absolute spectral intensity in units of $\mu W/cm^2/nm$.

The calibration is based on the time integrated intensity from the particular optical emission line of interest and is separately conducted for each emission line and optical setup, either using the spectrograph or the optical filters as wavelength selectivity tool. Figure 8.4 illustrates the calibration of the ICCD camera.

For the same discharge conditions, the emitted spectrum from the plasma is recorded via both the spectrometer and the ICCD camera. Because the spectral resolution for both devices are different, it is insufficient to just compare the maxima of the emission, but the integrated emission for each optical line. The actual calibration factor C_{λ_0} is then obtained from the ratio of the integrated emission:

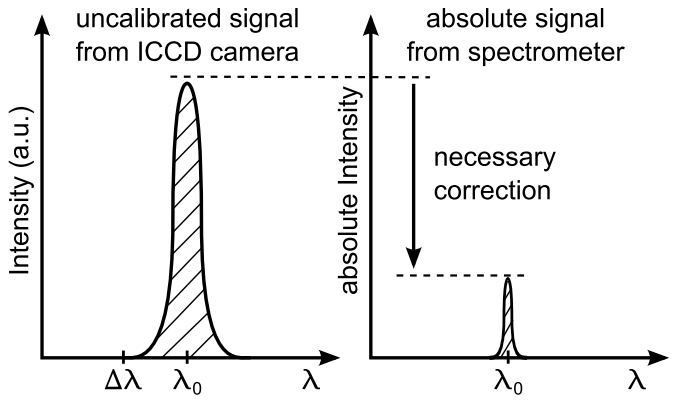

Figure 8.4.: Illustration of spectral sensitivity calibration of ICCD camera.

$$C_{\lambda_0} = \frac{\int_{\lambda_0-\Delta\lambda}^{\lambda_0+\Delta\lambda} I_{ICCD}\, d\lambda}{\int_{\lambda_0-\Delta\lambda}^{\lambda_0+\Delta\lambda} I_{Spectrometer}\, d\lambda} \tag{8.3}$$

The $\Delta\lambda$ is thus chosen so that the total emission from the optical emission line of interest is fully covered without integrating over neighbouring optical emission lines. This is especially important for the argon 750.4 nm optical emission line which is in the vicinity of another argon line (751.5 nm). For the two oxygen optical emission lines (777.4 nm and 844.6 nm) that consist of three superimposed lines each, at same energy level but different spin states, the integration covers all three lines.

The resulting spectral calibration factors for the ICCD camera are shown in table 8.2.

Table 8.2.: Spectral sensitivity calibration factors for the ICCD camera in two different optical system setups.

	Spectrograph (Andor Shamrock SR-500i-B1)	Custom optical narrow bandpass filter (L.O.T. Oriel)
$C_{Ar,750}$	0.2163	0.9987
$C_{O,777}$	0.2705	0.3470
$C_{O,844}$	0.6607	0.8799

Comment: The influence of the optical lens is equally accounted for in both setups.

8.3.2. Correction for ICCD Camera Limitations

Operating the ICCD camera at its limits (2 ns optical gate) has proven to cause a periodic acquisition signal breakdown to occur due to internal hardware restrictions. To quantify

and correct for this signal breakdown a constant direct current powered LED light source was used. The LED light emission was then observed time resolved with the ICCD camera at various wavelengths.

Figure 8.5 exemplarily shows the obtained normalised emission from the LED light source at 750.0 nm for 25 consecutive time frames (2 ns time step) and the corresponding sinusoidal fit.

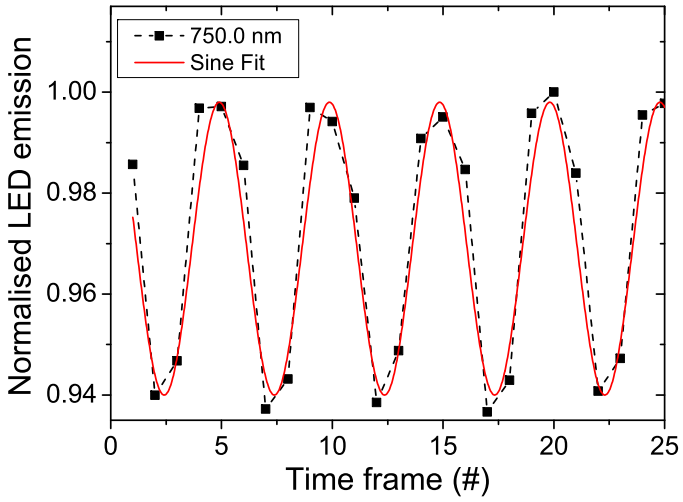

Figure 8.5.: Normalised LED emission at 750.0 nm for 25 consecutive time frames (2 ns time step each frame) and the corresponding sinusoidal fit.

The signal breaks down periodically by about 6% from the maximum intensity and reoccurs every 5 time steps, i.e. 10 ns. This is verified by a sinusoidal fit with amplitude of 0.03 and frequency of 4.97.

A signal breakdown of 6% has a substantial impact on the observed excitation dynamics that take place on a nanosecond timescale, because the excitation is directly proportional the first derivative of the observed emission intensity. Hence, a negative gradient, as occuring during signal breakdown, can artificially evoke a negative excitation signal, which is unphysical. To minimise this effect, the inverse of the sinusoidal fit is applied for each corresponding time step as correction.

8.3.3. Angle of Incidence Considerations

When the plasma is observed with the optical filters, thus allowing the full discharge extension to be spatially resolved, the actual angle of incidence needs to be taken into

account. This is due to a wavelength shift λ_S that is dependent on the central wavelength λ_0 of the filter, its effective refractive index n_* and the angle of incidence θ:

$$\lambda_S = \lambda_0 \left(1 - \frac{sin^2\theta}{n_*^2}\right)^{1/2} \tag{8.4}$$

Since the optical filters are strongly narrow bandpass filters (FWHM < 2 nm), the angle of incidence can have a significant influence on the transmittance of the filters. Due to the actual transmittance function of the utilised optical filters the angle dependent transmittance is always smaller for the particular observed wavelength than the maximum transmittance.

To quantify the transmittance of the optical filters under discharge conditions, three cases are investigated experimentally, as illustrated in figure 8.6(a). Firstly, the optical filter is tilted to the left so that the plasma emission from the left discharge edge is perpendicular to the filter surface. Secondly, the optical filter is aligned centrally so that the plasma emission from the discharge centre is perpendicular to the filter surface. And thirdly, the optical filter is tilted right to maximise the transmittance from the right discharge edge.

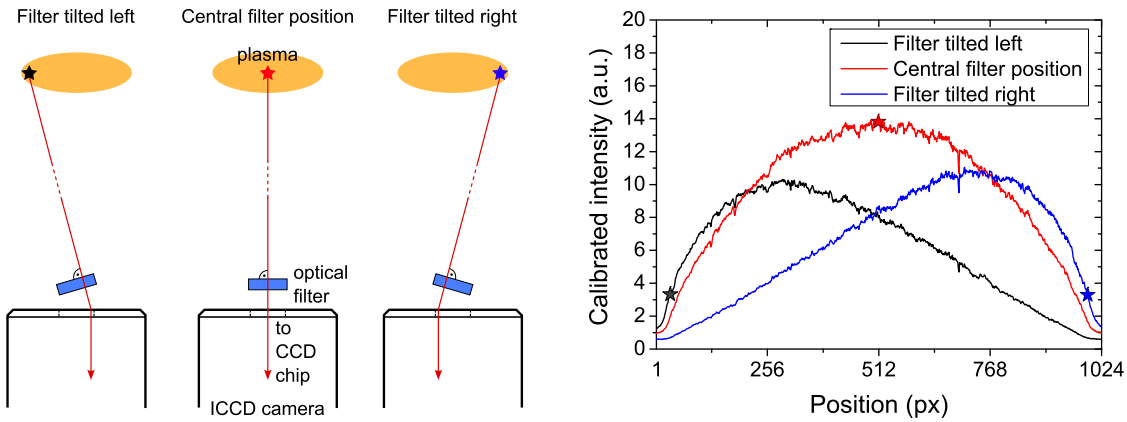

Figure 8.6.: (a) Illustration of optical setup for angle of incidence calibration and (b) typical emission profiles for the three optical filter positions using the 777.4 nm optical emission line averaged over 14 pixels as example.

Figure 8.6(b) shows typical line profiles obtained by this method (the star symbol in each case marks the observed point that is perpendicular to the optical filter surface). As

expected, the central filter position produces a symmetrical profile, while the other two positions create highly asymmetrical profiles with their maxima near the corresponding observed edges. It has to be noted that the actual observed maximum is not at the position to which the optical filter is aligned because the discharge is not uniform. The measurement is repeated several times to minimise errors.

The ratio of the observed emission strength at the edges and the corresponding emission strength from the central filter position are a direct measure of the transmittance ratio $T(\lambda_S)/T(\lambda_0)$ at the corresponding points. Similar to the correction factors for the delay generator (see section 8.3.2), the inverse of the transmittance ratio serves as spatial calibration factor.

To obtain the transmittance ratios for all spatial positions, a more rigorous approach is pursued. Here, the initial measurements serve as anchor points to which the exact expression for the transmittance ratio is fitted. First, the pixel number on the CCD chip is converted into an angle of incidence, based on the optical setup. Secondly, the wavelength shift is expressed in terms of the angle of incidence following equation 8.4. Finally, the transmittance ratio is fitted based on the actual optical filter wavelength dependent transmittance, which varies significantly for the employed filters (see appendix C).

The measured transmittance ratios as well as the corresponding fits as function of the angle of incidence are shown in figure 8.7 for each optical filter separately. For the 750 nm and 844 nm filters the transmittance gradually drops to about 70%, whereas for the 777 nm filter the transmittance stays relatively constant near the centre and then decreases quickly to about 50% compared to the central transmittance. A welcome side effect of the fitting procedure is that the effective refractive index is one of the variables that is being changed in order to obtain the best fit. The obtained refractive indices are in good agreement with literature data, which suggests that typical values for refractive indices of optical filters lie in the range of $1 - 3$ [150–153].

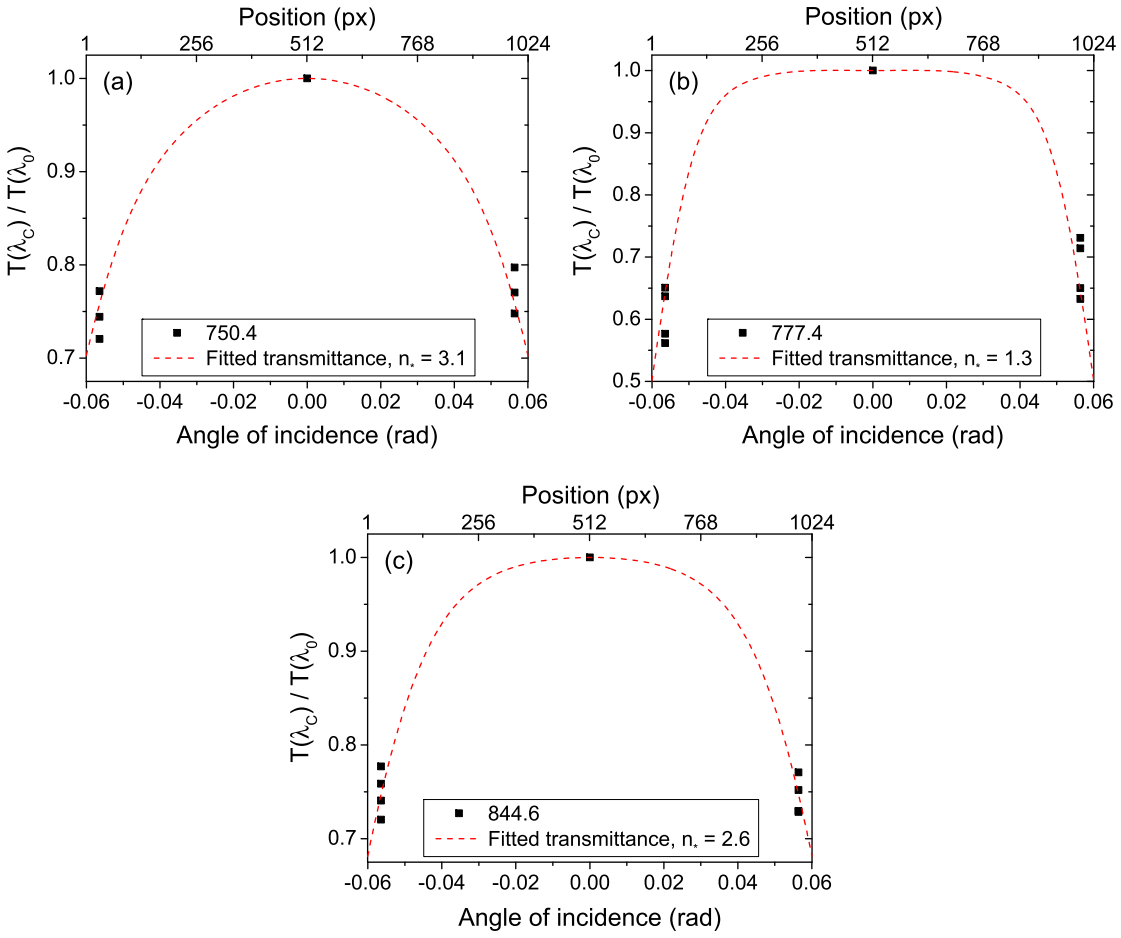

Figure 8.7.: Measured (black square symbols) and fitted (red dashed lines) transmittance ratios as function of the angle of incidence for the (a) 750.4 nm, (b) 777.4 nm, and (c) 844.6 nm optical bandpass filters.

9. Characteristics of Investigated Wafer Materials

In this chapter, a total of 9 investigated wafer materials are characterised. The work function of the utilised materials is discussed by means of a critical literature review. Furthermore, power-voltage trends are presented for two exemplary cases, i.e. stainless steel and silicon dioxide and compared to results from numerical simulations. The effect of hysteresis is briefly examined. Finally, surface modifications due to plasma treatment are illustrated qualitatively.

The investigated materials are: Teflon, glass, aluminium, stainless steel, tungsten, copper, 50 nm gold coating on stainless steel, n-type silicon ⟨100⟩*, and 50 nm silicon dioxide coating on n-type silicon* ⟨100⟩*. The diameter of each wafer is 100 mm, however, the thickness varies between 0.5 mm and 2 mm, but is found not to play a significant role.*

9.1. Work Function Analysis

The work function analysis serves as general characterisation of the investigated wafer materials. It can be regarded as one of the surface condition properties and also provides insight on the secondary electron emission properties of the wafers as discussed in section 3.4.2.

Generally, the work function is very sensitive to the cleanliness and structure of the surface. Experimentally, it can be measured using the photoelectric effect, field emission, thermionic emission or contact potential difference. Due to the differences in the experimental methods and the dependence on the surface condition, work functions can usually only be given as ranges.

Work functions for elements can be found in a revised database [67]. For compounds, literature data is more ambiguous by means of not clearly defining the composition

or crystalline structure of the material. Therefore, the given work function ranges for stainless steel [154], silicon dioxide (chem: SiO_2) [155–157] and Teflon (chem: $[C_2F_4]_n$) [158, 159] have to be regarded critically. Work function data for glass is not available, however, since glass mainly consists of SiO_2 (typically $\geq$ 80%), it is assumed that it has a similar work function. Figure 9.1 shows the surface work function ranges of the investigated wafer materials according to literature data.

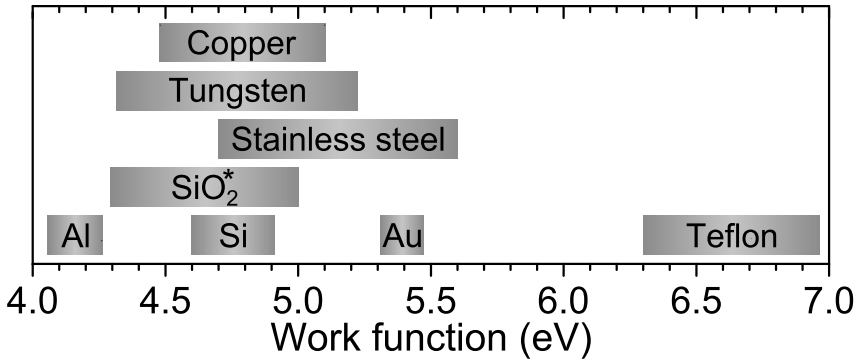

Figure 9.1.: Surface work functions of various wafer materials.
*Glass is assumed to have a similar work function as SiO_2.

Unfortunately, the exact work functions are unknown. Nevertheless, all of the investigated metallic wafers have very similar work functions, ranging from 4 eV−5.5 eV. Copper, tungsten and stainless steel seem to have the biggest spread. The least spread and thereby the best defined work functions are given for aluminium, silicon, and gold. The dielectric materials such as silicon dioxide, glass and Teflon have very different work functions, with SiO_2 and glass having similar work functions as metals, whereas Teflon shows a much higher work function in the range of 6.3 eV to about 7 eV.

The rather unknown work functions for the metals copper, tungsten and stainless steel, but also for SiO_2 and glass, might be specified by relating them to the more defined materials Al, Si and Au using excitation dynamics, as discussed in chapter 7.

9.2. Power-Voltage Characteristics

To create an easier access for the characterisation of the studied wafer materials power-voltage measurements for various pressure values are conducted. Furthermore, the findings are directly compared to simulation results for equivalent discharge conditions.

A first observation is that the power-voltage curves show very similar trends for all the investigated materials, no matter whether metal or dielectric. The only noticeable difference is in the absolute values of the voltage for any given power. The voltage difference of the highest to lowest observed values is less than 10%. Therefore, the general power-voltage characteristics will be discussed for a stainless steel wafer only.

Figure 9.2 shows the power-voltage curves of the stainless steel wafer for pressures from 40 Pa to 100 Pa and the direct comparison to 1D simulation results at 40 Pa. The power from the experiment is the total power in units of W and from the simulation in units of kW/m^2.

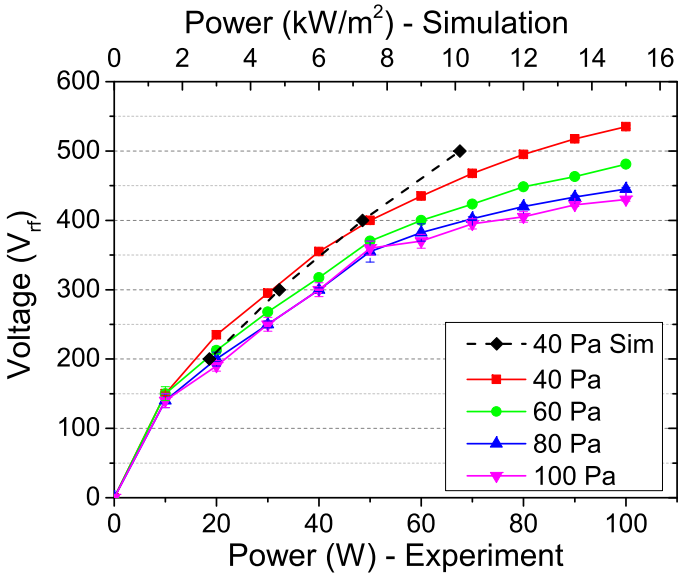

Figure 9.2.: Power-voltage characteristics obtained with a stainless steel wafer for $p = (40 - 100)$ Pa in comparison to 1D simulations at $p = 40$ Pa. For an effective electrode surface radius of 46 mm, the simulated power corresponds to the experimental power value.

The experimental measurements shows that the voltage follows a square root dependency on the applied power. This trend corresponds very well to the simulation result for a power variation in a helium-oxygen model, as described in section 4.3.1 (see figure 4.7). Furthermore, an increasing pressure evokes a voltage drop at same power. This is also in good agreement with the observed trends from the simulation, see section 4.3.2. There, the voltage drop could be explained by a phase change between voltage and current because the plasma becomes more conductive with increasing pressure, which eventually results in an impedance change. Neither the current nor the phase angle between voltage

and current were measured in the experiment, nevertheless, considering the simulation results, this explanation seems to be applicable for the observed power-voltage trend, and is confirmed experimentally in [160].

The simulation results for the pure oxygen model show very good agreement for voltage values between 300 V and 400 V at 40 Pa. For lower voltages the power dissipation in the simulation seems to be overestimated, while it is underestimated for higher voltage values. This can be explained by means of analysing the surface area over which the power is dissipated. In the experiment, the power is not homogeneously dissipated over the total surface area but shows more power dissipation at the cylindrical electrode edge where strong electric fields are present. Hence, the effective area is smaller than the total electrode surface. This leads to an overestimation in the simulation. With increasing applied power, the plasma expands over the electrode and becomes more evenly distributed, thus increasing the effective surface area, which in turn leads to an underestimation of power dissipation in the model. For the best stated agreement, the effective surface area can be estimated by correlating experimental power measurement with simulated power density. This leads to an effective electrode radius of 46 mm which is in good agreement with the actual electrode radius of 51 mm.

The DC self bias voltage follows roughly a $V_{dc} \approx -V_{rf}$ relationship, as expected considereing the powered to grounded electrode surface ratios (see equation 2.8).

Another interesting observation is a hysteresis like power-voltage characteristic which appears at pressures $\geq$ 80 Pa and is exemplarily shown in figure 9.3 for a SiO_2 wafer at 80 Pa.

The arrows in figure 9.3 indicate the direction of power-voltage change. In the power range of 30 W to 60 W the measured voltage values are higher when increasing the power from 0 W onwards, whereas they are lower when decreasing the power from high values. Qualitatively, the plasma shows a transition from an unstable (flickering) to a stable regime in this region. This instability can be attributed to attachment-induced ionisation instabilities and is discussed in more detail in chapter 11.

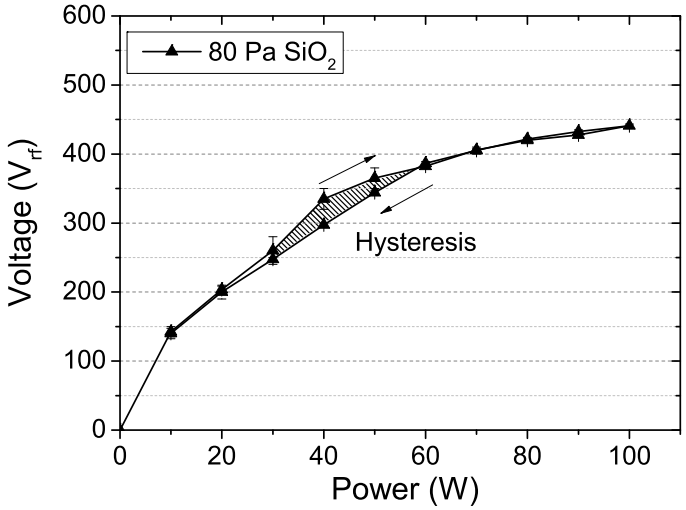

Figure 9.3.: Illustration of hysteresis effect in power-voltage characteristic for a SiO_2 wafer at 80 Pa.

9.3. Surface Modifications due to Plasma Treatment

Exposing the wafer materials to an oxygen plasma for several hours during the PROES measurements resulted in significant modification of the surface. Figure 9.4 shows photographs of the investigated wafer materials before and after plasma treatment. These photographs have to be regarded as preliminary and only qualitative examination of surface modifications under plasma exposure and do not include a quantitative characterisation.

Teflon (figure 9.4(a)) is the only wafer material that does not show any obvious surface modification, except for a slight change of surface roughness. The surface of glass (figure 9.4(b)) on the other hand has turned cloudy after plasma treatment. However, this modification is not evenly spread but spotted, which suggests that the plasma treatment is not homogeneous. Another explanation might be that the oxygen plasma reacts more effectively with one of the compounds found in glass.

The metallic wafers (figures 9.4(c)-9.4(g)) also show significant changes in the surface condition, especially at the wafer edge. It seems, that due to the high electric fields present at the wafer edge the ion impact and heating effects are enhanced in this region. The wafers show a strong darkening at the edges which is less pronounced towards the wafer centre. In the case of the copper wafer, the surface roughness is decreased such that the surface becomes highly reflective.

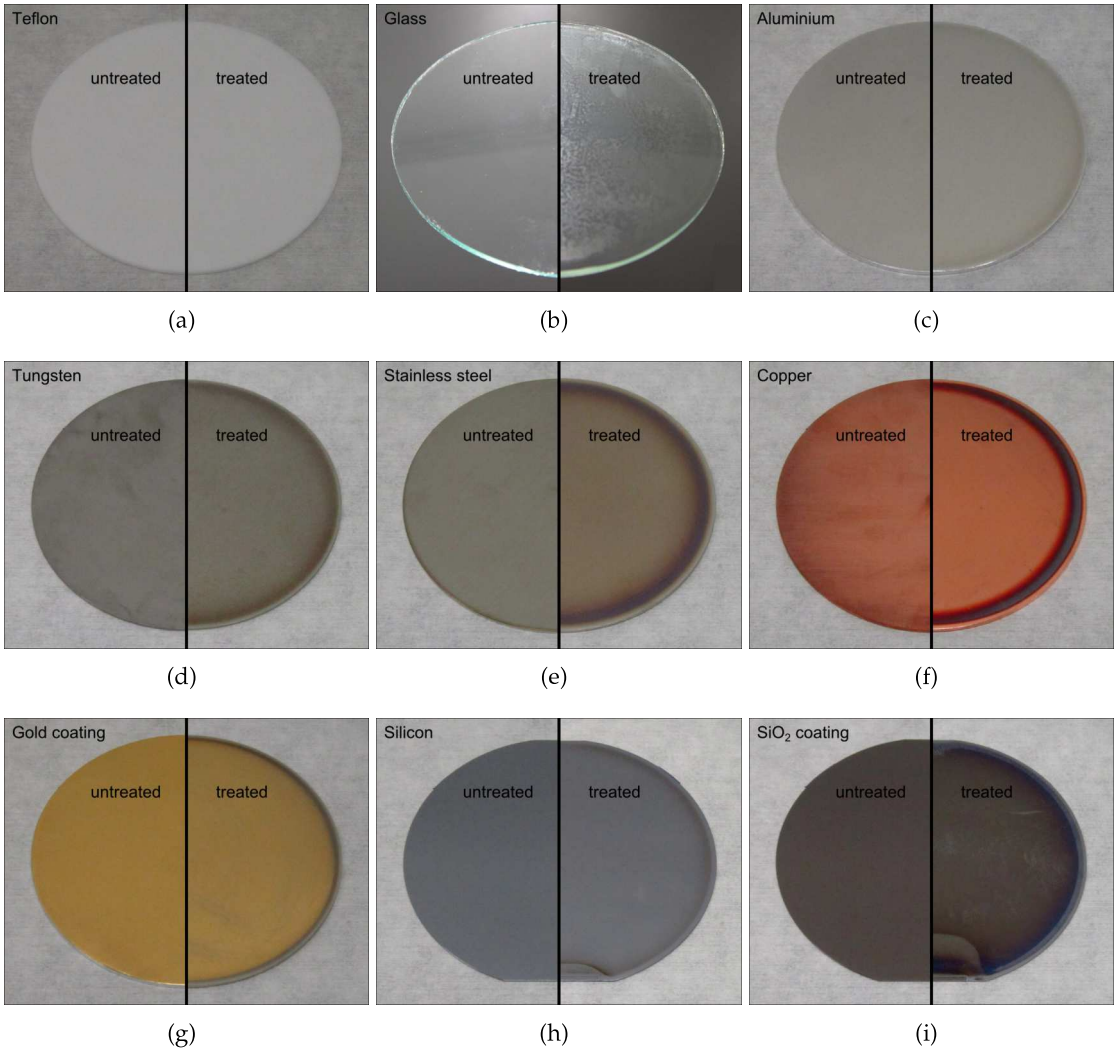

Figure 9.4.: Visual comparison of wafer materials before and after exposed to an oxygen plasma for several hours.

The gold coating (figure 9.4(g)) is etched away due to plasma treatment so that the stainless steel underneath the coating becomes visible.

The semiconductor wafers with silicon and SiO_2 coating on silicon are not perfectly round but have two cut-outs on the top and bottom (figures 9.4(h) and 9.4(i)). These cut-outs are an indication of the crystallographic orientation and impurity doping of the wafers. Here, the bottom cut-out indicates a $\langle 100 \rangle$ crystallographic orientation and the top cut-out stands for n-type silicon.

However, due to the cut-outs the plasma treatment is even less homogeneous than in the case of the round metallic wafers because the cut-outs create additional edges in

which vicinity the ion impact is significantly enhanced. Hence, the darkened regions can be found further towards the centre. Especially, in the case of the SiO_2 coated wafer (figure 9.4(i)), the coating is removed at the immediate edge similar to the gold coating, but also in extended regions around the cut-outs revealing the silicon base layer underneath.

10. Determination of Surface Parameters from Excitation Dynamics

In this chapter excitation dynamics are investigated experimentally and compared to numerical simulations to derive the relevant surface parameters. Initially, work functions of the investigated wafer materials are estimated using phase resolved optical emission spectroscopy. For a selected wafer material (silicon) excitation dynamics are discussed under power and pressure variation. On the one hand, the power variation shows that increasing power promotes excitation through secondary electrons and heavy particles. On the other hand, a pressure variation indicates that the overall excitation decreases with increasing pressure due to the increasing collisionality of the plasma discharge.

Furthermore, phase resolved excitation as well as the temporal evolution of the excitation function are presented separately. Both measurements enable the determination of surface parameters by coupling them with numerical simulations.

Finally, an overview of the obtained SDO surface loss probabilities and secondary electron emission coefficients as indicators of the actual surface condition for the investigated wafer materials is given.

10.1. Excitation Dynamics under Power and Pressure Variation

As described earlier in section 3.4.2, the surface work function is assumed to be responsible for secondary electron release and subsequent excitation through this fast electron group. To verify this, direct electron-impact excitation into the $Ar(2p_1)$ state leading to emission of $\lambda = 750.4$ nm is examined for the rather well defined work functions of aluminium, silicon, and gold. This will consequently allow the work functions of the

other not well defined wafer materials to be classified by comparison (see figure 9.1).

Aluminium, exhibiting the lowest work function, is expected to have the highest contribution of excitation through secondary electrons, followed by silicon and gold, which has the highest work function of these three materials.

Figure 10.1 shows a direct comparison of phase resolved excitation into the Ar($2p_1$) state along the radial centre axis of the discharge for aluminium, silicon, and gold wafers, respectively. The discharge parameters are equal for all three wafers (40 Pa, 400 V) and the excitation is given on a common false colour scale. To increase contrast, the scaling starts at a negative value instead of zero.

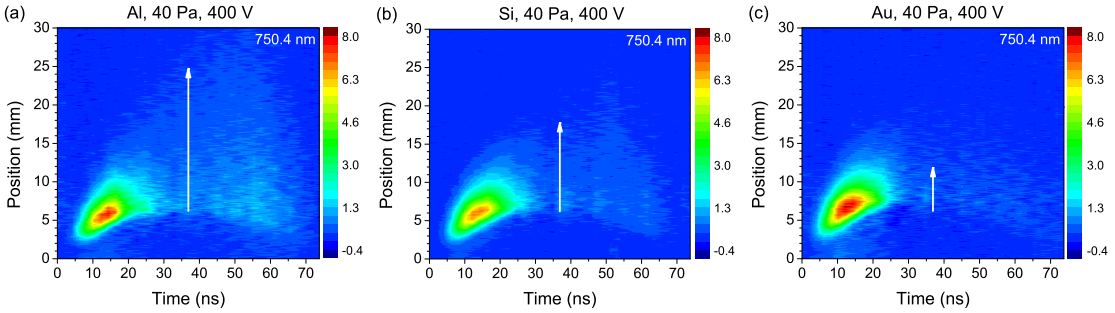

Figure 10.1.: Comparison of excitation into the Ar($2p_1$) state leading to emission of $\lambda = 750.4$ nm for (a) aluminium, (b) silicon, and (c) gold wafers under equal discharge conditions. Arrows denote the contribution to excitation through secondary electrons.
($p = 40$ Pa, $V_{rf} = 400$ V, 98% O_2, 2% Ar)

The x-axis covers the time over one full RF cycle (≈ 73.75 ns) and the y-axis denotes the spatial position where the powered electrode is at the bottom, i.e. at 0 mm. To facilitate the comparison, the y-axis is cut-off at 30 mm. In each case, the dominant excitation takes place during the sheath expansion phase. Nevertheless, it is evident that the contribution to excitation through secondary electrons released from the wafer surface varies, as indicated by white arrows of different length. Secondary electron excitation is highest in the case of an aluminium wafer and subsequently lower for silicon and gold, as expected.

In a qualitative manner, the work functions of the other wafer materials can be estimated. The work function of the investigated stainless steel wafer lies approximately half way between silicon and gold ($\epsilon_{\Phi,SS} \approx 5.1$ eV); tungsten appears to be very close to silicon, exhibiting a slightly lower work function ($\epsilon_{\Phi,W} \approx 4.5$ eV); the work functions

of copper and silicon dioxide seem to be very similar to the work function of silicon ($\epsilon_{\Phi,Cu} \approx \epsilon_{\Phi,SiO_2} \approx 4.7$ eV); and the work function of glass can be estimated as slightly higher than silicon ($\epsilon_{\Phi,Glass} \approx 5.0$ eV). An overview of the estimated surface work functions and resulting secondary electron emission coefficient (from equation 3.21) can be found in table 10.1.

Table 10.1.: Overview of estimated surface work functions and resulting secondary electron emission coefficient (using equation 3.21)

Wafer material	Estimated surface work function (eV)	Secondary electron emission coefficient
Stainless Steel	5.1	≈ 0.030
Tungsten	4.5	≈ 0.043
Aluminium	4.1	0.060 ± 0.003
Gold	5.4	0.020 ± 0.002
SiO_2	4.7	≈ 0.040
Glass	5.0	≈ 0.033
Copper	4.7	≈ 0.040
Silicon	4.9	0.036
Teflon	> 6	≈ 0

To demonstrate how the excitation dynamics change in dependence of input power and pressure, excitation into the oxygen O($3p^3P$) state ($\lambda = 844.6$ nm) is investigated for the silicon wafer. The choice for the O($3p^3P$) state originates from its higher signal-to-noise ratio than for the Ar($2p_1$) state, especially at higher power input, and because it is less sensitive to heavy particle excitation than the oxygen O($3p^5P$) state [56].

Figure 10.2 shows a comparison of excitation into the O($3p^3P$) state leading to emission of $\lambda = 844.6$ nm for constant pressure and varying voltage. Similar to figure 10.1, the excitation image shown covers 30 mm of the discharge gap over one full RF cycle on a common false colour scale. Additional phase resolved excitation for all three examined excited states can be found in appendix B.

For low driving voltages ($V_{rf} \leq 400$ V) the dominant excitation takes place during the sheath expansion phase. At 200 V (figure 10.2(a)), sheath expansion excitation is virtually the only excitation process. Increasing the voltage amplitude from 200 V to 300 V (figure 10.2(b)) seems to increase the amplitude of the sheath expansion excitation, but also increases the excitation contribution from secondary electrons. This is due

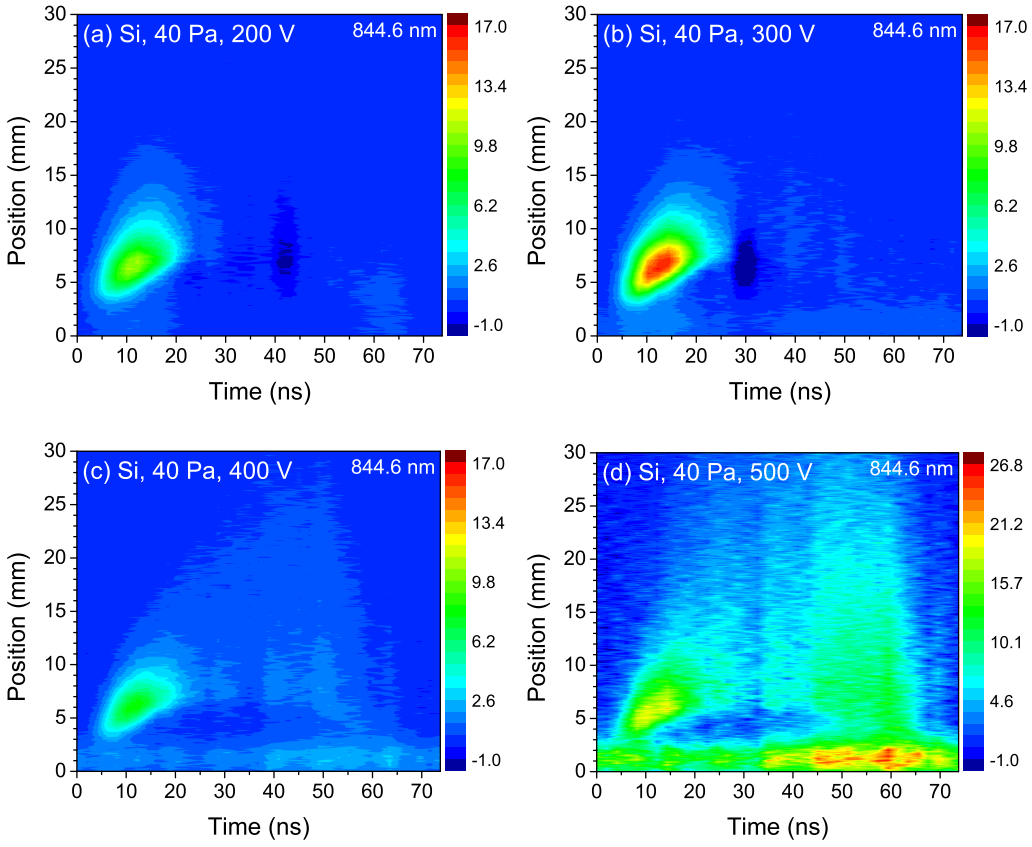

Figure 10.2.: Comparison of excitation into the O($3p^3$P) state leading to emission of $\lambda = 844.6$ nm for constant pressure and varying voltage (a) 200 V, (b) 300 V, (c) 400 V, and (d) 500 V. ($p = 40$ Pa, 98% O_2, 2% Ar)

higher electric fields that lead to an increase of ion energies. The contribution to excitation from secondary electrons becomes more pronounced when increasing the voltage further (figure 10.2(c)). In this case, the excitation through secondary electrons reaches much deeper into the plasma bulk. Furthermore, the maximum amplitude of sheath expansion excitation does not change, but appears to take place closer to the powered electrode, which indicates a smaller sheath thickness. Over the full phase of the RF cycle, a distinct excitation feature is observed near the electrode. This excitation feature is weakly modulated in time, exhibiting a maximum during the sheath collapse phase and can be attributed to heavy particle excitation. Since the ion flux is permanently directed towards the electrode, ions can gain enough energy to excite molecules and atoms or to produce fast neutrals by charge transfer collisions, which in turn can excite other particles [161]. Increasing the voltage to 500 V (figure 10.2(d)) further increases the excitation

from heavy particles, but also the contribution from secondary electrons and the sheath collapse phase, whereas excitation during the sheath expansion phase does not change significantly after reaching its maximum at about 300 V.

For a constant voltage, but changing pressure, the excitation mechanisms are governed differently. Figure 10.3 shows a comparison of excitation into the O($3p^3P$) state leading to emission of $\lambda = 844.6$ nm for constant voltage and varying pressure on a common false colour scale.

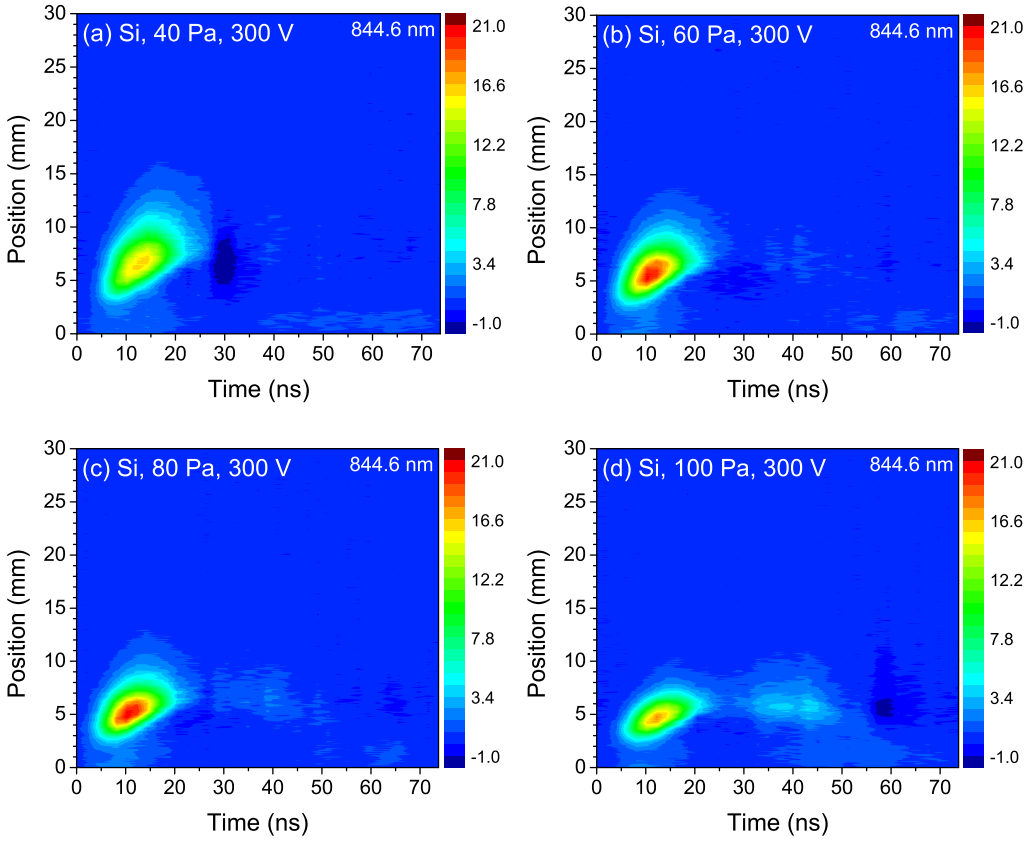

Figure 10.3.: Comparison of excitation into the O($3p^3P$) state leading to emission of $\lambda = 844.6$ nm for constant voltage and varying pressure (a) 40 Pa, (b) 60 Pa, (c) 80 Pa, and (d) 100 Pa. ($V_{rf} = 300$ V, 98% O_2, 2% Ar)

On the given colour scale, it seems that independent of pressure no excitation takes place during the sheath collapse phase. Sheath expansion excitation on the other hand is clearly the dominant excitation mechanism. With increasing pressure, the plasma becomes more collisional and this has two consequences for the excitation dynamics. Firstly, sheath expansion excitation starts taking place closer to the powered electrode

because the sheath thickness decreases. Secondly, secondary electrons cannot reach as far into the plasma as at lower pressures because, once they leave the sheath region, they undergo more collisions during the same time, so that they lose their excitation energy quicker. Furthermore, the pronunciation of the sheath expansion excitation decreases and excitation through secondary electrons gains in dominance. This is because the higher pressure supports electron avalanches in the sheath region, leading to a so called sheath breakdown [162].

10.2. Comparison with Simulations to Determine Surface Parameters

The determination of the surface condition from excitation dynamics is demonstrated by observing the atomic oxygen emission line at $\lambda = 844.6$ nm using two independent methods. Firstly, PROES is applied to obtain the spatio-temporal emission from which the phase resolved excitation is calculated and correlated both qualitatively and quantitatively with the numerical simulations. Secondly, only the temporal evolution of the emission is considered from which the excitation function is calculated and subsequently used to obtain the frequency resolved excitation spectrum. The frequency spectrum is then likewise compared to numerical simulations to derive the actual surface condition. In the simulations, only dissociative excitation is taken into account, because this is known to be the dominant excitation processes under the investigated conditions [33, 143]. As wafer materials silicon and Teflon are chosen because they entail strongly diverse excitation dynamics.

10.2.1. Surface Parameters from PROES Measurements

For the same operational conditions, only the surface parameters are varied in the model to find the best match between simulation and experiment. Hence, a variation of the SDO surface loss probability and the secondary electron emission coefficient is conducted for equal pressure, voltage and ambient temperature settings. Figure 10.4 shows the measured excitation of the $\lambda = 844.6$ nm optical emission line along the radial centre axis of the discharge on a normalised false colour scale and the best-fit simulated exci-

tation pattern, for two different wafer materials, namely silicon and Teflon. Please note that figure 10.4 only shows the lower part (0 mm−25 mm) of the total discharge gap of 40 mm to facilitate the comparison.

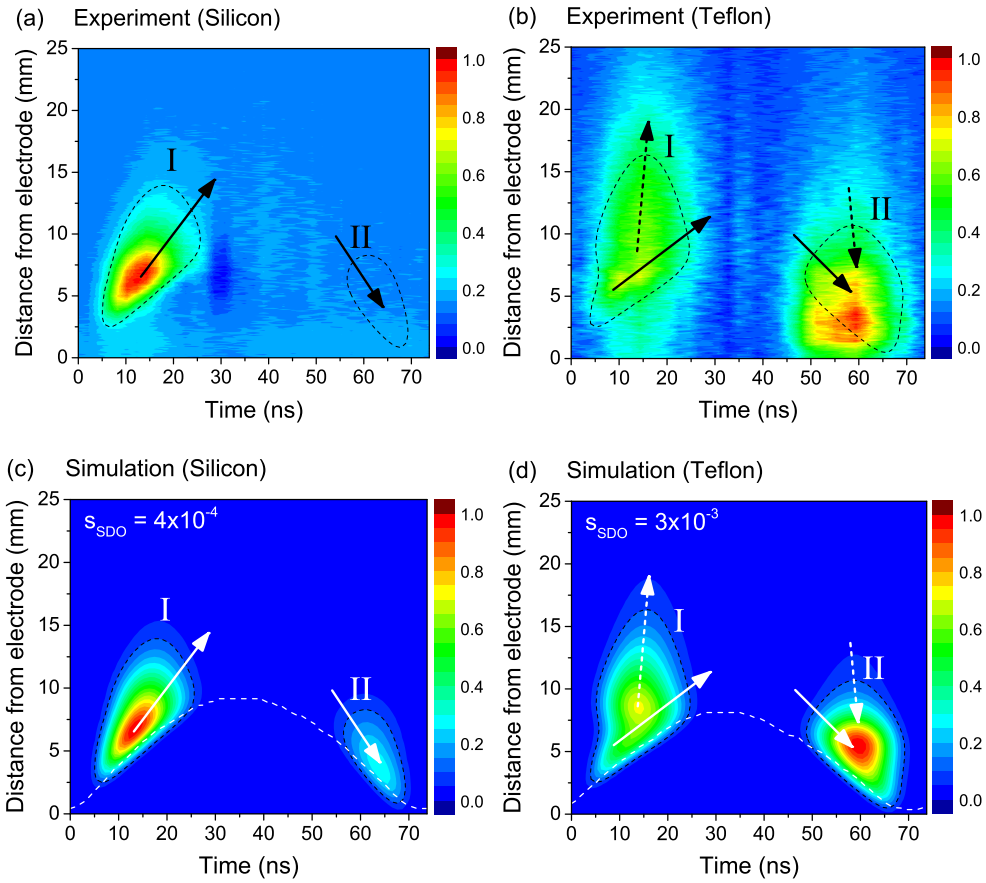

Figure 10.4.: Phase and space resolved excitation ($\lambda = 844.6$ nm) obtained experimentally for (a) silicon and (b) Teflon as wafer materials; (c) and (d) are corresponding simulations matching the experimental observation. Black dashed contour lines indicate the shape of the simulated excitation features. White dashed lines indicate the sheath edge positions. ($p = 40$ Pa, $V_{rf} = 300$ V)

For both wafer materials, there is a very good agreement both qualitatively in position and shape, and quantitatively between simulation and experiment for excitation features I and II. In particular, the weighting of the two excitation features during the sheath expansion and sheath collapse phases, apart from their individual spatio-temporal shapes, strongly depends on the SDO surface loss probability. For low SDO surface loss probability the dominant excitation takes place during the sheath expansion phase (feature

I). With increasing SDO surface loss probability the amplitude of the sheath expansion feature (I) remains almost constant, while the sheath collapse feature (II) becomes more pronounced. This trend reflects an increased global electronegativity and explains a correspondingly deeper extension of the excitation features into the plasma bulk [139, 140].

The simulation matching the experimental observation for the silicon wafer indicates a relatively low SDO surface loss probability ($s_{SDO} = 4 \times 10^{-4}$), which corresponds to a SDO content of 4.4% and an electronegativity of *en* = 2.95. For Teflon as wafer material the best match results in a SDO surface loss probability of $s_{SDO} = 3 \times 10^{-3}$, which is almost one order of magnitude higher than for the silicon wafer. Thereby, the SDO content is pushed down to less than 1% and the discharge becomes more electronegative (*en* = 12.3). The secondary electron emission coefficient can be identified to be about zero in both cases, because the input power is relatively low. From this follows that Teflon appears to be much more efficient in destroying SDO than silicon.

Furthermore, arrows indicating the expansion velocity of the excitation features in figure 10.4 are shown. In the case of an increasing SDO surface loss probability the sheath expansion excitation (I) takes place on different timescales (different gradients of arrows in figure 10.4(d)). This can be explained due to the increased electronegativity and hence, a higher electric field in the bulk [49, 163, 164]. In these high electric fields in the quasi-neutral bulk, electrons are significantly accelerated enhancing excitation in this region. The same applies for the sheath collapse phase (II), where a stronger electric field reversal can be identified due to the higher electronegativity [165].

10.2.2. Surface Parameters from Excitation Frequency Spectrum

To obtain the frequency spectrum of the excitation dynamics, first the temporal evolution of the excitation function needs to be obtained. This is done by averaging the phase resolved excitation over space.

Figure 10.5 shows the normalised excitation functions resulting from the observed optical emission line $\lambda = 844.6$ nm for silicon and Teflon and the matching simulations, respectively.

In the case of the silicon wafer (figure 10.5(a)), the simulated excitation function matches the experimentally obtained excitation function perfectly for the sheath expan-

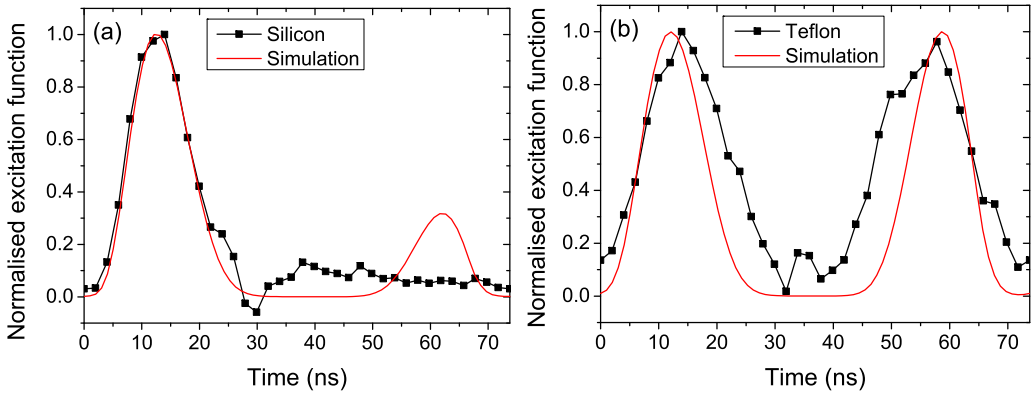

Figure 10.5.: Normalised excitation functions resulting from the observed optical emission line $\lambda = 844.6$ nm for (a) silicon and (b) Teflon and the matching simulations. ($p = 40$ Pa, $V_{rf} = 300$ V)

sion excitation feature in the beginning of the RF cycle. For later times, virtually no excitation is observed experimentally, whereas the simulation predicts a distinct sheath collapse excitation feature. This discrepancy might be a result of an overestimated electron flux towards the surfaces in the numerical simulations. However, the particle interaction and fluxes in the vicinity of the surface can only be described properly in the frame of a fully-kinetic model, which would require a computational effort far beyond the needs of the presented fluid model approach. Furthermore, additional excitation and de-excitation processes and their possible influence on the excitation function are not taken into account in the simulations. It seems that the applied model is able to describe the sheath expansion excitation properly, but is inadequate for the sheath collapse excitation.

In the case of Teflon (figure 10.5(b)), the simulation matches both the sheath expansion excitation as well as the sheath collapse excitation very good qualitatively. Nevertheless, the experimentally obtained excitation function seems to be broader than the simulated, which indicates additional excitation processes not accounted for in the model.

The conversion of the excitation functions into their frequency spectrum is achieved via Fast Fourier Transformations. Figure 10.6 shows a direct comparison of simulated and experimentally obtained frequency components of the excitation as multiples of the angular frequency ω. To demonstrate the applicability of this method over the full simulated SDO surface loss probability range, results for three different wafer materials,

namely silicon, Telfon, and stainless steel are presented.

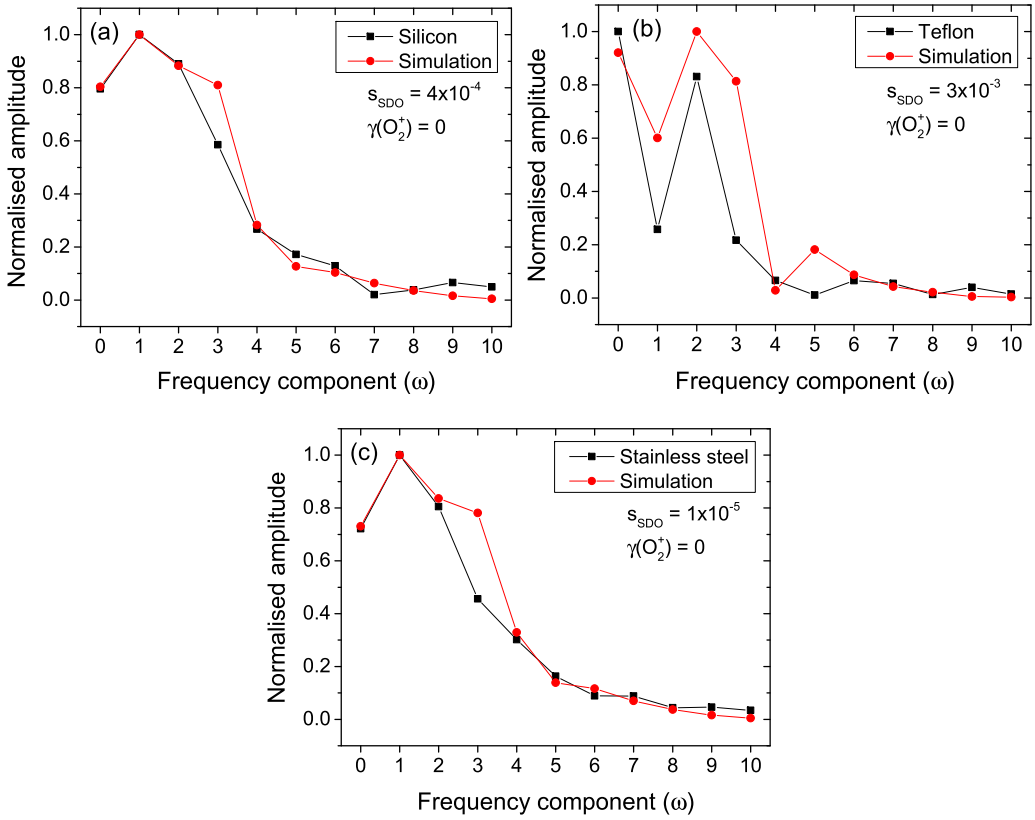

Figure 10.6.: Simulated and experimentally obtained frequency components (multiples of the angular frequency ω) of the excitation rate for the wafer materials (a) silicon, (b) Telfon, and (c) stainless steel.

Generally, the simulation matches the experiment very well regarding the amplitude distribution of the different frequency components. Especially for silicon and stainless steel wafers, the simulation quantitatively matches the experiment for a given set of SDO surface loss probability and secondary electron emission coefficient, apart from the 3rd harmonic. The 3rd harmonic seems to be majorly responsible for the contribution of sheath collapse excitation, hence leading to the observed discrepancy between experiment and simulation.

For silicon (figure 10.6(a)) and stainless steel (figure 10.6(c)) the driving frequency component (1st harmonic) has the highest contribution, indicating that the sheath expansion excitation is the dominant excitation process.

In the case of Teflon (figure 10.6(b)), the discrepancy between simulation and exper-

iment appears to be higher. However, the qualitative trend is well described by the simulation, showing that the dc component and 2nd harmonic have the highest contributions.

Due to the high sensitivity of the frequency components on the actual surface condition, it is possible to identify the surface parameters better than via PROES measurements alone. From the best matches between simulation and experiment, it follows that the metallic and dielectric wafers seem to be less reactive with SDO than Teflon and silicon, exhibiting SDO surface loss probabilities $s_{SDO} \leq 2 \times 10^{-4}$.

Table 10.2 gives an overview of the determined SDO surface loss probabilities for all investigated materials.

Table 10.2.: Overview of determined SDO surface loss probabilities.

Wafer material	SDO surface loss probability
Stainless Steel	1×10^{-5}
Tungsten	1×10^{-5}
Aluminium	6×10^{-5}
Gold	6×10^{-5}
SiO_2	1×10^{-4}
Glass	1×10^{-4}
Copper	2×10^{-4}
Silicon	4×10^{-4}
Teflon	3×10^{-3}

Stainless steel and tungsten have the lowest SDO surface loss probabilities ($s_{SDO} = 1 \times 10^{-5}$), which corresponds to a relatively high SDO content of 14.8% and a low electronegativity of 1.2. This is in very good agreement with independent research work in similar plasma systems [112, 120].

Aluminium and gold can be identified to exhibit a SDO surface loss probability of $s_{SDO} = 6 \times 10^{-5}$. The SDO surface loss probability for SiO_2 and glass can be estimated as $s_{SDO} = 1 \times 10^{-4}$, while it is slightly higher in the case of the copper wafer ($s_{SDO} = 2 \times 10^{-4}$) and silicon ($s_{SDO} = 4 \times 10^{-4}$). Teflon shows the highest SDO surface loss probability of all materials ($s_{SDO} = 3 \times 10^{-3}$).

These determined SDO surface loss probabilities should be regarded critically since they are discharge and geometry specific values. To obtain more accurate values all

chamber walls would need to be coated in the same material.

Regarding the secondary electron emission coefficient directly determined from the coupling of simulations and experiments, only aluminium can be attributed a secondary electron emission coefficient ($\gamma_{O_2^+} = 0.01$) for $p = 40$ Pa and $V_{rf} = 300$ V, while it appears to be zero for all other investigated materials under these conditions. This is in contradiction to the estimated secondary electron emission coefficients shown in table 10.1 and measured values in [68, 166] and references therein. However, this can be explained by the fluid modelling limitations of treating secondary electrons not as separate fluid species, so that the qualitative determination method of the secondary electron emission coefficients, presented in section 10.1, seems to be a more reliable approach in the context of measurements from other groups. Nevertheless, the estimated secondary electron emission coefficients in this work should be regarded as first approximation only, because it is known that secondary electron emission can vary substantially with surface morphology, incident ion energy, and incident angle [166].

11. Oxygen Dissociation Degree using Advanced Actinometry

In this chapter, advanced actinometry is used to determine the chemically active radical species atomic oxygen and local electron energies for an industrially relevant oxygen plasma discharge over a variety of wafer materials.

Initial measurements are conducted at the discharge centre under variation of the voltage and pressure. It is found that local electron energies increase with voltage but decrease with increasing pressure. Furthermore, atomic oxygen densities generally increase with increasing pressure and voltage, however can undergo fluctuations induced by negative ions. Differences when using varying wafer materials are attributed to their atomic oxygen surface loss probabilities.

Although, the radial emission profile from the plasma discharge is highly inhomogeneous, the radial spatial distribution of electron energies and atomic oxygen is homogeneous over most of the wafer surface. At the wafer and electrode edge it is found that electron energies increase due to enhanced electric fields, whereas atomic oxygen densities decrease. A transition from an α-mode to a γ-mode discharge evokes the atomic oxygen density to form a peaked density profile with the central density about one order of magnitude higher than near the wafer edge.

11.1. Local Atomic Oxygen Densities

Advanced actinometry, as described earlier, is implemented to quantify local atomic oxygen densities and electron energies by comparing experimentally obtained excitation ratios of the 750.4 nm Ar I, 777.4 nm O I, and 844.6 nm O I optical emission lines with simple kinetic simulations.

Only maximum excitation during the sheath expansion phase along the central discharge axis is considered to minimise errors, thereby localising the determination of

atomic oxygen densities and electron energies in the spatial and temporal domains. Since atomic oxygen is not modulated within a RF cycle the determined local atomic oxygen densities can be regarded in first approximation as average values. However, the electron energy is strongly modulated on the RF timescale so that the obtained energy values are to be regarded critically. The numerical simulations suggest that the energy during maximum excitation is higher than the average bulk energy. Hence, using advanced actinometry an upper limit for the bulk electron energy can be estimated.

Due to calibration the determined absolute values are subject to errors of at least 10%, in addition to the uncertainty in the used cross section data.

Figure 11.1 shows the simulated excitation ratios for selected dissociation degrees and the experimentally determined excitation ratios for maximum excitation under variation of driving voltage and pressure, respectively. The investigated wafer material is silicon. The voltage variation is conducted beginning at 200 V, subsequently increasing the voltage in 100 V steps up to 500 V, while the investigated pressure range is $20 - 100$ Pa, varied in 20 Pa steps.

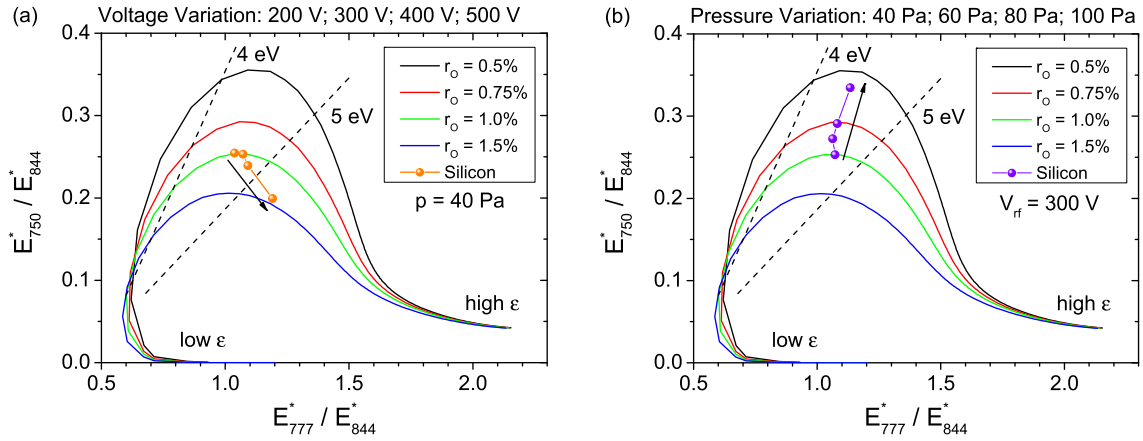

Figure 11.1.: Experimentally determined maximum excitation ratios (symbols) under variation of (a) driving voltage ($p = 40$ Pa) and (b) pressure ($V_{rf} = 300$ V); arrows indicate the direction of parameter increase. Solid lines represent simulated excitation ratios for varying dissociation degree and electron energy. Dashed lines show a change in dissociation degree for constant energy values.

The abscissa is the ratio of excitation leading to emission of the $\lambda = 777.4$ nm and $\lambda = 844.6$ nm optical emission lines and the ordinate is the ratio of excitation leading to emission of the $\lambda = 750.4$ nm and $\lambda = 844.6$ nm optical emission lines. Dashed lines in

figure 11.1 represent a dissociation degree change under equal electron energy, whereas the energy increases from left (low ϵ) to right (high ϵ) for any given dissociation degree.

From figures 11.1(a) and 11.1(b) values for the electron energies and dissociation degrees under voltage and pressure variation can be easily extracted.

For electron energies at maximum excitation, it follows that on the one hand, they increase with increasing voltage from 4.5 eV at 200 V to about 5.7 eV at 500 V. This trend is equally obtained in the numerical simulations and most likely corresponds to an increase of the non-weighted electron energies, as shown in figure 4.8(a). However, the absolute values of the electron energies at maximum excitation in the simulations are slightly higher than the measured energies. On the other hand, a pressure increase evokes a subsequent decrease of electron energies from 4.6 eV at 20 Pa to 4.3 eV at 100 Pa, which is also in good agreement with the numerical simulations. Hence, the bulk energy level is believed to lie below the determined upper limit at approximately 3 eV$-$4 eV, as predicted by the simulations earlier (see figure 7.3).

The other investigated materials show very similar energy dependencies, excluding Teflon, which exhibits the lowest energy of 3.9 eV at maximum excitation.

The extracted dissociation degree in dependence of the pressure is exemplarily shown in figure 11.2 for three different surface materials, namely, silicon, SiO_2, and tungsten, as typical examples for a semiconductor, dielectric, and metal. The driving voltage is kept constant at 300 V.

SiO_2, as dielectric material, has the highest dissociation degree of the three materials shown starting with about 1.2% at 40 Pa and gradually decreasing to 0.9% at 100 Pa. Teflon shows an even higher dissociation degree of 1.5% at 40 Pa while glass behaves very similar to SiO_2. A slightly lower dissociation degree shows the semiconductor wafer starting at 1.0% and decreasing to about 0.6%, whereas the tungsten and the other metallic wafers exhibit a further overall smaller dissociation degree than silicon by approximately 0.1 percentage points.

The dependence of the dissociation degree on the properties of the surface material seems evident. A possible explanation is that the atomic oxygen surface loss probability is strongly dependent on the surface material, indicating that dielectric materials have a lower atomic oxygen surface loss probability than semiconducting and metallic materi-

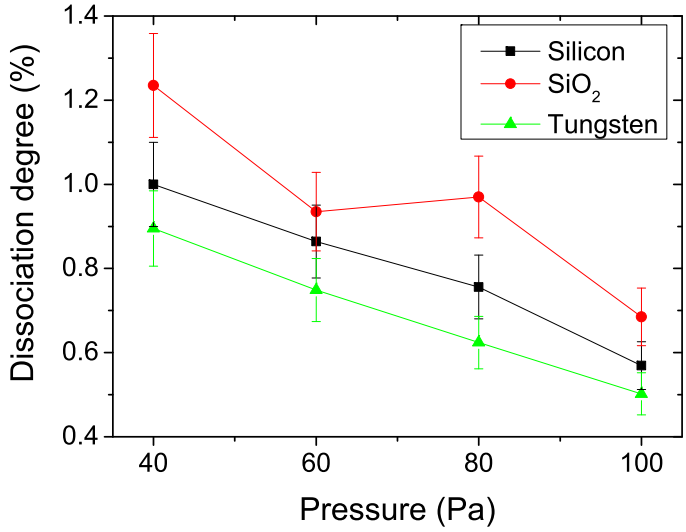

Figure 11.2.: Dissociation degree as a function of pressure for different wafer materials. (V_{rf} = 300 V, 98% O_2, 2% Ar)

als. This assumption can be confirmed considering reported atomic oxygen surface loss probabilities in the literature of $\approx 10^{-4}$ for Pyrex glass [167], 1.8×10^{-4} for Quartz [168], and 0.5 for stainless steel [169]. However, these values should be regarded critically since the atomic oxygen surface loss probability has been found to decrease over linearly with increasing pressure [170].

Although, the dissociation degree decreases approximately linearly with increasing pressure the actual atomic oxygen density increases with pressure, as shown in figure 11.3. A similar observation of the pressure dependence of the atomic oxygen density was made by Katsch *et al.* [34] using two-photon absorption laser-induced fluorescence (TALIF) in a CCP GEC reference cell with 25 mm discharge gap.

A similar hierarchy can be observed in figure 11.3 as before, where SiO_2 evokes the highest and tungsten the lowest atomic oxygen densities. At high pressures (100 Pa), the atomic oxygen density seems to saturate or even decrease. This might be due to a balance of production and destruction processes for atomic oxygen. The increasing background gas density is the main source of atomic oxygen through direct electron-impact dissociation. Thus, the observed change in atomic oxygen densities may be a result of changing electron properties of over proportionally increasing wall losses and recombination with negative and positive ions.

The determined absolute atomic oxygen densities are in good agreement with litera-

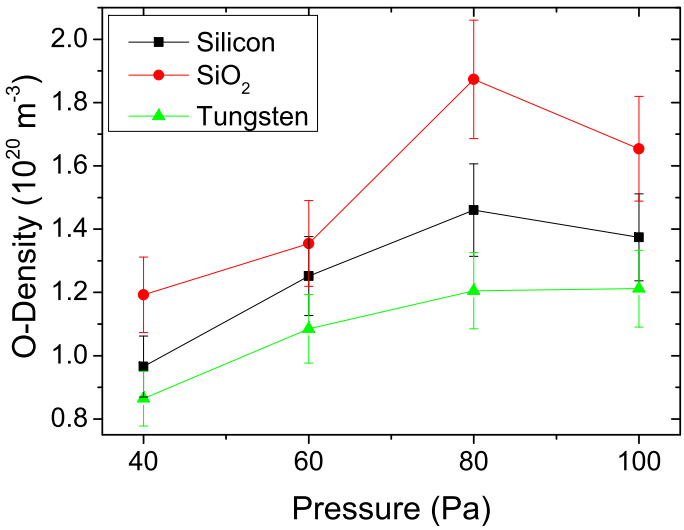

Figure 11.3.: Atomic oxygen density as a function of pressure for different wafer materials. ($V_{rf} = 300$ V, 98% O_2, 2% Ar)

ture [100, 171] considering the differences in system geometry and power coupling.

The voltage dependency of the dissociation degree and atomic oxygen density at constant pressure (40 Pa) is shown in figure 11.4.

Generally, the atomic oxygen density increases with increasing voltage, because the electron density increases, thus enhancing the production of atomic oxygen through direct electron-impact dissociation of the background gas oxygen. However, the gradients are different for the investigated wafer materials. Silicon and tungsten both show a monotonic increase, with the latter exhibiting a steeper gradient. At high voltages, more secondary electrons are released so that the electron density increases over linearly, thereby entailing an over linear increase of atomic oxygen. Since the estimated work functions, which are responsible for the secondary electron emission coefficient, are similar for the materials shown, the determined atomic oxygen densities at high voltages are also similar. Atomic oxygen surface losses on the other hand seem not to play a dominant role in the variation of the atomic oxygen density. This assumption can be verified by measuring the atomic oxygen density for an aluminium wafer, which has a similar surface loss probability as silicon for 40 Pa [170]. Aluminium is known to have the lowest work function of all investigated materials, thus the highest secondary electron emission coefficient. As expected, this results in a 30%−50% higher atomic oxygen density at 500 V driving voltage than for materials with higher work functions.

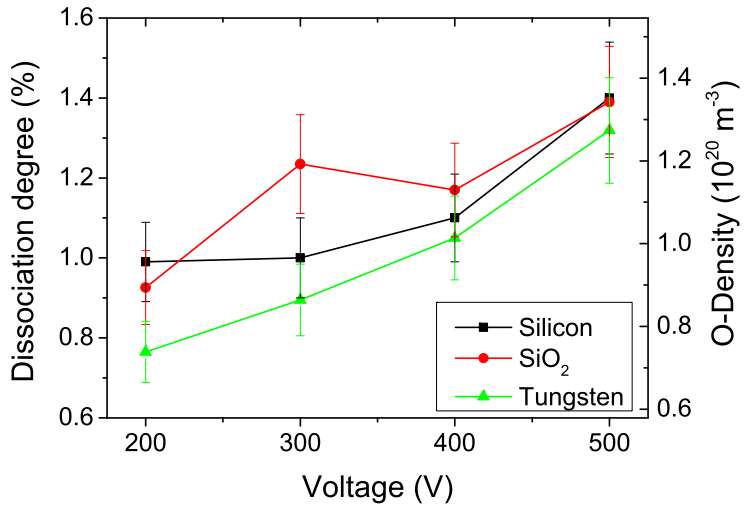

Figure 11.4.: Dissociation degree and atomic oxygen density as a function of voltage for different wafer materials. (p = 40 Pa, 98% O_2, 2% Ar)

SiO_2 shows a rather surprising behaviour, where the atomic oxygen density first increases with voltage, then goes through a minimum at 400 V before increasing again. Atomic oxygen densities determination using glass, copper, aluminium, and gold wafers shows a similar voltage dependency as SiO_2. Analogous observations have been reported and attributed to an attachment-induced ionisation instability due to considerable formation of negative ions [119]. If the attachment rate coefficient increases more strongly than the ionisation rate coefficient with T_e and if electron and negative ion densities are of the same order of magnitude, a small increase in n_e can rapidly grow via a decrease in T_e, so that the plasma becomes unstable, and electron and negative ion densities increase alternately [172].

11.2. Radial Atomic Oxygen Distribution

For industrial plasma applications not only the global reactive species densities are of importance but also their radial distribution across the wafer due to homogeneity and reproducibility requirements. Therefore, the atomic oxygen distribution across a silicon wafer is investigated using the same method as in the previous section.

For the two-dimensional measurements, optical bandpass filters are applied which are more sensitive to calibration, so that the error for absolute values is about 20%.

Figure 11.5 exemplarily shows the normalised, spectrally and angle of incidence cal-

ibrated emission across the wafer surface from the 844.6 nm optical emission line at $t = 15$ ns when the emission is maximum and the corresponding radial emission profile at 5 mm above the electrode.

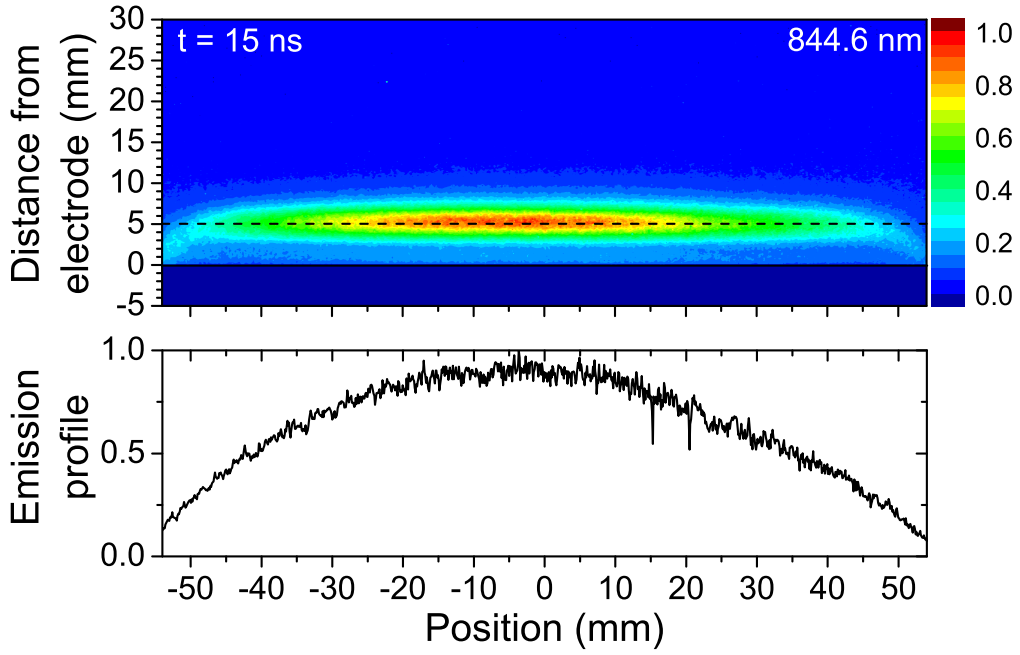

Figure 11.5.: Normalised emission across the wafer surface from the 844.6 nm optical emission line at $t = 15$ ns and corresponding radial emission profile at 5 mm above the electrode.

The asymmetry of the discharge is evident since most of the emission originates near the electrode. Furthermore, the emission is radially inhomogeneous with a inverted parabola like profile. At the wafer edge, at ± 50 mm, the emission from the plasma moves down over the edges of the electrode.

Several steps are necessary to obtain a radial distribution of the excitation ratios from which the atomic oxygen density as well as the electron energies are extracted. Firstly, the phase resolved emission is recorded with the ICCD camera, followed by the corrections for spectral sensitivity (see section 8.3.1) and angle of incidence (see section 8.3.3). Secondly, the recorded images are divided into 32 columns of equal distance and width over which the emission is averaged. Then, PROES images are created for each individual radial position. Finally, the excitation is calculated from the phase resolved emission, as described earlier, and the excitation ratios from maximum excitation are obtained. The excitation ratios are subsequently used to extract radial profiles of elec-

tron energies and dissociation degrees. However, using this method, axial profiles are not possible to obtain since only the maximum excitation is taken into account, which occurs at a specific axial distance from the electrode.

The central electron energies correspond to the measurements conducted in the previous section, ranging from 4.5 eV to 5 eV for 40 Pa under voltage variation (200 V−400 V). As shown in figure 11.6, the central energy value of 4.3 eV at 80 Pa and 300 V lies well within error of the previous measurement, in which the energy value was determined to be 4.4 eV. At higher voltages at 80 Pa, the electron energy significantly increases to about 7 eV. This can be attributed to a shift from a sheath expansion dominated excitation regime (α-mode) to a secondary electron dominated excitation regime (γ-mode).

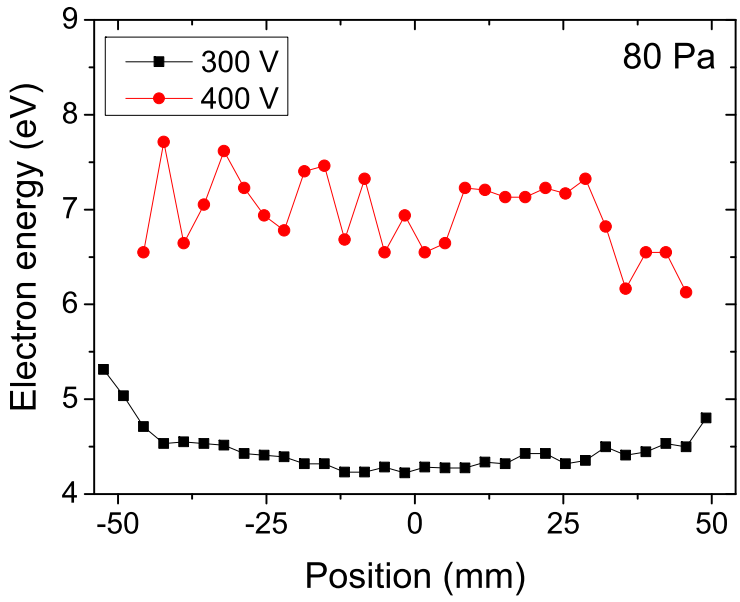

Figure 11.6.: Radial distribution of electron energy under driving voltage variation and constant pressure of 80 Pa. (98% O_2, 2% Ar)

The actual electron energy radial profile also reveals interesting insight. The profile is flat over most of the surface (±48 mm) but increases towards the edges by about 25%. This is probably due to edge effects that enhance the electric fields in the vicinity of the wafer and electrode edges, thus entailing an electron energy increase.

The atomic oxygen density profiles also exhibit distinct radial dependencies and undergo a distinct transformation, especially at increased voltages, as shown in figure 11.7.

The profiles are symmetrically distributed due to the cylindrical symmetry of the

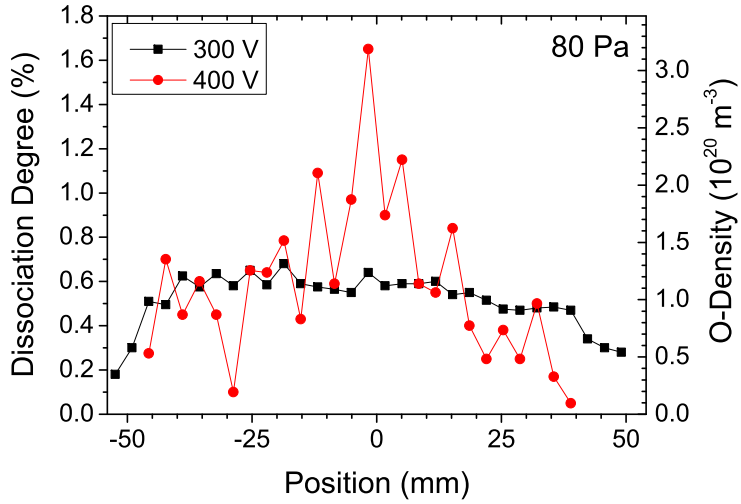

Figure 11.7.: Radial distribution of dissociation degrees and corresponding atomic oxygen densities under driving voltage variation and constant pressure of 80 Pa. (98% O_2, 2% Ar)

electrode. At 300 V, the central density value (1.20×10^{20} m^{-3}) correspond well within error to the previous measurement of 1.45×10^{20} m^{-3} (see figure 11.3).

However, at 400 V when the plasma transitions into γ-mode, the atomic oxygen density profile shows a distinct peak at the central axis position and quickly drops towards the edge. The error from this measurement is higher than the error for the lower input voltage, which seems to be counter intuitive since one would expect the signal-to-noise ratio to increase with increasing voltage because the intensity increases. As discussed earlier, increasing voltage amplitudes promote excitation through secondary electrons and heavy particles, while the sheath expansion excitation is less affected (see also figure B.1 in appendix B). As result, the total emission intensity increases and the ICCD camera exposure times is shorter for higher voltages. This decreases the effective signal-to-noise ratio for the sheath expansion phase, so that the resulting error is bigger.

Figure 11.8 shows radial atomic oxygen density profiles for two driving voltage values at constant pressure of 40 Pa.

The central density values are very close to one another at about 10^{20} m^{-3} under the conducted voltage variation, which was expected when comparing to figure 11.4. The radial profiles seem to be approximately constant over more than half of the wafer surface, with a slight convex shape. In the vicinity of the edge the density profiles steeply drop by more than 50%.

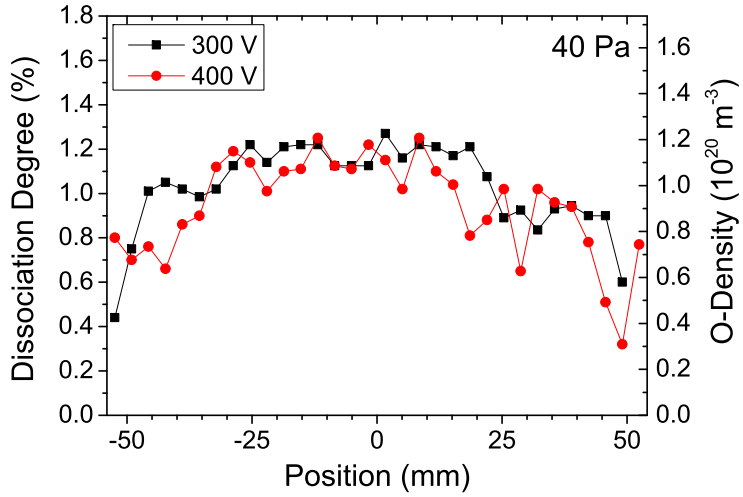

Figure 11.8.: Radial distribution of dissociation degrees and corresponding atomic oxygen densities under driving voltage variation and constant pressure of 40 Pa. (98% O_2, 2% Ar)

Nevertheless, the obtained profiles give a valuable insight on the atomic oxygen distribution within the discharge. These findings could be used in future industrial applications to tailor not only the electron energies and atomic oxygen content in a relevant plasma discharge but also their distribution across the wafer surface.

12. Conclusions

The main focus of this thesis is to combine numerical simulations with advanced ultrafast optical diagnostics to investigate the dynamics of the plasma-surface interface region in capacitively coupled radio-frequency oxygen plasmas.

The developed fluid model, with semi-kinetic treatment of electrons and an improved ion transport treatment, was in first place applied to systematically study the influence of residual oxygen on discharge dynamics in an established helium-oxygen environment for capacitively coupled radio-frequency plasmas. It was found, that independent of the actual oxygen admixture to the feed gas helium, oxygen constitutes the main dominant positive and negative ion species in the discharge due to its significantly lower ionisation threshold. Furthermore, Penning-ionisation of oxygen through helium metastables plays an important role in promoting the oxygen ion dominance. The average charged particle densities decrease with increasing oxygen admixture, but the spatial particle distribution, electronegativity and electron-impact induced ionisation pass through a maximum for an oxygen content of $5\%-10\%$. This could be attributed to an increasingly collisional plasma so that balances of particle production and destruction processes shift. Furthermore, the influence of the applied power on numerous plasma properties was discussed to establish the discharge regime and transition from an α-mode to a γ-mode discharge. The subsequent voltage-current analysis under pressure variation indicated the plasma to become more conductive, which was reflected in an increasing current density. This resulted in a change of the impedance and explained the decreasing phase between current density and voltage with increasing pressure. A critical analysis of reaction rates revealed that certain reactions can easily be neglected without exhibiting a major effect on the results.

As a consequence, the simulations were reduced to an oxygen only model to speed up computational time and to provide best possible insight into the fundamental under-

lying plasma physics. Therefore, a simplified reaction scheme including one dominant positive (O_2^+) and negative ion (O^-) species, the background gas (O_2), and electrons was considered. Additionally, the use of voltage instead of power input as preferred reference to experimental measurements was motivated. The main focus was put on modifications to the standard fluid model approach for plasma modelling and their impact on phase resolved charged particle dynamics in geometrically symmetric as well as asymmetric discharges. In particular, a correct treatment of energy dependent ion mobilities for radio-frequency plasmas was incorporated in the numerical simulations. This has been found to play a significant role in the presence of high electric fields in the interface region between plasma and surface. Ionisation dynamics caused by direct electron-impact for the non-modified and modified models were compared in the symmetric as well as the asymmetric modelling regime. In both regimes, the pronunciation of ionisation features is significantly reduced due to the modifications. In contrast to the standard modelling approach, ionisation through secondary electrons loses its dominance over ionisation in the sheath expansion phase. This is mainly a result of the improved ion mobility treatment. Furthermore, deviations in the simulated weighted ion energies are significantly dependent on the specific treatment of ion mobilities and geometry of the discharge chamber. However, the spatial distribution of particles remains generally unaffected despite any changes in the model. This makes an absolute comparison between experiments and simulations difficult, especially if access to additional optical diagnostics with which the excitation or ionisation features can be observed is limited. Although the spatial particle distribution is comparable in both model regimes, secondary electrons can only be accounted for with the introduced approximation. Despite the fact that secondary electrons are not accounted for as separate group in the standard modelling approach it has been shown that they play a major role as the dominant electron group at the electrodes affecting charged particle dynamics. Furthermore, a critical comparison to experimental and computational work from several independent groups with special regard to particle densities, particle distributions, and excitation dynamics for a range of parameters showed that the presented modified model is capable of closing the gap on the usual discrepancies between PIC and fluid simulations. This is mainly due to the modified ion mobility treatment describing more realistically the ion

kinetics, which become especially important at low pressures near the surface. Generally, a very good agreement was achieved, particularly with regard to the RF excitation dynamics. It was found that the modified model is able to decrease the lower limit of applicable pressure as opposed to the non-modified approach. It can therefore be a valuable tool in the intermediate pressure regime, where typical PIC simulations become slow and conventional fluid models fail.

With the help of the simplified oxygen model the importance of metastable singlet delta oxygen (SDO) in oxygen discharges, in particular its influence on the charged particle dynamics in the investigated parameter regime was identified. Typically, it is assumed that SDO, as a long living metastable species with a natural lifetime of 64.4 minutes, has no effect on the fast plasma dynamics within the RF cycle. However, under the investigated discharge conditions, the plasma is a detachment dominated discharge, in which SDO is the main collision partner for negative ions. As a consequence, the effective SDO lifetime decreases significantly and was determined to be ≤ 1 s, mainly driven by volume processes and the gas flow. Surface loss processes, induced by thermal flux of SDO towards the chamber walls and affected by the SDO surface loss probability, do not play a significant role for the effective lifetime. However, the SDO surface loss probability is strongly responsible for the actual equilibrium SDO content in the discharge. Although, this leads to a still long enough effective lifetime to allow a build up of significant SDO metastable densities in O_2 discharges up to 15%, SDO can actually respond to surface changes on a timescale below seconds that is likely to occur in plasma processing applications, and consequently it is important to take this into account. Despite the strong modulation of the SDO content due to the SDO surface loss probability, the electronegativity was found to also be strongly modulated. In this regard, discrepancies between simple analytical models and the presented fluid model were discussed. Exemplarily, two different SDO surface loss probability values were chosen in order to examine and compare the corresponding spatial distributions of the charged particles and the phase and space resolved ionisation. From this was deduced that the SDO surface loss probability plays an important role for plasma dynamics and can therefore be used as a first sensitive indicator for the actual surface condition under the investigated regime.

Apart from this, other physical and chemical plasma-surface interaction processes can play a vital role for determining gas-phase species concentrations and the discharge equilibrium. Therefore, a second relevant surface reaction mechanism was identified as positive ion neutralisation inducing secondary electron emission. Consequently, modelling a set of different SDO surface loss probabilities and secondary electron emission coefficients was used to gain further insight into their effects on plasma parameters and excitation dynamics and to improve understanding of these important plasma-surface interaction processes. Both processes were found to be decoupled regarding their impact on global charged particle densities as well as excitation mechanisms. Hence, providing a unique fingerprint that can be used to correlate numerical simulations to phase resolved experimental observations in order to determine the actual surface condition and draw conclusions on other relevant plasma parameters.

To verify the synergistic coupling of numerical simulations and fast optical diagnostics, a total of nine wafer materials with different characteristics have been examined in a capacitively coupled oxygen plasma with 2% argon admixture. The investigated materials were Teflon, glass, aluminium, stainless steel, tungsten, copper, 50 nm gold coating on stainless steel, n-type silicon, and 50 nm silicon dioxide coating on n-type silicon. Power-voltage characteristics followed very similar trends, regardless whether the utilised wafer consisted of a dielectric, semiconducting or metallic material. For elevated pressures a hysteresis effect was observed and surface modifications due to plasma treatment were discussed qualitatively.

From a comparison of excitation dynamics between different wafers, a first surface parameter, i.e. the surface work function, could be estimated. Further detailed analysis of general excitation dynamics behaviour under voltage and pressure variation revealed that on the one hand, a voltage increase promotes excitation through secondary electrons and heavy particles. Whereas on the other hand, a pressure increase indicated that the overall excitation decreases due to the increasing collisionality of the plasma discharge. Observing the phase resolved excitation as well as its Fast Fourier Transform and coupling them with numerical simulations has proven to enable the determination of surface parameters. With the help of both methods, of which the temporal evolution turned out to be more sensitive, an overview of the obtained SDO surface loss probabilities and

secondary electron emission coefficients as indicators of the actual surface condition for the investigated wafer materials was given. There, Teflon showed the highest probability to destroy SDO (3×10^{-3}), while stainless steel and tungsten were least effective in the destruction of SDO showing a more than two orders of magnitude lower probability (1×10^{-5}). Silicon was found to lie between Teflon and stainless steel (4×10^{-4}). The secondary electron emission coefficient was determined to be 0 at voltages below 300 V, except of aluminium (0.01), and gradually increased with increasing voltage.

For the determination of the important chemically active radical species atomic oxygen and local electron energies for industrially relevant oxygen plasma discharges, the use of an advanced actinometry approach was motivated. It takes direct electron-impact excitation into the argon $Ar(2p_1)$ state and the oxygen $O(3p^5P)$ and $O(3p^3P)$ states as well as dissociative excitation into the two latter states into account. In this context, electron-impact excitation is responsible for the creation of transient excited states and through the subsequent optical emission, and associated temporal evolution, distinct atoms and molecules can be identified. The power and sensitivity of this method originates from exploiting both the energy dynamics as well as the population dynamics in the non-linear plasma-surface interface region. With the help of simple kinetic simulations the corresponding population dynamics can be calculated and used to obtain the ratios of the effective excitation rates. However, advanced actinometry is only applicable when the population of an excited state reaches its maximum. In this regard, the resulting local electron energy gives an estimation for the upper limit of the mean electron energy, while the atomic oxygen density can be regarded as absolute value.

Initial measurements, conducted at the discharge centre under variation of the voltage and pressure, showed that local electron energies increase with voltage but decrease with increasing pressure. Although the absolute local electron energies varied for the different investigated wafer materials, they stayed in approximately the same range of 4.5 eV$-$6 eV. This was in very good agreement with the simulations that predicted a mean electron energy in the range of 4 eV. Furthermore, atomic oxygen densities were found to generally increase with increasing pressure and voltage, however can undergo attachment-induced ionisation instabilities due to considerable formation of negative ions. Differences using varying wafer materials are attributed to their atomic

oxygen surface loss probabilities. Generally, metallic wafers were found to have the highest atomic oxygen surface loss probabilities, followed by semiconducting and dielectric wafers. Therefore, the resulting atomic oxygen densities were in the range of $(0.8 - 2.0) \times 10^{20}$ m^{-3}.

Subsequent spatially resolved measurements revealed that the radial emission profile from the plasma discharge is highly inhomogeneous. Nevertheless, the radial spatial distribution of electron energies and atomic oxygen is homogeneous over most of the wafer surface. At the wafer and electrode edge electron energies were found to increase due to enhanced electric fields, whereas atomic oxygen densities decreased. Furthermore, a clear transition from an α-mode to a γ-mode discharge promoted a central peak of the atomic oxygen density to form with the density near the wafer edge about one order of magnitude lower than at the centre.

Conclusively, the demonstrated synergistic coupling of numerical simulations and phase resolved optical emission spectroscopy measurements, presented in this thesis has been proven to be capable of enabling the determination of important surface parameters as well as measurement of important reactive species such as atomic oxygen in industrially relevant plasma discharges. This will not only provide more accurate results from the simulations, but also give the opportunity to create spatially resolved maps of atomic oxygen in different chemical environments. This information can then be used to obtain optimal experimental conditions under which the production of atomic oxygen as main radical species can effectively be tailored.

For future research, it would be interesting to show the applicability of the demonstrated experimental methodology for a range of different plasma sources. Here, high pressure or atmospheric discharges, used for surface modifications or medical applications, are of same interest as ultra-low pressure discharges, mainly implemented in industrial tools for plasma surface processing. Particularly, extremely low pressure discharges are of interest because there the presented fluid modelling approach is known to fail. Nevertheless, due to the understanding gained of the mutual dependence of surface condition and plasma dynamics, those complex discharges could now be described better and important *in-situ* measurements of surface condition and radical species densities could be conducted.

A. Relevant Energy Levels of Oxygen and Argon

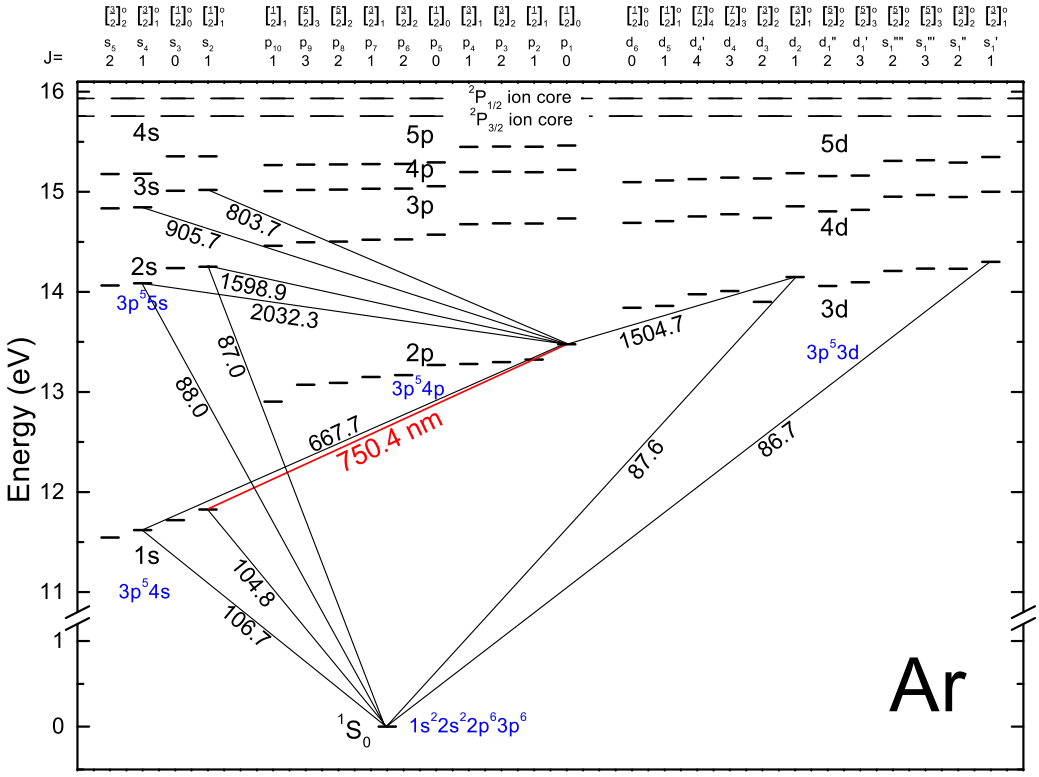

Figure A.1.: Energy levels of Ar I [173].

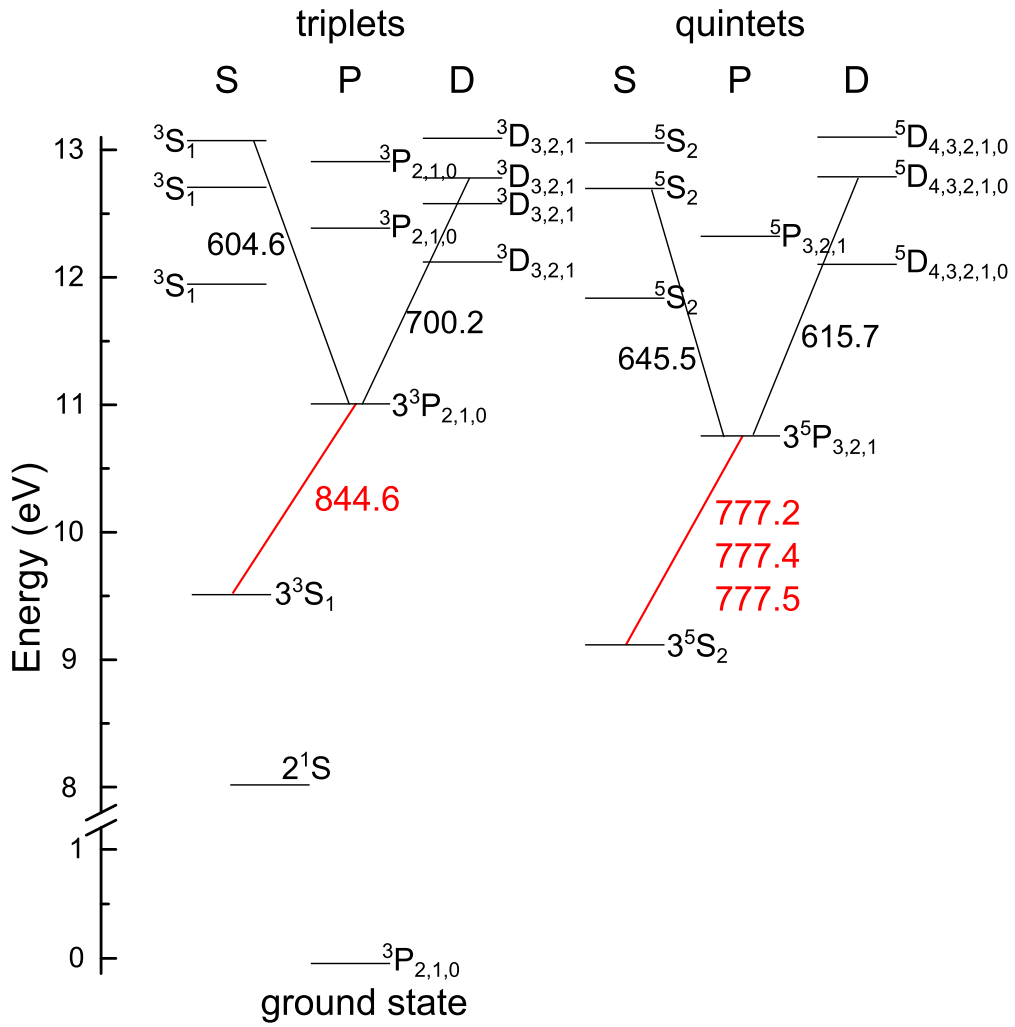

Figure A.2.: Energy levels of O I [174, 175].

B. Additional Excitation Profiles

For the two industrially most relevant wafer materials, silicon and silicon dioxide, all obtained phase resolved excitation rates will be illustrated under voltage and power variation for the sake of completeness. Please note, that although the observations are qualitatively the same, the quantitative differences lead to individually unique surface parameters, electron energies and atomic oxygen densities as determined in the course of this thesis.

- Silicon (Si) wafer: Voltage variation

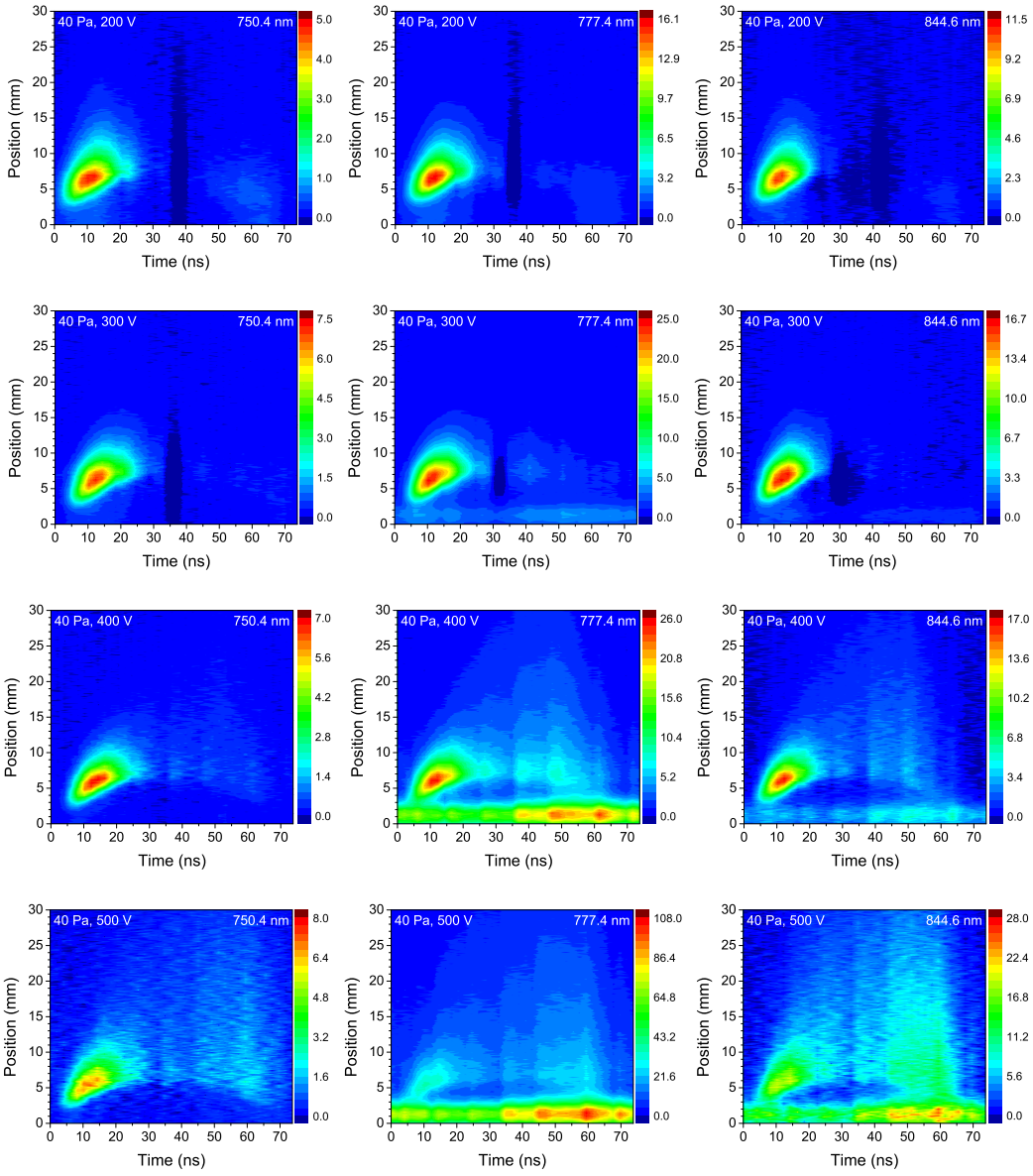

Figure B.1.: Phase resolved excitation into the Ar($2p_1$), O($3p^5P$), and O($3p^3P$) states using a silicon (Si) wafer under voltage variation.

- Silicon (Si) wafer: Pressure variation

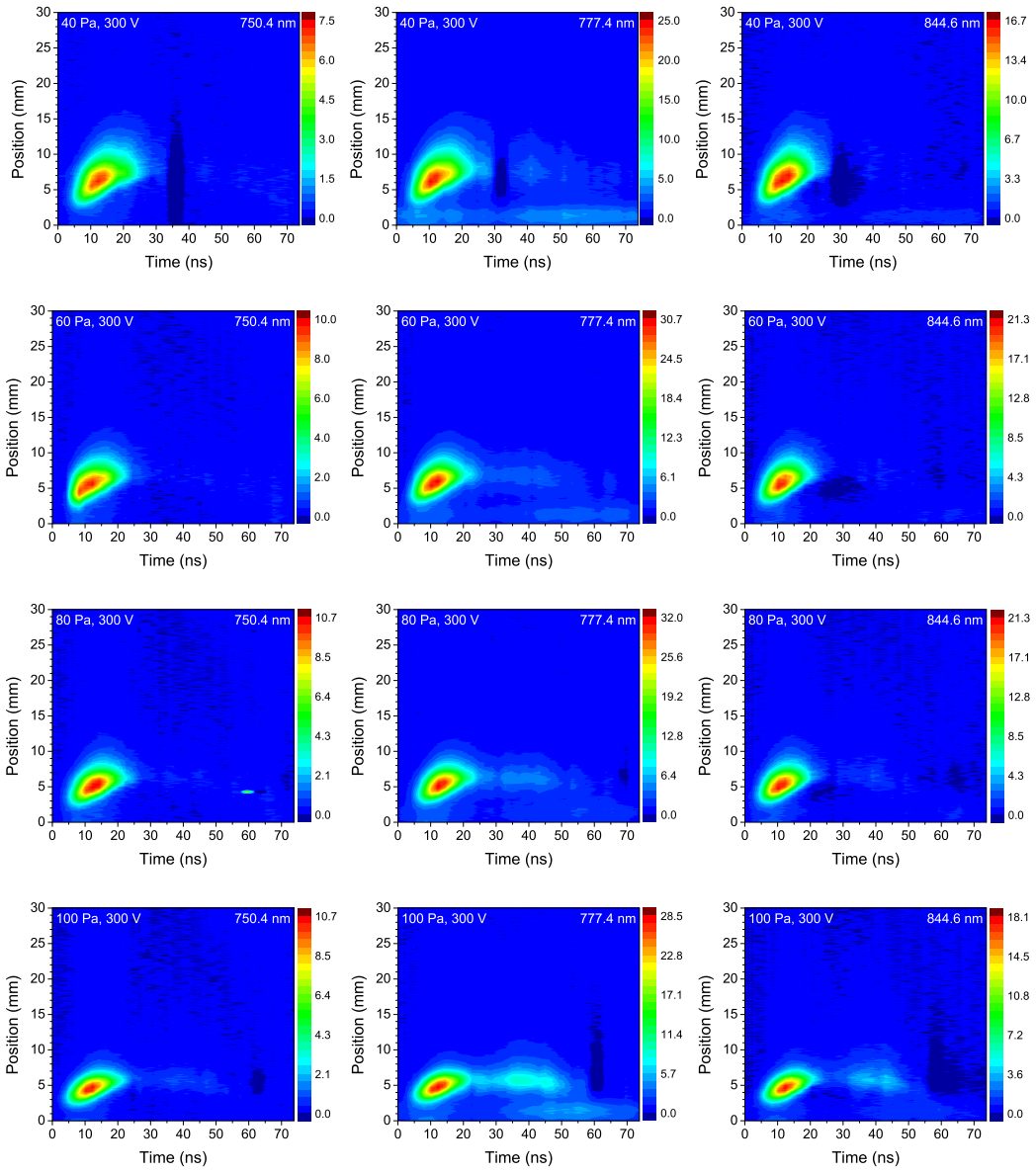

Figure B.2.: Phase resolved excitation into the $Ar(2p_1)$, $O(3p^5P)$, and $O(3p^3P)$ states using a silicon (Si) wafer under pressure variation.

- Silicon dioxide (SiO_2) wafer: Voltage variation

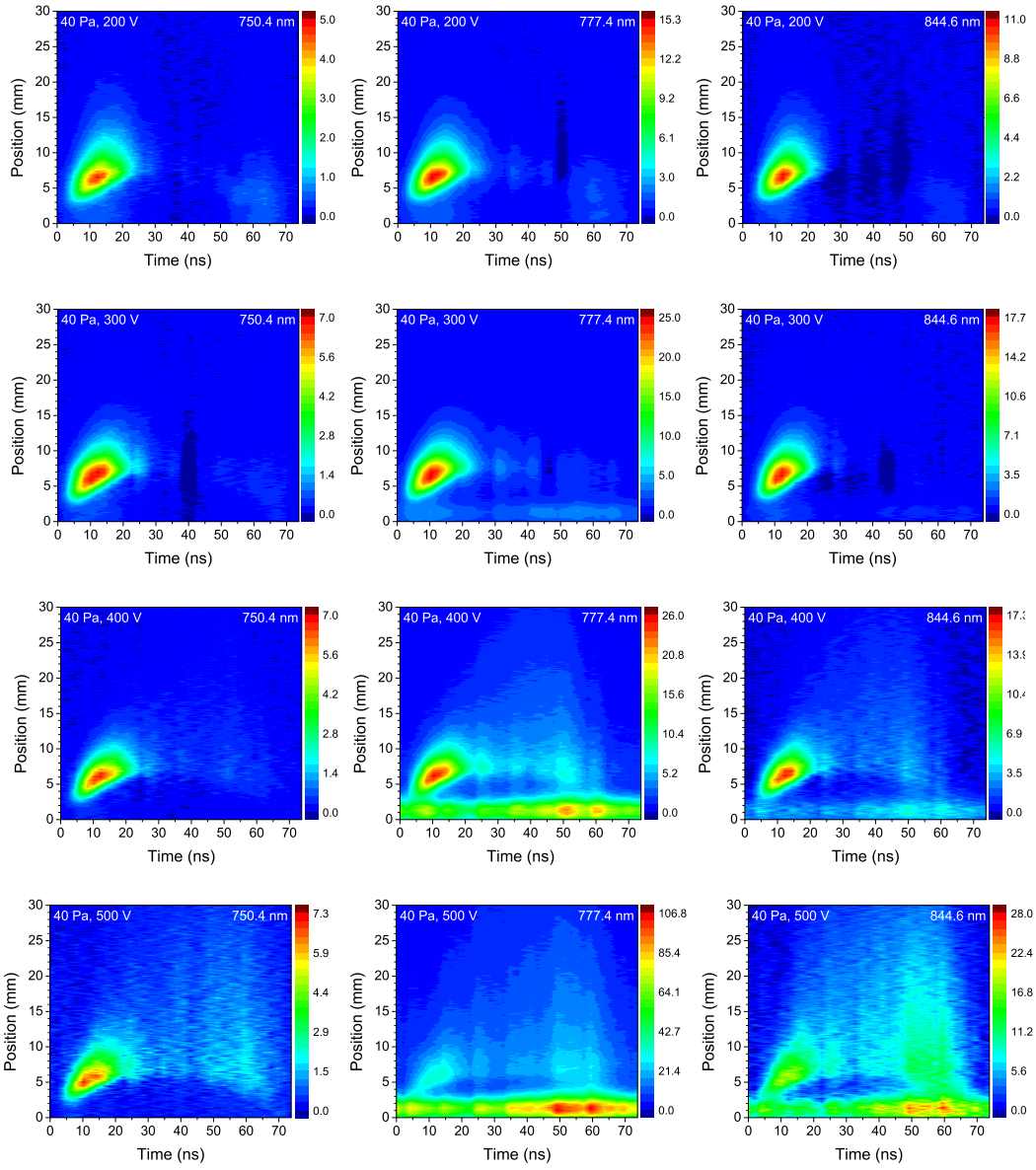

Figure B.3.: Phase resolved excitation into the $Ar(2p_1)$, $O(3p^5P)$, and $O(3p^3P)$ states using a silicon dioxide (SiO_2) wafer under voltage variation.

- Silicon dioxide (SiO_2) wafer: Pressure variation

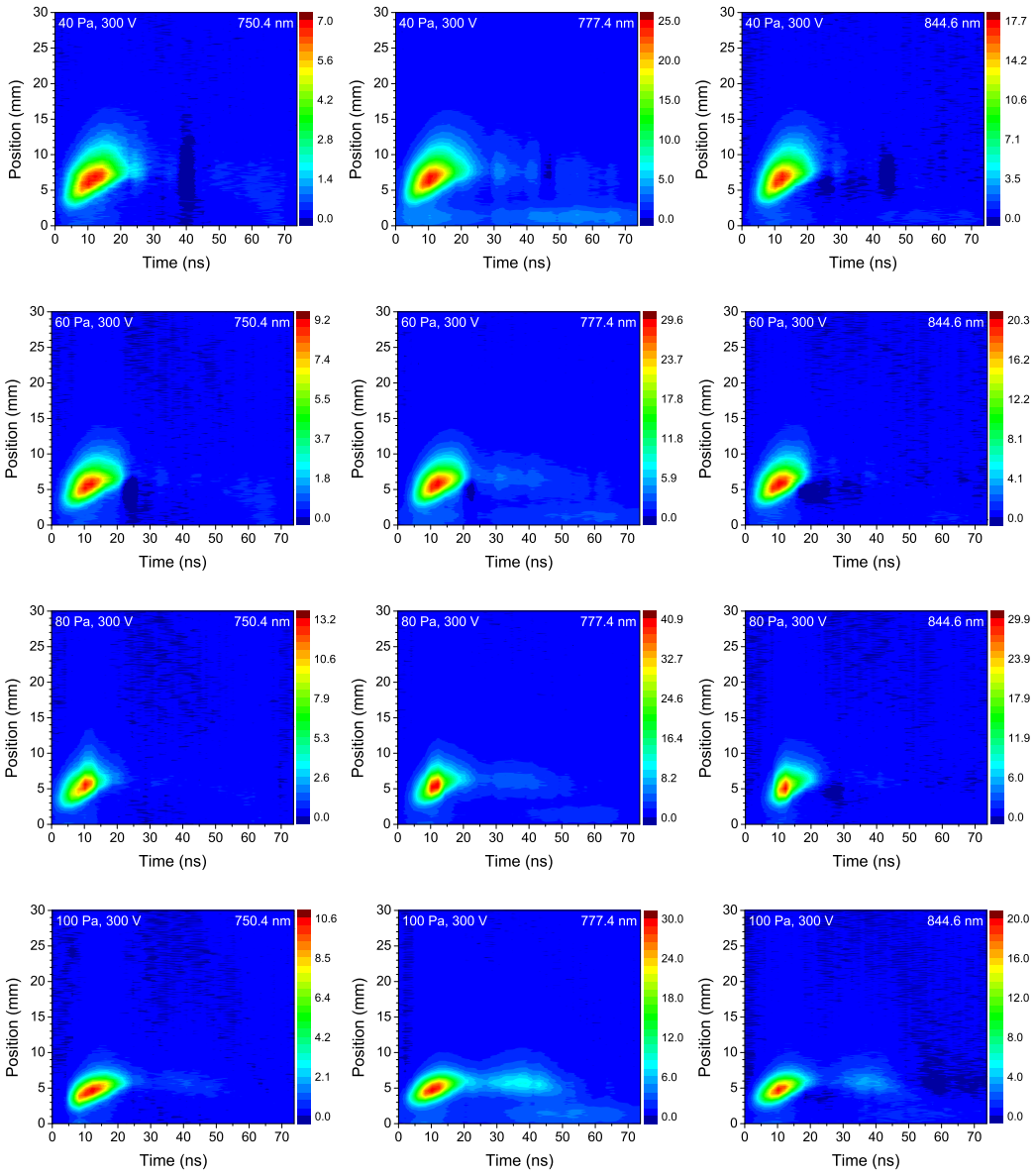

Figure B.4.: Phase resolved excitation into the $Ar(2p_1)$, $O(3p^5P)$, and $O(3p^3P)$ states using a silicon dioxide (SiO_2) wafer under pressure variation.

C. Optical Narrow Bandpass Filter Transmittance Data

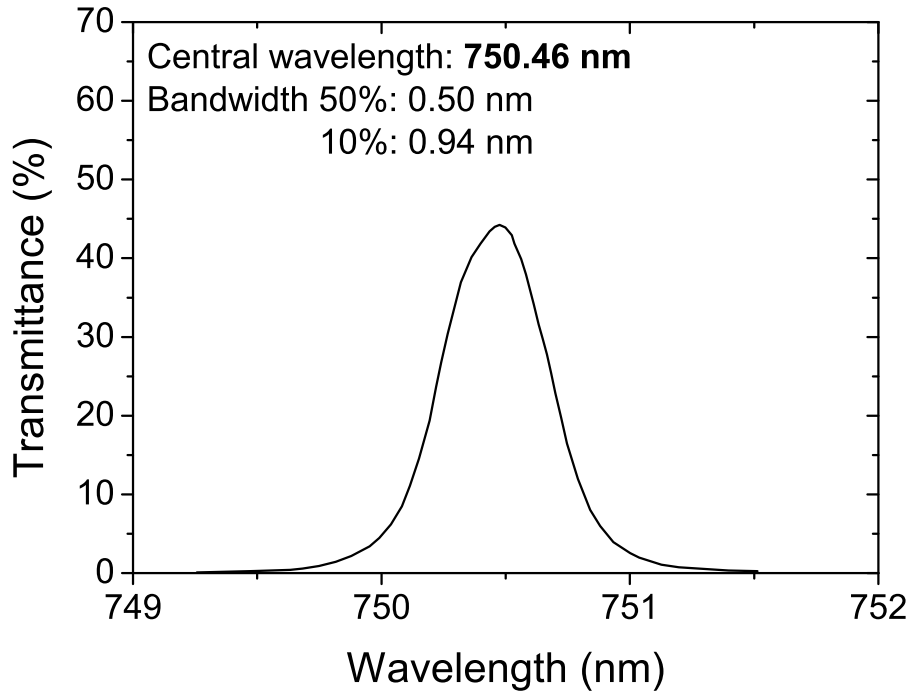

Figure C.1.: Transmittance data for (750.46 ± 0.50) nm optical bandpass filter.

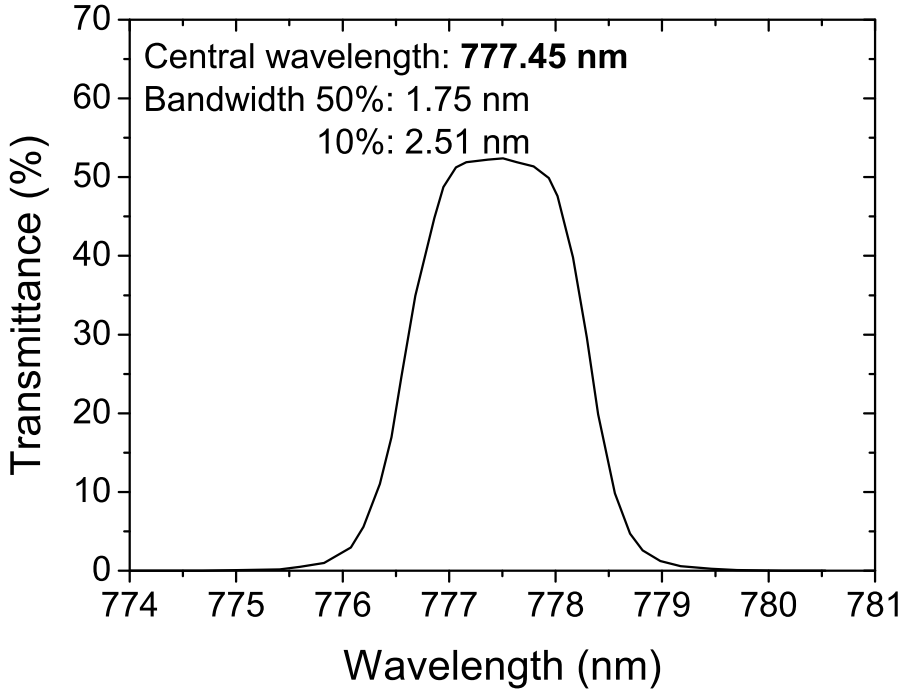

Figure C.2.: Transmittance data for (777.45 ± 1.75) nm optical bandpass filter.

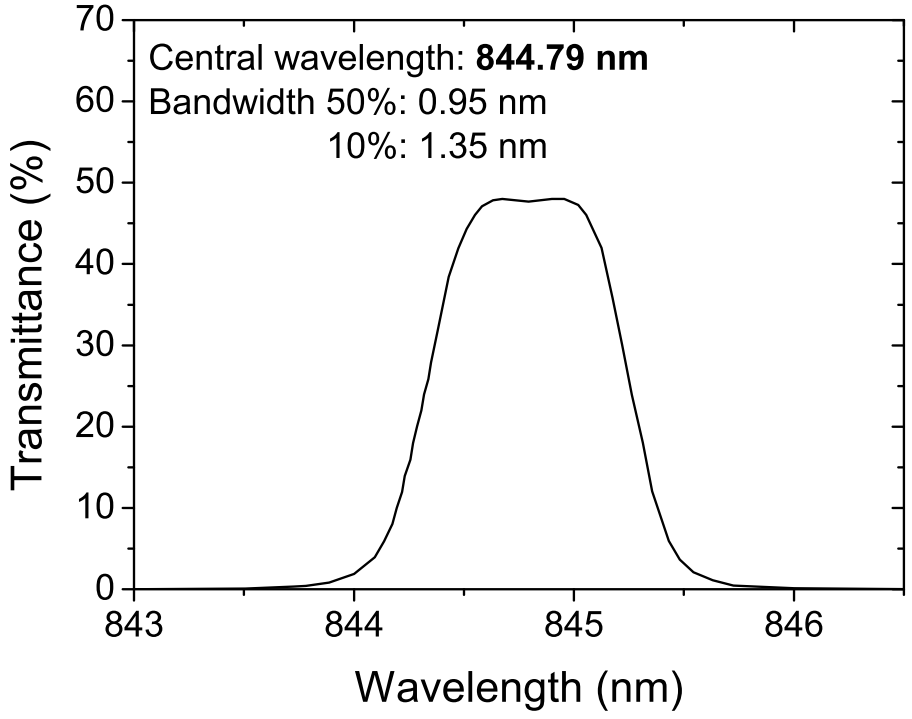

Figure C.3.: Transmittance data for (844.79 ± 0.95) nm optical bandpass filter.

D. List of Publications and Conference Contributions

Publications directly related to this work:

- *Improved fluid simulations of radio-frequency plasmas using energy dependent ion mobilities*
  A. Greb, K. Niemi, D. O'Connell, G.J. Ennis, N. MacGearailt, and T. Gans
  Phys. Plasmas **20**, 053502 (2013)

- *The influence of surface properties on the plasma dynamics in radio-frequency driven oxygen plasmas: measurements and simulations*
  A. Greb, K. Niemi, D. O'Connell, and T. Gans
  Appl. Phys. Lett. **103**, 244101 (2013)

Other publications:

- *Excitation dynamics of a kHz driven micro-structured plasma channel device operated in argon*
  A. Greb, H. Boettner, J. Winter, and V. Schulz-von der Gathen
  Plasma Sources Sci. Technol. **20** 055010 (2011)

Conference contributions:

- 2013:
  - Oral: *Novel diagnostic technique to probe atomic oxygen densities and electron energies simultaneously through the synergy of simulations and experiments*. TPW, York, UK, 16.-17. Dec.
  - Oral (**invited**): *Obtaining surface parameters through the synergy of simulations and measurements in capacitively coupled oxygen rf plasmas*. Intel IRC, Dublin, Ireland, 21.-22. Nov.
  - Oral: *The role of surface properties in the dynamics of radio-frequency plasma sheaths: measurements and simulations*. GEC, Princeton, USA, 30. Sep.-3. Oct.
    (American Physical Society Student Award for Excellence)
  - Oral: *New approaches for metrology in plasma processing*. EPS, Helsinki, Finland, 1.-5. Jul.
  - Poster: *Plasma Dynamics under Changing Surface Conditions*. IoP conference, York, UK, 25.-28. Mar.
- 2012:
  - Poster: *Study of plasma-surface interaction processes and their influence on plasma dynamics*. TPW, Milton Keynes, UK, 16.-17. Dec.
  - Poster: *Study of excitation and emission features in low pressure electronegative oxygen discharges with special regard to the actual electrode surface condition*. GEC, Austin, USA, 22.-26. Oct.
  - Oral (**invited**): *Understanding and Controlling Plasma-Surface Interaction Processes*. Intel IRC, Dublin, Ireland, 3.-4. Oct.
  - Poster: *Combination of Modelling and Simple Real-Time Measurements to Control Plasma-Surface Interaction Processes*. ICOPS, Edinburgh, UK, 8.-12. Jul.
  - Oral: *Plasma-surface interaction processes in electronegative low-pressure radio-frequency oxygen discharges*. IoP conference, Oxford, UK, 2.-5. Apr.

- Oral: *Influence of the metastable oxygen $O_2(^1\Delta)$ surface loss on plasma dynamics*. TPW, Manchester, UK, 5.-6. Jan.

- 2011:
  - Oral: *Surface loss probability of metastable oxygen and its impact on plasma dynamics*. WELTPP, Kerkrade, Netherlands, 1.-2. Dec.
  - Poster: *Discharge dynamics in a helium capacitively coupled plasma with variable oxygen admixture*. GEC, Salt Lake City, USA, 14.-18. Nov.
  - Oral (**invited**): *Modelling the surface condition for metastable oxygen destruction in a low pressure oxygen capacitively coupled plasma system*. Intel ERIC, Leixlip, Ireland, 12.-14. Oct.
  - Poster: *Modelling the surface conditions for metastable oxygen destruction in a low pressure oxygen capacitively coupled plasma system*. Intel ERIC, Leixlip, 12.-14. Oct.
  - Poster: *Influence of helium admixture on charged particle dynamics in an electronegative oxygen capacitively coupled plasma*. ICPIG, Belfast, UK, 28. Aug.-2. Sep.
  - Poster: *Comparison of excitation dynamics of two-dimensional kHz driven microstructured plasma devices operated in argon*. ICPIG, Belfast, UK, 28. Aug.-2. Sep.
  - Poster: *Impact of a variable oxygen admixture on dominant charged particle dynamics in a helium capacitively coupled radio frequency plasma*. Workshop on RF plasmas, Dublin, Ireland, 26.-27. Aug.
  - Oral: *Discharge dynamics of a micro-structured atmospheric pressure plasma channel*. International Workshop on Microplasmas, Paris, France, 3.-6. Apr.

List of Abbreviations

1D	One-dimensional
AC	Alternating current
C	Capacitor
CCD	Charge-Coupled Device
CCP	Capacitively coupled plasma
DC	Direct current
DD	Drift-Diffusion approximation
EEDF	Electron energy distribution function
FFT	Fast Fourier Transformation
FWHM	Full Width at Half Maximum
GEC	Gaseous Electronics Conference
ICCD	Intensified Charge-Coupled Device
LED	Light-Emitting Diode
MCC	Monte Carlo Collisions
MCP	Micro-Channel Plate
MFC	Mass Flow Controller
OES	Optical Emission Spectroscopy
PIC	Particle-in-Cell
PROES	Phase Resolved Optical Emission Spectroscopy
RCT	Relaxation Continuum
RF	Radio-Frequency
SDO	Singlet Delta Oxygen
TALIF	Two-Photon Absorption Laser-Induced Fluorescence
TTL	Transistor-Transistor Logic
VIH	Visible and near infrared region

Bibliography

[1] F. F. Chen, *Introduction to plasma physics and controlled fusion* (Springer, 2006), 2nd ed.

[2] M. A. Liebermann and A. J. Lichtenberg, *Principles of plasma discharges and materials processing* (John Wiley & Sons, Inc., 2005), 2nd ed.

[3] J. D. Cobine, *Gaseous Conductors: Theory and Engineering Applications* (Dover Publications, New York, 1958).

[4] R. Hippler, H. Kersten, M. Schmidt, and K. H. Schoenbach, *Low Temperature Plasmas. Fundamentals, Technologies, and Techniques*, vol. 1 and 2 (WILEY-VCH Verlag GmbH & Co KGaA, Weinheim, 2008), second, revised and enlarged ed.

[5] G. Chen and L. L. Raja, J. Appl. Phys **96**, 6073 (2004).

[6] M. A. Liebermann, IEEE Trans. Plasma Sci. **16**, 638 (1988).

[7] B. P. Wood, M. A. Liebermann, and A. J. Lichtenberg, IEEE Trans. Plasma Sci. **23**, 89 (1995).

[8] G. Gozadinos, M. M. Turner, and D. Vender, Phys. Rev. Lett. **87**, 135004 (2001).

[9] I. D. Kaganovich, O. V. Polomarov, and C. E. Theodosiou, Physics of Plasmas **11**, 2399 (2004).

[10] T. Mussenbrock and R. P. Brinkmann, Appl. Phys. Lett. **88**, 151503 (2006).

[11] C. D. Child, Phys. Rev. **32**, 0492 (1911).

[12] I. Langmuir, Phys. Rev. **2**, 450 (1913).

[13] G. Gozadinos, D. Vender., M. M. Turner, and M. A. Lieberman, Plasma Sources Sci. Technol. **10**, 117 (2001).

[14] V. A. Godyak and N. Sternberg, IEEE Trans. Plasma Sci. **18**, 159 (1990).

[15] P. Chabert, J. Phys. D: Appl. Phys. **40**, R63 (2007).

[16] M. M. Turner and P. Chabert, Plasma Sources Sci. Technol. **16**, 364 (2007).

[17] A. Salabas and R. P. Brinkmann, Jpn. J. Appl. Phys. **45**, 5203 (2006).

[18] T. Gans, Ph.D. thesis, University of Essen, Germany (2001).

[19] R. H. Huddlestone and S. Leonard, *Plasma Diagnostics Techniques* (Academic Press, New York, 1965).

[20] W. Lochte-Holtgreven, *Plasma Diagnostics* (North-Holland, Amsterdam, 1968).

[21] I. H. Hutchinson, *Principles of Plasma Diagnostics* (Cambridge University Press, New York, 2002), 2nd ed.

[22] V. Alekseev and D. W. Setser, J. Chem. Phys. **100**, 5766 (1996).

[23] V. Alekseev and D. W. Setser, J. Chem. Phys. **105**, 4613 (1996).

[24] W. Demtröder, *Laserspektroskopie, Grundlagen und Techniken* (Springer-Verlag, Berlin, 1993).

[25] G. Zikratov and D. W. Setser, J. Chem. Phys. **104**, 2243 (1996).

[26] M. B. Faist and R. B. Bernstein, J. Chem. Phys. **64**, 3924 (1976).

[27] M. B. Faist and R. B. Bernstein, J. Chem. Phys. **64**, 2971 (1976).

[28] M. J. Wouters, J. Khachan, I. S. Falconer, and B. W. James, J. Phys. B: At. Mol. Opt. Phys. **32**, 2869 (1999).

[29] V. N. Ochkin, *Spectroscopy of Low Temperature Plasmas* (WILEY-VCH Verlag GmbH & Co KGaA, Weinheim, 2009).

[30] H. R. Griem, *Principles of Plasma Spectroscopy* (Cambridge University Press, New York, 1997).

[31] W. R. Harshbarger, R. A. Porter, T. A. Miller, and P. Norton, Appl. Spectrosc. **31**, 201 (1977).

[32] J. W. Coburn and M. Chen, J. Appl. Phys. **51**, 3134 (1980).

[33] J. P. Booth, O. Joubert, J. Pelletier, and N. Sadeghi, J. Appl. Phys. **69**, 618 (1991).

[34] H. M. Katsch, A. Tewes, A. Goehlich, T. Kawetzki, E. Quandt, and H. F. Döbele, J. Appl. Phys. **88**, 6232 (2000).

[35] K. J. Taylor and G. R. Tynan, J. Vac. Sci. Technol. A **23**, 643 (2005).

[36] A. Ershov and J. Borysow, Plasma Sources Sci. Technol. **16**, 798 (2007).

[37] K. Niemi, S. Reuter, L. M. Graham, J. Waskoenig, and T. Gans, Appl. Phys. Lett. **95**, 151504 (2009).

[38] J. Conway, S. Kechkar, N. O. Connor, C. Gaman, M. M. Turner, and S. Daniels, Plasma Sources Sci. Technol. **22**, 045004 (2013).

[39] J. E. Chilton, J. B. Boffard, R. S. Schappe, and C. C. Lin, Phys. Rev. A **57**, 267 (1998).

[40] R. R. Laher and F. R. Gilmore, J. Phys. Chem. Ref. Data **19**, 277 (1990).

[41] M. B. Schulman, F. A. Sharpton, S. Chung, C. C. Lin, and L. W. Anderson, Phys. Rev. A **32**, 2100 (1985).

[42] C. K. Birdsall and A. B. Langdon, *Plasma Physics via Computer Simulation* (McGraw-Hill, New York, 1985).

[43] M. A. Lieberman, J. Appl. Phys. **66**, 2926 (1989).

[44] A. J. Lichtenberg, V. Vahedi, M. A. Lieberman, and T. Rognlien, J. Appl. Phys. **75**, 2339 (1994).

[45] Y. Sakiyama, D. B. Graves, and E. Stoffels, J. Phys. D: Appl. Phys. **41**, 095204 (2008).

[46] K. Niemi, J. Waskoenig, N. Sadeghi, T. Gans, and D. O'Connell, Plasma Sources Sci. Technol. **20**, 055005 (2011).

[47] R. W. Hockney and J. W. Eastwood, *Computer Simulation Using Particles* (McGraw-Hill, New York, 1981).

[48] J. P. Verboncoeur, Plasma Phys. Control. Fusion **47**, A231 (2005).

[49] J. P. Boeuf, Phys. Rev. A **36**, 2782 (1987).

[50] T. Makabe, N. Nakano, and Y. Yamaguchi, Phys. Rev. A **45**, 2520 (1992).

[51] T. Makabe, *Advances in Low Temperature RF Plasmas: Basis for Process Design* (Elsevier, Amsterdam, 2002).

[52] H. C. Kim, F. Iza, S. S. Yang, M. Radmilovic-Radjenovic, and J. K. Lee, J. Phys. D: Appl. Phys. **38**, R283 (2005).

[53] G. J. M. Hagelaar and L. C. Pitchford, Plasma Sources Sci. Technol. **14**, 722 (2005).

[54] D. O'Connell, R. Zorat, A. R. Ellingboe, and M. M. Turner, Phys. Plasmas **14**, 103510 (2007).

[55] M. Zaka-ul-Islam, K. Niemi, T. Gans, and D. O'Connell, Appl. Phys. Lett. **99**, 041501 (2011).

[56] K. Dittmann, Ph.D. thesis, Ernst-Moritz-Arndt-Universität Greifswald, Germany (2009).

[57] P. A. Miller, G. A. Hebner, K. E. Greenberg, P. D. Pochan, and B. P. Aragon, J. Res. Natl. Inst. Stand. Technol. **100**, 427 (1995).

[58] J. Meunier, P. Belenguer, and J. P. Boeuf, J. Appl. Phys. **78**, 731 (1995).

[59] J. P. Boeuf and L. C. Pitchford, Phys. Rev. E **51**, 1376 (1995).

[60] R. Veerasingam, R. B. Campbell, and R. T. McGrath, Plasma Sources Sci. Technol. **6**, 157 (1997).

[61] J. Waskoenig, K. Niemi, N. Knake, L. M. Graham, S. Reuter, V. Schulz-von der Gathen, and T. Gans, Plasma Sources Sci. Technol. **19**, 045018 (2010).

[62] X. Yuan and L. L. Raja, IEEE Trans. Plasma Sci. **31**, 495 (2003).

[63] S. Yonemura and K. Nanbu, IEEE Trans. Plasma Sci. **31**, 479 (2003).

[64] B. G. Heil, U. Czarnetzki, R. P. Brinkmann, and T. Mussenbrock, J. Phys. D: Appl. Phys. **41**, 165202 (2008).

[65] T. Lafleur and J. P. Booth, J. Phys. D: Appl. Phys. **45**, 395203 (2012).

[66] Y. P. Raizer and M. N. Shneider, High Temperature **29**, 833 (1991).

[67] W. M. Haynes, ed., *CRC Handbook of Chemistry and Physics* (CRC Press/Taylor and Francis, Boca Raton, Internet Version 2014), 94th ed.

[68] M. Konuma, *Film Deposition by Plasma Techniques* (Springer, New York, 1992).

[69] K. Wittmaack, Surf. Sci. **419**, 249 (1999).

[70] H. D. Hagstrum, Phys. Rev. **119**, 940 (1960).

[71] *Electron Scattering Database* (retrieved August 8, 2013), URL `http://www.lxcat.laplace.univ-tlse.fr/database.php`.

[72] A. V. Phelps, J. Chem. Phys. **69**, 1055 (1978).

[73] W. P. Allis, Phys. Rev. A **26**, 1704 (1982).

[74] L. C. Pitchford, S. V. ONeil, and J. R. Rumble, Jr., Phys. Rev. A **23**, 294 (1981).

[75] E. W. McDaniel, *Collision Phenomena in Ionized Gases* (Wiley, New York, 1964).

[76] P. Langevin, Ann. Chim. Phys. **28**, 289 (1903).

[77] P. Langevin, Ann. Chim. Phys. **5**, 245 (1905).

[78] S. Chapman, Phil. Trans. Roy. Soc. (London) A **216**, 279 (1916).

[79] S. Chapman and T. G. Cowling, *The Mathematical Theory of Non-Uniform Gases* (Cambridge University Press, London, 1952), 2nd ed.

[80] G. H. Wannier, Bell Syst. Tech. J. **32**, 170 (1953).

[81] H. W. Ellis, R. Y. Pai, E. W. McDaniel, E. A. Mason, and L. A. Viehland, At. Data Nucl. Data Tables **17**, 177 (1976).

[82] H. W. Ellis, M. G. Thackston, E. W. McDaniel, and E. A. Mason, At. Data Nucl. Data Tables **31**, 113 (1984).

[83] W. Lindinger and D. L. Albritton, J. Chem. Phys. **62**, 3517 (1975).

[84] A. F. Ferguson and B. L. Moiseiwitsch, Proc. Phys. Soc. **74**, 457 (1959).

[85] E. C. Beaty and P. L. Patterson, Phys. Rev. **137**, A346 (1964).

[86] J. E. Jones, Proc. R. Soc. Lond. A **106**, 463 (1924).

[87] J. Perrin, O. Leroy, and M. C. Bordage, Contrib. Plasma Phys. **36**, 3 (1996).

[88] R. C. Reid, J. M. Prausnitz, and B. E. Poling, *The Properties of Gases and Liquids* (McGraw-Hill, New-York, 1954), 4th ed.

[89] R. J. Kee, G. Dixon-Lewis, J. Warnatz, M. E. Coltrin, and J. A. Miller, SANDIA Report (1986).

[90] N. C. Bera, I. Bhattacharyya, and A. K. Das, Int. J. Quantum Chem. **107**, 824 (2007).

[91] J. H. Whealton, E. A. Mason, and R. E. Robson, Phys. Rev. A **9**, 1017 (1974).

[92] L. A. Viehland and E. A. Mason, Ann. Phys. **91**, 499 (1975).

[93] N. S. J. Braithwaite, Plasma Sources Sci. Technol. **9**, 517 (2000).

[94] *COMSOL Multiphysics*, COMSOL Ltd., Cambridge CB3 0FA, UK (2013).

[95] C. Johnson, *Numerical Solution of Partial Differential Equations by the Finite Element Method* (Cambridge University Press, 1988).

[96] O. C. Zienkiewicz, R. L. Taylor, and P. Nithiarasu, *The Finite Element Method for Fluid Dynamics* (Elsevier, 1991).

[97] *MathWorks MATLAB*, MathWorks, Cambridge CB4 0HH, UK (2013).

[98] K. Niemi, S. Reuter, L. M. Graham, J. Waskoenig, N. Knake, V. Schulz-von der Gathen, and T. Gans, J. Phys. D: Appl. Phys. **43**, 124006 (2010).

[99] D. Vender, W. W. Stoffels, E. Stoffels, G. M. W. Kroesen, and F. J. de Hoog, Phys. Rev. E: Stat., Nonlinear, Soft Matter Phys. **51**, 2436 (1995).

[100] E. Stoffels, W. W. Stoffels, D. Vender, M. Kando, G. M. W. Kroesen, and F. J. de Hoog, Phys. Rev. E: Stat., Nonlinear, Soft Matter Phys. **51**, 2425 (1995).

[101] B. F. Gordiets, C. M. Ferreira, V. L. Guerra, J. M. A. H. Loureiro, J. Nahorny, D. Pagnon, M. Touzeau, and M. Vialle, IEEE Trans. Plasma Sci. **23**, 750 (1995).

[102] L. Vriens, Phys. Lett. **8**, 260 (1964).

[103] R. Deloche, P. Monchicourt, M. Cheret, and F. Lambert, Phys. Rev. A **13**, 1140 (1976).

[104] K. A. Berrington, P. G. Burke, L. C. G. Freitas, and A. E. Kingston, J. Phys. B: At. Mol. Phys. **18**, 4135 (1985).

[105] F. Emmert, H. H. Angermann, R. Dux, and H. Langhoff, J. Phys. D: Appl. Phys. **21**, 667 (1988).

[106] V. Vahedi and M. Surendra, Comput. Phys. Commun. **87**, 179 (1995).

[107] D. Rapp and D. D. Briglia, J. Chem. Phys. **43**, 1480 (1965).

[108] F. X. Bronold, K. Matyash, D. Tskhakaya, R. Schneider, and H. Fehske, J. Phys. D: Appl. Phys. **40**, 6583 (2007).

[109] D. S. Stafford and M. J. Kushner, J. Appl. Phys. **96**, 2451 (2004).

[110] J. M. Pouvesle, A. Khacef, J. Stevefelt, H. Jahani, V. T. Gylys, and C. B. Collins, J. Chem. Phys. **88**, 3061 (1988).

[111] J. Waskoenig and T. Gans, Appl. Phys. Lett. **96**, 181501 (2010).

[112] H. M. Katsch, T. Sturm, E. Quandt, and H. F. Döbele, Plasma Sources Sci. Technol. **9**, 323 (2000).

[113] S. Nemschokmichal, K. Dittmann, and J. Meichsner, IEEE Trans. Plasma Sci. **36**, 1360 (2008).

[114] F. C. Fehsenfeld, D. L. Albritton, J. A. Burt, and H. I. Schiff, Can. J. Chem. **47**, 1793 (1969).

[115] J. Waskoenig, Ph.D. thesis, Queen's University Belfast, UK (2010).

[116] K. Dittmann, K. Matyash, S. Nemschokmichal, J. Meichsner, and R. Schneider, Contrib. Plasma Phys. **50**, 942 (2010).

[117] K. Matyash, R. Schneider, F. Taccogna, A. Hatayarna, S. Longo, M. Capitelli, D. Tskhakaya, and F. X. Bronold, Contrib. Plasma Phys. **47**, 595 (2007).

[118] S. V. Berezhnoj, C. B. Shin, U. Buddemeier, and I. Kaganovich, Appl. Phys. Lett. **77**, 800 (2000).

[119] H. M. Katsch, A. Goehlich, T. Kawetzki, E. Quandt, and H. F. Döbele, Appl. Phys. Lett **75**, 2023 (1999).

[120] C. Küllig, K. Dittmann, and J. Meichsner, Plasma Sources Science and Technology **19**, 065011 (2010).

[121] M. Shibata, N. Nakano, and T. Makabe, J. Appl. Phys. **80**, 6142 (1996).

[122] Y. Sakiyama and D. B. Graves, J. Appl. Phys. **101**, 073306 (2007).

[123] J. J. Shi and M. G. Kong, J. Appl. Phys. **97**, 023306 (2005).

[124] J. T. Gudmundsson, A. M. Marakhtanov, K. K. Patel, V. P. Gopinath, and M. A. Liebermann, J. Phys. D: Appl. Phys. **33**, 3010 (2000).

[125] A. Greb, K. Niemi, D. O'Connell, G. J. Ennis, N. MacGearailt, and T. Gans, Phys. Plasmas **20**, 053502 (2013).

[126] S. G. Belostotsky, D. J. Economou, D. V. Lopaev, and T. V. Rakhimova, Plasma Sources Sci. Technol. **14**, 532 (2005).

[127] A. Midey, I. Dotan, S. Lee, W. T. Rawlins, M. A. Johnson, and A. A. Viggiano, J. Phys. Chem. A **111**, 5218 (2007).

[128] A. Midey, I. Dotan, and A. A. Viggiano, J. Phys. Chem. A **112**, 3040 (2008).

[129] R. P. Wayne, *Singlet molecular oxygen - Advances in Photochemistry*, vol. 7 (Wiley-Interscience, New-York, 1969).

[130] D. R. Kearns, Chem. Rev. **71**, 395 (1971).

[131] T. G. Slanger and G. Black, Geophys. Res. Lett. **8**, 535 (1981).

[132] M. E. Ryskin and B. R. Shub, React. Kinet. Catal. Lett. **17**, 41 (1981).

[133] A. A. Ionin, I. V. Kochetov, A. P. Napartovich, and N. N. Yuryshev, J. Phys. D: Appl. Phys. **40**, R25 (2007).

[134] R. L. Sharpless and T. G. Slanger, J. Chem. Phys. **91**, 7947 (1989).

[135] P. J. Chantry, J. Appl. Phys. **62**, 1141 (1987).

[136] S. M. Newman, A. J. Orr-Ewing, D. A. Newnham, and J. Ballard, J. Phys. Chem. A **104**, 9467 (2000).

[137] A. J. Lichtenberg, M. A. Liebermann, I. G. Kouznetsov, and T. H. Chung, Plasma Sources Sci. Technol. **9**, 45 (2000).

[138] J. T. Gudmundsson, A. M. Marakhtanov, K. K. Patel, V. P. Gopinath, and M. A. Lieberman, J. Phys. D: Appl. Phys. **33**, 1323 (2000).

[139] D. L. Flamm and V. M. Donnelly, J. Appl. Phys. **59**, 1052 (1986).

[140] E. Gogolides, J. P. Nicolai, and H. H. Sawin, J. Vac. Sci. Technol. A **7**, 1001 (1989).

[141] T. Gans, D. O'Connell, J. Schulze, V. A. Kadetov, and U. Czarnetzki, AIP Conf. Proc. **876**, 260 (2006).

[142] J. K. Olthoff and K. E. Greenberg, J. Res. Natl. Inst. Stand. Technol. **100**, 327 (1995).

[143] T. Gans, D. O'Connell, V. Schulz-von der Gathen, and J. Waskoenig, Plasma Sources Sci. Technol. **19**, 034010 (2010).

[144] C. M. O. Mahony, R. Al Wazzan, and W. G. Graham, Appl. Phys. Lett. **71**, 608 (1997).

[145] J. B. Shumaker, Jr. and C. H. Popenoe, J. Opt. Soc. Am. **57**, 8 (1967).

[146] N. Sadeghi., D. W. Setser, A. Francis, U. Czarnetzki., and H. F. Döbele, J. Chem. Phys. **115**, 3144 (2001).

[147] A. Hibbert, E. Biémont, M. Godefroid, and N. Vaeck, J. Phys. B: At. Mol. Opt. Phys. **24**, 3943 (1991).

[148] P. J. Dagdigian, B. E. Forch, and A. W. Miziolek, Chem. Phys. Lett. **148**, 299 (1988).

[149] K. Niemi, V. Schulz-von der Gathen, and H. F. Döbele, Plasma Sources Sci. Technol. **14**, 375 (2005).

[150] H. A. Macleod, *Thin-film optical filters* (Taylor and Francis Group, LLC, 2010), 4th ed.

[151] H. Y. Joo, H. J. Kim, S. J. Kim, and S. Y. Kim, Thin Solid Films **368**, 67 (2000).

[152] D. J. Poxson, F. W. Mont, M. F. Schubert, J. K. Kim, J. Cho, and E. F. Schubert, Optical Express **18**, A596 (2010).

[153] M. V. Jacoba, N. S. Olsen, L. J. Anderson, K. Bazaka, and R. A. Shanks, Thin Solid Films **Article in Press** (2013).

[154] R. J. D'Arcy and N. A. Surplice, Surface Science **34**, 193 (1973).

[155] J. Lindmayer, Solid-State Electronics **8**, 523 (1965).

[156] V. S. Fomenko, *Handbook of thermionic properties* (Plenum Press Data Devision, New York, 1966).

[157] R. Yan, Q. Zhang, W. Li, I. Calizo, T. Shen, C. A. Richter, A. R. Hight-Walker, X. Liang, A. Seabaugh, D. Jena, et al., Appl. Phys. Lett. **101**, 022105 (2012).

[158] D. A. Seanor, *Polymer Science*, vol. 2 (North-Holland, London, 1972).

[159] A. Wåhlin and G. Bäckström, J. Appl. Phys. **45**, 2058 (1974).

[160] P. J. Hargis, K. E. Greenberg, P. A. Miller, J. B. Gerardo, J. R. Torczynski, M. E. Riley, G. A. Hebner, J. R. Roberts, J. K. Olthoff, J. R. Whetstone, et al., Rev. Sci. Instrum. **65**, 140 (1994).

[161] D. A. Scott and A. V. Phelps, Phys. Rev. A **43**, 3043 (1991).

[162] A. Anders, Appl. Phys. Lett. **76**, 28 (2000).

[163] D. O'Connell, T. Gans, E. Semmler, and P. Awakowicz, Appl. Phys. Lett. **93**, 081502 (2008).

[164] M. Yan, A. Bogaerts, R. Gijbels, and W. J. Goedheer, J. Appl. Phys. **87**, 3628 (2000).

[165] K. Dittmann, C. Küllig, and J. Meichsner, Plasma Phys. Control. Fusion **54**, 124038 (2012).

[166] H. Bruining, *Physics and Applications of Secondary Electron Emission* (McGraw-Hill Book Co., Inc., New York, 1954).

[167] S. Wickramanayaka, N. Hosokawa, and Y. Hatanaka, Japanese Journal of Applied Physics **30**, 2897 (1991).

[168] J. C. Greaves and J. W. Linnett, Trans. Faraday Soc. **55**, 1355 (1959).

[169] J. P. Booth and N. Sadeghi, J. Appl. Phys. **70**, 611 (1991).

[170] S. Gomez, P. G. Steen, and W. G. Graham, Appl. Phys. Lett. **81**, 19 (2002).

[171] H. M. Katsch, C. Manthey, and H. F. Döbele, Plasma Sources Sci. Technol. **12**, 475 (2006).

[172] A. Descoeudres, L. Sansonnens, and C. Hollenstein, Plasma Sources Sci. Technol. **12**, 152 (2003).

[173] L. Minnhagen, J. Opt. Soc. Am. **63**, 1185 (1973).

[174] V. Margetić and D. Veža, Fizika A **7**, 49 (1998).

[175] C. E. Moore, *Tables of Spectra of Hydrogen, Carbon, Nitrogen, and Oxygen Atoms and Ions in CRC Series in Evaluated Data in Atomic Physics* (CRC Press, Boca Raton, FL, 1993).